UNIVERSITÀ DELLA CALABRIA

Dipartimento di Ingegneria Civile

Dottorato di Ricerca in

Ingegneria Civile e Industriale

XXXII CICLO

POST-FAILURE ANALYSIS OF LANDSLIDES USING THE MATERIAL POINT METHOD

Settore Scientifico Disciplinare: ICAR/07

Coordinatore: Ch.mo Prof. Franco Furgiuele

Supervisore/Tutor: Ch.mo Prof. Antonello Troncone

Dottorando: Dott. Luigi Pugliese

UNIVERSITÀ DELLA CALABRIA

UNIVERSITÀ DELLA CALABRIA

Dipartimento di Ingegneria Civile

Dottorato di Ricerca in

Ingegneria Civile e Industriale

XXXII CICLO

POST-FAILURE ANALYSIS OF LANDSLIDES USING THE MATERIAL POINT METHOD

Settore Scientifico Disciplinare: ICAR/07

Coordinatore: Ch.mo Prof. Franco Furgiuele

Firma 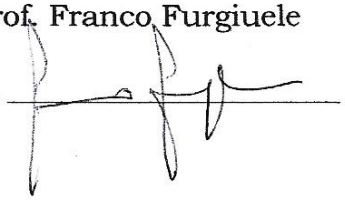

Supervisore/Tutor: Ch.mo Prof. Antonello Troncone

Firma 

Dottorando: Dott. Luigi Pugliese

Firma 

Acknowledgment

The work presented in this research has been developed under the thorough supervision of Professor Antonello Troncone, who has always guided me with perseverance and dedication. Therefore, I would like to express my sincere gratitude to him for his guidance, for believing in me and for the trust he has always been putting on me.

Abstract

Slope stability analysis is undoubtedly one of the most complex problems that civil engineers deal with. The evolution of deformation mechanisms of slopes is commonly schematized in four different stages: pre-failure, failure, post-failure and eventual reactivation. Traditional numerical methods, such as the finite element method and the finite difference method, are commonly employed to analyze the slope response in the pre-failure and failure stages under the hypothesis of small deformations. On the other hand, these methods are unsuitable for simulating the post-failure behavior due to the occurrence of large deformations. However, an adequate analysis of this latter stage and a reliable prediction of the landslide kinematics could be particularly useful for minimizing the associated risk or to establish the most suitable mitigation measures for land protection.

Among the numerical techniques which have been recently developed to overcome the above-mentioned limitation, the material point method (MPM) is employed in this dissertation to analyze the post-failure stage of two real landslides: the Senise landslide (Basilicata) and the Maierato landslide (Calabria), both in Southern Italy, occurred in 1986 and 2010, respectively. The numerical analyses allow to faithfully simulate the real phenomena.

In particular, with referring to the Senise landslide, the numerical analysis provides results that match satisfactorily well the field observations when both the slip surfaces detected by the installed inclinometers are accounted for. Besides, the lowest values of the shear strength parameters obtained from the laboratory tests have to be used. Moreover, an improvement of results is gained accounting for the presence of the existing structures as well.

Concerning the Maierato landslide, symbol of the hydrogeological instability in Calabria (Southern Italy), the analysis performed using the material point method allows to successfully simulate the observed phenomenon, despite the complexity of this landslide regarding its size, catastrophic failure and long run-out distance.

The obtained results demonstrate that an adequate analysis of the post-failure stage can lead to a better understanding of the complex mechanical mechanisms that characterize some landslides, and therefore help significantly to establish the most effective stabilization measures.

Sommario

L'analisi di stabilità dei pendii naturali ed artificiali è senza dubbio uno dei problemi più complessi che un ingegnere civile si trova ad affrontare. L'evoluzione dei processi deformativi dei pendii viene generalmente schematizzata in quattro fasi: pre-rottura, rottura, post-rottura ed eventuale riattivazione. I metodi numerici tradizionali, quali il metodo degli elementi finiti ed il metodo delle differenze finite, vengono generalmente utilizzati per studiare la risposta del pendio nelle fasi di pre-rottura e rottura nell'ipotesi di piccole deformazioni. Tuttavia, tali metodi sono per loro natura del tutto incapaci di simulare la fase post-rottura a causa dei grandi valori di deformazione e spostamento che spesso la caratterizzano. Un'analisi adeguata del comportamento post-rottura ed un'affidabile predizione della cinematica di un fenomeno franoso risultano di particolare importanza per valutare il rischio ad esso connesso e per progettare i più idonei interventi di mitigazione del rischio frana.

Tra le tecniche numeriche di recente sviluppo finalizzate al superamento delle suddette limitazioni, il metodo del punto materiale (MPM) è applicato in tale tesi per analizzare la fase post-rottura di due frane reali: la frana di Senise (Potenza, Basilicata) e la frana di Maierato (Vibo Valentia, Calabria), verificatesi rispettivamente nel 1986 e nel 2010. Le analisi numeriche consentono di simulare fedelmente i due fenomeni franosi.

Nello specifico, con riferimento alla frana di Senise, le simulazioni numeriche rendono conto del fenomeno realmente occorso quando entrambe le superfici di scorrimento, rilevate dalle misure inclinometriche, vengono portate in conto nelle analisi. Inoltre, è necessario utilizzare i valori più bassi dei parametri di resistenza al taglio tra quelli determinati dalle prove di laboratorio. In aggiunta, un miglioramento dei risultati si ottiene portando in conto anche la presenza delle strutture esistenti.

Per quanto riguarda la frana di Maierato, simbolo del dissesto idrogeologico in Calabria, le analisi eseguite con il metodo del punto materiale consentono di simulare con successo il fenomeno realmente occorso, nonostante la sua complessità relativamente a dimensioni, natura catastrofica e distanza percorsa dal corpo di frana.

In definitiva, i risultati ottenuti dimostrano che un'adeguata analisi della fase post-rottura delle frane può contribuire a migliorare significativamente la comprensione dei complessi processi meccanici che caratterizzano siffatti fenomeni, rappresentando in ottica predittiva un utile strumento per la definizione delle più idonee soluzioni progettuali per la mitigazione del rischio frana.

Index

Introduction

Stability analysis of natural and artificial slopes is undoubtedly one of the most complex problems that civil engineers have to deal with. Indeed, it is well known that deformation and failure mechanisms of slopes depend not only on physics, mechanics and structural characteristics of soil, but also on the evolution of the stress state (stress path) and the deformation state (velocity of deformation and progressive failure). Generally speaking, the evolution of deformation mechanisms of slopes is schematized in four different stages (Leroueil, 2001), in each of which the soil behavior is different and consequently the concerning criteria of analysis should be different. These stages are known as pre-failure, failure, post-failure and eventual reactivation.

Currently, the problem of slope stability is tackled in a simplified manner and it is simply reduced to failure and eventual reactivation stages, in order to employ simplified methods which are usually based on the limit equilibrium approach. It is well known that such methods are based on a model that is unsuitable to account for the complex mechanisms that lead the slope to failure, in which the material strength is independent on the level of deformation. Substantially, the analysis completely ignores the deformations occurring before the collapse, the progressive failure and the kinematics of the landslide body after the crisis, which both the risk and eventual measures of stabilization depend on.

Deformation and failure mechanisms of slopes can only be studied whereby numerical methods, capable to account for the numerous factors that influence the complex mechanic behavior of soils, and to simulate the formation and the progressive development of deformations that lead the slope to failure (pre-failure stage) as well as the kinematics of the landslide body after the collapse (post-failure stage).

Owing to these latter reasons, such aspects have a fundamental relevance and, until some years ago, they had been neglected in engineering practice due to the lack of adequate techniques of analysis as well as calculation tools which would allow the study of them. However, important progresses have been recently made and, therefore, advanced tools to satisfactorily deal with these problems have become available.

The employment of such tools is practically essential in order to account for the numerous factors that the behavior of soils depends on, such as non-linearity, irreversibility, water content, time dependency, progressive failure, behavior under large deformations, etc. This is such a relevant aspect from an engineering point of view, because it allows a more complete analysis of landslides and a more accurate design of eventual stabilization measures to be performed.

Among the main approaches currently used, it is possible to identify the Lagrangian and Eulerian ones. In the Lagrangian

approach, the continuum is discretized whereby a mesh whose deformation represents the one of the material. By contrast, in the Eulerian approach, the mesh, which has only a computational role, is kept fixed in space, rather the mass moves through it.

In research activities and especially in engineering practice, it is common the use of Lagrangian approaches in order to solve boundary problems. In particular, the most used one in geotechnical engineering field is the Finite Element Method (FEM) that allows the pre-failure, failure and reactivation stages to be properly analyzed. However, such method is unsuitable for dealing with the post-failure stage of landslides, especially when large values of displacements and deformations are involved, because also finite elements would be undergone large deformations and displacements and this would rapidly lead to a highly distorted mesh and as a consequence to an inaccurate calculation, characterized by the lack of convergence of the solution. Instead, by using an Eulerian approach, the difficulties related to the mesh distortion are overtaken. Then, such approach can be easily applied to solve problems characterized by large displacements. However, special procedures are required to identify interfaces between materials and the dependency on the load path, making such approach much more expensive from a computational point of view, if compared with the Lagrangian one (Zhang et al. (2017)).

Recently, more and more advanced numerical methods have been developed, in order to take advantages from both Eulerian and Lagrangian approaches, avoiding the shortcomings of each. Among these methods, the one chosen to work with in this dissertation is the Material Point Method (MPM), which was initially introduced by Sulsky et al. ((1994); (1995)) and which is suitable to be successfully applied in the geotechnical engineering field and, therefore, to study extreme events such as the post-failure stage of landslides characterized by high values of displacement. In this method, the continuum body is discretized by a set of subdomains. The properties of each subdomain are concentrated in a Lagrangian point, called material point. Besides, a background fixed Eulerian mesh is required only to solve governing equations. Soil displacements are simulated by means of material points moving throughout the computational mesh.

Different authors have recently published several papers about the material point method. Many of them (Maljaars et al., (2017); Kularathna & Soga (2017); Redaelli et al., (2017); Wobbes at al., (2018), among others) focus the attention on theoretical aspects, numerical features and new developments. Different applications are available as well in the literature (Wang et al., (2016); Fern et al., (2017); Martinelli et al., (2017); Troncone et. al., (2019); among others), which however refer to ideal cases study or to real slopes

characterized by extremely simple geometries. On the other hand, it would be extremely interesting from an engineering point of view to check the suitability of such a method for dealing with real problems, characterized by the common difficulties of geotechnical engineering. However, the application of the material point method to real and complex landslides is still limited to just few cases (Pinyol et al., (2018); Yerro et al., (2018)). In this connection, the goal of this dissertation consists in the validation of this interesting tool by applying it to analyze some real landslides of great dimensions, whose post-failure stage is characterized by extremely large displacements. Particularly, the material point method is applied in this dissertation in order to analyze the post-failure stage of two real landslides that occurred in Italy in 1986 and 2010, respectively. These landslides, which are characterized by many complications and uncertainties typical of geotechnical engineering, have obtained the attention of researchers from all over the world due to their catastrophic nature. They are the Senise landslide, which occurred after the execution of deep excavations causing eight fatalities, and the Maierato landslide that occurred after a long rainy period and that was outstanding by its size, catastrophic failure and long run-out distance.

The dissertation is subdivided into four chapters. The first chapter reports a literature review regarding deformation and failure

mechanisms of slopes, with particular attention to the description of the pre-failure, failure, post-failure and reactivation stages. Afterwards, the second chapter is devoted to the material point method. Particularly, the calculation scheme, mathematical formulation, integration schemes and numerical features are treated. Besides, in the final section of this chapter the main constitutive relationships used within this work are mentioned. Subsequently, the following chapters contain the innovative features of this work, i.e. the analyses of the post-failure stage of the Senise and Maierato landslides. Particularly, the Senise landslide is analyzed in Chapter 3, whereas the Maierato landslide is analyzed in Chapter 4. Both Chapters 3 and 4 report an extensive study of the concerning landslides (including the description of the area, the geomorphological aspects of the landslides, geological and geotechnical characteristics of the involved soils) as well as the analysis of their post-failure stage. Furthermore, for the sake of completeness, the analysis of the trigger phase of both landslides is reported as well.

Chapter 1 - Deformation and failure mechanisms of slopes

1.1 - Introduction

According to Skempton & Hutchinson (1969), the term *landslide* includes all down-slope movements, occurring as the result of shear failures at the boundary of the moving mass. Varnes (1978) and Cruden & Varnes (1996) proposed the system of landslide classification which has become the most widely used one all over the world. According to this system, landslides can be grouped into the following categories: *falls*, *topples*, *slides*, *lateral spreads*, *flows* and *complex landslides*. Movements of slopes represent a complex problem, indeed it can be considered one of the most difficult problems that a civil engineer can deal with, since a variety of geomaterial in a variety of geological and climatic contexts are involved. Even in the case of homogenous and continuous material, the behavior of slopes is still complex. Therefore, in order to simplify the analysis, Vaunat et al. (1994), Leroueil & Marques (1996) and Leroueil (2001) suggested dividing slope movements into four phases:

1) The pre-failure stage, which includes all the deformation mechanisms which precede and lead the slope to the

collapse. Deformations in this stage occur due to changes in stresses, creep and progressive failure.

2) The onset of failure, characterized by the formation of a continuous shear band through the entire soil mass, above which the unstable soil mass will slide.
3) The post-failure stage, including movements of the soil mass involved in the landslide, from the onset of failure until it stops, when a new condition of equilibrium is reached.
4) Eventual reactivation stages, which occur when a soil mass slides above a pre-existing slip surface.

Currently, in engineering practice, the problem of slope stability is simplified and only the failure stage and eventual reactivations are studied. Besides, the study of slope stability is only limited to those movements which can be classified as *slides*. This happens because the problem is restricted to the calculation of the *safety factor*, defined as the ratio of the average shear strength available on the slip surface to the average shear stress acting on the slip surface to ensure the equilibrium. This is the definition of safety factor commonly used within the context of *limit equilibrium methods*, in which all the quantities required to compute the safety factor are obtained only from the solution of the equilibrium equations, under simplified hypothesis which differentiate the different methods. The calculation is made without accounting for

neither the mechanical mechanisms that lead the slope to failure nor their consequences on the failure itself. Besides, the analysis neglect the kinematics of the landslide after the collapse, which both the risk and the eventual stabilization measures depend on (Esu, 1986).

For these reasons, in the more modern concept of the problem, such aspects are considered of paramount importance, and their analysis has been obtaining an increasingly stronger attention for the last decades from both researchers and engineers. Therefore, it is clear that an adequate understanding of mechanisms that control deformation and failure mechanisms cannot be disregarded. Indeed, it is possible to develop specific calculation tools capable to provide an adequate solution to the problem only when the scenario of the possible responses of the system to assigned changes of boundary and initial conditions is defined. Therefore, although the aim of this dissertation is the numerical modelling of deformation and failure mechanisms of slopes, it has been considered worthwhile to dedicate this chapter to their description. In particular, the following sections are dedicated to the description of the four stages previously mentioned as well as to the description of the movement and failure mechanisms of the two most common landslides: an excavation–induced landslide and a rainfall induced landslide.

1.2 - Movements and failure mechanisms of slopes

1.2.1 – The pre-failure stage

This phase includes all the deformations and displacements that occur before a first-time failure, and which could result from a combination of different phenomena: elasto-plastic deformations associated with changes in effective stresses, viscous deformations and strains and displacements associated with progressive failure.

In the literature, there is evidence of many landslides that were characterized by creep movements during the pre-failure phase in soft clays (see Eden (1977), Tavenas (1984), Moller et al. (1989), Ottosson & Johansson (1995), Demers et al. (1999)) but also in stiff clays and rock masses (see Terzaghi (1950), Nemcok et al. (1972), Varnes (1978)). As documented by Leroueil (2001) from both laboratory tests and *in situ* investigations, such deformations increase when failure is to be approached.

One of the most common and important phenomenon which affects the pre-failure phase is, undoubtedly, the *progressive failure*, which occurs when the following necessary conditions are satisfied: brittleness of soil, non-uniformity in the distribution of the shear stresses, local shear stresses that exceed the peak strength of the soil and boundary conditions such that strains exceeding that at failure might develop.

Brittleness is a characteristic of many natural soils, such as overconsolidated soils and weak rocks. Besides, owing to the geometry of the problem, the distribution of shear stresses is not uniform within slopes, and therefore above a potential slip surface. Initially, Terzaghi & Peck (1948) recognized the progressive failure, but such phenomenon was not completely understood until the works of Skempton (1964), Bjerrum (1967) and Bishop (1967). After their contributions, the progressive failure can be summed up as mentioned in the following.

If shear stresses locally reach the peak shear strength of the material, there is a local failure. If the soil is characterized with a strain softening behavior, the failed soil will support a decreasing shear stress as strain increases (see Figure 1.1).

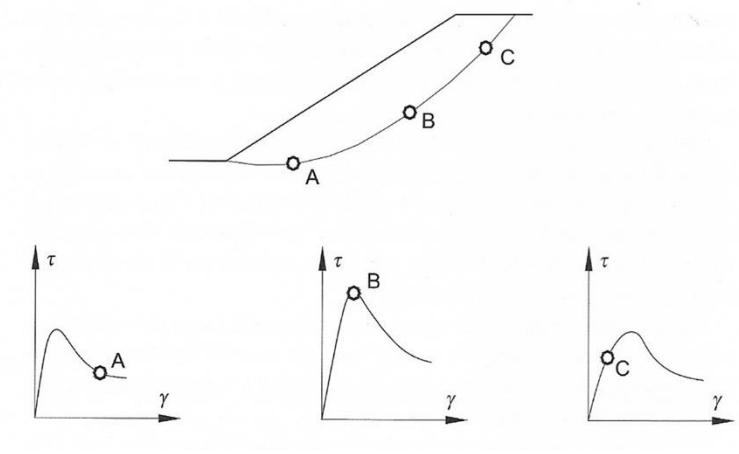

Figure 1.1 – Progressive failure within a slope (from Lancellotta (2011))

The part of the shear stress that is no longer supported by the failed elements is then transferred to the neighboring soil elements, which can reach the failure in turn. This process continues until an equilibrium condition between shear stresses

and strain is reached. At this time, along a potential slip surface, part of it can exceed the peak, with possibly some elements at large deformation or residual strength, whereas another part of the potential surface has not reached the peak yet. If such equilibrium cannot be reached, the process will continue until the failure condition extends along the entire failure surface. Even if a condition of equilibrium seems to exist at a given time, it can be modified and the progressive failure can continue.

This situation could happen due to: a change in the geometry of the problem and in shear stresses (for instance, erosion at the toe or loading at the top of a slope); a decrease in normal effective stress, and thus in peak and residual strength (for instance, excavation during pore pressure equilibration or pore pressure increase in general); a decrease in strength parameters (for instance, due to creep, fatigue or weathering).

The major factor in the development of progressive failure is constituted by brittleness, which can be characterized by the brittleness index, introduced by Bishop (1967):

$$I_B = \frac{\tau_p - \tau_r}{\tau_p} \tag{1.1}$$

where τ_p and τ_r are the peak and residual strengths defined under the same effective normal stress. Vaughan & Hamza (1977) and Chandler (1984) stated that the brittle index alone is not sufficient to characterize the susceptibility of a soil to progressive failure. The rate at which the strength decreases from the peak strength

to the ultimate strength is important as well. Therefore, it is possible to refer to a generalized brittleness index, as proposed by D'Elia et al. (1998):

$$I_{GB} = \frac{\tau_p - \tau_{mob}}{\tau_p} \tag{1.2}$$

where τ_{mob} is the mobilized shear stress at the considered strain or displacement. The generalized brittleness index varies with strains or displacements from zero at the peak to a value equal to I_B at large displacements. Besides, when dealing with slopes, I_{GB} must be associated with stress path that are representative of those followed *in situ*, and therefore must not be seen as a fundamental characteristic of a soil.

The process of progressive failure was confirmed by direct field observations, in particular by Burland et al. (1977), who observed the propagation of a horizontal shear band near the base of an excavation in overconsolidated Oxford Clay, and by Cooper et al. (1998), who brought to failure a well-instrumented experimental cut by increasing pore pressure within the slope. The mechanism of progressive failure represented the trigger cause of an iconic landslide, which occurred in the South of Italy, in the Senise village (26 July 1986), as documented by Guerricchio & Melidoro (1988), Viggiani & Di Maio (1991) and Del Prete & Hutchinson (1988), and as afterwards confirmed by Troncone (2005) and Troncone et al. (2014).

When the mechanism of progressive failure occurs, a significant part of a slope might reach local failure without or before the occurrence of a general failure. Reaching the peak means destruction in most soils and therefore a decrease in strength, as asserted by Leroueil & Vaughan (1990). This phenomenon must be clear and observable in natural slopes of precarious stability. The corresponding zones are named *weakened zones* (Leroueil, 2001).

Therefore, it can be stated that pre-failure phenomena and movements precede slope failures. Indeed, as well indicated by Terzaghi (1950): "if a landslide comes a surprise to the eyewitnesses, it would be more accurate to say that the observers failed to detect the phenomena which preceded the slide". Leroueil (2001) stated that as consequence, we should pay attention to precursory signs of landslides more that it is usually done, and learn how to detect them, interpret them and react.

1.2.2 – The failure stage

The failure condition is characterized by the formation of a continuous failure or slip surface through the entire soil or rock mass. As said in the previous section, there is a documented evidence that the failure or the slip surface in a slope develops within a weakened zone. However, observations show that there is an intermediate structure surrounding the slip surface, called

shear zone and schematically shown in Figure 1.2. According to the Mohr-Coulomb theory, shear surfaces form at an inclination $\alpha = 45° + \varphi'/2$ to the direction of the minor principal stress. When these shear surfaces cannot develop, due to kinematic constrains, there is at first the formation of a shear zone, which is followed by the development of a kinematically possible slip surface. Several authors who worked on it explained such aspect (see Riedel (1929), Skempton & Petley (1967), Morgenstern & Tchalenko (1967), Wilcox et al. (1973)). The mechanism of failure is characterized by initial formation of single, separate shear surfaces, which are slightly inclined to the direction of main shear, and by some conjugate discontinuities. The displacement discontinuities are formed in the direction of the shear. Finally, these latter link to form a unique principal displacement continuity.

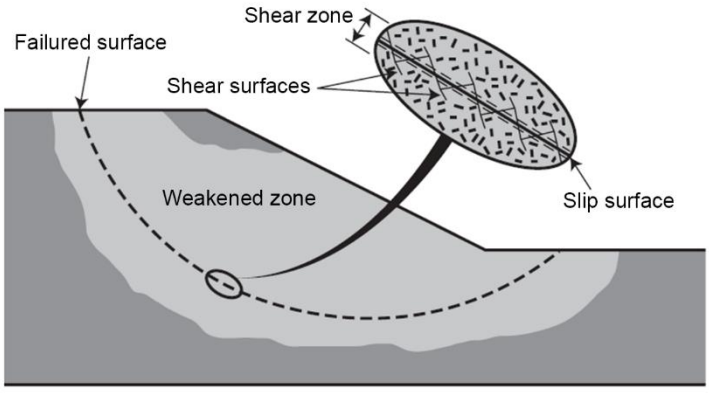

Figure 1.2 – Schematic detail of shear zone (from Leroueil (2001))

The described zone of discrete thickness, including the system of minor shears, is the shear zone (Skempton, 1967). Morgenstern

& Tchalenko (1967) indicate that, in slopes, shear zones are characterized with a thickness of a few centimeters and they present several sets of shears with different directions. Therefore, as already indicated in Figure 1.2, there are several "structures" associated with failure in slopes:

1) A weakened zone where soil reaches local failure should be generally destructured;
2) A shear zone, surrounding the shear surface, with a thickness varying from a few centimeters to a few decimeters and including shears and lenses of soil;
3) The failure surface itself, along which there is localization and possible particle orientation.

However, it is worth pointing out that there is no evidence that weakened zones and shear zones develop or can be observed in all cases.

As indicated in the previous section, progressive failure and failure itself mainly depend on the brittleness of the material, which can be characterized by the generalized brittleness index I_{GB} defined in Equation (1.2), as a function of strain or displacement. An important aspect is that such index has to be defined for the stress path that is really followed *in situ*. For instance, stress path are under approximately constant shear stress and decreasing effective mean stress in rainfall-induced landslides. Two important factors are associated with the

generalized brittleness index, i.e. the peak strength and the ultimate strength. Peak strength is influenced by the following factors:

1) Swelling, destructuration, strain rate and accumulation of strain, fatigue and weathering, which progressively lower peak strength value with time (time-softening process (Popescu, 1993));
2) Changes in effective stress or suction;
3) Anisotropy and stress axis rotation.

Instead, the ultimate strength depends on the nature of the material and on the effective condition existing under ultimate conditions, which include the influence of void ratio and applied stresses. Due to the occurrence of the progressive failure, the average strength mobilized on the slip surface will generally be intermediate between the peak and the ultimate strength. Therefore, progressive failure seriously questions the meaning of the safety factor usually computed by limit equilibrium analyses, owing to the difficulties related to the choice of the parameters needed to the calculation of the safety factor.

Among the causes of landslides, Terzaghi (1950) mentioned the fatigue-creep phenomena. However, probably because they are difficult to evidence and to explain with classical soil mechanics concepts, they are poorly documented in the literature.

Another important condition which can lead a slope to the failure is the loss of suction. Brand (1981) emphasized that the stress paths followed in a natural slope due to the infiltration are different from those followed in conventional triaxial tests. Shear and deviatoric stresses are essentially constant with a possible small increase during infiltration, since the unit weight of the soil increases. If strain rate effects and progressive failure are not accounted for, the soil behavior in terms of stress path can be summed up as shown in Figure 1.3, in which the shear stress, τ, versus the total net normal stress, $(\sigma_n - u_a) = \sigma_n$ (assuming that the air pressure is at atmospheric pressure), when the soil is unsaturated and pore water pressure negative.

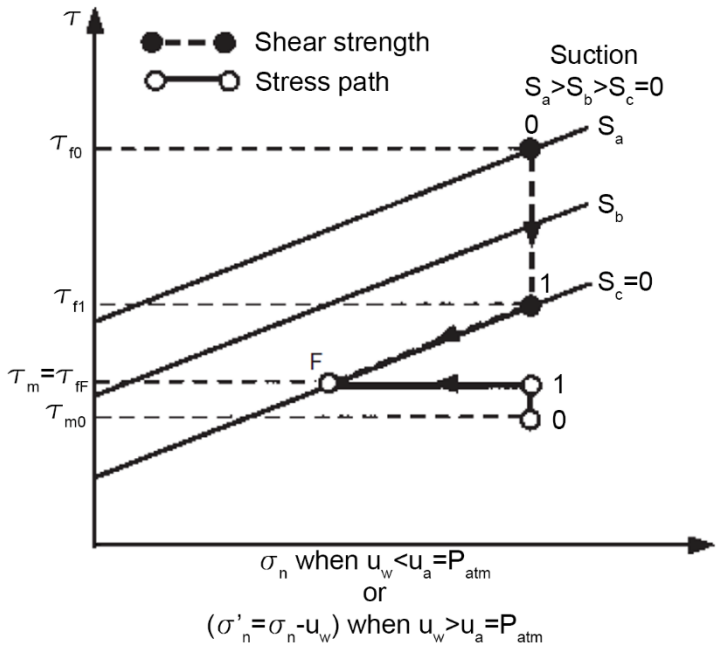

Figure 1.3 – Variation of shear stress and shear strength when suction decreases and pore water pressure increases from zero to its value at failure in an initial unsaturated slope subjected to infiltration (from Leroueil (2001))

When the soil is essentially saturated and the pore water pressure is larger or equal to the atmospheric pressure, τ is considered against the effective normal stress $\sigma'_n = \sigma_n - u_w$. Consider an element of soil in an unsaturated natural slope, characterized by a negative pore pressure $u_w = -S_a$, and represented by point 0 in Figure 1.3. The mobilized shear stress is τ_{mo} and the strength, a function of the suction S_a, is equal to τ_{fo}. With infiltration, the suction progressively decreases and the stress and strength conditions move towards point 1. Due to the slight increase in the unit weight of the soil, the mobilized shear stress increases to τ_m and the available strength decreases to τ_{f1}. When the saturation of the soil becomes close to 100%, point 1, its strength becomes controlled by effective stresses. As pore water pressure increases in the positive range, the normal effective stress decreases from point 1 to point F, and failure is reached at this latter point when the effective stress path reaches the strength envelope of the saturated soil, $S = S_c = 0$. All this process, from 0 to F, is drained: that is, the soil adapts to the new conditions by changing its water content and void ratio. Therefore, in order to understand and analyze the stability of unsaturated slopes, the knowledge of the variation of shear strength with suction is essential. With this aim, an example of failure criterion to refer to is that proposed by Fredlund (2000):

$$\tau_f = c' + (\sigma - u_a)\tan\varphi' + \chi s \tan\varphi' \qquad (1.3)$$

where τ_f is the failure shear strength, c' and φ' are the effective cohesion and friction angle of soil respectively, σ is the total normal stress, u_a is the pore air pressure, s is the suction ($s = u_a - u_w$), and χ is a parameter whose values can range between 0 and 1. Such parameter can be expressed according to Fredlund et al. (1996):

$$\chi = \left(\frac{\theta - \theta_r}{\theta_s - \theta_r}\right)^{\lambda} \tag{1.4}$$

where θ is the volumetric water content at a given suction, θ_s is the volumetric water content at saturation, θ_s is the residual volumetric water content, whereas λ is a parameter depending on the type of soil. A schematic representation of a landslide in unsaturated soils is shown in Figure 1.4. However, it is important to highlight that the behavior of soils under the effect of suction loss is characterized by a relevant complexity and is still under investigation.

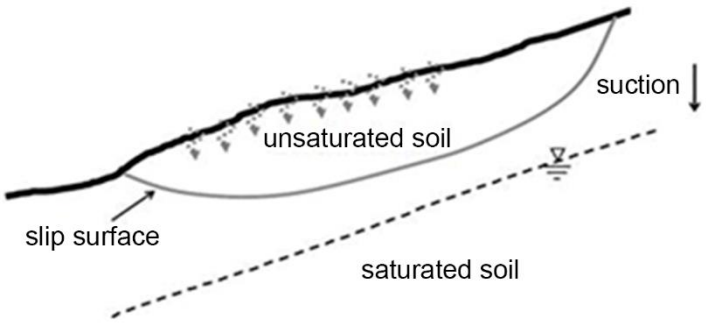

Figure 1.4 – Schematic representation of a landslide in unsaturated condition

1.2.3 – The post-failure stage

The post-failure phase includes the movements of the unstable soil mass from the onset of failure until it stops. At the time of failure, some potential energy, E_P, becomes available and what happens then depends on how this energy is redistributed. Part of the potential energy will dissipate into friction, E_F; the rest will be dissipated in breaking up, disaggregating and remodeling the soil, E_D, and for generating movement, i.e. kinetic energy, E_K. Over a time interval during the post-failure stage the balance of energy can be written according to Equation (1.5).

$$\Delta E_P + \Delta E_F + \Delta E_D + \Delta E_K = 0 \qquad (1.5)$$

Vaunat et al. (1994) and D'Elia et al. (1998) made this description of post-failure movements from an energy perspective. The disaggregating or remodeling energy, E_D, may play an important role at the post-failure stage in microstructured materials, but it is poorly documented in the literature. The proportion of the energy dissipated in friction depends on the brittleness of the material, defined for the stress path followed in *in situ* conditions, up to failure and after. Anderson & Riemer (1995), Anderson & Sitar (1995) and Santos et al. (1996) have evidenced the importance of this aspect in relation to slides induced by pore pressure increase. Indeed, *in situ* behavior corresponds to a decrease in effective mean stress under an approximately constant shear stress, whereas most laboratory tests are

performed in compression or in extension. Equation (1.5) indicates that the kinetic energy and the post-failure rates of movement result from the part of the potential energy that is not dissipated into frictional and disaggregation of soils. In ductile materials (I_{GB} close to zero), most of the available potential energy is dissipated into friction and kinetic energy, and rates of movements are small. Instead, for materials which show a loss of shear strength (i.e. I_{GB} increases with strains or displacements), the driving forces become unbalanced and there is an acceleration of the soil mass. Therefore, high rates as well as long run-out distances can be reached. Thus, a parameter of particular importance in the case where flow slide might develop is the value of the ultimate strength obtained at large strains or displacements. Such strength, could be the residual strength in stiff plastic clays, the remolded strength for clays in undrained conditions, or the steady-state strength in cohesionless soils (Leroueil, 2001).

Another implication, which must be accounted for about the post-failure phase, is the possible development of flow-like movements. These take the characteristics of a flow, either fast or slow, wet or dry. In particular, the term *debris flow* is usually associated to coarse materials, whereas *mud flow* refers to clays with silt and sand layers. Common features to flow-like landslides are a steep upper zone, where the movement is triggered, usually as the result

of high intensity rainfall; a downstream path along which transportation and erosion occur; a lower flatter zone where deposition in a fan-shaped area occurs. Because the velocity of flow may range from very slow rates to more than 20 m/s, consequences in this latter case may be catastrophic. Therefore, safeguarding measures are objects of intensive research efforts (as pointed out by Hungr et al. (1984) and Pirulli (2005)). An iconic example of flow-like landslide of great dimensions occurred in the South of Italy (Maierato, Vibo Valentia, Calabria) on 15 February 2010. Such a landslide can be classified as a slide that evolved into a rapid flow after a long heavy-rainy period that involved the months preceding the event (Conte et al., (2016); (2018)).

Regarding flow-like landslides, after the failure is initiated, flow develops only if the ultimate strength is less than or equal to the driving shear stress, as explained and discussed by Lee et al. (1988). They suggested evaluating the potential for debris flows by considering the position of initial void ratio-effective stress condition relative to the CSL line of the soil. From field observations and laboratory tests performed in relation to sites prone to flow-like movement development, they found an association between initial states lying above the CSL and debris flow occurrence, whereas initial states near or below the CSL corresponded to the occurrence of slow-moving, non-disintegrative failures. In order to evaluate the possibility of flow-

like movements, it seems more appropriate to consider state conditions at yielding rather than initial stress conditions (Leroueil, 2001). If the soil is contractant in undrained conditions, the collapse may be very sudden, as observed by Eckersley (1990), who triggered flow-slides in instrumented coal stockpiles by slowly increasing pore pressures. Eckersley (1990) also observed increases in pore pressure during flow-slides.

When soils are dilatant after reaching yielding, the strength has a tendency to increase with strains, and the movement should stop at that point. However, if water is easily available, the water content of the soil may increase and the large strain strength may decrease along the CSL. From some observation made by Casagrande (1975), Fleming et al. (1989) and Harp et al. (1990) it appears that a decrease in pore pressure could be a precursory sign of debris flow in some slopes prone to this kind of movement. Consideration of the critical-state approach for predicting the transformation of shallow slides into flow-like movements is theoretically interesting but difficult to apply in practice, in particular because of soil variability in *in situ* conditions and uncertainty in the location of the steady-state line from laboratory tests. It can be easier to perform CSD tests on intact specimens and see whether they show contractant or dilatant behavior after yielding of the soil (Anderson & Sitar, 1995). At the post-failure stage, if the nature of the material and the rate of movement allow

some consolidation of the moving mass, brittleness of the soil decreases. In these conditions, less energy will be transferred into kinetic energy.

Finally, a discussion about the influence of temperature on the post-failure stage of landslides is shortly mentioned in the following. Strain localization processes in shear zones may produce a significant weakening phenomenon due to the thermal pressurization of pore water pressure. Such a phenomenon consists in the dissipation of frictional-work heat. Soil skeleton and water undergo dilation due to heating, with the consequent increase in pore water pressure. Consequently, the effective stresses reduce, leading to an acceleration of the landslide due to the subsequent loss of strength. For this reason, the post-failure stage of some landslides is characterized by high velocity and sudden acceleration. In turn, this acceleration and the consequent increase of velocity induce additional increments of temperature, becoming a self-feeding process which could sometime result in a catastrophic accelerated landslide. A more detailed study on the landslide motion assessment including thermal interaction is proposed by Alvarado (2018). However, this aspect will not further be deepened in this dissertation, since the landslides analyzed in this context are not interested by this aspect.

1.2.4 – The reactivation stage

According to Leroueil (2001), the term reactivation refers to the movement of a soil mass above one or more pre-existing slip surfaces. In these cases, the mobilized shear strength on the slip surface corresponds to the residual condition. Since this represents the lower limit of the shear strength, the soil does not present any strain softening. Therefore, limit equilibrium analyses are suitable to evaluate the slope stability. Among reactivations, Leroueil (2001) defined the difference between 'active landslides' and 'reactivated landslides'. In active landslides, the rate of displacement varies with the seasonal changes in pore pressures. This is particularly true for translational landslides in which the driving forces do not change significantly with time. The rates of displacement are generally small, varying between some centimeters and some meters per year (Urciuoli, 1990). By contrast, reactivated landslides may be associated with sudden and fairly rapid displacements (see Hutchinson (1987) and D'Elia et al. (1998)). These authors listed mechanisms that can produce such movements, among which the most common seem to be:

1) Rapid pore pressure increase due to filling of cracks or breaking of pipes;
2) Stress change during excavation;
3) Rapid change in load distribution along the shear surface;

4) Increase in strength along the shear surface due to cementation that could give a little brittleness to soil during the failure;
5) Seismic forces.

The residual strength can be influenced by applied stresses, presence of coarser and stiffer particles, the chemistry of pore water and the rate of displacement. Therefore, one should be encouraged to test the soil in conditions as close as possible to the *in situ* ones. Skempton (1985) and Bromhead (1992) reported that tests on specimens including natural slip surfaces allow residual strength close to those deduced from back-analyses to be obtained. However, the evaluation of the residual shear strength might depend on the type of test performed in the laboratory. The ring shear apparatus, which allows a continuous displacement of large magnitude on a well-defined shear surface, provides the lowest values of residual shear strength. If viscosity has no significant influence on residual strength, it has an important influence on the rate of movement and its variations in *in situ* conditions. Owing to the viscous nature of soils (Bracegirdle et al. (1992); Leroueil & Marques (1996)), the rate of movement, v, does not abruptly vary from 0 when the safety factor is larger than 1 to infinity when it becomes equal to 1, but increases progressively with the applied shear stress level. Because the particles arrangement does not change significantly after large

displacements, the rate of displacement is not influenced by the amount of displacement, time or history of the movement. Vulliet (1986), who reviewed the literature on the topic, suggested that v should be expressed as follows:

$$v = F(\sigma_n', \tau)\tau \tag{1.6}$$

where F is a function of the normal effective stress, σ_n', and the applied shear stress, τ. It can take several forms, such as the one of Equation (1.7).

$$F = \frac{A\tau^{n-1}}{(\sigma_n' \tan \varphi_r')^n} \tag{1.7}$$

1.3 - Excavation-induced landslides

Figure 1.5 shows the evolution of the horizontal displacement of a general point of an excavation-induced landslide, whereas Figure 1.6 represents a hypothetic evolution of the stress path with referring to the same point during the pre-failure phase. With referring to this point, the yielding surface and the limit state surface are shown, under the implicit hypothesis that they do not coincide and that the soil behaves according to the Critical State Theory, under the hypothesis of isotropic medium. The phases previously described are well pointed out in Figure 1.5, and they will be deepened in this section, focusing the attention on what happens when a landslide occurs after an excavation. In this section, particular emphasis will be dedicated on the pre-failure and failure stages, postponing the description of the post-failure

phase as well as reactivation in the following section, since they have similar characteristics for both excavation-induced and water-induced landslides.

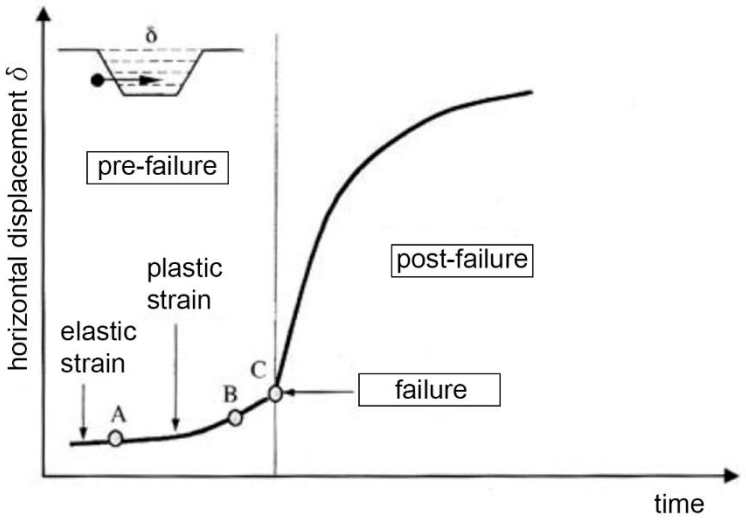

Figure 1.5 – Hypothetic horizontal displacement evolution for a point close to an excavation (adapted from Picarelli (2000))

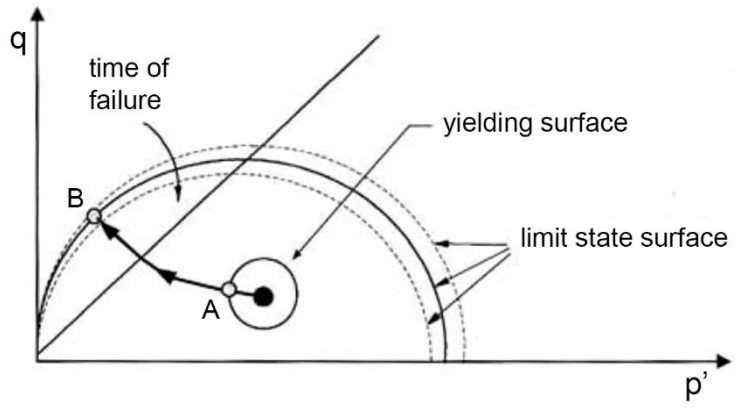

Figure 1.6 – Hypothetic stress path evolution for a point close to an excavation (adapted from Picarelli (2000))

PRE-FAILURE STAGE

An excavation is a well-defined mechanics action which causes the change of total stresses and water pressure. The change of

groundwater regime depends on both the variation of the hydraulics boundary condition due to the excavation (which implies the lowering of the water level) and the variation of total stresses, if the excavation is quite fast (undrained condition in clays). The combined effect of the variation of the total stress state and water pressure regime implicates a substantial change in the effective stresses field, which occurs in a volume of soil, whose dimensions depend on those of the excavation, and gives rise to a deformation field. Nature and entity of such deformations depend on both the stress field and on the soil properties. They can be computed only by means of advanced numerical methods, by using adequate constitutive laws.

Where the induced stress is low (i.e. at the beginning of the excavation as well as far from the interested area), the stress state remains within the yielding surface (Figure 1.6) and the consequent deformations are elastic. Therefore, if the excavation is performed rapidly (undrained condition in clays), negative values of water pressure are induced and the soil is prone to swelling. In the short term condition, only distortions occur, determining a displacement field and the deformation of the excavation boundaries: in particular, since the change of volume must be nil, the bottom of the excavation lifts up whereas the ground beside the scarp lowers. In drained conditions, both the bottom of the excavation and the ground beside the scarp raise.

In this phase, the velocity of deformation depends on both the velocity that boundary conditions vary with and on the nature of soil. If the excavation is performed fast and the involved soils are characterized by a low permeability, on this latter the velocity of deformation strongly depends, and the soil keeps on deforming after the excavation is completed as well. If the excavation is performed slowly, or if soils are characterized by high values of permeability, the velocity of deformation essentially depends on the velocity of excavation.

When the excavation goes on, as consequence the stresses increase, with different stress paths from point to point. When the yielding surface is reached in a general element of soil (point A in Figure 1.6), local elasto-plastic deformations occur and the strain rate induced from further changes of stress state significantly increases.

In the volume affected by the excavation, there are zones where deviatoric stresses increase, and zones where they reduce. This depends on the position of the element of soil under consideration and on the coefficient of earth pressure at rest, k_0 (and then on the soil history). Where deviatoric stresses decrease, the principal stress direction might rotate. When stresses increase, viscous deformations become more relevant, especially the deviatoric ones (the only ones if drainage is impeded). This, as well as the induced water pressure dissipation, causes delayed displacements in time.

In this phase, the velocity of displacement is substantially independent on the velocity of variation of boundary condition. If the entity of the excavation is sufficient, some points might reach the limit state condition and, eventually, the failure (see Figure 1.6). The following deformations determine local yielding phenomena. Such a local failure phenomena do not mean the collapse of the slope is reached yet, since this will occur afterwards, when the shear zone will be completely developed, giving rise to the slip surface. In the points where the crisis is reached, a further stress increase cannot occur, thus, each further modify of the boundary conditions determines a redistribution of the stress state, more significant in fragile soils. Such a redistribution involves, first of all, the closest zones to the yielded one, and causes the propagation of the plastic zone with the intact soil. Although the zone where the soil reaches the failure condition is commonly called slip surface, such zone has an its thickness with a complex structure, and it is called shear zone, as already discussed in the previous sections.

A schematization of the development process of the shear zone is reported in Figure 1.7. In the moment when the shear zone closes on the ground surface, the general failure of the slope is reached. The volume of soil that is delimited from the ground surface at the top and from the shear zone at the bottom is called *body of the landslide*.

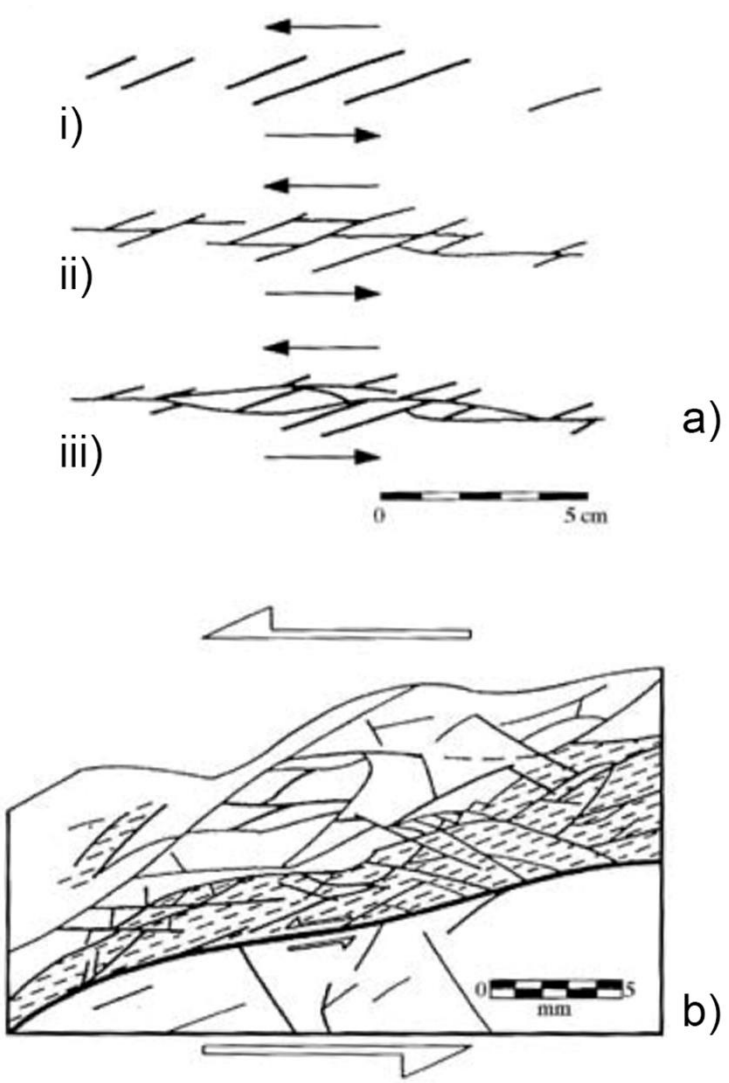

Figure 1.7 – Schematization of: a) process of formation of a shear zone (adapted from Skempton (1967)); b) mesostructural detail of the shear zone of the Guilford (adapted from Skempton & Petley (1967))

FAILURE STAGE

The extension of the shear zone until the ground surface leads to the global failure of the slope, which has been considered a *first-time slide* so far. Starting from the time of failure, which can occur under different drainage conditions (based on the relationship existing between velocity of deformation and velocity of dissipation

of the excess in groundwater pressure), the behavior of soil, which at the beginning is assimilated to a continuum medium, becomes conditioned by the presence of a shear discontinuity. Further displacements are mainly due to slices concentrated on it.

Obviously, the induced stress state (continuously variable) could give rise to further discontinuities and cracks, along which softening phenomena are prone to develop. This usually happens when the shear zone is not uniform and determines, during the post-failure stage, kinematic incompatibilities between different parts that the body of landslide splits up into.

With referring to the failure phase, slope stability analyses are commonly carried out whereby limit equilibrium methods, which allow the safety factor to be computed, by assimilating the soil to a rigid-plastic medium, which reach the failure condition simultaneously in every point of an infinitesimal-thick shear zone, called *slip surface*. Actually, deformation mechanisms that occur during the pre-failure phase, especially when mechanisms of progressive failure are involved, have a strong influence on the failure condition, but are often neglected. A way to account for the complex phenomena which lead the slope to the failure is an accurate calibration of the geotechnical parameters. Therefore, only judgement and good sense allow shortcoming of limit equilibrium method to be overcome. However, the induced stress state of an element of soil is dependent on its position and on the

pre-existing stress state. The rotation of the principal stress direction is likely to happen. Experience shows that excavation-induced stress paths have influence on the normal effective stress distribution acting on the slip surface and, somehow, control the shear strength parameters, especially when they are expressed in terms of total stresses (Picarelli, 2000). As a consequence, the results of numerous back analyses of excavation-induced landslides show that the obtained values of the safety factors, computed by using the shear strength parameters obtained from laboratory tests, are pretty larger than unit values (Chandler, 1984).

Besides, due to the progressive failure and generally speaking the pre-failure phase, before the entire slope reaches the crisis, relevant slides develop in the subsoil, which first cause the mobilization of the peak shear strength, then the reduction towards the residual condition, with different values in each point. Therefore, the operative shear strength is intermediate between peak and residual when the collapse condition is reached.

Bjerrum (1967) was the first author who impressively described the mechanism of progressive failure with referring to the simple case of an infinitive slope undergone a vertical excavation in drained condition. In particular, he observed that the phenomenon has a stronger influence in the following situations:

1) When the ratio of the initial average normal stress on a general vertical section to the shear strength on the slip surface is high;
2) When the ratio of the lateral deformation induced by the excavation to the deformation at failure is high;
3) When the ratio of the peak strength and the residual one is high.

It clearly appears that in many cases (usually in plastic strongly overconsolidated soils) the phenomenon cannot be neglected. In such cases, indeed, when the slope stability is analyzed, it is not preventive to rely on the peak shear strength; therefore a lower value should be adopted. In many cases, the operative strength is close to the critical one (Picarelli, 2000). Some laboratory experiences carried out by Burland (1990) justify such statement. Indeed, such experiments demonstrated that the critical strength is more or less equal to the post-peak strength measured just after the formation of the shear surface, whereas the residual strength, which represents the lower boundary of the operative strength, is usually mobilized at very large displacements, much higher than those needed to determine the global failure of the slope.

However, since nowadays we have available strong calculation tools, a more adequate analysis of the failure phase should be performed by means of advanced numerical methods, rather than using limit equilibrium methods and penalizing empirically the

operative strength. As already said, the post-failure phase as well as reactivation will be discussed in the following section, since similar consideration can be made about these phases for excavation-induced and rainfall-induced landslides.

1.4 - Rainfall-induced landslides

Figure 1.8 shows the evolution of the horizontal displacement of a general point of a landslide induced by a change of the groundwater pressure regime due to water level oscillations, whereas in Figure 1.9 a hypothetic pre-failure stress path evolution for the considered point is reported.

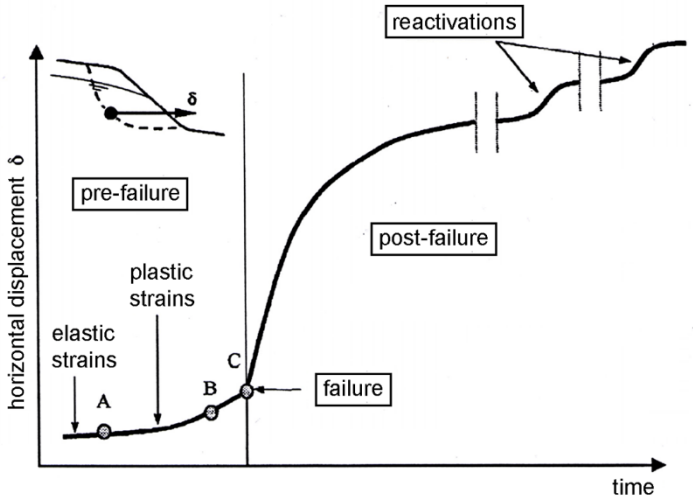

Figure 1.8 – Hypothetic evolution of horizontal displacements for a point within a slope due to water level fluctuations (adapted from Picarelli (2000))

For this point, the yielding surface and the limit state surface are shown, under the implicit hypothesis that they do not coincide and that the soil behaves according to the Critical State Theory, under the hypothesis of isotropic medium. The four phases

previously described are well pointed out in Figure 1.8, and they will be deepened in this section, focusing the attention on what happens when a landslide occurs after water level fluctuation.

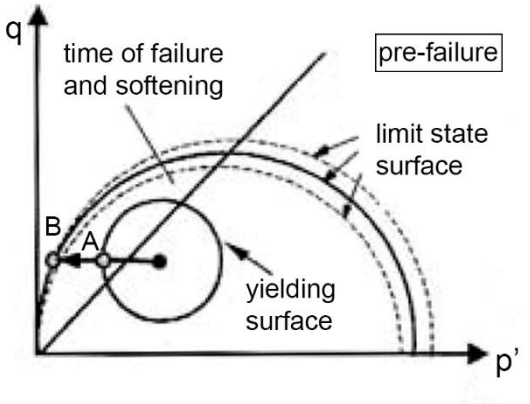

Figure 1.9 – Hypothetic pre-failure stress path evolution for a point within a slope due to water level fluctuation (adapted from Picarelli (2000))

PRE-FAILURE STAGE

Rainfall, erosion and seismic actions as well as deterioration processes of soil properties are the main causes of natural slopes instability (Picarelli, 2000). They are natural causes, which produce changes at the boundary conditions and at soil properties difficult to predict, making natural slope stability problems much more difficult than those of artificial slopes. Differently, artificial causes of slope instability are related to human activities. In this connection, it is worthwhile distinguishing between natural and artificial slopes. Particularly, the term natural slopes refers to those slopes resulting from geological formation processes and which have never been interested by any construction activities.

On the other hand, the term artificial slopes is used to indicate those slopes that have undergone any modifications related to civil engineering constructions.

Figure 1.8 schematizes the evolution of displacements regime in a generic point owing to water level fluctuations. This figure is suited for analogues considerations to those discussed in the previous section. Anyway, it is convenient to deepen some aspects that are peculiar of natural slopes behavior.

In this case, the unstabilizing action is the water level fluctuation and stress condition is mainly cyclic, characterized by continuous variations of normal average effective stresses. Such oscillation of stresses occur within the same stress values range, whose extremes have been reached only few times in the whole slope history. According to the most traditional constitutive models of soil, the stress ranges that stress paths move into should be delimited by the yielding surface generated due to the maximum groundwater pressure reduction, and therefore, permanent deformations induced by water level fluctuations should be negligible. Eigenbrod et al. (1992) carried out specific laboratory tests about lightly overconsolidated clays behavior undergone cyclic oscillation of the *back pressure*, simulating in this way groundwater pressure regime fluctuations. They observed that effects are analogous to those due to creep induced by monotonic increments of deviatoric stresses, and consist in the accumulation

of irreversible strains whose entity depends on the number of cycles or on the time. Therefore, also water level excursions produce strains and displacements of soil, especially if the additional effect of the time on soil properties is accounted for.
Indeed, viscous effects and mechanisms of softening as well as alteration determine a progressive reduction in the time of the limit state surface (see Figure 1.9) and of the shear strength. With the progression of time, such phenomena could lead to the failure. Progressive failure represents an important mechanism of failure also for natural slopes. In this case, the time has an important role though, since the trigger of such a mechanical process could have been due to particular events previously occurred (for instance an earthquake), which currently show no evidence. This aspect highlights the importance of carrying out a detailed investigation, in order to individuate eventual shear zones.

FAILURE STAGE

The collapse of natural slopes is strongly influenced by deformation mechanisms occurring during the pre-failure phase, more than artificial slopes. Figure 1.10 shows the progressive reduction of the safety factor with the time of a slope undergone cyclic groundwater pressure fluctuations and phenomena of strength reduction due to softening. Although it is qualitative, it highlights the relationship existing between the phenomena

which lead to failure, such as those that determine the limit state surface contraction (see Figure 1.9), and trigger factors, related to groundwater pressure oscillations. These latter represent only a contributory cause of the collapse, as previously discussed and as it clearly appears from Figure 1.10.

For creep and softening phenomena as well as progressive failure, the lower limit of strength for overconsolidated clays is the one corresponding to the critical condition as documented by Skempton (1970) and Morgenstern (1977). This indication is confirmed from experiences on first-time slides on regional scale.

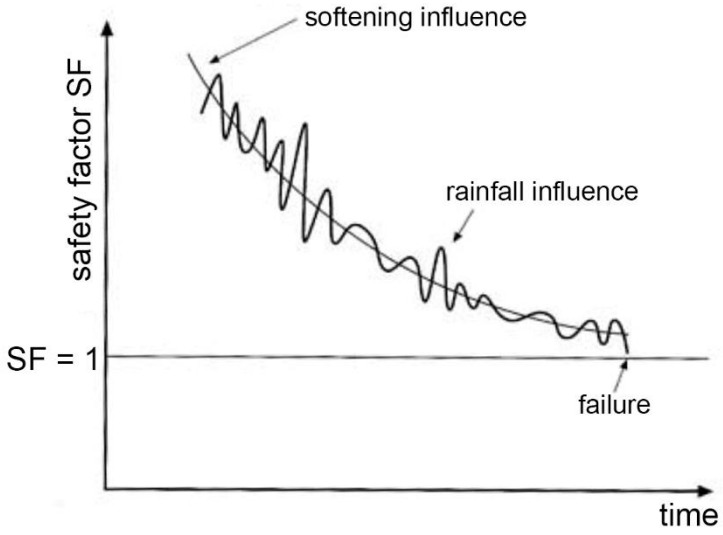

Figure 1.10 – Hypothetic evolution of the factor of safety with time of a slope undergone groundwater level fluctuations (adapted from Picarelli (2000))

As an example, Figure 1.11 shows that the operative strength at failure in several cases of first-time slides in London clays and Lias clays is quite less than that measured from laboratory tests (Chandler, 1984). It was proved that it is similar to the critical one measured on reconstructed samples. This can be somehow

explained if we consider that, at least from a theoretical point of view about the behavior of overconsolidated or cemented soils, the critical strength represents the strength rate still available when, due to the phenomena first mentioned, the *bonus* due to the overconsolidation or cementation is lost. In the case of progressive failure, especially in plastic soils with flat particles and subjected to high local deformation during the pre-failure phase (for instance in the case of long slopes), the mechanism of collapse can cause a higher loss of strength, towards the residual condition.

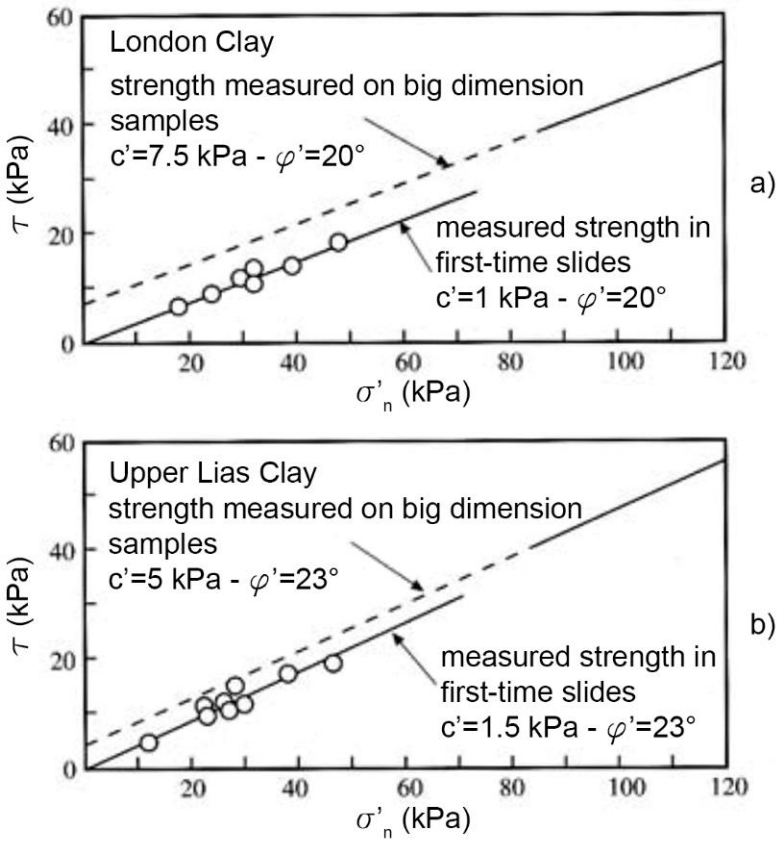

Figure 1.11 – Mobilized shear strength at failure in natural slopes in: a) London clay; b) Lias clay (adapted from Chandler (1984))

POST-FAILURE STAGE

At the time when the shear zone closes on the ground surface and the failure is reached, the body of landslide, which is then completely defined, has the possibility to slide above the shear surface, which is within this zone, releasing the available potential energy. The body of landslide moves until a new condition of equilibrium is reached, which must be compatible with the stresses acting on its boundaries. In many cases, such condition is reached at the end of a dynamic phase in which the soil mass is undergone an initial acceleration followed by a velocity reduction (see Figure 1.8). Afterwards, in the reached condition of equilibrium, further little deformations and visco-plastic slides could occur in the body of landslide, in the shear zone and along the slip surface. Such *residual* deformation are due to the continuous changes of the stress state owing to the fluctuations of the groundwater pressure regime (see Figure 1.12), or owing to the slow re-equilibrium of groundwater pressures, during the failure phase, within the shear zone, due to the dilatant behavior of overconsolidated soils, as observed for the Selborne experiment (Bromhead, 1998).

The *risk* of goods, human lives, structures and infrastructures depends on the *amount of the possessed kinetic energy* (Hungr, 1981). In the post-failure phase, the landslide is characterized by both internal deformation and displacements on the lower

boundary. In several cases, the shear zone is undergone important distortions, so that structure and water content can be changed (Picarelli, 1993).

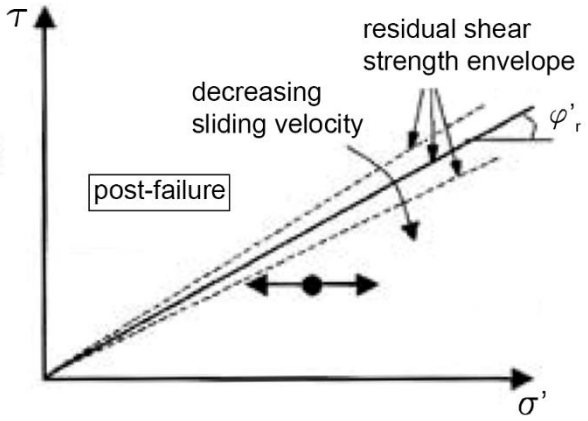

Figure 1.12 – Hypothetic stress path evolution during the post failure phase of a landslide triggered by groundwater level fluctuation (adapted from Picarelli (2000))

Furthermore, along the slip surface within the shear zone large deformations occur, whose entity is definitely higher than the contribute of other strain components.

As already discussed, the characteristics of the movement in the post-failure phase can be analyzed by means of energetic considerations, assuming that the potential energy initially available is partially dissipated due to the friction along the sliding surface and due to irreversible deformations within the body of landslide and the shear zone, and partially transformed in kinetic energy (see Figure 1.13).

The percentage of kinetic energy available during the motion depends on such balance, and it can be measured whereby the velocity of the body of landslide. Obviously, the travelled distance of this latter depends exactly on the available kinetic energy.

Approximately, both the kinetic energy and the velocity could be simply calculated by applying the First Principle of Dynamics.

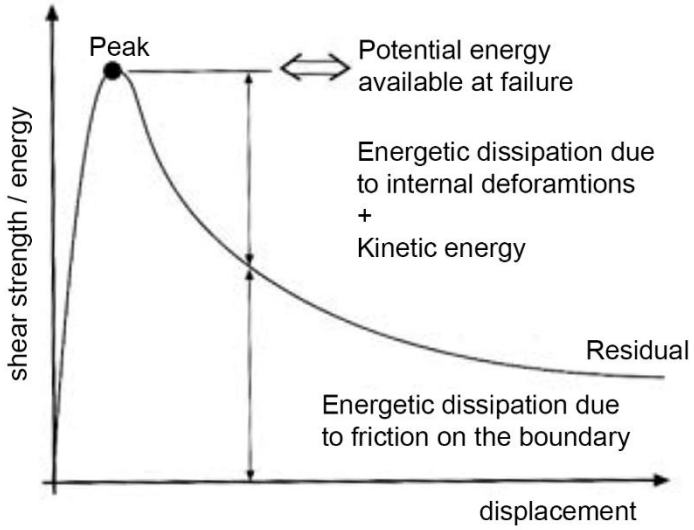

Figure 1.13 – Energy dissipation mechanisms for an overconsolidated clay during the post-failure phase (adapted from Leroueil et al. (1996))

If we reckon that groundwater pressure is constant or nil, the operative shear strength does not depend on the entity of movements for perfectly ductile soils. In other words, the energy that can be dissipated due to the friction along the sliding surface, which under equilibrium conditions is equal to the potential energy released during the failure, does not change during the post-failure phase.

Therefore, the body of landslide remains in the limit equilibrium condition and the potential energy is totally dissipated due to friction. If the soil is fragile, the shear strength will decrease immediately after the collapse and it will be no longer in equilibrium with external actions. In other words, only a part of the available potential energy is dissipated due to the friction,

whereas the remaining part is transformed in kinetic energy and it is used to deform the body of landslide.

Reik & Hesselmann (1977) performed a physical experiment of a slope made by many rigid blocks, variably assembled and laying on an inclined slope. They led the slope to failure by increasing the inclination of the slope. By monitoring accurately the induced displacements and velocities, they measured the potential and kinetic energy and estimated the energy dissipated due to friction along the boundaries. They concluded that the dissipation due to friction should be negligible if compared with other rates.

From what said, it is possible to deduce that, for a given geometry and if drainage is allowed, the rate of potential energy which is transformed in kinetic energy is bigger when the involved soils are fragile and weak.

In saturated soils, the mobilized friction stress and the internal deformation can depend on eventual excesses of groundwater pressure, which might occur during or after the failure. If deformation mechanisms are fast enough to give rise to positive excesses of groundwater pressure within the body of landslide and on its boundaries (as typically happens in cohesionless soils and slightly overconsolidated clays), the kinematics of the landslide is strongly affected, since both the frictional strength along the sliding surface and the stiffness of involved soils reduce. This happens, for example, in those mechanisms which lead to the

transition from slide to flow-like landslides, which are characterized by velocities and internal strains so high to make the motion similar to the flow of a viscous liquid (Picarelli, 1999). Positive excesses of groundwater pressure due to shear stresses typically happen in slightly overconsolidated clays. When flow-like landslides happen in strongly consistent clays, the phenomenon can occur due to softening effects that happen in such soils during the pre-failure and failure phases (see Picarelli (1993) and Guerriero (1995)). As already said, the post-failure kinematics depends on the nature of involved soils and on their capacity to dissipate energy. Indeed, experience shows that flow-like landslides can reach velocity of the order of m/s, whereas those in cohesive soils, which are likely more dissipative due to the soil viscosity, reach much lower velocities, of the order of m/h.

REACTIVATION

Reactivation phenomenon affects all those slopes which have already been undergone landslides. Therefore, their main characteristic is that they affect slopes crossed by a shear zone (or more than one). It is possible to identify the pre-failure and post-failure phases for reactivations as well. In all cases, deformations are mainly concentrated within the shear zone. Typical profiles obtained from *in situ* measurement whereby inclinometers are reported in Figure 1.14, with referring to the Fosso San Martino

reactivation (Bertini et al., (1986)), and show that the soil mass moves substantially as a rigid body.

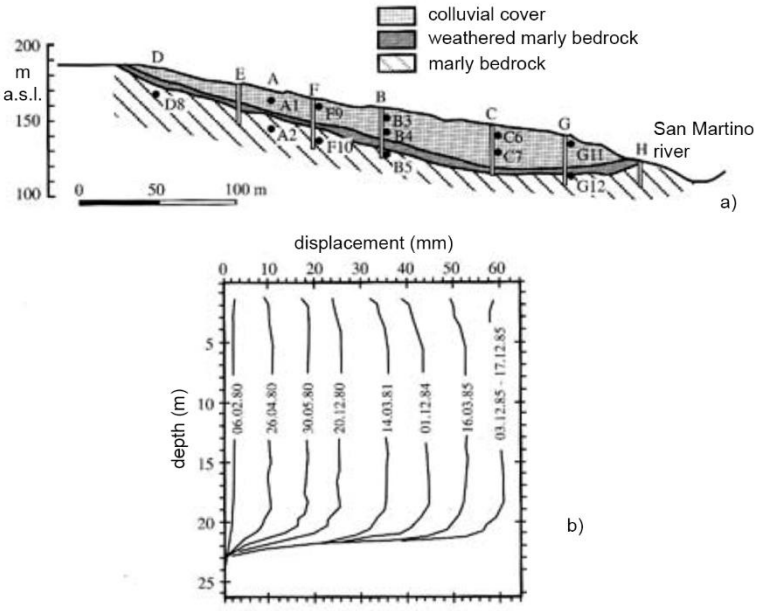

Figure 1.14 – Horizontal displacements measured for the reactivated landslide of Fosso San Martino (adapted from Bertini et al. (1986))

Russo (1997) examined, by means of numerical analyses, some possible mechanism of pre-failure of landslides characterized by a pre-existing planar sliding surface, parallel to the ground surface. The adopted hydraulic conditions were those of seepage parallel to the ground surface. The analyses were aimed to study the movements induced by external loads, an excavation or water table oscillations. By introducing in the model the deformability of the body of landslide, it was possible to simulate behaviors observed during accurate tests in real situations. In each analyzed case, it was observed that the reactivation could also develop due to a mechanism of progressive deformation of the body of landslide with its contemporary sliding along the pre-existing

shear surface. As an example, Figure 1.15 reports the evolution of displacements for a hypothetic slope made up of soils with an elasto-plastic constitutive law, undergone a non-uniform raising of the water table (which rotates upstream in Figure 1.15a).

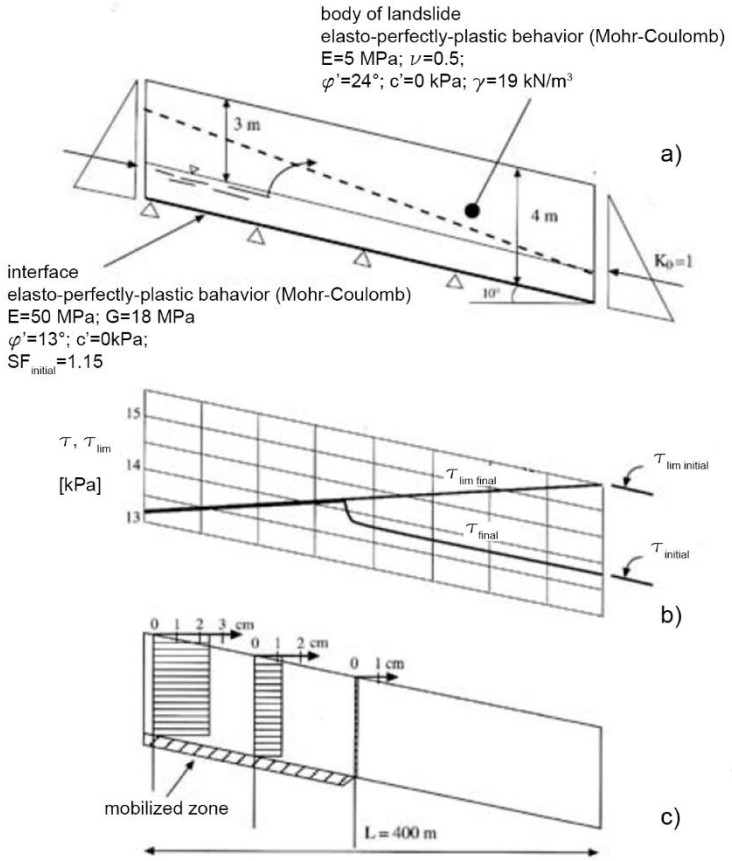

Figure 1.15 – Numerical simulation of displacements and stress state at the base of a translational landslide due to groundwater level fluctuation: a) model; b) shear stresses along the slip surface; c) profiles of displacement (adapted from Russo (1997))

This usually happens during winter and spring, in slopes whose toe is submerged in a river, a lake or another water resource with a constant hydraulic head.

Owing to the raising of groundwater pressures, the shear strength reduces upstream with a linear law. If the strength becomes less than the shear stress due to its own weight along this part of the

sliding surface (Figure 1.15b), to ensure the translational equilibrium, the stress that is no longer equilibrated by friction must be transferred to the body of landslide as a thrust increment. The mass deforms with a compression, and slides not necessarily involving the toe of the slope (Figure 1.15c).

Therefore, the global safety factor along the sliding surface is still greater than one. Obviously, the movement evolution occurs gradually with the water table raising, and all the available strength along a growing part of the sliding surface is mobilized. However, it is possible to reckon that the slope shows viscous deformations as well, concentrated along the sliding surface (creep). By using a more complex elasto-visco-plastic constitutive law, Russo (1997) showed that it is possible to explain the cyclic reactivation of movements due to the raising of groundwater pressure in the common case of groundwater pressure fluctuations always in the same stress range.

Indeed, every time the groundwater pressure regime reduces due to the lowering of the water table (during summer), the body of landslide is undergone a stress relaxation, which can be simulated right by using a viscous law. During the next rainy season, the raising of groundwater pressures produce a re-establishment of the stress state and the re-compression of the body of landslide. Contrarily to the case of progressive failure, in the reported example, the reduction of strength with sliding

cannot be verified, since it is the minimal possible; in such a case it would be appropriate to talk about *progressive deformation*. All in all, such a mechanism is analogous to that of sliding along weak surfaces made up of bentonite layers, observed by Chan & Morgenstern (1987) after the Edmonton Convention Center excavation. The global failure of the slope (reactivation) entails the mobilization of the entire pre-existing slip surface. In this sense, the mechanism of reactivation is suitable to be interpreted by using the principles of the mechanics of rigid and discontinuous medium. Besides, if we consider that the sliding surface is characterized by a constitutive law, obviously "almost rigid"-perfectly plastic, with a strength equal to the residual one (moreover, barely influenced by the sliding velocity), it is easy to understand that, in this case, pre-failure phenomena have a negligible influence on the mechanics of reactivation, and soil parameters can be univocally defined. Therefore, this is the best case which limit equilibrium methods can be applied in. When rainfall represents the trigger cause of movement, the reactivation will occur only if, along the entire sliding surface, groundwater pressure reaches greater than or equal values to the maximum ones ever happened during the history of the slope. According to Picarelli (2000) this is unlikely. Indeed, he stated that landslide movements induced by pore water pressure oscillations usually happen according to mechanisms of development like those

previously described (see Figure 1.15) and therefore, without completely mobilizing the body of landslide. Since the soil is ductile along the shear surface, post-failure (or post-reactivation) movements are usually slow. However, in some cases, when the reactivation is due to a sudden increase of groundwater pressure or due to deep excavations respect to the available strength, so that a non-equilibrium between external actions and soil strength is entailed, important velocities were measured (D'Elia et al. (1998)).

1.5 – Methods of analysis

In the previous sections of this chapter, deformation and failure mechanisms of slopes are described, and the four stages that characterize a landslide are discussed: pre-failure, failure, post-failure and reactivation. However, the problem is currently tackled in a simplified way and only the failure stage and eventual reactivations are studied. This happens because of the possibility to use simplified methods, such as limit equilibrium methods, which totally neglect any deformations that precede and follow the collapse. Indeed, in such methods, an arbitrarily chosen volume of soil, defined by the ground surface at the top and by a possible slip surface at the bottom, is assimilated to a perfectly rigid-plastic medium, which reaches the failure condition simultaneously on all points belonging to the slip surface. Indeed, the aim of such

methods is the calculation of the safety factor, defined as the ratio of the average shear strength on the slip surface to the average mobilized shear stress. Such quantities are computed only by means of equilibrium equations, under simplified hypotheses. Therefore, the analysis totally ignores the deformations preceding the collapse, the progressive failure and the kinematics of the landslide after the collapse, which have a paramount importance, because on them both the risk and eventual stabilization measures depend.

Deformation and failure mechanisms of slopes can be properly studied only by means of advanced numerical methods, which are suitable to simulate the development of the deformations which lead the slope to the failure (i.e. the pre-failure stage) and the kinematics of the landslide after the collapse (i.e. the post-failure stage). Based on the way the motion is described, the available numerous numerical methods are commonly subdivided into two main categories: Lagrangian methods and Eulerian methods.

In Lagrangian methods, a computational mesh is attached to the material and deforms with it. As a result, material interfaces can be easily tracked, and history-dependent constitutive models can be readily implemented. However, since the mesh deforms with the material, Lagrangian methods suffer severe element distortion and element entanglement, which result in significant errors in the numerical solution, and even lead to a negative volume or

area, which would cause abnormal termination of the computation when large displacements or large deformations are simulated (Zhang et al. (2017)). The application of the Lagrangian approach to solve boundary problems is common in engineering practice, and in particular, among the various available techniques, the most common one is the finite element method. Within geotechnical engineering field, such a method allows almost the most common problems to be solved, such as the study of the pre-failure stage of landslides, as well as the study of the failure stage and eventual reactivations. However, this method is unsuitable for studying the post-failure stage, because of the shortcomings above-mentioned. Indeed, the finite element method is generally based on the assumption of small deformations and, therefore, it is unable for dealing with problems involving large deformations.

In Eulerian approaches, a computational mesh is kept fixed in space and does not move, while mass flows through it. In this case, there is not any difficulties associated with mesh distortion and element entanglement so that they can be easily used in order to simulate problems that involve extreme events (Zhang et al. (2017)), such as the post-failure stage of landslides. However, special procedures are required to identify material interfaces and history-dependency. This aspect makes Eulerian methods computationally much more expensive than the Lagrangian ones.

Both the Lagrangian and Eulerian methods have pros and cons; therefore, it is desirable to combine them in order to take the advantages avoiding the drawbacks. Most methods proposed in the literature to solve large deformation problems refer to two distinct approaches: the discrete approach and the continuum one (Scaringi et al., (2018)).

The distinct element method (DEM) and the discontinuous deformation analysis method (DDA) fall into the former category. In the discrete element method, the soil is discretized as a collection of rigid bodies, interacting via contact laws. It is particularly suitable for modelling the micro-mechanical behavior of soils. On the other hand, it would be computationally expensive for modelling large-scale problems, unless an up-scaling of grain sizes is performed. It generally employs an explicit formulation and uses forces as unknown variables. The discontinuous deformation analysis method, as the discrete element method, falls inside the family of discrete methods, but contrary to this latter employs an implicit formulation. It is commonly employed for analyzing jointed rock masses. Application of these methods to simulate the landslide evolution after failure can be found in several studies (Tang et al., (2015); Zhang et al., (2015); Calvetti et al., (2017); Scaringi et al., (2018)).

The smoothed particle hydrodynamics method (SPH) (Bui et al., (2011); Pirulli & Pastor, (2012); Pastor et al., (2009); Dai et al.,

(2014)) and the material point method (MPM) (Zabala & Alonso, (2011); Solowsky & Sloan, (2015); Alonso et al., (2015); Bandara & Soga, (2015); Yerro et al., (2015); Bhandari et al., (2016); Li et al., (2016); Soga et al., (2016); Yerro et al., (2016); Rohe & Martinelli, (2017); Zhang et al., (2017); Fern et al., (2019); Conte et al., (2019)) are the most used continuum approaches for modeling extreme events within geotechnical engineering field, such as the post-failure stage of landslides characterized by extremely large displacements, from sliding to flow-like landslides. Smooth particle hydrodynamics (SPH) is a mesh-free technique, in which the domain is discretized into particles that have a spatial distance referred to as the smoothing length. Material properties are 'smoothed' over this distance by a kernel function. Although SPH has been successfully used in the past, it has a few drawbacks. Indeed, it exhibits spatial instabilities, because of the point-wise integration (Bonet & Kulasegaram, (2000)). Insufficient neighboring particles potentially cause inconsistencies, and the boundary treatment is complex. It is computationally expensive as a result of the search for the neighboring particles (Bandara, (2013)). The material point method (MPM) is a particle-based method that represents the material as a collection of material points, taking advantage of the combined Eulerian–Lagrangian approach. It uses moving material points and computational nodes on a background mesh. Soga et

al. (2016) described a more extensive review of the numerical techniques available to model large problems in geotechnical engineering.

Among these methods, the one used to carry out the work presented in this dissertation is the material point method, which is described in detail in Chapter 2. The main reasons why MPM is chosen in this dissertation is that it can be used with large-scale failure analysis that undergoes large deformations since this method is based on continuum description of material flow using an Eulerian–Lagrangian approach. Furthermore, its application of boundary conditions is more straightforward than other mesh-free methods, such as the SPH method, owing to the presence of the background grid.

The material point method is employed in this dissertation to analyze the post-failure stage of two landslides.

Chapter 2 - The Material Point Method

2.1 – Introduction

It has already been pointed out in Section 1.5 that limit equilibrium methods are useful techniques for assessing the safety factor of a slope in traditional geotechnical analysis. However, no information can be provided about the deformation mechanisms of the slope and these methods are therefore unable for simulating the real soil behavior. Numerical methods, such as the finite element method or the finite difference method, can be used to model complex geometries and soil behaviors, but are generally limited to small deformation analyses and are consequently unsuitable for modelling post-failure behaviors. In Section 1.5, an overview of the more advanced numerical methods developed in the recent years was presented. These methods are developed to provide an engineering tool capable of simulating the entire instability process, from the static stability analysis at small deformations to the dynamic post-failure run-out behavior. Among these methods, the material point method (MPM) is chosen to carry out the work presented in this dissertation.

This whole chapter is dedicated to the theoretical description of this method, whereas its application to real landslides is presented afterwards.

2.2 – Basic concepts

The origins of the Material Point Method date back to the work of Harlow (1964), in which the Particle-In-Cell method (PIC) was introduced with the aim of representing fluids flow whereby a set of material points moving throughout a fixed mesh. Afterwards, this approach was extended by Sulsky et al. (1994); (1995) in order to model problems of solid mechanics involving large displacements and large deformations, taking advantages from both Eulerian and Lagrangian methods, overcoming the shortcomings of each.

This method is suitable to be successfully applied in the geotechnical engineering field, and therefore for studying the post-failure phase of landslides characterized by large values of displacements, such as flow-like landslides. In this approach, the continuum medium is discretized as a set of subdomains (see Figure 2.1), whose information (density, acceleration, velocity, displacement, mechanical characteristics, external loads, state variables, etc.) is concentrated within a Lagrangian point, called Material Point. Therefore, each material point represents an initially defined part of the domain. One of the main and most important features of the material point method is that the mass of each material point remains strictly constant and, consequently, mass conservation is automatically satisfied, whereas the volume of the material point can change enabling

material compression or extension. Each material point moves attached to the deformation of the body. This aspect provides the Lagrangian description of the continuum.

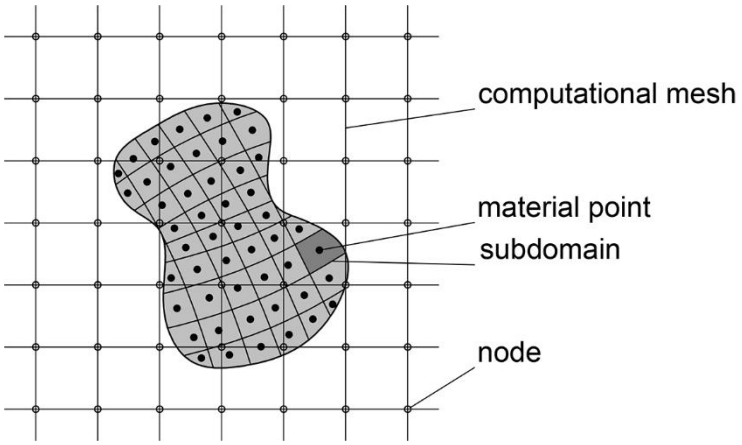

Figure 2.1 – Continuum medium discretization in the material point method approach

Furthermore, the continuum medium, which is discretized as a set of many Lagrangian points (material points), is overlaid on a computational mesh (Eulerian mesh), whose aim is simply to solve the governing equations, but which is kept fixed during the whole simulation, and which does not carry any permanent information. Such a mesh is the same of the one used for the conventional Finite Element Method (FEM), and it has to be built so that it can cover the entire domain of the problem. Therefore, empty elements are required to cover the space where material points are expected to move during the simulation.

The discretized momentum balance equations are generally solved in correspondence of the nodes of this computational mesh, whereas mass conservation and constitutive equations are solved in correspondence o material points. The variable needed to solve

equations are transferred from material points to mesh nodes whereby specific shape functions for each time-step, such as the typical linear shape function commonly used within the FEM approach. After solving the balance equations by using an incremental time integration scheme, the quantities carried by material points are updated by interpolating the mesh results, using the same mapping functions. All information associated with the mesh is not required for the next step of the analysis, therefore it can be discarded avoiding any mesh distortion. In this way, therefore, large displacements are simulated whereby material points moving throughout the mesh, which remains undeformed.

Therefore, the material point method takes advantages from both Eulerian and Lagrangian approaches. If compared with the Eulerian approach, the computational cost is substantially reduced although the load path is accounted for; on the other hand, if compared with the Lagrangian approach, mesh distortion problems are avoided. Therefore, the material point method is particularly suitable for analyzing extreme events, among which landslides characterized by large displacements.

In the last years, many applications of the material point method have been published (Zabala & Alonso (2011); Solowsky & Sloan (2015); Ceccato (2015); Yerro (2015); Yerro et al. (2015); Ceccato et al. (2016); Soga et al. (2016); Yerro et al. (2016); Ceccato et al.

(2017); Martinelli et al. (2017); Rohe & Liang (2017); Ceccato et al. (2018); Conte et al. (2019); Fern et al. (2019)).

2.3 – Calculation scheme

The algorithm of the material point method for a single calculation step of a time increment is illustrated in Figure 2.2. At the beginning of each time step, information contained within material points is transferred, whereby suitable interpolation shape function, from material points to mesh nodes (Figure 2.2a), where governing equations are solved obtaining the primary unknown variables, such as nodal accelerations (Figure 2.2b).

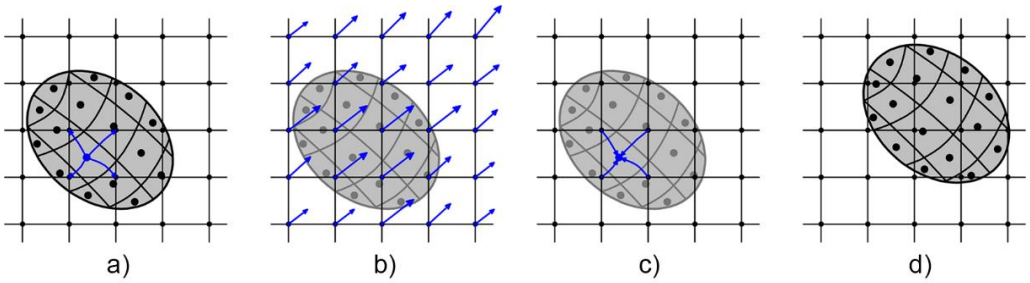

Figure 2.2 – Material point method calculation scheme

Such nodal values are used in order to update values of accelerations, velocities, and displacements of material points and, moreover, to calculate stresses and deformations of material points (Figure 2.2c). Finally, based on the quantities just calculated, it is possible to update the position of material points (Figure 2.2d). Following this scheme, no permanent information is stored within the mesh, therefore it can be freely redefined at

the end of each time step, but it is usually kept fixed. In this way, the computational mesh remains undeformed during the whole simulation, ensuring the accuracy of the analyses even when material points undergo large displacements.

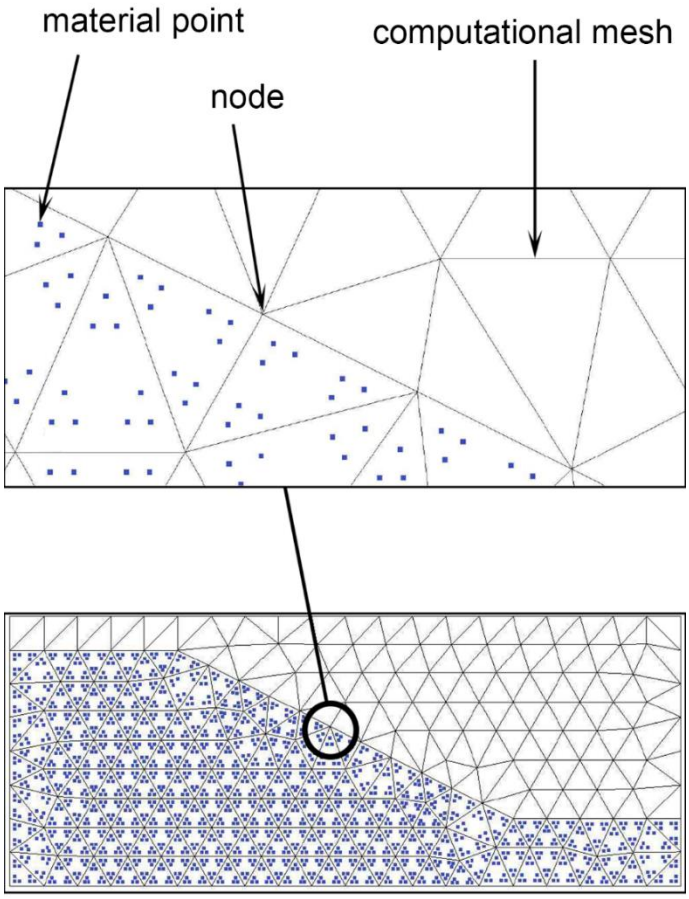

Figure 2.3 – Detail of the material point method framework

It is necessary to observe that, while the mesh is kept undeformed during the whole simulation, material points move throughout it. This means that the boundaries of the initial geometry have to be different from the boundaries of the computational mesh, which have to be characterized by a geometry suitable to capture material points that will leave the original position. Definitively,

the computational mesh has to be built within a space which can be subdivided into two parts: the first one, which represents the initial configuration of the problem, made by elements containing material points in their initial position; the second one, made by initially empty elements, which represents the domain where soil will move after an eventual collapse. The two parts are shown in Figure 2.3, which reports the initial configuration of a slope characterized with a simple geometry. In particular, it shows a plane side view of a 3D mesh made up of tetrahedral elements with an initial distribution of four material points per element.

2.4 – Mathematical formulation

Soil is a multiphase material, i.e. it is made up of a mixture of three constituents (solid, liquid and gas) which interact with each other. On their interaction, the mechanical and hydraulic response of the material depend. However, taking rigorously into account these interaction might be often unnecessarily complicated, computationally expensive and even not feasible for engineering applications.

Therefore, in order to simulate different types of problem, two different approaches have been developed for the last years: the "single-point" approach and the "multi-point" one. In the "single-point" approach, soil is discretized as a unique continuum medium by means of a set of material points. Each material point

represents both solid and fluid phases. Therefore, this approach is suitable for modeling problems such as slope failures, consolidation problems, dike stability, water reservoir, among others. Dry soil, pure liquid and saturated soils in fully drained or undrained conditions can be modelled with the 'one-phase single-point' formulation (Fern et al., (2017), Conte et al., (2019); Martinelli et al., (2019); Tran & Solowsky, (2019)), whereas saturated soils in transitory conditions can be modelled using the 'two-phase single-point' formulation (Ceccato et al., (2016); Yerro et al., (2016); Troncone et al., (2019)).

Besides, the behavior of unsaturated soils can be studied by means of the 'three-phase one-point' formulation (Yerro et al., (2015); Bandara et al., (2016)).

In the "multi-point" approach, solid and fluid phases are represented separately by means of different sets of material points. Each material point carries only information of the phase that it represents. Therefore, this approach is suitable for modeling problems where water moves separately from the solid phase, such as seepage flow, slope liquefaction, erosion and in wider terms the soil-water-structure interaction (Martinelli & Rohe, (2015); Bolognin et al., (2017); Martinelli et al., (2017)).

A schematization of the different approaches is shown in Figure 2.4.

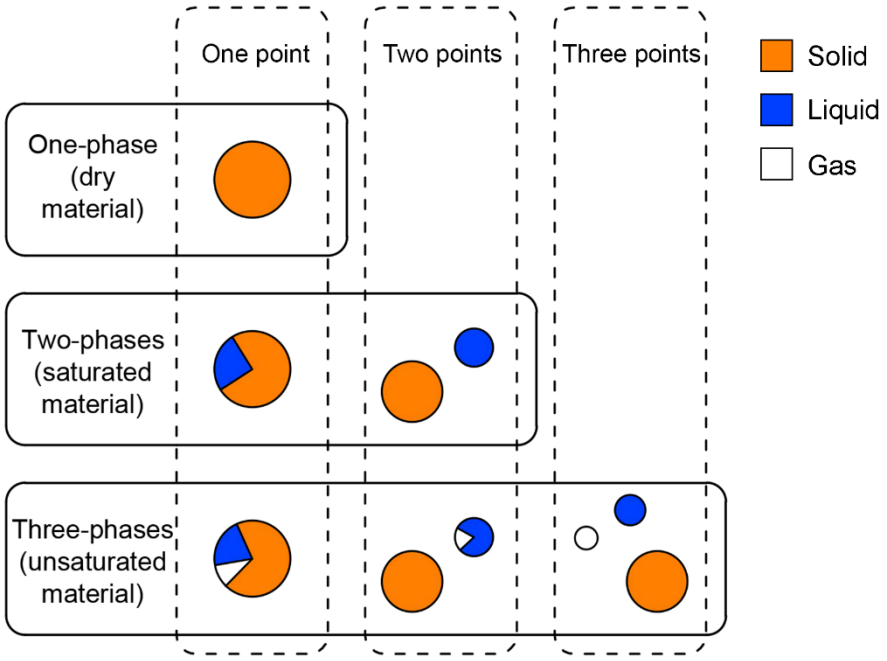

Figure 2.4 – Schematization of different approaches of the material point method depending on the number of set of material points and phases (adapted from Yerro et al. (2015))

The aim of this section is to describe the mathematical formulation of the material point method, analyzing the dynamic equilibrium equations within the context of the continuum mechanics. The attention in this dissertation will only be focused on the 'single-point' formulation, since the case studies analyzed in the following chapters are characterized by dry soils for which was proved that the effect of suction can be disregarded, as well as fully saturated soils. Particularly, attention will be given to the 'one-phase single-point' and the 'two-phase single-point' formulations. Nevertheless, with referring to the post-failure stage of landslides and considering the complex processes occurring in natural landslide phenomena, from a general point of view, it would also be important to extend the MPM formulations

described and used in this dissertation towards either a 'two-phase two-point' formulation or a 'three-phase formulation'. Indeed, since the former is suitable to model groundwater flow, dry and saturated areas separately, it would provide a more complete description of the hydraulic behavior of soil and the interaction between water and solid skeleton. Furthermore, the latter is capable to account for the contribution of suction on soil behavior for unsaturated materials. However, the application of these formulations is not strictly required for analyzing the case studies considered in this dissertation and, therefore, their description is avoided.

2.4.1 – One-phase single-point formulation

The mathematical formulation of material point method for the analysis of the soil behavior when it is undergone large displacements is based on the work of Sulsky et al. (1994) and (1995). Although the soil is a multiphase material, made up of solid particles whose voids are filled with water or more fluids, it can be treated like a homogeneous, one-phase material. Saturated soils can be in drained, partially drained and undrained conditions, depending on the soil permeability and velocity of load. In drained conditions, a negligible excess pore pressure is generated and it dissipates rapidly. For this reason, it can be disregarded. In undrained conditions, the velocity of load is so fast

that a significant excess pore water pressure generates in the initial condition, but at the same time water cannot flow out soil voids and, therefore, pore pressure dissipation can be disregarded. Both cases allow a simplified approach to be used, in which only the solid velocity field is considered. In this cases, the one-phase single-point formulation can be applied. Instead, it is not suitable for analyzing other situations.

Since the material point method can be seen as an extension of the FEM procedure, it is necessary to notice that these the methods have much in common. For instance, the weak form of the governing equations as well as the final system of equations within computational mesh nodes are the same for both methods. The main difference between MPM and FEM is the calculation of numerical integrations on the volume of a finite element. Indeed, whereas in the FEM formulation integrations are calculated in correspondence of Gaussian points, in the MPM formulation they are calculated in correspondence of material points.

2.4.1.1 – Governing equations

When problems that involve large deformations are tackled, such as the study of the post-failure phase of landslides, the finite deformations theory must be used in order to define the governing equations. Within the context of mechanics of continuum, such equations are based on the conservation of mass, balance of

momentum and energy, constitutive models and kinematic conditions. Physics systems must always observe such conditions. Since such formulation is referred to the one-phase medium, all the quantities appearing in the equations described in this section are referred to the considered phase.

Mass conservation

Consider a continuum body *C*, made by a set of subdomains *D*. For each subdomain it is possible to define the mass *m(D)* in function of the density ρ whereby Equation (2.1).

$$m(D) = \int_D \rho \mathrm{dV} \tag{2.1}$$

According to the principle of conservation of mass, the mass of each subdomain *D* is constant with the time, then Equation (2.2) must be true.

$$\frac{\mathrm{d}}{\mathrm{dt}} \int_D \rho(\mathbf{x}, \mathrm{t}) \mathrm{dV} = 0 \tag{2.2}$$

By applying the *transport theorem* (*or Reynolds' theorem*) to Equation (2.2) and considering that it must be true for any material volume, the *local* or *Eulerian expression* is obtained (Equation (2.3)).

$$\frac{\partial \rho}{\partial x} + \nabla \cdot (\rho \mathbf{v}) = 0 \tag{2.3}$$

In Equation (2.3), **v** represents the vector of velocity of the solid phase. One of the basic assumptions of the material point method

is that the mass of each material point remains constant during the deformation process. Therefore, mass conservation is automatically satisfied and Equation (2.3) can be used to update density.

Balance of linear momentum

According to the principle of linear momentum, the rate of change of the linear momentum of any subdomain D of a continuum body C is equal to the resultant of forces acting on it from its exterior. Within the context of continuum mechanics, such forces are commonly classified in two classes:

- those forces acting on the subdomain D from the exterior of C, such as mass forces represented by vector field $\mathbf{b}$ (per unit mass);
- those forces interior to C and acting on the boundary ∂D of the subdomain D, called contact forces.

In order to represent these contact forces, it is necessary to resort to the Cauchy's theorem, which states that the action of a continuum on the portion D is represented through the stress vectors $\mathbf{t}$ acting on the boundary ∂D. To express the distribution of such vectors in mathematical terms, the following clarification are necessary:

- in each point of the boundary ∂D and in every instant t, such values express contact actions;

- the stress vector **t** depends, at every instant, on the point and on the perpendicular direction to ∂D in the considered point, i.e. **t** depends on the local shape of the boundary ∂D only for the first order.

With the latter assumption, the principle of the linear momentum in the global form writes as expressed by Equation (2.4).

$$\frac{\mathrm{d}}{\mathrm{d}t}\int_D \rho\mathbf{v}\mathrm{dV} = \int_{\partial D} \mathbf{t}\mathrm{dS} + \int_D \rho\mathbf{b}\mathrm{dV} \tag{2.4}$$

The integral in the first member of Equation (2.4), by using the transportation theorem and the mass conservation, can be written according to Equation (2.5).

$$\int_V \rho\frac{\mathrm{d}\mathbf{v}}{\mathrm{d}t}\mathrm{dV} \tag{2.5}$$

Further, the stress vector can be expressed according to the Cauchy's lemma:

$$t_i = \sigma_{ij}n_j \tag{2.6}$$

and by applying the Gauss theorem to the surface integral, the principle of the linear momentum assumes the form of Equation (2.7).

$$\rho\frac{\mathrm{d}\mathbf{v}}{\mathrm{d}t} = \nabla\cdot\boldsymbol{\sigma}^{\mathrm{T}} + \rho\mathbf{b} \tag{2.7}$$

Equation (2.7) is known as the Cauchy's first law of motion, and depends on the density ρ as well as on the acceleration $\frac{\mathrm{dv}}{\mathrm{dt}}$, on the stress state tensor **σ** and on the mass forces vector **b**. If the

acceleration $\frac{\mathrm{d}\mathbf{v}}{\mathrm{dt}}$ vanishes, then the Cauchy's first law of motion reduces to the indefinite equilibrium equations:

$$\frac{\partial \sigma_{ji}}{\partial x_j} + \rho b_i = 0 \tag{2.8}$$

Conservation of energy

Assuming the mechanical work as the only source of energy, neglecting heat effects and any source of thermal energy, the conservation of energy can be written in the following form:

$$\rho \frac{\mathrm{d}r}{\mathrm{d}t} = \dot{\boldsymbol{\varepsilon}}\boldsymbol{\sigma} \tag{2.9}$$

in which r is the internal energy per unit mass and $\dot{\boldsymbol{\varepsilon}}$ is the deformation rate tensor. In order to describe the mechanical behavior of a material, to complete the specification of the mechanical properties, additional equations are required. Such equations are known as constitutive equations. Such equations specify, as known from the basis of continuum mechanics, the relationship existing between static and kinematic quantities, describing the behavior of the material strictly depending on its composition.

Initial conditions and boundary conditions

Let us indicate $\partial\Omega$ the boundary of the domain Ω covered by the material, which can be divided into two parts, $\partial\Omega_u$ and $\partial\Omega_\tau$. The boundary $\partial\Omega_u$ represents the prescribed displacement boundary,

whereas $\partial\Omega_\tau$ denotes the prescribed stress boundary or prescribed traction boundary. The displacement boundary conditions on $\partial\Omega_u(t)$ can be written as given in Equation (2.10):

$$\vec{u}(\vec{x},t) = \vec{U}(t) \tag{2.10}$$

where $\vec{U}(t)$ is the prescribed surface displacement vector. The traction boundary conditions on $\partial\Omega_\tau(t)$ are defined by Equation (2.11):

$$\boldsymbol{\sigma}(\vec{x},t)\vec{n} = \vec{\tau}(t) \tag{2.11}$$

where $\vec{n}$ is the outward unit normal vector of the boundary surface $\partial\Omega_\tau$, whereas $\vec{\tau}(t)$ is the prescribed surface traction vector.

Initial conditions are given by Equations (2.12):

$$\vec{u}(\vec{x},t_0) = \overrightarrow{U_0}; \quad \vec{v}(\vec{x},t_0) = \overrightarrow{V_0}; \quad \boldsymbol{\sigma}(\vec{x},t)\vec{n} = \boldsymbol{\sigma}_0 \tag{2.12}$$

2.4.2 – Two-phase single-point formulation

The previous section was dedicated to the description of the governing equations of the MPM one-phase formulation, which is suitable for analyzing problems in which dry soils, pure liquids or saturated soils in fully drained or undrained conditions are involved. However, for fully saturated soils it is sometimes necessary to account for the coupling between solid and fluid phases, in order to take into account the excess pore pressure generation and its dissipation process. Therefore, in order to analyze some common problems of geotechnical engineering, a

more complex formulation is required. Among the main works about the theoretical approach describing the coupling between solid and fluid phases, it is possible to refer to the following ones: Biot (1941); Biot (1955); Biot (1972); Zienkiewicz et al. (1980); Zienkiewicz (1982); Zienkiewicz & Shiomi (1984); Zienkiewicz et al. (1990); Zienkiewicz et al. (1999).

The easiest way to account for the coupling between the soil skeleton and the fluid phase within the context of the material point method theory is the two-phase single-point formulation. The two-phase single-point approach is consistent with a purely macroscale continuum theory where the behavior of the porous medium is described based on the kinematics of the solid skeleton (Biot (1941)). In this approach, the saturated porous medium is discretized by a single set of material points that move according to the solid velocity field. Each material point describes a representative volume element of a fully saturated soil, carrying information of both solid and liquid phases together. While material points are attached to the solid skeleton giving a Lagrangian description of its movement, an Eulerian approach with respect to the solid represents the motion of the liquid phase. In this manner, the volume associated to a material point, V_{MP}, is the total volume of the mixture, i.e. it is the sum of the partial volumes of solid, V_S^{MP}, and the partial volume of liquid, V_L^{MP}, (Equation (2.13)).

$$V_{MP} = V_S^{MP} + V_L^{MP} \tag{2.13}$$

In this approach, the solid mass of each material point remains constant, whereas the total mass can change as a result of inflow or outflow of liquid. Therefore, only the conservation of the solid mass is automatically fulfilled throughout the calculation.

2.4.2.1 – Governing equations

In what follows the soil is supposed to be saturated, and isothermal conditions are assumed. Under these assumptions, the formulation of the mathematical model requires to account for the mass conservation and the momentum balance equations of both phases, as well as the state equations and the constitutive equations of the solid and liquid phases. State equations, mass conservation, momentum balance equations and the constitutive relationship of the liquid phase are described in the followings, whereas the constitutive modelling of the solid phase will be discussed in detail in Section 2.8.

State equations

If β is the water compressibility, then the state equation, which in isothermal conditions relates the density to the pore pressure, writes:

$$\rho_w = \rho_{w0} e^{\beta(u-u_0)} \tag{2.14}$$

where ρ_{w0} and u are reference values. Indeed, in Soil Mechanics the compressibility of the solid particles is usually neglected, therefore

$$\rho_s = \text{const} \tag{2.15}$$

Mass conservation

The mass conservation principle postulates that during the motion the mass of any material portion does not change in time. Accordingly, the local formulation of this principle for the solid and for the fluid phases writes according to Equations (2.16) and (2.17).

$$\frac{\partial[(1-n)\rho_s]}{\partial t} + \nabla \cdot [(1-n)\rho_s \mathbf{v_s}] = 0 \tag{2.16}$$

$$\frac{\partial(n\rho_w)}{\partial t} + \nabla \cdot (n\rho_w \mathbf{v_w}) \tag{2.17}$$

If we introduce the state equations into the mass conservation equations, and we neglect the terms $n\mathbf{v}_w \cdot \nabla\rho_w$ and $(1-n)\mathbf{v}_s \cdot \nabla\rho_s$, the previous equations become Equations (2.18) and (2.19).

$$-\frac{\partial n}{\partial t} + \nabla \cdot [(1-n)\mathbf{v_s}] = 0 \tag{2.18}$$

$$\frac{\partial n}{\partial t} + n\beta\frac{\partial u}{\partial t} + \nabla \cdot (n\mathbf{v}_w) = 0 \tag{2.19}$$

Summing up these equations, we eliminate the term $\frac{\partial n}{\partial t}$. Further, taking into account the definition of discharge velocity:

$$\mathbf{v} = n(\mathbf{v}_w - \mathbf{v}_s) \tag{2.20}$$

and observing that $\nabla \cdot \mathbf{v}_s = -\frac{\partial \varepsilon_v}{\partial t}$ (the negative sign is needed because the compression is assumed positive, whereas the displacement u_k is positive if oriented as the x_k axis), we obtain the mass conservation of the porous medium:

$$n\beta \frac{\partial u}{\partial t} - \frac{\partial \varepsilon_v}{\partial t} + \nabla \cdot \mathbf{v} = 0 \tag{2.21}$$

This equation is called *storage equation* and can be interpreted as follows: the rate of compression of a soil element is equal to the rate of compression of the fluid plus the flow of the fluid expelled from the element.

Momentum balance equation

The conservation of momentum of the solid phase can be expressed as:

$$\begin{aligned}(1-n)\rho_s \frac{\partial \mathbf{v}_s}{\partial t} - \nabla \boldsymbol{\sigma}' - (1-n)\nabla p_l + \\ -(1-n)\rho_s \mathbf{g} - \frac{n^2 \rho_l g}{k}(\mathbf{v}_l - \mathbf{v}_S) = 0\end{aligned} \tag{2.22}$$

where k is the isotropic Darcy permeability. It can be expressed in terms of intrinsic permeability κ and the dynamic viscosity of the liquid μ_d Equation (2.23).

$$k = \kappa \frac{\rho_l g}{\mu_d} \tag{2.23}$$

The conservation of momentum of the liquid phase is written as Equation (2.24).

$$n\rho_l \frac{\partial \mathbf{v}_l}{\partial t} - n\nabla p_l - n\rho_l \mathbf{g} + \\ + \frac{n^2 \rho_l g}{k}(\mathbf{v}_l - \mathbf{v}_S) = 0 \tag{2.24}$$

The term $(\mathbf{v}_l - \mathbf{v}_S)$ represents the relative velocity of the liquid respect to the solid. By combining the momentum of the solid phase with the momentum of the liquid phase, the momentum conservation for the mixture can be written as expressed in Equation (2.25).

$$(1-n)\rho_s \frac{\partial \mathbf{v}_s}{\partial t} + n\rho_l \frac{\partial \mathbf{v}_l}{\partial t} = \\ = \nabla \cdot \boldsymbol{\sigma} + \rho_{sat}\mathbf{g} \tag{2.25}$$

Constitutive relation

In order to fully describe the behavior of saturated soils, the constitutive equations for both solid and liquid phases are required. Assuming the validity of Terzaghi's effective stress concept, the mechanical behavior of the soil can be modelled in terms of effective stresses. The constitutive relationship for the solid phase will be discussed in detail in Section 2.8. The constitutive relationship considered for the pore liquid, which relates volumetric strain of the liquid to liquid pressure, is expressed by Equation (2.26):

$$\frac{D^s p_L}{Dt} = K_L \frac{D^s \varepsilon_{vol_L}}{Dt} \tag{2.26}$$

where K_L is the elastic bulk modulus of the liquid.

2.4.2.2 – Hypotheses

The spatial variation of density and porosity is neglected assuming incompressible soil grains. Additionally, flow is considered laminar and stationary in the slow velocity regime. Therefore, the interaction force between the solid and liquid phases (i.e. the drag force, $\boldsymbol{f}_L^d$) is governed by Darcy's law (Equation (2.27)).

$$\boldsymbol{f}_L^d = \frac{n_L \mu_L}{\kappa_L}(\mathbf{v}_l - \mathbf{v}_S) \tag{2.27}$$

This hypothesis can be controversial in high velocity flows where drag forces can become non-linear. In Equation (2.27), n_L is the volumetric concentration ratio of fluid, μ_L is the dynamic viscosity of the liquid and κ_L is the liquid intrinsic permeability. For the sake of simplicity, these parameters are assumed constant throughout the simulation. The isotropic intrinsic permeability of the liquid, κ_L, can be expressed in terms of Darcy permeability, k_L (Equation (2.28)).

$$\kappa_L = k_L \frac{\mu_L}{\rho_L g} \tag{2.28}$$

In the context of the two-phase single-point approach, the solid mass conservation is naturally fulfilled since the solid mass remains constant in each material point. However, such a condition is not automatically satisfied for the liquid because it can move apart from the solid skeleton depending on solid volumetric strain changes. Therefore, the liquid mass in each

material point can change and, consequently, the conservation of the liquid mass is completely controlled by the accuracy in which the liquid mass balance is solved. Fluxes due to spatial variations of liquid mass are neglected in the two-phase single-point formulation. Therefore, the total mass balance is given only by Equation (2.26), and describes the volumetric strain rate of the liquid phase. Such a hypothesis is reasonable when gradients of porosity are relatively small, but can induce errors when two material with very different porosity are in contact. Additionally, to obtain Equations (2.26) and (2.28), the liquid is assumed to be weakly compressible, and shear stresses in the liquid phase are neglected.

2.4.3 – Weak form of governing equations

The governing equations previously described result in a set of partial differential equations which describe the motion of a continuum. These governing equations could be solved exactly for some simple problems, whereas they cannot be solved exactly for most common problems of engineering. Indeed, such equations have to be solved numerically for the main modern engineering problems, characterized with complex domains and boundary conditions. There are two different kinds of numerical methods for solving partial differential equations. The first one obtains directly an approximate solution of the partial differential equations with

their initial and boundary conditions. As an example, the finite difference method (FDM) converts the partial differential equations in a set of linear equations by approximating the derivatives in the equations with corresponding differences at grid points. The second kind of method, first establishes an equivalent weak form of the original partial differential equations with their initial and boundary conditions, and then solves the weak form numerically. The material point method (MPM) as well as the finite element method (FEM) is based on the weak form.

Weak form of the one-phase single-point formulation

The conservation of the momentum (Equation (2.7)) is fundamental in continuum mechanics since it represents the equation of motion of the continuum. To discretize its strong form in the weak form, virtual quantities have to be considered. In particular, the momentum equation has to be multiplied by a virtual velocity $\delta\mathbf{v}$ and integrated over the current domain Ω occupied by the continuum:

$$\int_{\Omega} \delta\mathbf{v}\rho\frac{\mathrm{d}\mathbf{v}}{\mathrm{d}t}\mathrm{d}\Omega = \\ = \int_{\Omega} \delta\mathbf{v}(\nabla\cdot\boldsymbol{\sigma}_s)\mathrm{d}\Omega + \int_{\Omega} \delta\mathbf{v}\rho\mathbf{g}\mathrm{d}\Omega \tag{2.29}$$

with $\delta\mathbf{v} = 0$ on $\partial\Omega_u$.

The first term on the right-hand side of Equation (2.29) can be expressed as in Equation (2.30).

$$\int_{\Omega} \delta\mathbf{v}(\nabla \cdot \boldsymbol{\sigma}_s)\mathrm{d}\Omega = \\ = \int_{\Omega} (\nabla \cdot \delta\mathbf{v}\boldsymbol{\sigma}_s)\mathrm{d}\Omega - \int_{\Omega} (\nabla \cdot \delta\mathbf{v})\boldsymbol{\sigma}_s \mathrm{d}\Omega \tag{2.30}$$

Using Gauss theorem, also known as divergence theorem, the first term on the right-hand sand side of Equation (2.30) can be written as in Equation (2.31).

$$\int_{\Omega} (\nabla \cdot \delta\mathbf{v}\boldsymbol{\sigma}_s)\mathrm{d}\Omega = \int_{\partial\Omega_\sigma} \delta\mathbf{v}\boldsymbol{\tau}_s \mathrm{d}\,\partial\Omega \tag{2.31}$$

Substituting Equations (2.30) and (2.31), Equation (2.29) takes the form expressed by Equation (2.32).

$$\int_{\Omega} \delta\mathbf{v}\rho\frac{\mathrm{d}\mathbf{v}}{\mathrm{d}t}\mathrm{d}\Omega = \int_{\partial\Omega_\sigma} \delta\mathbf{v}\boldsymbol{\tau}_s \mathrm{d}\,\partial\Omega + \\ - \int_{\Omega} (\nabla \cdot \delta\mathbf{v})\boldsymbol{\sigma}_s \mathrm{d}\Omega + \int_{\Omega} \delta\mathbf{v}\rho\mathbf{g}\mathrm{d}\Omega \tag{2.32}$$

Equation (2.32) will be used in the formulation of the discrete equations.

Weak form of the two-phase single-point formulation

To obtain the weak form when more phases are accounted for, Equations (2.24) and (2.25) have to be multiplied by weighting

function **t** and integrating over the current domain Ω (Equations (2.33) and (2.34)).

$$\int_{\Omega} \delta\mathbf{t}\rho_l \frac{\mathrm{d}\mathbf{v}_l}{\mathrm{d}t}\mathrm{d}\Omega = \int_{\Omega} \delta\mathbf{t}\nabla p_l \mathrm{d}\Omega + \\ + \int_{\Omega} \delta\mathbf{t}\rho_l \mathbf{g}\mathrm{d}\Omega - \int_{\Omega} \delta\mathbf{t}\frac{n\rho_l g}{k}(\mathbf{v}_l - \mathbf{v}_S)\mathrm{d}\Omega \tag{2.33}$$

$$\int_{\Omega} \delta\mathbf{t}(1-n)\rho_s \frac{\mathrm{d}\mathbf{v}_s}{\mathrm{d}t}\mathrm{d}\Omega = \int_{\Omega} \delta\mathbf{t}\nabla\cdot\boldsymbol{\sigma}'\mathrm{d}\Omega + \\ + \int_{\Omega} \delta\mathbf{t}\rho_{sat}\mathbf{g}\mathrm{d}\Omega - \int_{\Omega} \delta\mathbf{t}n\rho_l \frac{\mathrm{d}\mathbf{v}_l}{\mathrm{d}t}\mathrm{d}\Omega \tag{2.34}$$

Applying the divergence theorem and the traction boundary conditions, the final weak forms are expressed according to Equations (2.35) and (2.36).

$$\int_{\Omega} \delta\mathbf{t}\rho_l \frac{\mathrm{d}\mathbf{v}_l}{\mathrm{d}t}\mathrm{d}\Omega = \int_{\partial\Omega_{\mathrm{p}}} \delta\mathbf{t}\bar{p}_l \mathrm{dS} - \int_{\Omega} \nabla\delta\mathbf{t}p_l \mathrm{d}\Omega + \\ + \int_{\Omega} \delta\mathbf{t}\rho_l \mathbf{g}\mathrm{d}\Omega - \int_{\Omega} \delta\mathbf{t}\frac{n\rho_l g}{k}(\mathbf{v}_l - \mathbf{v}_S)\mathrm{d}\Omega \tag{2.35}$$

$$\int_{\Omega} \delta\mathbf{t}(1-n)\rho_s \frac{\mathrm{d}\mathbf{v}_s}{\mathrm{d}t}\mathrm{d}\Omega = \int_{\partial\Omega_{\sigma}} \delta\mathbf{t}\boldsymbol{\tau}\mathrm{dS} + \\ - \int_{\Omega} \nabla\delta\mathbf{t}\boldsymbol{\sigma}\mathrm{d}\Omega + \int_{\Omega} \delta\mathbf{t}\rho_{sat}\mathbf{g}\mathrm{d}\Omega - \int_{\Omega} \delta\mathbf{t}n\rho_l \frac{\mathrm{d}\mathbf{v}_l}{\mathrm{d}t}\mathrm{d}\Omega \tag{2.36}$$

The left-hand side terms in Equations (2.35) and (2.36) represent the inertia. In the right-hand side, the first terms represent the external load applied at the boundary, the second ones represent the internal force, and the third terms represent the gravity load. The last term in Equation (2.35) is the drag force, whereas the last term in Equation (2.36) is the liquid inertia, where the porosity is accounted for.

2.5 – Explicit-Dynamic scheme

The governing equations described in the previous sections are differential equations with respect to the time and can be solved whereby an explicit or an implicit integration scheme. The explicit integration scheme finds the state variable $y(t + \Delta t)$ at the next step based on the state variable $y(t)$ at the current time step, whereas the implicit integration scheme finds the state variable $y(t + \Delta t)$ by solving an equation $F(y(t), y(t + \Delta t))$ that involves both the current and the later state variables. In the MPM, all material properties are carried by points, and no permanent information is stored in the grid nodes. When solving the grid nodal momentum equation at time t^k, hence, the mass momentum and stress of each point are mapped to the corresponding grid nodes. After solving the grid nodal momentum equations with an explicit time integrations scheme, the grid nodal accelerations are mapped back to the corresponding points to update their velocities and

positions. The stress state of a point can be updated with the use of a suitable constitutive model, which first finds the incremental strain of the point, and then calculates its current stress with the constitutive model.

In this dissertation, the Material Point Method is applied whereby the software ANURA3D, developed by the ANURA3D MPM Research Community (www.anura3d.com), whose computational scheme adopted in the dynamic explicit formulation is mentioned in the following sections, with referring to the one-phase single-point and two-phase single-point formulations. The reason why the explicit time integration scheme is adopted in this dissertation consists in the fact that since it does not solve a system of simultaneous equations, it is consequently characterized by an efficient step-by-step solution scheme for large-scale computer simulations. Therefore, its computational cost is much lower than that required for an implicit method.

2.5.1 – Explicit-Dynamic scheme for one-phase single-point formulation

Discretized momentum of balance equation

The linear momentum equation previously discussed in Section 2.4 can be expressed in the weak form over the domain Ω (Equation (2.37)).

$$\int_{\Omega} \delta\mathbf{v}\rho\frac{\partial\mathbf{v}}{\partial t}d\Omega = \int_{\partial\Omega_\sigma} \delta\mathbf{v}\tau d\partial\Omega + \\ -\int_{\Omega} (\nabla\cdot\delta\mathbf{v})\boldsymbol{\sigma}d\Omega + \int_{\Omega} \delta\mathbf{v}\rho\mathbf{g}d\Omega \tag{2.37}$$

The domain Ω is decomposed into finite subdomains Ω_{el} called finite elements. Each element is joined with its surrounding elements by points called nodes. The state variables have interpolation shape functions within the element and the solution is then obtained at the nodes. According to the rules commonly used within the finite element theory, Equation (2.37) can be written in the discretized form:

$$\mathbf{f}^{\text{ext}} - \mathbf{f}^{\text{int}} = \mathbf{M}\hat{\mathbf{a}} \tag{2.38}$$

with:

$$\mathbf{f}^{\text{ext}} = \int_{\partial\Omega} \bar{\mathbf{N}}^T\mathbf{t}\cdot\mathbf{n}d\partial\Omega - \delta\hat{\mathbf{v}}^T\int_{\Omega}\rho\mathbf{N}^T\mathbf{g}d\Omega \tag{2.39}$$

$$\mathbf{f}^{\text{int}} = \int_{\Omega}\mathbf{B}^T\boldsymbol{\sigma}'d\Omega \tag{2.40}$$

$$\mathbf{M} = \int_{\Omega}\rho\bar{\mathbf{N}}^T\bar{\mathbf{N}}d\Omega \tag{2.41}$$

In the latter expressions, $\mathbf{f}^{\text{ext}}$ is the vector of nodal external forces, $\mathbf{f}^{\text{int}}$ is the vector of nodal internal forces and $\mathbf{M}$ is the nodal mass matrix.

Besides, $\bar{\mathbf{N}}$ is the interpolation function or shape function matrix, $\mathbf{n}$ is the unit vector which is normal to the boundary of the domain, $\hat{\mathbf{v}}$ is the vector of nodal velocities and $\mathbf{B}$ is the strain-displacement matrix.

Initialization of material points

Material points carry all the information of the continuum body. The initialization of material points within the background mesh is here discussed. Initializing a material point means to associate mass, body forces and other properties of the continuum to a material point. Mesh elements filled with material points are called active elements and their nodes contribute to solve the governing equations, whereas the empty elements (those with no material points inside) are ignored. Each material point is initially in a pre-defined local position inside the parent element, therefore a local position vector $\boldsymbol{\xi}_{\mathrm{MP}}$ is initialized. The global position vector $\mathbf{x}_{\mathrm{MP}}$ is then obtained:

$$\mathbf{x}_{\mathrm{MP}}(\boldsymbol{\xi}_{\mathrm{MP}}) \approx \sum_{i=1}^{N_{nodes}} \mathrm{N}_i(\boldsymbol{\xi}_{\mathrm{MP}}^{\mathrm{t}})\mathbf{x}_i \tag{2.42}$$

where N_{nodes} is the number of nodes per element, $\mathrm{N}_i(\boldsymbol{\xi}_{\mathrm{MP}}^{\mathrm{t}})$ is the shape function of the node i evaluated at the local position of the material point and $\mathbf{x}_i$ are the nodal coordinates. Volumes associated with material points are calculated so that all the

material points inside the element have initially the same portion of the element volume:

$$\Omega_{\mathrm{MP}} = \frac{1}{N_{\mathrm{MP,el}}} \int_{\Omega_e} d\Omega \approx$$
$$\approx \frac{1}{N_{\mathrm{MP,el}}} \sum_{i=1}^{N_{\mathrm{q,el}}} \mathrm{w}_{\mathrm{MP}} |\mathbf{J}(\boldsymbol{\xi}_{\mathrm{MP}})| \tag{2.43}$$

where Ω_{MP} is the volume associated with the material point, $N_{\mathrm{MP,el}}$ is the number of material points in the element, $N_{\mathrm{q,el}}$ is the number of Gauss points in the element, w_{MP} is the local integration weight associated with Gauss points and material points, and **J** is the Jacobian matrix. Therefore, all the active elements are assumed to be fully filled by the continuum body at the beginning of the calculation. An element is said to be partially filled if the sum of the volumes of the contained material points is less than the element volume.

Therefore, the mass of each material point can be calculated according to Equation (2.44).

$$\mathrm{m}_{\mathrm{MP}} = \Omega_{\mathrm{MP}} \rho_{MP} \tag{2.44}$$

The gravity force vector is simply calculated using the mass of the material point and the vector of gravitational acceleration according to Equation (2.45).

$$\mathbf{f}_{\mathrm{MP}}^{\mathrm{grav}} = \mathrm{m}_{\mathrm{MP}} \mathbf{g} \tag{2.45}$$

The external forces applied at the traction boundary are mapped to the material points located next to the element border, which

carry surface traction throughout the computation. For tetrahedral elements, the traction vector $\boldsymbol{\tau}_e$ applied at the triangular surface is interpolated from the nodes of this surface to boundary material points. Therefore, the traction at boundary material point is expressed by Equation (2.46):

$$\boldsymbol{\tau}_e(\mathbf{x}_\mathrm{p}) \approx \sum_{i=1}^{N_{tri}} \mathrm{N}_i(\boldsymbol{\xi}_q)\boldsymbol{\tau}_e(\mathbf{x}_i) \tag{2.46}$$

where N_i is the shape function of the node i of the triangular surface element and $\boldsymbol{\xi}_q$ are the coordinates of the boundary material point inside the parent triangular element. These coordinates simply represent the projection of the material point on the triangular surface element. The traction force vector $\mathrm{f}_\mathrm{p}^{\mathrm{trac}}$ is defined in Equation (2.47).

$$\begin{aligned} \mathbf{f}_\mathrm{p}^{\mathrm{trac}} &= \boldsymbol{\tau}_e(\mathbf{x}_{\mathrm{MP}})\frac{S_e}{N_{\mathrm{ebMP}}} = \\ &= \frac{S_e}{N_{\mathrm{ebMP}}}\sum_{i=1}^{N_{tri}} \mathrm{N}_i(\boldsymbol{\xi}_{\mathrm{MP}})\boldsymbol{\tau}_e(\mathbf{x}_i) \end{aligned} \tag{2.47}$$

In Equation (2.47), N_{ebMP} is the number of boundary material points located next to the loaded surface and S_e is the area of the corresponding loaded surface of the element *e*.

Calculation of internal forces

In the finite element formulation, the numerical integration of the integrals above-described is not carried out along the global coordinate system. Indeed, it is more convenient to convert the

global coordinates (**x**) of each element into a reference (or parent) element system (**ξ**), and the mapping procedure is done using the Jacobian matrix.

Using a unit 4-node tetrahedron with linear shape functions as the reference element, the internal force is expressed by Equation (2.48):

$$\mathrm{f}^{\mathrm{int}} = \sum_{el=1}^{N_{el}} \int_{\Omega_{el}} \mathbf{B}^T \boldsymbol{\sigma} d\Omega = \sum_{el=1}^{N_{el}} \int_{\xi} \mathbf{B}^T \boldsymbol{\sigma} |\boldsymbol{J}| d\xi \tag{2.48}$$

in which Ω_{el} is the volume of the element *el* in the global coordinate system, N_{el} is the number of active elements, ξ is the volume of the parent element, $d\xi = d\xi_1 d\xi_2 d\xi_3$ is the infinitesimal volume in the parent element system, $|\boldsymbol{J}|$ is the determinant of the Jacobian matrix and **B** is the matrix of the shape function gradients calculated at the location ξ with respect to the parent coordinate system. If numerical integration is applied, the equations leads as follows:

$$\mathrm{f}^{\mathrm{int}} = \sum_{el=1}^{N_{el}} \sum_{i=1}^{N_{nodes,el}} \sum_{k=1}^{N_{int,el}} \mathbf{B}^T \boldsymbol{\xi_k} \boldsymbol{\sigma_k} |\boldsymbol{J_k}| \mathrm{W_k} \tag{2.49}$$

where $N_{nodes,el}$ and $N_{int,el}$ are respectively the number of nodes and integration points inside the element *el*, and $\mathrm{W_k}$ is the weight factor (or integration weight) of the integration point *k*. In the material point method, material points carry all the information of the continuum, including stresses. The internal forces are computed in the form expressed by Equation (2.50):

$$\mathrm{f}^{\mathrm{int}} = \sum_{el=1}^{N_{el}} \sum_{i=1}^{N_{nodes,el}} \sum_{MP=1}^{N_{MP,el}} \mathbf{B}^T \boldsymbol{\xi}_{\boldsymbol{MP}} \boldsymbol{\sigma}_{\boldsymbol{MP}} \Omega_{MP} \tag{2.50}$$

where $N_{MP,el}$ is the number of material points within the element *el*.

Calculation of external forces

The external forces can be classified in two parts: the body force, due to the gravity acceleration, and the external loading due to distributed forces applied to the body. The body force can be computed as follows according to Equation (2.51):

$$\mathrm{f}^{\mathrm{ext,grav}} = \sum_{el=1}^{N_{el}} \int_{\Omega_{el}} \rho \bar{\mathbf{N}}^T \mathbf{g} d\Omega = \sum_{el=1}^{N_{el}} \int_{\xi} \rho \bar{\mathbf{N}}^T \mathbf{g} |\boldsymbol{J}| d\xi \tag{2.51}$$

where $\mathbf{N}$ is the shape function matrix calculated at the location ξ with respect to the parent coordinate system. Applying the material point integration, Equation (2.51) turns into Equation (2.52).

$$\mathrm{f}^{\mathrm{ext,grav}} = \sum_{el=1}^{N_{el}} \sum_{i=1}^{N_{nodes,el}} \sum_{MP=1}^{N_{MP,el}} m_{MP} \mathbf{N}_i{}^T(\boldsymbol{\xi}_{\boldsymbol{MP}}) \mathbf{g} \Omega_{MP} \tag{2.52}$$

The external forces due to traction are computed according to Equation (2.53):

$$\begin{aligned} \mathrm{f}^{\mathrm{ext,trac}} &= \sum_{el=1}^{N_{el}} \int_{\partial\Omega_{el}} \bar{\mathbf{N}}^T \mathbf{t} \cdot \mathbf{n} d\partial\Omega = \\ &= \sum_{el=1}^{N_{el}} \sum_{i=1}^{N_{nodes,el}} \sum_{MP=1}^{N_{MP,el}} \mathbf{N}^T(\boldsymbol{\xi}_{\boldsymbol{MP}}) \mathbf{f}_{MP}^{ext} \end{aligned} \tag{2.53}$$

in which $\mathbf{f}_{MP}^{ext}$ is the force stored in the material point due to distributed external forces applied at the boundary of the body.

The complete form of the external force is expressed by Equation (2.54).

$$\mathrm{f}^{\mathrm{ext}} = \mathrm{f}^{\mathrm{ext,grav}} + \mathrm{f}^{\mathrm{ext,trac}} \tag{2.54}$$

Mass matrix

In order to solve Equation (2.38), the mass matrix has to be inverted. To simplify the computation, a lumped mass matrix could be used instead of the consistent mass matrix given by Equation (2.41). The lumped mass matrix is a diagonal matrix in which each entry m_i is obtained by summing over the corresponding row of the consistent mass matrix.

Matrix inversion becomes pretty easy. Using the property expressed by Equation (2.55):

$$\sum_{j=1}^{N_n} \mathrm{N}_{\mathrm{j}}^{\mathrm{p}} = 1 \tag{2.55}$$

the lumped mass matrix takes the form of Equation (2.56).

$$\mathbf{M}^{lump} = \sum_{el=1}^{N_{el}} \sum_{i=1}^{N_{Nodes,el}} \sum_{MP}^{N_{MP,el}} \mathbf{N}^{T}(\boldsymbol{\xi_{MP}}) m_{MP} \tag{2.56}$$

In what follows, the superscript *lump* is removed from the lumped mass matrix for the sake of simplicity, and mass matrix will always refer to a lumped matrix.

Time discretization

Time is discretized in different instants k. Considering Δt the time step size, the time discretization approach is that defined by Equation (2.57).

$$t^{k+1} = t^k + \Delta t \tag{2.57}$$

If the general system of equations (2.38) is posed at time t^k, it can be written:

$$\mathbf{M}^k \cdot \hat{\mathbf{a}}^k = \mathrm{f}^{\mathrm{int},k} + \mathrm{f}^{\mathrm{ext},k} \tag{2.58}$$

where the acceleration $\hat{\mathbf{a}}^k$ is the unknown. An explicit Euler time integration scheme is used to update the velocity (Equation (2.59)).

$$\hat{\mathbf{v}}^{k+1} = \hat{\mathbf{v}}^k + \Delta t \hat{\mathbf{a}}^k \tag{2.59}$$

This is a first-order numerical procedure for solving ordinary differential equations with a given initial value. On the other hand, displacements at time t^{k+1} are calculated using the updated velocity $\hat{\mathbf{v}}^{k+1}$ (Equation (2.60)).

$$\hat{\mathbf{u}}^{k+1} = \hat{\mathbf{u}}^k + \Delta t \hat{\mathbf{v}}^k \tag{2.60}$$

Solution algorithm for single time-step

The solution algorithm here mentioned is the one initially introduced by Sulsky et al. (1994) and (1995). The key point is to work with momentum instead of velocity as much as possible, avoiding divisions by nodal masses. In each time-step, the

material point method computational cycle can be divided in the steps listed below.

1) The nodal mass is calculated using the shape functions and the lumped mass matrix at time t^k is formed (Equation (2.56)). Internal and external forces are evaluated in nodes (Equations (2.50) and (2.54)).
2) The momentum balance equation (Equation (2.58)) is solved and the nodal accelerations $\hat{\mathbf{a}}_i^k$ are determined (Equation (2.61)).

$$\hat{\mathbf{a}}_i^k = \left[\mathbf{M}_i^k\right]^{-1}\left(\mathrm{f}_i^{\mathrm{ext},k} - \mathrm{f}_i^{\mathrm{int},k}\right) \tag{2.61}$$

3) Velocity at material points is updated according to Equation (2.59).

$$\mathbf{v}_{MP}^{k+1} = \mathbf{v}_{MP}^k + \Delta t \sum_{i=1}^{N_{nodes}} \mathrm{N}_i\left(\boldsymbol{\xi}_{MP}^k\right)\hat{\mathbf{a}}_i^k \tag{2.62}$$

4) Update nodal momentum (Equation (2.63)).

$$\mathbf{p}_i^{k+1} = \sum_{el=1}^{N_{el,i}} \sum_{MP=1}^{N_{MP,el}} m_{MP}\mathrm{N}_j\left(\boldsymbol{\xi}_{MP}^k\right)\hat{\mathbf{v}}_{MP}^{k+1} \tag{2.63}$$

5) Update nodal velocities (Equation (2.64)).

$$\hat{\mathbf{v}}_i^{k+1} = \frac{\mathbf{P}_i^{k+1}}{\mathbf{M}_i^k} \tag{2.64}$$

6) Compute incremental nodal displacement for solid and liquid constituent (Equation (2.65)).

$$\Delta\hat{\mathbf{u}}_i^{k+1} = \Delta t\hat{\mathbf{v}}_i^{k+1} \tag{2.65}$$

7) Compute strain increment (Equation (2.66)).

$$\Delta\varepsilon_{MP}^{k+1} = \mathbf{B}(\mathbf{x}_{MP})\Delta\hat{\mathbf{u}}_i^{k+1} \tag{2.66}$$

8) Stresses are updated using a suitable material constitutive model.

9) Update volume and density of material points (Equation (2.67)).

$$\Omega_{MP}^{k+1} = \Omega_{MP}^{k}\left(1 + \Delta\varepsilon_{vol,MP}\right);\ \rho_{MP}^{k+1} = \frac{\rho_{MP}^{k}}{\Delta\varepsilon_{vol,MP}} \tag{2.67}$$

10) Point positions are updated (Equation (2.68)).

$$\mathbf{x}_{MP}^{k+1} = \mathbf{x}_{MP}^{k} + \sum_{i=1}^{N_{nodes}} \mathrm{N}_i\left(\boldsymbol{\xi}_{MP}^{k}\right)\Delta\hat{\mathbf{u}}_i^{k} \tag{2.68}$$

11) Computational grid is initialized for the next step, nodal values are discarded and material points carry all the updated information.

2.5.2 - Explicit-Dynamic scheme for two-phase single-point formulation

Discretized momentum balance equation of liquid phase

The weak discretized form of the moment balance equation of liquid phase can be written as expressed by Equation (2.69).

$$\mathbf{f}_{\mathrm{L}}^{\mathrm{ext}} - \mathbf{f}_{\mathrm{L}}^{\mathrm{int}} - \mathbf{f}^{\mathrm{d}} = \mathbf{M}_{\mathrm{L}}\hat{\mathbf{a}} \tag{2.69}$$

The terms appearing in Equation (2.69) are defined in Equations from (2.70) to (2.73).

$$\mathbf{f}_{\mathrm{L}}^{\mathrm{ext}} = \int_{\partial\Omega} \overline{\mathbf{N}}^{\mathrm{T}}\mathbf{t}_{\mathrm{L}} \cdot \mathbf{n}\mathrm{d}\partial\Omega + \int_{\Omega} \rho_{\mathrm{L}}\overline{\mathbf{N}}^{\mathrm{T}}\mathbf{g}\mathrm{d}\Omega \tag{2.70}$$

$$\mathbf{f}_{\mathrm{L}}^{\mathrm{int}} = \int_{\Omega} \mathbf{B}^{\mathrm{T}} \boldsymbol{\sigma}_{\mathrm{L}} \mathrm{d}\Omega \tag{2.71}$$

$$\mathbf{f}^{\mathrm{d}} = \int_{\Omega} \overline{\mathbf{N}}^{\mathrm{T}} \mathrm{n} \frac{\rho_{\mathrm{L}} \mathrm{g}}{k} \overline{\mathbf{N}} \mathrm{d}\Omega \, (\hat{\mathbf{v}}_{\mathrm{L}} - \hat{\mathbf{v}}_{\mathrm{s}}) \tag{2.72}$$

$$\mathbf{M}_{\mathrm{L}} = \int_{\Omega} \rho_{\mathrm{L}} \overline{\mathbf{N}}^{\mathrm{T}} \overline{\mathbf{N}} \mathrm{d}\Omega \tag{2.73}$$

In the latter expressions $\mathbf{f}_{\mathrm{L}}^{\mathrm{ext}}$ is the vector of nodal external forces, $\mathbf{f}_{\mathrm{L}}^{\mathrm{int}}$ is the vector of nodal internal forces, $\mathbf{f}^{\mathrm{d}}$ is the vector of drag forces and $\mathbf{M}_{\mathrm{L}}$ is the nodal mass matrix.

Discretized momentum balance equation of mixture

The weak discretized form of the moment balance equation of liquid phase can be written as expressed by Equation (2.74).

$$\mathbf{f}_{\mathrm{L}}^{\mathrm{ext}} - \mathbf{f}_{\mathrm{L}}^{\mathrm{int}} - \mathbf{M}_{\mathrm{L}} \hat{\mathbf{a}}_{\mathrm{L}} = \mathbf{M}_{\mathrm{s}} \hat{\mathbf{a}}_{\mathrm{s}} \tag{2.74}$$

The term appearing in Equation (2.74) are defined in Equations from (2.75) to (2.78).

$$\mathbf{f}_{\mathrm{L}}^{\mathrm{ext}} = \int_{\partial\Omega} \overline{\mathbf{N}}^{\mathrm{T}} \mathbf{t}_{\mathrm{L}} \cdot \mathbf{n} \mathrm{d}\partial\Omega + \int_{\Omega} \rho \overline{\mathbf{N}}^{\mathrm{T}} \mathbf{g} \mathrm{d}\Omega \tag{2.75}$$

$$\mathbf{f}_{\mathrm{L}}^{\mathrm{int}} = \int_{\Omega} \mathbf{B}^{\mathrm{T}} \boldsymbol{\sigma} \mathrm{d}\Omega \tag{2.76}$$

$$\mathbf{M}_{\mathrm{L}} = \int_{\Omega} \rho_{\mathrm{L}} \overline{\mathbf{N}}^{\mathrm{T}} \overline{\mathbf{N}} \mathrm{d}\Omega \tag{2.77}$$

$$\mathbf{M}_{\mathrm{s}} = \int_{\Omega} (1 - \mathrm{n}) \rho_{\mathrm{s}} \overline{\mathbf{N}}^{\mathrm{T}} \overline{\mathbf{N}} \mathrm{d}\Omega \tag{2.78}$$

In the latter expressions $\mathbf{f}_{\mathrm{L}}^{\mathrm{ext}}$ is the vector of nodal external forces, $\mathbf{f}_{\mathrm{L}}^{\mathrm{int}}$ is the vector of nodal internal forces, $\mathbf{M}_{\mathrm{L}}$ is the nodal mass matrix (including porosity) and $\mathbf{M}_{\mathrm{s}}$ is the nodal mass matrix of the solid phase.

Calculation of internal forces

Starting by saying that all the same considerations exposed in the previous section keep on being valid, the internal force vector turns into Equation (2.79):

$$\mathbf{f}_{\mathrm{L}}^{\mathrm{int}} = \sum_{el=1}^{N_{el}} \int_{\Omega_{\mathrm{el}}} \mathbf{B}^{\mathrm{T}} \boldsymbol{\sigma}_{\mathrm{L}} \mathrm{d}\Omega = \sum_{el=1}^{N_{el}} \int_{\xi} \mathbf{B}^{\mathrm{T}} \boldsymbol{\sigma}_{\mathrm{L}} |\mathbf{J}| \mathrm{d}\xi \tag{2.79}$$

where Ω_{el} is the volume of the element *el* in the global coordinate system, N_{el} is the number of active elements, ξ is the volume of the parent element, $\mathrm{d}\xi = \mathrm{d}\xi_1 + \mathrm{d}\xi_2 + \mathrm{d}\xi_3$ is the infinitesimal volume of the parent element system, $|\mathbf{J}|$ is the determinant of the Jacobian matrix and $\mathbf{B}$ is the matrix of the shape function gradients calculated at the location $\boldsymbol{\xi}$ with respect to the parent coordinate system.

In the material point method, material points carry all the information of the continuum, including stresses. Thus, the internal forces are computed according to Equation (2.80):

$$\mathbf{f}_{\mathrm{L}}^{\mathrm{int}} = \sum_{el=1}^{N_{el}} \sum_{i=1}^{N_{nodes,el}} \sum_{MP=1}^{N_{MP,el}} B_i^T(\boldsymbol{\xi}_{MP})\boldsymbol{\sigma}_{\mathrm{L},MP}\Omega_{MP} \tag{2.80}$$

where $N_{MP,el}$ is the number of material points within element *el*.

Calculation of external forces

As for the one-phase single-point formulation, the external forces can be subdivided in two parts: the body force, which is generated by gravity acceleration, and the external loading due to distributed forces applied to the boundary of the liquid body.

The body force can be computed in the according to Equation (2.81):

$$\begin{aligned}\mathbf{f}_{\mathrm{L}}^{\mathrm{ext,grav}} &= \sum_{el=1}^{N_{el}} \int_{\Omega_{el}} \rho_L \bar{\mathbf{N}}^{\mathrm{T}}\mathbf{g}\mathrm{d}\Omega = \\ &= \sum_{el=1}^{N_{el}} \int_{\xi} \rho \bar{\mathbf{N}}^{\mathrm{T}}\mathbf{g}|\mathbf{J}|\mathrm{d}\xi\end{aligned} \tag{2.81}$$

where all the symbols have the same meaning defined for the internal forces. Furthermore, $\bar{\mathbf{N}}$ is the shape function matrix calculated at the location $\boldsymbol{\xi}$ with respect to the parent coordinate system. Applying the material point integration, the equation yields to Equation (2.82).

$$\mathbf{f}_{\mathrm{L}}^{\mathrm{ext,grav}} = \sum_{el=1}^{N_{el}} \sum_{i=1}^{N_{nodes,el}} \sum_{MP=1}^{N_{MP,el}} m_{MP} N_i^T(\boldsymbol{\xi}_{MP})\mathbf{g}\Omega_{MP} \tag{2.82}$$

The external forces due to traction are computed in the following according to Equation (2.83):

$$\mathbf{f}_{\mathrm{L}}^{\mathrm{ext,trac}} = \sum_{el=1}^{N_{el}} \int_{\partial\Omega_{el}} \bar{\mathbf{N}}^{\mathrm{T}} \mathbf{t}_{\mathrm{L}} \cdot \mathbf{n} \mathrm{d}\, \partial\Omega = \\ = \sum_{el=1}^{N_{el}} \sum_{i=1}^{N_{nodes,el}} \sum_{MP=1}^{N_{MP,el}} \mathbf{N}^{\mathrm{T}}(\boldsymbol{\xi}_{MP}) \mathbf{f}_{\mathrm{L},MP}^{\mathrm{ext,trac}} \tag{2.83}$$

where $\mathbf{f}_{\mathrm{L},MP}^{\mathrm{ext,trac}}$ is the force stored in the material point due to distributed external forces applied at the boundary of the body.

Lumping procedure: Mass matrix and Drag matrix

The solution of the system of Equation (2.74) requires the inversion of the mass matrix. Analogously to the previous section, a lumped mass matrix is used instead of the consistent mass matrix given by Equation (2.78). The lumped mass matrix is a diagonal matrix in which each entry m_i is obtained by summing over the corresponding row of the consistent mass matrix. Matrix inversion becomes really easy. Using the property expressed by Equation (2.84):

$$\sum_{j=1}^{N_n} \mathrm{N}_{\mathrm{j}}^{\mathrm{p}} = 1 \tag{2.84}$$

the lumped mass matrix assumes the form expressed by Equation (2.85).

$$\bar{\mathbf{M}}_L^{lump} = \sum_{el=1}^{N_{el}} \sum_{i=1}^{N_{nodes,el}} \sum_{MP=1}^{N_{MP,el}} \mathbf{N}^{T}(\boldsymbol{\xi}_{\boldsymbol{MP}}) m_{L,MP} \tag{2.85}$$

In what follows, the superscript *lump* is removed from the lumped mass matrix for the sake of simplicity, and mass matrix will always refer to a lumped matrix.

The same procedure is used to calculate the lumped mass matrix for the solid phase $\mathbf{M}_\mathrm{S}$.

The drag force $\mathbf{f}^\mathrm{d}$ can be written according to Equation (2.86):

$$\mathbf{f}^\mathrm{d} = \mathbf{Q}(\hat{\mathbf{v}}_\mathrm{L} - \hat{\mathbf{v}}_\mathrm{S}) \tag{2.86}$$

with $\mathbf{Q}$ expressed according to Equation (2.87).

$$\mathbf{Q} = \int_\Omega \bar{\mathbf{N}}^\mathrm{T} \mathrm{n} \frac{\rho_\mathrm{L} \mathrm{g}}{k} \bar{\mathbf{N}} \mathrm{d}\Omega \tag{2.87}$$

The lumping technique is also applied to the drag matrix $\mathbf{Q}$ (Equation (2.88)).

$$\mathbf{Q}^{lump} = \sum_{el=1}^{N_{el}} \sum_{i=1}^{N_{nodes,el}} \sum_{k=1}^{N_{int,el}} \mathbf{N}_i^T \mathrm{n}_k \frac{\rho_\mathrm{L} \mathrm{g}}{k} |\mathbf{J}_k| \tag{2.88}$$

Numerical implementation

The discrete system of equations is defined by Equations (2.89) and (2.90).

$$\mathbf{M}_\mathrm{L} \hat{\mathbf{a}}_\mathrm{L}^\mathrm{k} = \mathbf{f}_\mathrm{L}^{\mathrm{ext,k}} - \mathbf{f}_\mathrm{L}^{\mathrm{int,k}} - \mathbf{f}^{\mathrm{d,k}} \tag{2.89}$$

$$\mathbf{M}_\mathrm{S} \hat{\mathbf{a}}_\mathrm{S}^\mathrm{k} = \mathbf{f}^{\mathrm{ext,k}} - \mathbf{f}^{\mathrm{int,k}} - \mathbf{M}_\mathrm{L} \hat{\mathbf{a}}_\mathrm{L}^\mathrm{k} \tag{2.90}$$

It is worth noticing that in Equations (2.89) and (2.90) the subscripts “L” and “S” denote that the quantity is referred to the liquid or solid phase respectively, whereas no subscript indicates that the quantity belongs to the mixture.

The Euler-Cromer scheme is used to integrate the equation in time. Form Equation (2.89) the fluid acceleration at time t is

calculated and used to update the fluid velocity $\mathbf{v}_{\mathrm{L}}^{t+\Delta t}$. The solid acceleration is calculated solving Equation (2.90) and used to update the solid velocity $\mathbf{v}_{\mathrm{s}}^{t+\Delta t}$. Incremental strains are calculated in the material points from the updated velocities, after that the constitutive relations are used to calculate stresses and pore water pressure.

Solution algorithm for single time-step

The initialization of material points explained in the previous section can be easily extended to the two-phase single point formulation. The solution sequence of a single time step is described in the following:

1) The momentum equations for the fluid and the mixture are initialized by mapping the main quantities from material points to mesh nodes. The procedure is similar to step 1 of the algorithm discussed for the one-phase single-point formulation.
2) Equation (2.89) is solved for $\hat{\mathbf{a}}_{\mathrm{L}}^{\mathrm{t}}$ (Equation (2.91)).

$$\hat{\mathbf{a}}_{\mathrm{L}}^{\mathrm{t}} = (\mathbf{M}_{\mathrm{L}})^{-1}\left[\mathbf{f}_{\mathrm{L}}^{\mathrm{ext,t}} - \mathbf{f}_{\mathrm{L}}^{\mathrm{int,t}} - \mathbf{f}^{\mathrm{d,t}}\right] \tag{2.91}$$

3) The acceleration vector $\hat{\mathbf{a}}_{\mathrm{s}}^{\mathrm{t}}$ is calculated from Equation (2.90), which turns into Equation (2.92).

$$\hat{\mathbf{a}}_{\mathrm{s}}^{\mathrm{t}} = (\mathbf{M}_{\mathrm{s}})^{-1}\left[\mathbf{f}^{\mathrm{ext,t}} - \mathbf{f}^{\mathrm{int,t}} - \mathbf{M}_{\mathrm{L}}\hat{\mathbf{a}}_{\mathrm{L}}^{\mathrm{t}}\right] \tag{2.92}$$

4) Velocities of material points are updated using nodal accelerations and shape functions (Equations (2.93) and (2.94)).

$$\mathbf{v}_{\mathrm{L,MP}}^{\mathrm{t}+\Delta\mathrm{t}} = \mathbf{v}_{\mathrm{L,MP}}^{\mathrm{t}} + \sum_{i=1}^{N_{en}} \Delta t \mathrm{N}_i(\xi_{MP}^t)\hat{\mathbf{a}}_{L,i}^t \tag{2.93}$$

$$\mathbf{v}_{\mathrm{s,MP}}^{\mathrm{t}+\Delta\mathrm{t}} = \mathbf{v}_{\mathrm{s,MP}}^{\mathrm{t}} + \sum_{i=1}^{N_{en}} \Delta t \mathrm{N}_i(\xi_{MP}^t)\hat{\mathbf{a}}_{s,i}^t \tag{2.94}$$

5) Nodal velocities $\mathbf{v}_{\mathrm{L,MP}}^{\mathrm{t}+\Delta\mathrm{t}}$ and $\mathbf{v}_{\mathrm{s,MP}}^{\mathrm{t}+\Delta\mathrm{t}}$ are then calculated from the updated momentum from Equations (2.95) and (2.96).

$$\mathbf{P}_{\mathrm{L,i}}^{\mathrm{t}+\Delta\mathrm{t}} = \bar{\mathbf{M}}_L^t \mathbf{v}_{\mathrm{L,MP}}^{\mathrm{t}+\Delta\mathrm{t}} \approx$$

$$\approx \sum_{MP=1}^{N_{MP}} m_{L,MP}\mathbf{N}^T(\xi_{MP}^t)\mathbf{v}_{\mathrm{L,MP}}^{\mathrm{t}+\Delta\mathrm{t}} \tag{2.95}$$

$$\mathbf{P}_{\mathrm{s,i}}^{\mathrm{t}+\Delta\mathrm{t}} = \bar{\mathbf{M}}_s^t \mathbf{v}_{s,\mathrm{MP}}^{\mathrm{t}+\Delta\mathrm{t}} \approx$$

$$\approx \sum_{MP=1}^{N_{MP}} m_{s,MP}\mathbf{N}^T(\xi_{MP}^t)\mathbf{v}_{\mathrm{s,MP}}^{\mathrm{t}+\Delta\mathrm{t}} \tag{2.96}$$

6) Nodal velocities are integrated to get nodal incremental displacements (Equations (2.97) and (2.98)).

$$\Delta\hat{\mathbf{u}}_{\mathrm{L},i}^{t+\Delta t} = \Delta\mathrm{t}\mathbf{v}_{\mathrm{L}}^{\mathrm{t}+\Delta\mathrm{t}} \tag{2.97}$$

$$\Delta\hat{\mathbf{u}}_{\mathrm{s},i}^{t+\Delta t} = \Delta\mathrm{t}\mathbf{v}_{\mathrm{s}}^{\mathrm{t}+\Delta\mathrm{t}} \tag{2.98}$$

7) Strains in correspondence of material points are calculated according to Equations (2.99) and (2.100).

$$\Delta\boldsymbol{\varepsilon}_{\mathrm{L,MP}}^{\mathrm{t+\Delta t}} = \mathbf{B}(\xi_{MP}^{t})\mathbf{v}_{\mathrm{L}}^{\mathrm{t+\Delta t}}\Delta t \tag{2.99}$$

$$\Delta\boldsymbol{\varepsilon}_{\mathrm{s,MP}}^{\mathrm{t+\Delta t}} = \mathbf{B}(\xi_{MP}^{t})\mathbf{v}_{\mathrm{s}}^{\mathrm{t+\Delta t}}\Delta t \tag{2.100}$$

Consequently, stresses are updated according to a proper constitutive relationship.

8) Water pressure in correspondence of each material point is updated (Equations (2.101) and (2.102)).

$$\Delta\bar{\varepsilon}_{\mathrm{L,MP}}^{\mathrm{t+\Delta t}} = \frac{1}{n_{MP}^{t}}\begin{bmatrix}(1-n_{MP}^{t})\Delta\boldsymbol{\varepsilon}_{\mathrm{s,MP}}^{\mathrm{t+\Delta t}} + \\ +n_{MP}^{t}\Delta\boldsymbol{\varepsilon}_{\mathrm{L,MP}}^{\mathrm{t+\Delta t}}\end{bmatrix} \tag{2.101}$$

$$\mathrm{p}_{\mathrm{L,MP}}^{\mathrm{t+\Delta t}} \approx \mathrm{p}_{L,MP}^{t} + \mathrm{K}_{L,MP}\Delta\bar{\varepsilon}_{\mathrm{L,MP}}^{\mathrm{t+\Delta t}} \tag{2.102}$$

9) Total stresses are calculated according to Equation (2.103):

$$\boldsymbol{\sigma}_{\mathrm{MP}}^{\mathrm{t+\Delta t}} = \boldsymbol{\sigma}'^{\mathrm{t+\Delta t}}_{\mathrm{MP}} + \delta\mathrm{p}_{\mathrm{L,MP}}^{\mathrm{t+\Delta t}} \tag{2.103}$$

where $\delta = [1 \quad 1 \quad 1 \quad 0 \quad 0 \quad 0]$.

10) Volumes associated with material points are updated using the solid volumetric strain increment (Equation (2.104)).

$$\Omega_{\mathrm{MP}}^{\mathrm{t+\Delta t}} = \left(1 + \Delta\boldsymbol{\varepsilon}_{\mathrm{vol,s,MP}}^{\mathrm{t+\Delta t}}\right) \tag{2.104}$$

11) Positions of material points are updated using displacements of the solid phase, as expressed by Equation (2.105).

$$\mathbf{x}_{\mathrm{MP}}^{\mathrm{t+\Delta t}} = \mathbf{x}_{\mathrm{MP}}^{\mathrm{t}} + \sum_{i=1}^{N_{nodes}} \mathrm{N}_i(\xi_{MP}^{t})\Delta\hat{\mathbf{u}}_{s,i}^{t+\Delta t} \tag{2.105}$$

12) The book-keeping is updated using the new position of points.

2.5.3 - Stability criterion

The explicit dynamic formulation described in this chapter is conditionally stable, which means that the time step Δt must be less than a critical value of time step, Δt_{crit}, i.e. $\Delta t < \Delta t_{crit}$. This critical value can be evaluated according to the Courant–Friedrichs–Levy condition (Courant et al. (1967)). For an undamped linear system, the critical time step is given by Bathe (1996):

$$\Delta t_{crit} = \frac{T_n}{\pi} \tag{2.106}$$

where T_n is the smallest natural period of the system. For a damped linear system, the critical time step is given by (Hallquist (2006) and Belytschko et al. (2014)):

$$\Delta t_{crit} = \frac{T_n}{\pi}\left(\sqrt{1+\xi^2} - \xi\right) \tag{2.107}$$

where ξ is the fraction of critical damping. For a nonlinear system, the time step can be chosen as:

$$\Delta t = \alpha \Delta t_{crit} \tag{2.108}$$

where α is a constant, and it is usually taken to be $0.8 \leq \alpha \leq 0.98$, depending on the nonlinearity of the system.

In the finite element method, it has been proved that the smallest period of a mesh is always greater than or equal to the smallest

period of any element in the mesh (Irons (1970); Flanagan & Belytschko (1981)).

Therefore, the critical time step can be chosen as:

$$\Delta t_{crit} = \min_{e} \frac{T^{e}_{min}}{\pi} = \min_{e} \frac{L_{min}}{c} \tag{2.109}$$

where T^{e}_{min} is the smallest period of element *e*, L_{min} is the characteristic length of the element *e*, i.e. the shortest distance from the side of the maximum area to the opposite node, whereas c is defined as expressed in Equation (2.110):

$$c = \sqrt{\frac{E_c}{\rho}} \tag{2.110}$$

where E_c is the constrained modulus of the solid medium. Such criterion keep on being true in the material point method, for the one-phase single-point formulation, and it can be easily extended for the two-phase single-point formulation whereby Equation (2.111) (Mieremet, 2015).

$$\Delta t_{crit} = \min\{\Delta t_{crit,1}; \Delta t_{crit,2}\} \tag{2.111}$$

The quantities in Equation (2.111) are defined as expressed in Equations from (2.112) to (2.117).

$$\Delta t_{crit,1} = \frac{L_{min}}{c_1} \tag{2.112}$$

$$\Delta t_{crit,2} = \frac{2\tilde{\rho}k}{\rho_L g} \tag{2.113}$$

$$c_1 = \sqrt{\frac{E_c^u}{\rho}} \tag{2.114}$$

$$E_c^u = E_c + \frac{K_L}{n} \tag{2.115}$$

$$\rho = (1-n)\rho_s + n\rho_L \tag{2.116}$$

$$\tilde{\rho} = \rho + \rho_L \left(\frac{1}{n} - 2\right) \tag{2.117}$$

In these equations, E_c^u is the undrained modulus of the saturated soil, E_c is the laterally confined modulus of the solid skeleton and K_L is the bulk modulus of the liquid.

It is worth noticing that $\Delta t_{crit,1}$ is a function of the size of the mesh, the stiffness, the porosity and the density of the material, whereas $\Delta t_{crit,2}$ is a function of the permeability, the porosity and the density. In many cases, the time step required to ensure the stability in low permeable soils can be smaller than the real one required for high permeable soils, i.e. $\Delta t_{crit,2} < \Delta t_{crit,1}$.

2.6 – Additional algorithms

The material point method is a numerical technique which requires some governing equations to be solved. Such equations are mentioned in the previous sections of this chapter. However, additional algorithms are required in order to obtain a numerically

stable and computationally efficient solution (Ceccato & Simonini (2019)). These additional algorithms regard: boundary conditions, absorbing boundaries, stress initialization, local damping, artificial bulk viscosity damping, contact between bodies, moving mesh, anti-locking algorithms, mass scaling and mixed-integration. All these numerical features are described in details by Ceccato & Simonini (2019). In this section, only some of them are mentioned, based on the applications that are described in the following chapters. Particularly, the additional algorithms required to solve the problems considered in this dissertation are: boundary conditions, stress initialization, local damping and anti-locking algorithms. For the sake of simplicity, the other features are not considered in this context.

2.6.1 – Boundary conditions

Generally, it is possible to differentiate boundary conditions in two categories, essential and natural. Essential boundary conditions are directly imposed on the solution, whereas the degrees of freedom are directly eliminated from the system of equations. Example of essential boundary conditions are fixities, prescribed velocities or displacements. Instead, natural boundary conditions are imposed on a secondary variable, for instance stresses or pressures. In the traditional finite element method, the application of prescribed boundary conditions is simple, since

they can be directly specified on the boundary nodes, which correspond with the boundary of the continuum body and are well defined during the whole calculation. Instead, in the material point method, the computational mesh is not necessarily aligned with the boundaries of the material, giving rise to some difficulties, especially when dealing with non-zero boundary conditions. Zero kinematic boundary conditions, also known as fixities, can be applied at the degree of freedom of the computational mesh similarly to the finite element method. However, such conditions have to be applied to boundary nodes which might become active during the computation, for example when a material point is located in the element connected to the node.

Zero-traction boundary conditions are automatically enforced to be satisfied by the solution of equations of motion. Dealing with such boundary conditions is more complex. Traction loads can be applied on either the element boundaries or the material points. The first option is feasible only if the boundary of the body remains aligned with loaded element boundaries during the computation, whereas the second option consists in storing the load on selected material points that move through the grid. When the traction is assigned to the element boundary, the nodal traction force is integrated like in the finite element method applying Gauss quadrature and then used in the momentum

balance equation. The applied load is therefore integrated accurately and the traction nodal force is non-zero only for the nodes belonging to the loaded surface. When the traction is applied on material points, it is mapped from these latter to all nodes of the element where it is located by means of shape functions.

To deepen the topic, Remmerswaal et al. (2019) recently proposed a novel treatment on non-trivial boundary conditions in MPM, to enhance the simulation of flow within slopes or erosional and depositional processes, as well as to apply a load, for example on the top of a slope. However, this procedure is just mentioned here, since it is not used in this dissertation.

2.6.2 – Stress initialization

The solution of a general boundary problem needs the generation of initial conditions, which are defined by the initial stress state for engineering problems. Therefore, also for geotechnical analyses within the MPM context, the first step of every computation consists of the generation of the initial stress state. This is done by using a procedure commonly known as gravity loading, which consists in increasing the gravity from zero to its final value (9.81 m/s^2), until the solution converges to a quasi-static equilibrium. The condition of quasi-static equilibrium is reached when the normalized kinetic energy, E_{kin}, and the

normalized out-of-balance force fall below a predefined tolerance (tol_E and tol_F, respectively) as given by Equations (2.118) and (2.119).

$$\frac{E_{kin}}{W_{ext}} = tol_E \tag{2.118}$$

$$\frac{\left\|\vec{f}^{ext} - \vec{f}^{int}\right\|}{\left\|\vec{f}^{ext}\right\|} = tol_F \tag{2.119}$$

In such equations, W_{ext} is the work of the external forces, $\vec{f}^{ext}$ the external force, $\vec{f}^{int}$ the internal force and $\left\|\vec{f}^{ext} - \vec{f}^{int}\right\|$ the out-of-balance force. Instead, in the case of geostatic condition, the initial stress state can be initialized by using the K_0-procedure, which is based on the effective stress principle. With this approach, the vertical and horizontal stress increase linearly with the depth in a material point and can be computed referring to Equations (2.120) and (2.121).

$$\sigma'_{v,0} = \rho g z_p - \rho_w g z_w \tag{2.120}$$

$$\sigma'_{h,0} = k_0 \sigma'_{v,0} \tag{2.121}$$

In Equations (2.120) and (2.121), z_p is the depth of the considered material point below the ground surface, z_w is the depth of the considered material point below the groundwater level, ρ_w is the density of water and K_0 is coefficient of earth pressure at rest.

2.6.3 – Local damping

As discussed in Section 2.5, governing equations are solved in the context of a dynamic-explicit formulation within this dissertation. This formulation is characterized by vibrations which might give rise to some issues when dealing with quasi-static problems. Indeed, although the material point method is a tool developed mainly to solve dynamic and fast problems, it could be also used to solve problems in which inertia does not play an important role. For instance, as explained in Section 2.6.2, the first step of every analysis should be the generation of the initial stress state, which is not a dynamic problem. However, using a dynamic-explicit formulation, the system would be characterized by oscillation even if the problem is not dynamic. Indeed the calculated solution will oscillate around the exact one, making the convergence a long process. In order to accelerate the convergence to quasi-static equilibrium, an artificial local damping can be included in the formulation in order to dissipate the energy in the dynamic momentum conservation. It is worth noticing that this is an artificial value and not a physical parameter of the soil. It is introduced just to damp the vibrations which occur due to the type of the used formulation. Therefore, if vibrations in quasi-static problems could be seen as an issue, then the artificial damping can be seen as a regularization technique. Local damping consists in adding a force to a node, which is

proportional to the out-of-balance force and which acts in the opposite direction of the velocity. The discretized momentum balance (Equation (2.38)) takes the form expressed by Equations (2.122), (2.123) and (2.124):

$$\mathbf{M}\vec{a} = \vec{f} + \vec{f}^{damp} \tag{2.122}$$

$$\vec{f} = \vec{f}^{ext} - \vec{f}^{int} \tag{2.123}$$

$$\vec{f}^{damp} = -\alpha\left\|\vec{f}\right\|\frac{\vec{v}}{\|\vec{v}\|} \tag{2.124}$$

where $\vec{f}^{damp}$ is the damping force and α is a dimensionless parameter which defines the artificial local damping.

In the two-phase formulation, the artificial local damping is applied separately for the liquid and solid phases. The momentum balance for the liquid (Equation (2.69)) is modified as Equation (2.125).

$$\mathbf{M_L}\vec{a}_L = \vec{f}_L + \vec{f}^{damp} - \vec{f}^{drag} \tag{2.125}$$

In Equation (2.125), $\vec{f}_L = \vec{f}_L^{ext} - \vec{f}_L^{int}$ represents the out-of-balance force for the liquid phase, whereas the damping force for the liquid takes the form of Equation (2.126).

$$\vec{f}_L^{damp} = -\alpha_L\left\|\vec{f}_L\right\|\frac{\vec{v}_L}{\|\vec{v}_L\|} \tag{2.126}$$

The momentum equation for the mixture is given by Equations (2.127) and (2.128).

$$\mathbf{M_S}\vec{a}_S = -\mathbf{M_L}\vec{a}_L + \vec{f}^{ext} - \vec{f}^{int} + \vec{f}^{damp} \tag{2.127}$$

$$\vec{f}^{damp} = \vec{f}_S^{damp} + \vec{f}_L^{damp} \tag{2.128}$$

In Equation (2.128), $\vec{f} = \vec{f}^{ext} - \vec{f}^{int}$ represents the out-of-balance force of the mixture, whereas the damping force for the solid phase can be written according to Equation (2.129).

$$\vec{f}_S^{damp} = -\alpha_S \left\| \vec{f} - \vec{f}_L \right\| \frac{\vec{v}_S}{\|\vec{v}_S\|} \tag{2.129}$$

As previously said, the artificial local damping is introduced to reduce the oscillation when quasi-static problems are solved. However, although it is a numerical parameter with no physical meaning, it could also be applied to account for natural damping in soils and rocks if the constitutive model does not properly account for it, by using appropriate values. For quasi static problems, high values of α should be used to accelerate the convergence to quasi-static equilibrium, i.e. $0.5 \leq \alpha \leq 0.75$. In dynamic problems, a small value of α could be used to simulate the natural energy dissipation of the material, if it is not accounted for in the constitutive model. Within the context of this dissertation, it is suggested to use values of the artificial local damping $\alpha \leq 0.05$, since it would otherwise change the dynamics of the problem, leading to inappropriate results. Finally, in highly dynamic problems, artificial local damping should not be used.

2.6.4 – Anti-locking algorithms

The material point method, analogously to the finite element method, can be undergone locking problems if low-order elements are used. Particularly, locking occurs when the deformation of an element is constrained by the surrounding elements, making the element almost incompressible. Therefore, this gives rise to an artificial further stiffness of the material, which leads to large errors in the solution. Particularly, small errors in strains will yield to large errors in stresses. The phenomenon of locking can be explained with the help of Figure 2.5. Consider the element e_1 (Figure 2.5a), which is defined by nodes 1 and 2 on the horizontal axis, and by node 3 on the vertical one. If the element is incompressible, its area remains constant. If node 1 and 2 are fixed, the vertical displacement of node 3 must be zero ($u_y^3 = 0$). Therefore, the only degree of freedom is the horizontal displacement u_x^3. Analogous consideration can be done for element e_2 (Figure 2.5b), defined by nodes 4, 5 and 6, whose only degree of freedom is represented by the vertical displacement u_y^5. If the two elements e_1 and e_2 are assembled as shown in Figure 2.5c, node 3 cannot move and, consequently, both elements are totally locked up. If nodes with number from 1 to 4 are locked up, nodes of the element with number from 3 to 8 (Figure 2.5c) will also be locked. This locking phenomenon propagates through the

entire grid leading to an unrealistic stiffness and, therefore, to an erroneous velocity field.

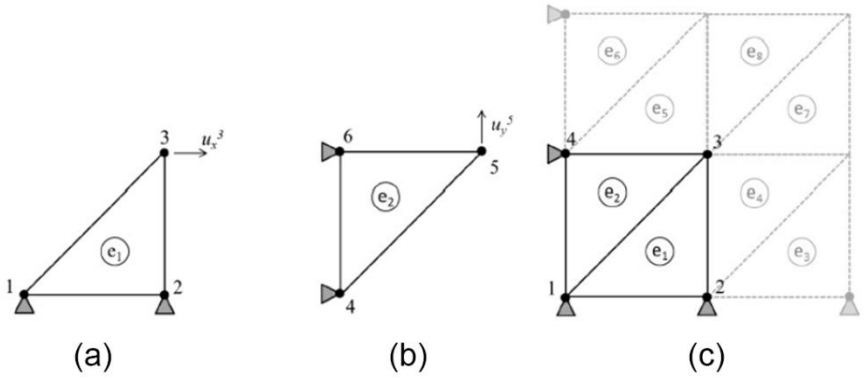

Figure 2.5 – Example of locking for triangular elements (from Ceccato & Simonini (2019))

A technique which allows the mitigation of such a problem for linear tetrahedral elements is the Nodal Mixed Discretization (NMD) proposed by Detournay & Dzik (2006). According to this procedure, the element volumetric behavior is averaged over the elements sharing its nodes via a least squares smoothing process. The effect of this scheme is the increment of the number of degrees of freedom per element. The strain rate of an element, $\dot{\varepsilon}$, is divided into its deviatoric and volumetric components. The volumetric strain rate for a node i is defined as a weighted average of the surrounding element values, $\dot{\varepsilon}_{vol,el}$, by using Equation (2.130):

$$\dot{\varepsilon}_{vol,i} = \frac{\sum_{el=1}^{n_{el,i}} \dot{\varepsilon}_{vol,el}\Omega_{el}}{\sum_{el=1}^{n_{el,i}} \Omega_{el}} \tag{2.130}$$

in which $n_{el,i}$ are the elements surrounding the node i, and Ω_{el} is the volume of the element *el*. A mean value for the element, $\bar{\dot{\varepsilon}}_{vol}$,

is calculated by taking the average of nodal quantities (Equation (2.131)):

$$\bar{\dot{\varepsilon}}_{vol} = \frac{1}{n_{node,el}} \sum_{i=1}^{n_{node,el}} \dot{\varepsilon}_{vol,i} \tag{2.131}$$

where $n_{node,el}$ is the number of nodes in an element. The element strain rates are defined by superposition of the deviatoric part, which is unchanged, and the volumetric part modified as explained above. This technique is also known as *strain smoothing*.

2.6.5 – MPM-mixed integration scheme

The original MPM formulation suffers from a "cell-crossing instability" when dealing with problems involving large displacements. Whenever material points cross the element boundaries of the computational background mesh, an unphysical unbalance force appears at the nodes shared between previous and new elements of the crossing point. This happens because of the lack of smoothness of the nodal shape functions used in the interpolation of information between grid and material points. Shape functions are linear C^0, which means that the gradients of the shape functions within the element are constant but they are discontinuous at the element borders. Therefore, when one material point crosses a border, the internal forces of those involved nodes suffer an unphysical instability due to a

jump discontinuity in the gradient of linear shape functions. The code employed in this dissertation, i.e. ANURA3D, uses a specific procedure to mitigate such a shortcoming. As in the finite element method, the Gauss integration is used to determine the internal forces, in which a single point with an average stress $\boldsymbol{\sigma}_{av}$ is considered in each element. The average stress is calculated according to Equation (2.132):

$$\boldsymbol{\sigma}_{av} = \frac{\sum_{MP=1}^{no_{MP,el}} \boldsymbol{\sigma}_{MP} \Omega_{MP}}{\sum_{MP=1}^{no_{MP,el}} \Omega_{MP}} \tag{2.132}$$

In Equation (2.132), $no_{MP,el}$ is the number of material points within the element, whereas $\boldsymbol{\sigma}_{MP}$ and Ω_{MP} are the stress and the volume of a material point, respectively. The calculation of the internal forces by means of the Gauss point integration is considered only for the elements located in the interior of the continuum. The Gauss point integration is also used for the elements located at the boundaries only if the condition expressed by Equation (2.133) is fulfilled:

$$\sum_{MP=1}^{no_{MP,el}} \Omega_{MP} > F_{fill} \Omega_{el} \tag{2.133}$$

In Equation (2.133), the factor F_{fill} is assumed to be 0.9. If Equation (2.133) is not fulfilled, the internal force in the boundary elements is calculated with the classic MPM procedure. This is a mixed approach which uses material points and Gauss points to calculate the internal force, and in the code ANURA3D is named MPM-mixed integration scheme.

2.7 – Comparison between Material Point Method and Finite Element Method

The material point method is very similar to the finite element method in each time step. The main differences are discussed in detail by Zhang et al. (2017) and, for the sake of completeness, are mentioned in this section.

Firstly, it is important to point out that the finite element method employs Gauss quadrature to evaluate the integrals in the weak form formulation, whereas the material point method employs particle quadrature. Therefore, constitutive equations are solved at Gauss points in the finite element method, whereas they are solved at points in the material point method. Secondly, in the finite element method, the computational mesh is attached to the material during the whole simulation, whereas a specific background mesh in attached to the material only for a time step in the material point method. At the end of each time step, the deformed mesh could be discarded to employ a new regular one in the next time step. Because all the material properties are carried by the points, the solution on the mesh at the next time step must be reconstructed from the point information. Therefore, the mass matrix in the material point method is not a constant matrix anymore as in the finite element method and has to be recalculated in each time step. Consequently, the material point method can be seen as a special Lagrangian finite element method

with particle quadrature and continuous mesh-update. Gauss quadrature can produce accurate results for polynomial integrands, but the particle quadrature usually cannot.

Besides, the number of points in the material point method is usually much larger than the number of Gauss points in the finite element method. Therefore, the accuracy and efficiency of the material point method are lower than those of the finite element method when small deformation problems are analyzed.

However, for large deformation problems, the accuracy of the Lagrangian finite element method deteriorates rapidly and the computational cost increases dramatically due to mesh distortion, making it unsuitable to deal with problems involving large deformations.

In the following, a comparison between the material point method and the finite element method concerning the efficiency and the accuracy is reported.

2.7.1 – Computational efficiency

Computational efficiency depends on the computational cost per time step and on the time step size. In the material point method, at the beginning of each time step, the mass and momentum of points are mapped to mesh nodes, whereas at the end of each time step, the updated mesh nodal velocity and acceleration are mapped to the points in order to update their position. In the finite

element method, instead, nodes carry the mass and momentum; therefore, they are not recalculated at the beginning of each time step. Besides, Gauss points do not move relative to each element during the whole simulation, then it is not necessary to update their position and velocity.

Furthermore, the number of Gauss points in each element for the finite element method is usually much less than the number of points in each element for the material point method, especially when three-dimensional problems are analyzed. Stress update and nodal internal force calculation will loop over the Gauss point (in the finite element method) or points (in the material point method), so that the computational cost of the material point method is much higher than that of the finite element method.

Both the explicit material point method and explicit finite element method employ the central difference method, whose critical time step size depends on the characteristic element length, which is constant during the whole simulation process in the material point method, whereas it decreases with element deformation in the finite element method.

Therefore, the time step of the finite element method is smaller than that of the material point method, and the total number of steps required in the finite element method is larger than that of the material point method. For small deformation problems, the characteristic element length in the finite element method will not

decrease significantly so that the computational efficiency of the finite element method is higher than that of the material point method. Whereas, for large deformation problems the characteristic element length in the finite element method decreases rapidly, which results in a significant decrease in the time step size and a significant increase in the total number of required time steps. Therefore, the computational efficiency of the finite element method is lower than that of the material point method for large deformation problems.

2.7.2 – Computational accuracy

If the mesh size in the material point method is comparable to the mesh size in the finite element method, the difference in accuracy depends mainly on the quadrature scheme used and on the technique adopted to deal with large deformations. In the both methods, polynomial-based shape functions are used, therefore the Gauss quadrature used in the finite element method can integrate accurately the weak form, whereas the particle quadrature used in the material point method cannot. Consequently, the accuracy of the weak form integration in the material point method is lower than that of the finite element method. On the other hand, for large deformation problems, the Jacobian of an element in the finite element method will decrease to zero or sometimes to negative values, due to strong mesh

distortion, which leads to a significant errors. Although remeshing techniques can alleviate the element distortion, remapping material properties of history-dependent materials will result in a significant error. Therefore, the accuracy of the material point method is lower than that of the finite element method when small deformation problems are analyzed, whereas could be much higher for large deformation problems.

2.8 – Constitutive models

Within the material point method, problems are tackled in the context of the continuum mechanics and, therefore, soil is assimilated to a continuum body. Fundamental equations of continuum mechanics, such as equilibrium and kinematics have general validity, since they do not depend on the properties of the body under consideration. However, the experience also proves that the way a continuum deformable body behaves after changes of actions depends on its internal constitution. Therefore, in order to predict its deformation process, it is necessary to introduce constitutive equations, which describe the response of the material, by relating static and kinematic quantities, with a relationship of the type of Equation (2.134).

$$\varepsilon_{hk} = C_{ijhk}\sigma_{ij} \tag{2.134}$$

In Equation (2.134), ε_{hk} represents the strain tensor, σ_{ij} is the stress tensor, whereas C_{ijhk} is a fourth-order tensor, defined as

stiffness tensor, and which depends on the mechanical behavior of the material.

As it is well known, the mechanical behavior of soils is extremely complex: it is not linear, irreversible, path dependent, and besides it depends also on parameters such as time, temperature, load velocity, degree of saturation etc. (Nova (2002)). In order to solve a generic problem of geotechnical engineering, it is necessary to clarify the Equation (2.134). There are many constitutive laws available in the literature, with different degrees of complexity. In the following, the main ones will be described, which will be also applied in the following chapters of this dissertation.

2.8.1 – Elastic theory

The elastic theory was historically the first one used to describe the mechanical behavior of soils. It is attractive because it provides closed form solutions for the analysis of some boundary problems of geotechnical interest, such as the stress distribution induced within the soil mass by loads applied at the surface, as well as the displacement of loaded areas of finite dimension. On the other hand, this kind of law is not suitable to describe neither the irreversibility of soil nor the path dependency on loads. However, simple calculations based on closed form solutions still offer the advantage of focusing on the most important parameters to be considered, as well as on their relative influence.

The behavior of a given body is defined elastic if there is a one-to-one correspondence between stress and strain, as shown in Figure 2.6.

Such an assumption implies that the work input during the deformation process is fully recovered when the perturbation actions are removed, which means that the process is completely reversible and, consequently, Equation (2.134) can be expressed and solved easily.

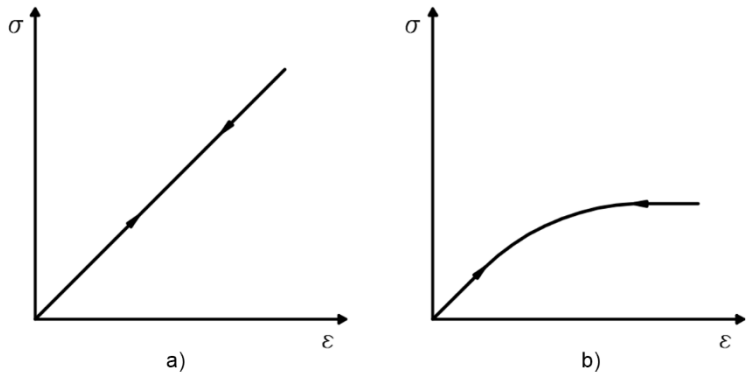

Figure 2.6 – Elastic behaviour: a) linear; b) non-linear

Under the assumption that the behavior of the material is linear, homogeneous and isotropic, and considering that both the stress and strain tensors are symmetric, it follows that in the tensor C_{ijhk} only two of eighty-one components are really independent. Therefore, Equation (2.134) assumes the following form:

$$\varepsilon_{ij} = -\frac{\nu}{E}\sigma_{kk}\delta_{ij} + \frac{1+\nu}{E}\sigma_{ij} \tag{2.135}$$

where E is the Young's modulus and ν is the Poisson's ratio, which are the most used elastic parameters in engineering, because of the direct experimental determination of them. However, in many

problems of soil mechanics, it is common to refer to alternative parameters: the shear modulus G and the bulk modulus K.

The shear modulus G is related to the Young's modulus and the Poisson's ratio by Equation (2.136).

$$G = \frac{E}{2(1+\nu)} \tag{2.136}$$

Instead, the bulk modulus K is usually obtained as the ratio of the mean pressure p to the volumetric strain ε_v (Equation (2.137)).

$$K = \frac{p}{\varepsilon_v} = \frac{E}{3(1-2\nu)} \tag{2.137}$$

It is relevant to observe that the elastic constants cannot take any values. Indeed, since the elastic energy of deformation must assume positive values, the elastic parameters have to satisfy the conditions expressed by Equations (2.138)-(2.141).

$$K > 0 \tag{2.138}$$

$$G > 0 \tag{2.139}$$

$$E > 0 \tag{2.140}$$

$$-1 \leq \nu \leq 0.5 \tag{2.141}$$

However, negative values of the Poisson's ratio have no physical meaning, therefore Equation (2.141) turns into Equation (2.142).

$$0 \leq \nu \leq 0.5 \tag{2.142}$$

2.8.2 – Elasto-plastic theory

Experimental data support the assumption that many materials exhibit a reversible behavior only at very small strains, whereas irrecoverable and permanent deformations occur beyond a threshold strain. An example of great practical relevance of this kind of behavior, described by means of the plasticity theory, is provided by soil, where the irreversible nature of deformations is mainly the result of relative movements between particles. Anyway, these microscopic processes are disregarded in the phenomenological representation given by the plasticity theory, which only reflects the most relevant effects we can observe at a macroscale.

A fundamental assumption of plasticity is that the total strain can be additively decomposed into the elastic (reversible) and plastic (irreversible) components. Besides, observations show that the one-to-one correspondence between stress and strain is not satisfied anymore, therefore relationship must be expressed in differential form (Equation (2.143)).

$$d\varepsilon_{ij} = d\varepsilon_{ij}^{e} + d\varepsilon_{ij}^{p} \tag{2.143}$$

The elastic component of strain can be computed according to the elastic constitutive relations already exposed in the previous section. In addition, it is worth noticing that because of the assumption of isotropy, the principal directions of the strain

tensor are coincident with those of the stress tensor, so that the elastic relationship also define the strain directions.

On the contrary, to identify the plastic deformations, it is required to introduce:

- a yield criterion
- a plastic flow rule
- a hardening/softening rule

which allow one to specify respectively: when plastic deformations occur, their direction and their magnitude.

Yield criterion

The observation of the behavior of real soils shows that permanent and irreversible deformations occur beyond a threshold strain. Therefore, it is possible to define a condition so that the behavior of soil is purely elastic if such condition is satisfied, whereas it is elasto-plastic otherwise.

For a general multi-axial situation, a yield function F is defined (Equation (2.144)), which is a scalar function of stresses and state parameters $\boldsymbol{k}$.

$$F(\boldsymbol{\sigma}'; \boldsymbol{k}) = 0 \qquad (2.144)$$

This function separates purely elastic from elasto-plastic behavior. In general, this surface is a function of the stress state $\boldsymbol{\sigma}'$ and its size also changes as a function of the state parameters $\boldsymbol{k}$, which can be related to hardening/softening parameters. For

perfect plasticity $\boldsymbol{k}$ is constant and represents the magnitude of the stresses at yield. For hardening and softening plasticity $\boldsymbol{k}$ varies with plastic straining to represent how the magnitude of the stress state at yield changes. If the hardening or softening is related to the magnitude of the plastic strains, the model is known as strain hardening/softening. Alternatively, if it is related to the magnitude of plastic work, the model is known as work hardening/softening.

The value of the yield function F is used to identify the type of material behavior. Purely elastic behavior occurs if Equation (2.145) is satisfied.

$$F(\boldsymbol{\sigma}'; \boldsymbol{k}) < 0 \tag{2.145}$$

Otherwise, elasto-plastic behavior occurs if the condition expressed by Equation (2.146) is respected.

$$F(\boldsymbol{\sigma}'; \boldsymbol{k}) = 0 \tag{2.146}$$

Finally, the third possibility (Equation (2.147)) signifies an impossible situation.

$$F(\boldsymbol{\sigma}'; \boldsymbol{k}) > 0 \tag{2.147}$$

If the yield function is expressed in terms of principal stresses, and it is plotted in the three-dimensional space $\sigma_1 - \sigma_2 - \sigma_3$, it defines a yield surface, such as the one shown in Figure 2.7. The space enclosed by this surface is called elastic domain. Without the assumption of isotropic behavior, the yield function should have been expressed in terms of six stress component and it

would have formed a surface in the six-dimensional space. Clearly, it would not have been possible to draw such a space and therefore its visualization would have been difficult.

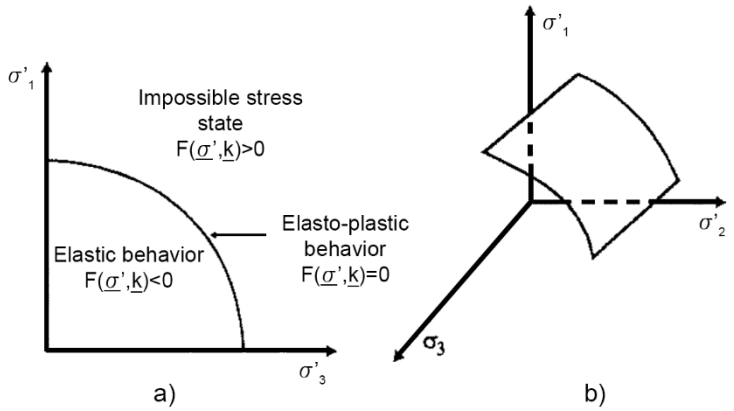

Figure 2.7 – Yield function representation: a) yield curve; b) segment of yield surface (adapted from Potts & Zdravkovic (1999))

Plastic flow rule

For a general multi-axial situation, it is necessary to have some means of specifying the direction of plastic straining at every stress state. This is done by means of a flow rule, which can be expressed according to Equation (2.148):

$$d\varepsilon_{ij}^{p} = \Lambda \frac{\partial P(\boldsymbol{\sigma}'; \boldsymbol{m})}{\partial \sigma_{ij}} \tag{2.148}$$

where P is the plastic potential function and Λ is a scalar multiplier. The plastic potential function has the form of Equation (2.149):

$$P(\boldsymbol{\sigma}'; \boldsymbol{m}) = 0 \tag{2.149}$$

where $\boldsymbol{m}$ is essentially a vector of state parameters whose values are immaterial, because only the differentials of P with respect to

the stress components are needed in the flow rule. Equation (2.149) is shown graphically in Figure 2.8.

Here, a segment of a plastic potential surface is plotted in principal stress space. Because of the assumption of coincidence of principal directions of accumulated stresses and incremental plastic strains, it is possible to plot incremental principal strains and accumulated principal stresses on the same axes. The outward vector normal to the plastic potential surface at the current stress state has components which provide the relative magnitudes of the plastic strain increment components.

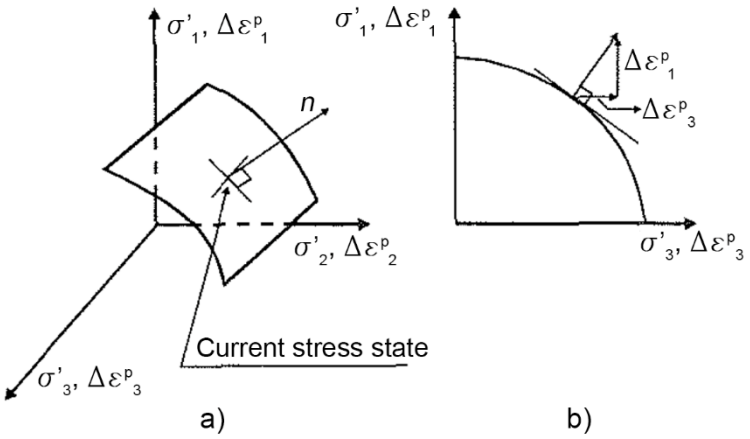

Figure 2.8 – Plastic potential representation: a) segment of the plastic potential surface; b) plastic potential curve (adapted from Potts & Zdravkovic (1999))

The value of the scalar Λ in Equation (2.148) controls the magnitude of strain components. Λ is dependent on the hardening/softening rule.

Sometimes a simplification is introduced by assuming the plastic potential function to be the same as the yield function (Equation (2.150)).

$$F(\boldsymbol{\sigma}';\boldsymbol{k}) = P(\boldsymbol{\sigma}';\boldsymbol{m}) \tag{2.150}$$

In this case the flow rule is said to be associated. The incremental plastic strain vector is therefore normal to the yield surface and the normality condition is said to be applied. In the general case in which the yield and plastic potential function differ, the flow rule is said to be non-associated.

Hardening/softening rule

The hardening/softening rules prescribe how the state parameters $\boldsymbol{k}$ (that appear in Equation (2.144)) vary with plastic straining. This enables the scalar parameter, Λ, to be quantified. If the material is perfectly plastic, no hardening or softening occurs and the state parameters $\boldsymbol{k}$ are constant. Consequently, no hardening or softening rules are required. In such materials, Λ is undefined. This follows from the fact that once the stress state reaches, and maintained at, yield the material strains indefinitely. However, for material which harden and/or soften during plastic straining, rules are required to specify how the yield function changes.

2.8.3 – Tresca model

Figure 2.9 shows the results of a conventional triaxial test performed on two different samples of a saturated clay, in undrained conditions. It is well known from the basis of

geotechnical engineering that if two samples are tested at different cell pressures, without allowing any consolidation, the Mohr's circles of stress at failure for the two samples have the same diameter. The Tresca failure criterion relates the undrained strength c_u to the diameter of the Mohr's circle (Equation (2.151)).

$$\sigma_1 - \sigma_3 = 2c_u \tag{2.151}$$

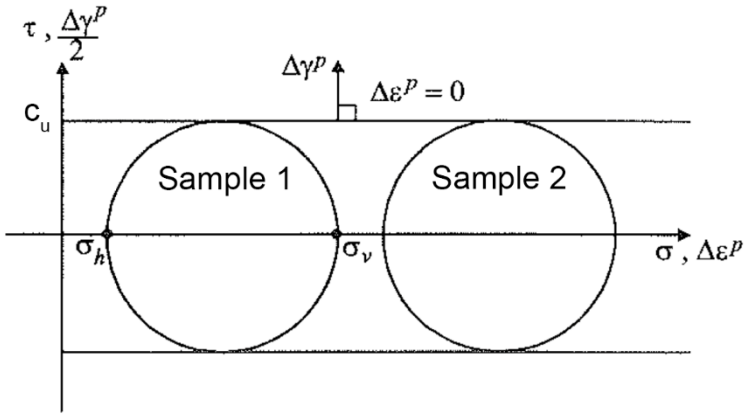

Figure 2.9 – Mohr's circles of total stress (adapted from Potts & Zdravkovic (1999))

In the Tresca model, this failure criterion is adopted as a yield surface and the yield function becomes Equation (2.152).

$$F(\boldsymbol{\sigma}'; \boldsymbol{k}) = \sigma_1 - \sigma_3 - 2c_u = 0 \tag{2.152}$$

For general stress states it is necessary to calculate all three principal stresses and determine the major, σ_1, and minor, σ_3, values before this equation can be evaluated. In the principal total stress space, this yield function plots as a regular hexagonal cylinder, which has the space diagonal as its line of symmetry, as shown in Figure 2.10. As this model is perfectly plastic, there is no hardening/softening law required. The only state parameter, i.e. the undrained strength c_u, is assumed constant, then it does

not depend on the plastic strain. The only remaining piece of information required to complete the plastic part of the model is the plastic potential function.

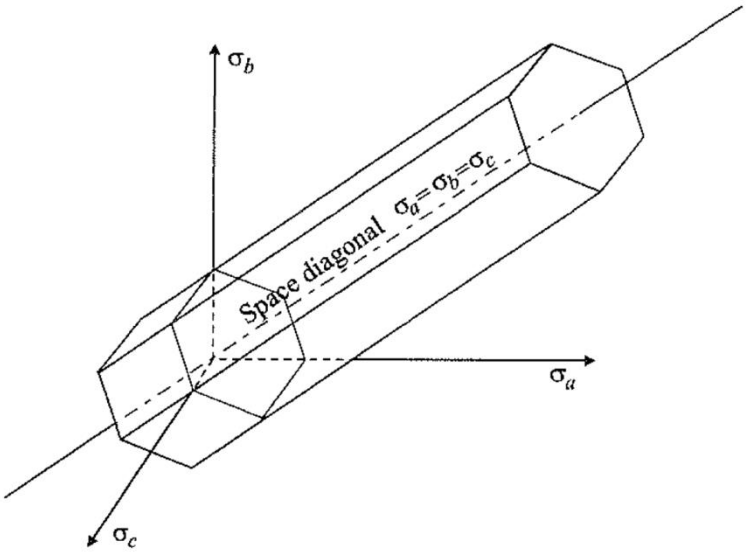

Figure 2.10 – Tresca yielding surface in principal stress space (from Potts & Zdravkovic (1999))

As the model is intended to simulate the undrained behavior of saturated clay, it should predict zero volumetric strains. Since the soil can be purely elastic (below the yield surface), or purely plastic (on the yield surface), both the elastic and plastic components of the volumetric strain must be zero. This clearly constrains the choice of the plastic potential. A convenient choice is to assume associated plastic flow and adopt the yield function given by Equation (2.153) as the plastic potential.

$$F(\boldsymbol{\sigma}'; \boldsymbol{k}) = J\cos\theta - c_u = 0 \qquad (2.153)$$

In Equation (2.153), J and θ are invariants, respectively named as deviatoric stress and Lode's angle and defined according to Equations (2.154) and (2.155).

$$J = \frac{1}{\sqrt{6}}\sqrt{(\sigma'_1 - \sigma'_2)^2 + (\sigma'_2 - \sigma'_3)^2 + (\sigma'_3 - \sigma'_1)^2} \qquad (2.154)$$

$$\theta = \tan^{-1}\left[\frac{1}{\sqrt{3}}\left(2\frac{(\sigma'_2 - \sigma'_3)}{(\sigma'_1 - \sigma'_3)} - 1\right)\right] \qquad (2.155)$$

Remembering that incremental plastic strains can be plotted on the same axes as accumulated stresses, then on Figure 2.9 the vector of incremental plastic strain is vertical (normal to the yield surface). This implies no incremental plastic direct strains and therefore no incremental plastic volumetric strains. To complete the model it is only necessary to define the elastic parameters. As there should be no elastic volumetric strains, $\nu = 0.5$. The model can therefore be defined by specifying the undrained strength, c_u, and the undrained Young's modulus, E_u.

2.8.4 – Mohr-Coulomb model

If the results of laboratory tests are plotted in terms of effective stresses, the Mohr's circles of stress at failure are often idealized as shown in Figure 2.11. It is usual to assume that the tangent of the failure circles from several tests, performed with different initial effective stresses, is straight. This line is called Coulomb failure criterion and can be expressed in function of the drained parameters, $c'$and φ', (Equation (2.156)).

$$\tau_f = c' + \sigma'_{nf}\tan\varphi' \qquad (2.156)$$

Equation (2.156) can be rewritten in the form of Equation (2.157).

$$\sigma'_1 - \sigma'_3 = 2c' \cos\varphi' + (\sigma'_1 + \sigma'_3) \sin\varphi' \qquad (2.157)$$

In principal effective stress space, the yield function plots as an irregular hexagonal cone as shown in Figure 2.12. It is interesting to note that if c_u is substituted for c' and if φ' is set to zero in Equation (2.158), the Tresca yield function given earlier is obtained. As the Mohr-Coulomb model is assumed to be perfectly plastic, there is no hardening/softening law required. The state parameters, $c'$and φ', are assumed constant, independent of plastic strain or plastic work.

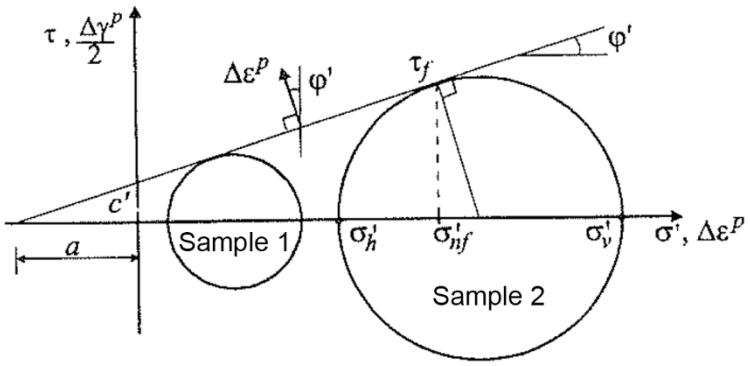

Figure 2.11 – Mohr's circles of effective stress (from Potts & Zdravkovic (1999))

This is often called the Mohr-Coulomb failure criterion and in the present model is adopted as the yield function, which is therefore defined by Equation (2.158).

$$F(\boldsymbol{\sigma}'; \boldsymbol{k}) = \sigma'_1 - \sigma'_3 - 2c' \cos\varphi' + \\ -(\sigma'_1 + \sigma'_3) \sin\varphi' \qquad (2.158)$$

To complete the plastic part of the model, a plastic potential function is required. Similar to the Tresca model, an associated

flow rule could be adopted. As shown in Figure 2.11, the plastic strain increment vector is then inclined at an angle φ' to the vertical direction and indicates negative (i.e. tensile) direct plastic strains. This in turn results in a dilatant plastic volumetric strain. For this situation, the angle of dilation, ψ, is defined by Equation (2.159) and is equal to the angle of shearing resistance, φ', as shown in Figure 2.13.

$$\psi = \sin^{-1}\left(-\frac{\delta\varepsilon_1^p + \delta\varepsilon_3^p}{\delta\varepsilon_1^p - \delta\varepsilon_3^p}\right) \tag{2.159}$$

There are two drawbacks to this approach. Firstly, the magnitude of the plastic volumetric strains (i.e. the dilation) is much larger than that observed in real soils, and secondly, once the soil yields it will dilate forever. Real soils, which may dilate initially on meeting the failure surface, will often reach a constant volume condition at large strains.

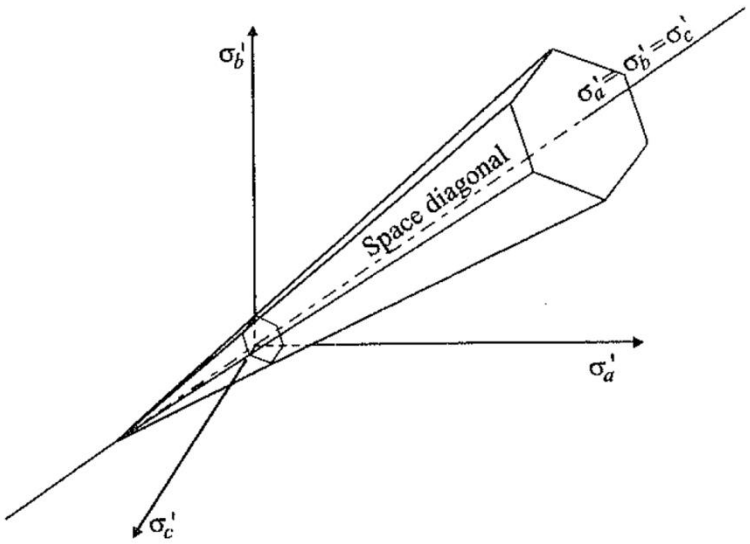

Figure 2.12 – Mohr-Coulomb yielding surface in principal stress space (from Potts & Zdravkovic (1999))

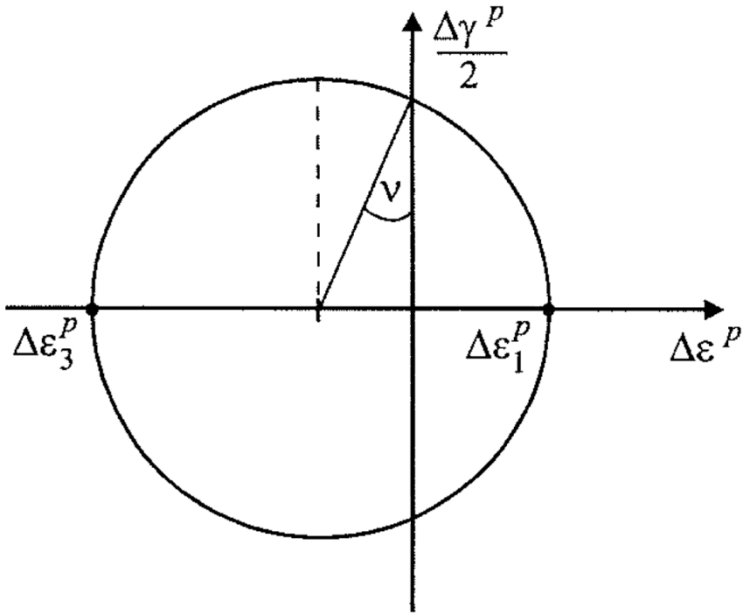

Figure 2.13 – Mohr's circle of plastic strains (from Potts & Zdravkovic (1999))

The first drawback can be partially rectified by adopting a non-associated flow rule, where the plastic potential function is assumed to take a similar form to that of the yield surface, but with φ' replaced by ψ. If $\psi = 0°$, zero plastic dilation occurs. Consequently, by prescribing the angle of dilation, ψ, the predicted plastic volumetric strain can be controlled. Furthermore, the value $\psi = 0°$ is strongly recommended when dealing with problems involving large deformations, since otherwise unrealistic and unlimited volumetric deformation would occur, making the constitutive model unsuitable to properly analyze this kind of problem. To summarize, the Mohr-Coulomb model requires five parameters. Three of these, c', φ' and ψ, control the plastic behavior, and the remaining two, E and ν, control the elastic behavior.

2.8.5 – Mohr-Coulomb model with strain-softening

It was already mentioned that a material that exhibits a hardening/softening behavior changes its threshold of yielding when plastic strains increase. This results in a change of the size of the yielding surface. In multi-axial situations it is common to relate changes in size of the yield surface to the components (or invariant) of the accumulated plastic strain. Such hardening/softening rules are then called strain hardening/softening.

In the Mohr-Coulomb model discussed in the previous section there is no hardening/softening rule, then the strength parameters are kept constant during the whole simulation. On the other hand, this hypothesis is not realistic for many soils, especially for stiff soils. Indeed, such soils exhibit a brittle behavior characterized by a reduction of the shear strength after reaching a threshold stress, which is commonly called peak condition. Indeed, immediately after the peak stress (which usually is reached in correspondence of small displacements), the strength drops to values defined by an intercept cohesion tending to zero and a friction angle which is less than the initial value. Such strength reduction continues until the residual strength is reached, at very large displacements. Therefore, the Mohr-Coulomb model described in the previous section is not suitable to describe this behavior, and an improvement is required. As

improvement, the strength parameters $c'$and φ', and the angle of dilation ψ, can all be allowed to vary with the accumulated plastic strains. Following an approach similar to that proposed by Potts et al. ((1990); (1997)), the strain softening behavior is accounted for in this dissertation by allowing the angle of shearing resistance, φ', and the intercept cohesion, c', to vary with the plastic strain invariant k_{shear}, defined by Equation (2.160), as shown in Figure 2.14:

$$k_{shear} = \int_0^t \sqrt{\frac{1}{2}\left[\left(\dot{\varepsilon}_1^p - \dot{\varepsilon}_2^p\right)^2 + \left(\dot{\varepsilon}_2^p - \varepsilon_3^p\right)^2 + \left(\dot{\varepsilon}_3^p - \dot{\varepsilon}_1^p\right)^2\right]}\, dt \qquad (2.160)$$

where t is time.

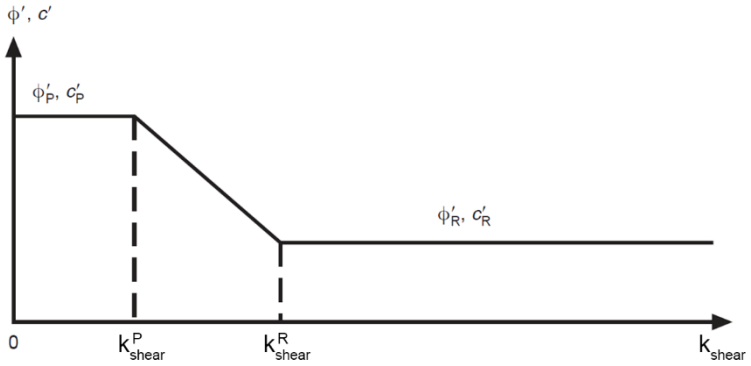

Figure 2.14 – Variation of the angle of shearing resistance and the intercept cohesion with the plastic strain invariant (modified from Potts et al. (1990))

Two thresholds values of the deviatoric plastic strain have to be defined: k_{shear}^P and k_{shear}^R.

When $k_{shear} < k_{shear}^P$ the strength parameters assume their peak values, whereas when $k_{shear} > k_{shear}^R$ the strength parameters are the ones corresponding to the residual condition. For intermediate values, i.e. $k_{shear}^P < k_{shear} < k_{shear}^R$, strength parameters assume

intermediate values with a linear relationship. Therefore, the model requires the specification of peak (φ'_p, c'_p) and residual (φ'_r, c'_r) strength parameters, the angle of dilation ψ, the elastic parameters (E and ν) and the threshold invariants k^P_{shear} and k^R_{shear}.

These latter values can be easily obtained by matching the experimental results of laboratory tests with those obtained by numerically simulating the same tests, within the framework of a trial and error procedure.

Another common way to account for the strain softening behavior of soils was proposed by Abbo & Sloan (1995), in which an exponential law defines the strength parameters reduction (Equations (2.161), (2.162) and (2.163)).

$$c' = c'_r + \left(c'_p - c'_r\right)e^{-\eta k_{shear}} \tag{2.161}$$

$$\varphi' = \varphi'_r + \left(\varphi'_p - \varphi'_r\right)e^{-\eta k_{shear}} \tag{2.162}$$

$$\psi = \psi_r + \left(\psi_p - \psi_r\right)e^{-\eta k_{shear}} \tag{2.163}$$

This model does not require the threshold invariants, whereas an additional parameter η is needed to control the brittleness of the material.

Analogously to the invariants k^P_{shear} and k^R_{shear}, the parameter η can be calibrated on the basis of available laboratory tests, such as triaxial tests and/or shear tests. However, attention has to be

paid in calibrating this parameter, since it is mesh-dependent. In order to reduce the influence of the mesh on the results, Yerro (2015) suggested to adapt the value of the parameter η for different mesh sizes maintaining fixed the dissipated work.

2.8.6 – Elasto-viscoplastic model

When the behavior of soil is analyzed whereby numerical simulations, especially when material characterized with a strain-softening behavior are involved, a common problem is the dependence of the solution on the adopted mesh. Among the techniques available to overcome this problem, it is worth mentioning the elasto-viscoplastic constitutive model. The model proposed by Di Prisco & Imposimato (1996) is mentioned below.

As for the elasto-plastic model discussed in the previous sections, also within the framework of elasto-viscoplasticity, the total strain rate tensor may be written as Equation (2.164):

$$d\varepsilon_{ij} = d\varepsilon_{ij}^{e} + d\varepsilon_{ij}^{vp} \tag{2.164}$$

where $d\varepsilon_{ij}^{vp}$ is the visco-plastic strain rate tensor.

The elastic strain rate tensor $d\varepsilon_{ij}^{e}$ is calculated again whereby the Equation (2.135), previously discussed.

According to Perzyna (1963), the visco-plastic strain increments are assumed to be delayed with time and are expressed using Equation (2.165).

$$d\varepsilon_{ij}^{vp} = \Phi(F)m_{ij} \tag{2.165}$$

In Equation (2.165) Φ is the viscous nucleus which depends on the yield function F, whereas m_{ij} is the gradient of the plastic potential, P (i.e. $m_{ij} = \partial P/\partial\sigma'_{ij}$). The gradient of P defines the direction of the visco-plastic strain rate tensor, and the yield function influences the modulus of this tensor by means of Φ. The viscous nucleus Φ can be expressed whereby the Equation (2.166).

$$\Phi(p', F) = \bar{\gamma}p'e^{\alpha F} \tag{2.166}$$

In Equation (2.166), $\bar{\gamma}$ and α are the constitutive parameters, whereas p' denotes the mean effective stress. A maximum value of 3 should be assumed for the product αF to prevent the exponent in Equation (2.166) from becoming excessively large (di Prisco & Imposimato, (2002)). The parameter $\bar{\gamma}$ considerably influences the rate with which strain occurs owing to a given stress increment (di Prisco & Imposimato, (1996)). In particular, strain rate increases with increasing values of $\bar{\gamma}$. In other words, a high value of $\bar{\gamma}$ should be used to reproduce a material with a rapid response to a prescribed stress increment. Following Zienkiewicz & Cormeau (1974), the viscous component of the constitutive model could also be used as a device to regularize the numerical solution when soils with a strain-softening behavior are modelled (Troncone et al., (2014)).

Chapter 3 - The Senise landslide

3.1 – Introduction

On 26 July 1986 at about 4.00 a.m., a landslide of great dimensions occurred at Senise, a little village located at about 70 km away from Potenza, Southern Italy (Figure 3.1), some months after the execution of deep excavations, performed in order to allow the construction of some new buildings.

Figure 3.1 – Location of Senise in Southern Italy

The area involved in the landslide is located on top of the Timpone hill. Such a landslide can be defined catastrophic since it tore

some buildings down and damaged more or less seriously other structures as well as it caused eight fatalities. On 6 September 1986 at about 2.00 a.m., a reactivation caused further movements of the unstable soil mass, when a campaign of *in situ* investigation was still underway and no stabilization measures could be adopted yet. This landslide is classified as a translational sliding and owing to the unusual entity of displacements, velocities and seasonal period of trigger, it obtained a great attention among researchers and, therefore, several authors provided a detailed documentation of the event: Del Prete & Hutchinson (1988), Guerricchio & Melidoro (1988), Viggiani & Di Maio (1991), Troncone (2005) and Troncone et al. (2014). The studies initially carried out by Del Prete & Hutchinson (1988), Guerricchio & Melidoro (1988) and Viggiani & Di Maio (1991) were aimed to describe the geomorphology, geology and geotechnical characterization of the interested area, whereas the more recent studies proposed by Troncone (2005) and Troncone et al. (2014) described the finite element analyses performed in order to successfully simulate the pre-failure and failure stages. However, such analyses could not be used in order to analyze the post-failure stage of the landslide, because of the issues manifested by the finite element method when dealing with large deformations, as explained in Chapter 2. Therefore, the main aim of this chapter is the description of the analyses performed in the context of this

research about the post-failure stage of the Senise landslide by using the material point method. The description of such analyses will follow an initial discussion about the aspects investigated during the previous studies, since on them depend the analyses performed in this dissertation.

3.2 – Landslide description and kinematics

In order to describe the event, it will be useful to refer to an aerial photo taken from a helicopter just after the collapse, and shown in Figure 3.2, which clearly highlights the mechanism of the event that consisted in the detachment and sliding of a volume of soil of about 400000 m^3, with a shape in plant similar to a drop and with a maximum width at the base of 150 m, and a length from the toe to highest point of the detachment surface of over 200 m. The overall thickness of the body of landslide varied from 10 m to 15 m, except at the toe and along the eastern boundary where it reduced to about 5 m, as asserted by Guerricchio & Melidoro (1988). The body of landslide slid downstream for over 30 m, on a surface approximately parallel to the ground; it moved with no relevant distortion and carried a house and two almost intact roads on it. Soil movement gave rise to a wide crack between the body of landslide and the soil behind it along the upper boundary of the landslide, which is commonly named graben. On the top of the hill, in correspondence of the crack, there used to be a little

building which fell into the graben and got totally destroyed, causing the loss of five human lives. In correspondence of the toe, the landslide assumed the shape of a detritus mass which buried and completely tore down four new buildings just built up.

Figure 3.2 – Aerial view of the Senise landslide (from Del Prete & Hutchinson (1988))

Besides, it partially buried or gravely damaged other three buildings. Other three people died in this area. Detailed information was available about the topography of the involved

area, both before and after the landslide. Such information allows more detailed elements about the kinematic of the landslide to be obtained. Thanks to a favorable and accidental circumstance, just two days before the landslide (i.e. on 24 July 1986) an aerophotogrammetric shooting was taken, which allowed a survey to be obtained. The involved area of such a survey is shown in Figure 3.3. The examination of such a survey highlights the aspects listed below:

- Before the landslide, the slope has a quite regular morphology, with an average incline of over 30% in the area upstream the road SP 107, whereas it is a little lesser downstream the same road, which appears in the lower boundary of Figure 3.3. In the eastern part, close to the ridge, the incline is greater.
- Just upstream the road, there are nine buildings just built up or under construction (indicated with numbers 1, 2, 3, 4, 5, 8, 9, 10, 11 in Figure 3.3). Other two buildings are located more upstream, one on the east side and the other one on the west side (indicated with numbers 12 and 7, respectively in Figure 3.3). Lastly, a further building is located on the top of the hill (indicated with number 6 in Figure 3.3).
- Still upstream the road, deep excavations are noticeable, both in the area that would afterwards be involved in the

landslide (whose perimeter is defined by a dotted line in Figure 3.3) and outside it.

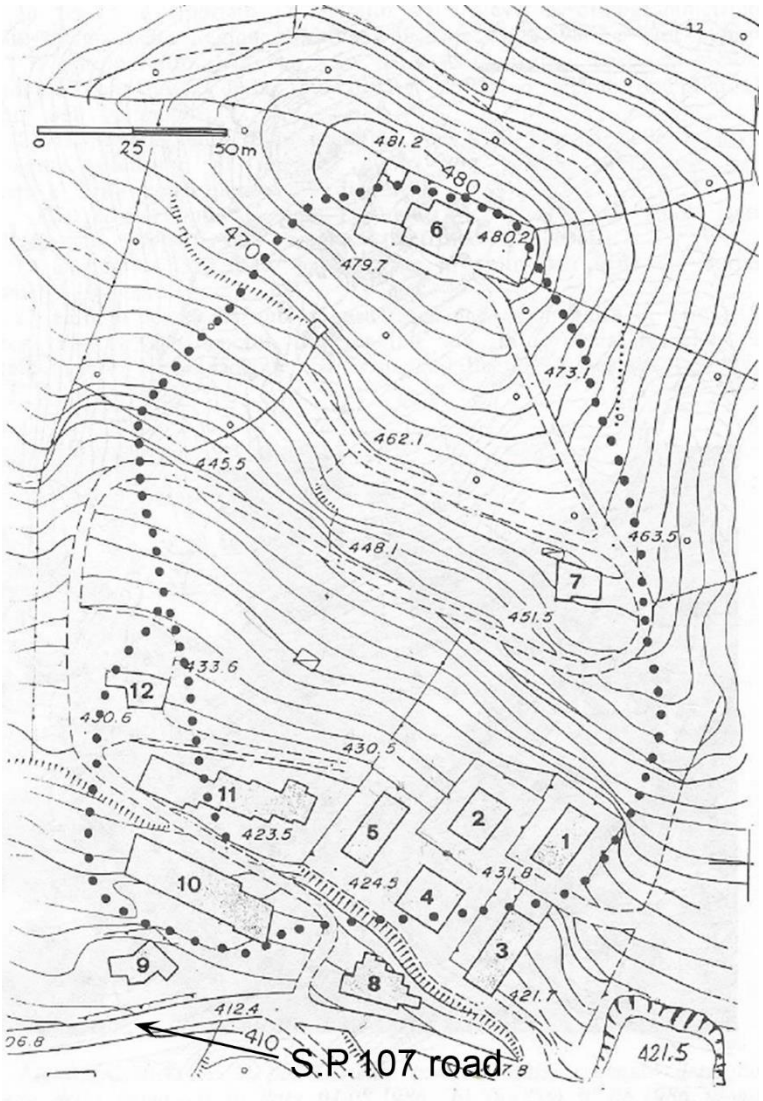

Figure 3.3 – Aerophotogrammetric survey of the involved area, taken on 24 July 1986 (i.e. two days before the landslide). The dotted line indicate the area involved in the landslide (modified from Viggiani & Di Maio (1991))

Figure 3.4 shows a piece of the aerophotogrammetric survey taken by Regione Basilicata on 5 August 1986. The comparison between Figure 3.3 and Figure 3.4 as well as the pictures taken *in loco* after the event allow realizing the characteristics and the consequences of the disaster with great precision. The buildings indicated with

the numbers 1, 2, 4 and 5 in Figure 3.3 were completely buried by the detritus mass and torn down. Building 3 were partially buried by the toe of the body of landslide (Figure 3.5).

Building 11 was undergone a downstream movement of about 15 m, with noticeable differential displacements both in the horizontal and vertical directions. It was deeply and irremediably damaged (Figure 3.6).

Figure 3.4 - Aerophotogrammetric survey of the involved area, taken on 5 August 1986 (i.e. some days after the landslide) (from (Viggiani & Di Maio (1991))

Building 10 was shifted downwards for about 12 m and partially crumpled, crushing and tearing down building 9. Building 12 was shifted downwards for about 15 m, and was gravely damaged. Building 7 was shifted downwards for over 30 m, but was kept intact (Figure 3.7).

As previously said, building 6 fell into the graben and was completely destroyed. The comparison between the plane-altimetric position of some elements, noticeable in Figure 3.3 and Figure 3.4, provides interesting data about the kinematics of the movement.

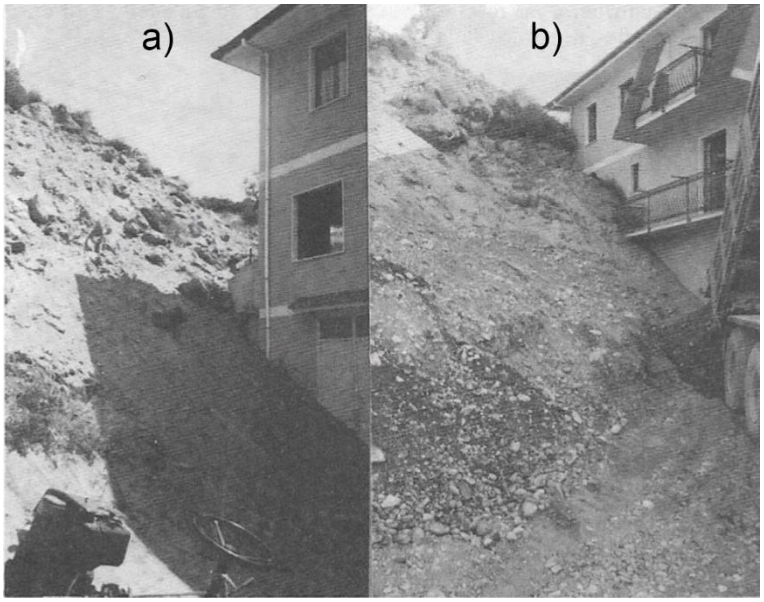

Figure 3.5 – Building 3, partially buried by the soil mass at the toe of the landslide: a) on 1 August 1986; b) on 7 August 1986, after further movements (from Viggiani & Di Maio (1991))

The planimetry reported in Figure 3.8 shows a graphic representation of the horizontal components of displacements of those elements. It results that the soil mass was undergone a translation in the North-South direction, with a horizontal

component of about 30 – 32 m. Only for building 7 the direction seems a little different, but this happened due to local rotations and displacements of the building, which is located right on the edge of the landslide. At the toe of the landslide, soil displacements tend to gradually reduce.

Figure 3.6 – Building 11, clearly damaged and carried downwards from the landslide for about 15 m (from Viggiani & Di Maio (1991))

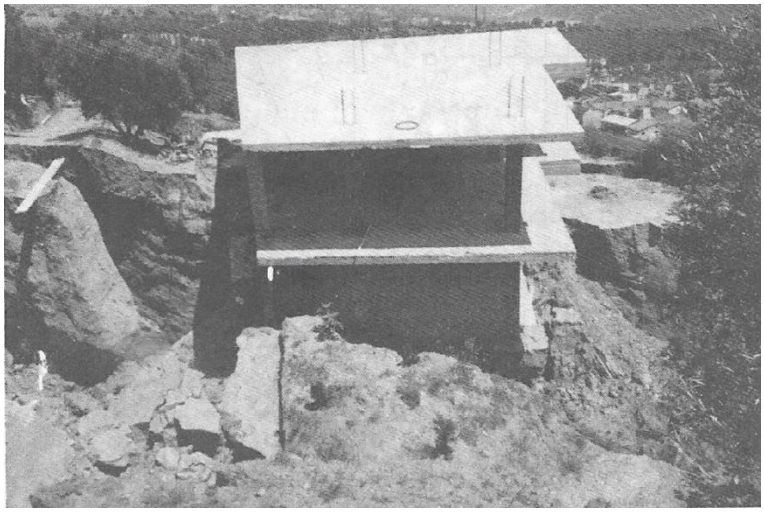

Figure 3.7 – Building 7, shifted downwards for over 30 m e rotated due to local deformations owing to movements towards the graben edge (from Viggiani & Di Maio (1991))

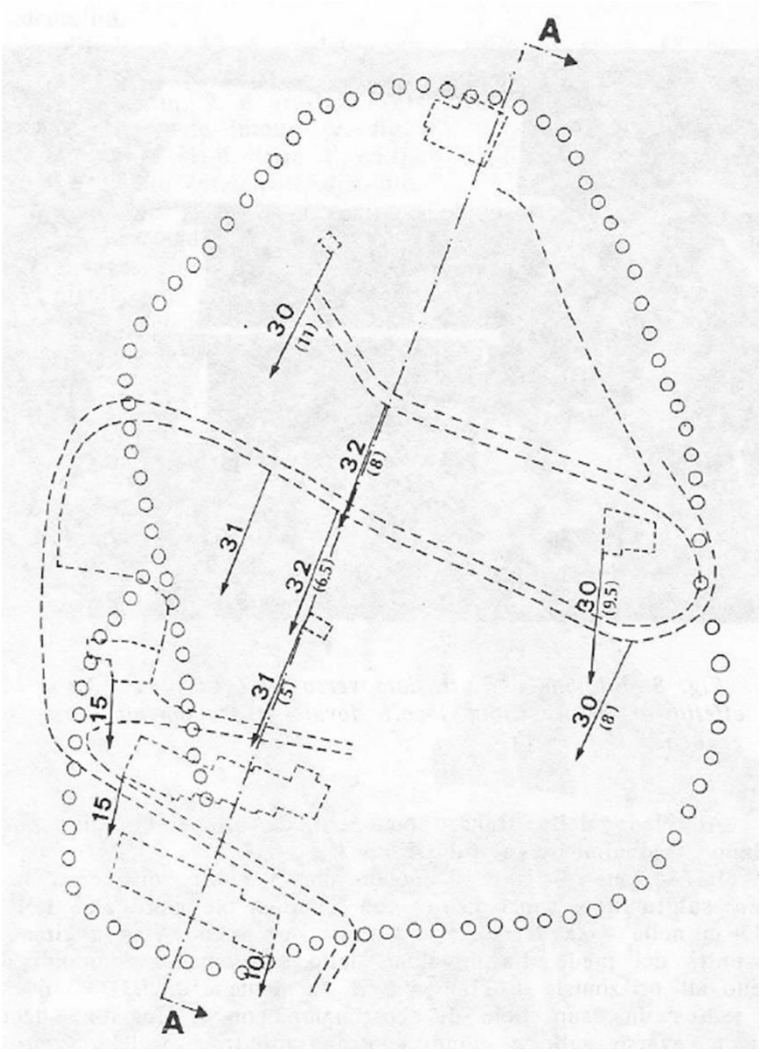

Figure 3.8 – Graphic representation of displacements of some points. Vectors represent, in the same scale of the picture, the horizontal components of displacements; the numerical value of such components, and of the vertical ones (in brackets), are indicated near the vectors (from Viggiani & Di Maio (1991))

The cross section reported in Figure 3.9 shows that points considered in Figure 3.8 were undergone a displacement with vertical component of about 11 m upstream, which gradually decrease up to about 5 m in proximity of the toe. This indicates a sliding surface with a decreasing incline from upstream to downstream. From the examination of the displacements field and considering the crack at the northern side and at the eastern one, it seems that the direction of the movement would be “driven”

whereby a sliding along the western edge of the body of landslide. The examination of the aerial pictures highlights that such an edge coincide with a tectonic line, maybe an important crack, which was already visible before the landslide.

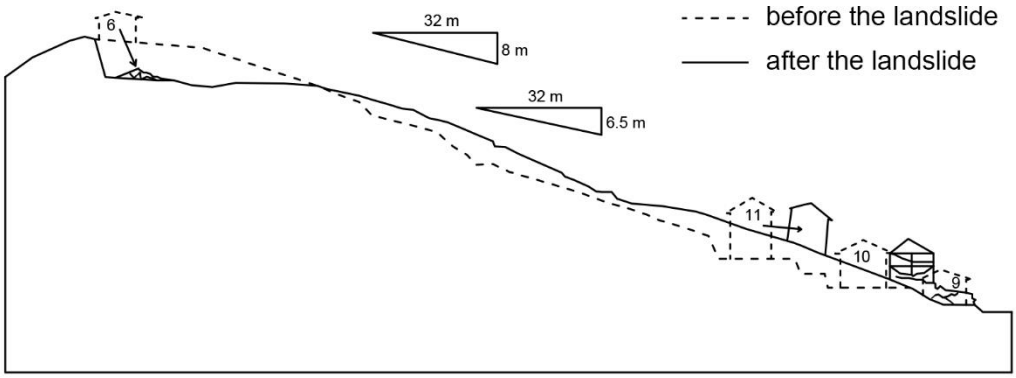

Figure 3.9 – Comparison between the pre-failure and post-failure profile, in correspondence of the cross section A-A reported in Figure 3.8, with the representation of the displacements of the involved buildings (adapted from Viggiani & Di Maio (1991))

3.3 – Geological and hydrogeological setting

The outcropping geological formation of the hill of Senise is made up of yellowish sand with interbedded thin layers of clayey silt (Aliano formation). These layers, with prevalent south-westward dip, have a thickness ranging from some centimeters to several decimeters, and an average inclination (downslope) of approximately 18° with respect to the horizontal plane. Sand is very dense and it is characterized by a significant degree of cementation. The Aliano formation overlies a base formation of blue-grey clay. The morphologic configuration of the ground gives rise to a hilly elevation with an approximatively conic shape

upstream; on the ridge of such a hill (480 m a.s.l.), there used to be the building that would afterwards be torn down during the landslide. The northern slope of this hill, on the opposite side of the landslide, shows an incline of over 65% upstream. In this side of the hill, the layers of clayey silt are anti-dip-slope; the slope is steeper uphill, where mainly sandy deposits emerge; whereas it is less steep downhill, where mainly clayey deposits emerge. The southern slope of the hill has a less steep incline: about 35% from the ridge to the SP107 road (where the landslide occurred); about 20-25% downhill. In the upper part of the hill, the morphology of the slope is regular; in this sector, mainly sandy deposits dip-slope emerge, with an incline slightly greater than that of the slope. Instead, downwards the road, the southern slope shows more pronounced irregularities such as concavities, ledges and scarps, which could likely be the effect of ancient landslides. The outcropping soils in this zone are mainly made up of sand, with a chaotic structure due to the likely ancient landslide.

Based on these data, the geological cross section shown in Figure 3.10 was deduced. Definitively, the geological structure of the hill is mainly made up of a sandy layer with thin seams of silt or sandy-silt interbedded inside it, laying on a mainly clayey layer with a less incline, which tends to emerge downwards. The thin layers of silt are frequently laminated with a thickness ranging from two to ten centimeters.

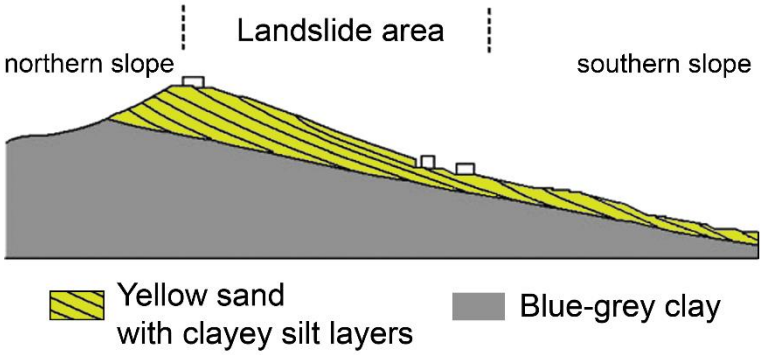

Figure 3.10 – Schematic geological cross-section of the hill (adapted from Viggiani & Di Maio (1991))

It is relevant to point out that no water level was detected in the proximity of the body of landslide, as asserted in the previous studies (Del Prete & Hutchinson (1988); Guerricchio & Melidoro (1988); Viggiani & Di Maio (1991)). Besides, neither wells nor springs were found in the study area (Del Prete & Hutchinson (1988)). Finally, it is worth noticing that the landslide occurred after a long period of scarce rain (Del Prete & Hutchinson (1988); Guerricchio & Melidoro (1988)).

3.4 – Geotechnical characterization

After the catastrophic event of July 1986 and before the reactivation of September of the same year, a site investigation consisting of boreholes, standard penetration tests and laboratory tests was performed. Several piezometers and inclinometers were also installed within the slope. The results from the laboratory tests showed that the grain size distribution of the Aliano sand varies from sand with gravel to sand with silt, whereas that of the

clayey silt varies from sandy and clayey silt to silt with clay. The grain size distribution curves for the soils constituting the slope are shown in Figure 3.11. Data available about blue-gray clay are limited, and they seem to point out that such formation is mainly composed of silt with sand, from the point of view of the grain size distribution.

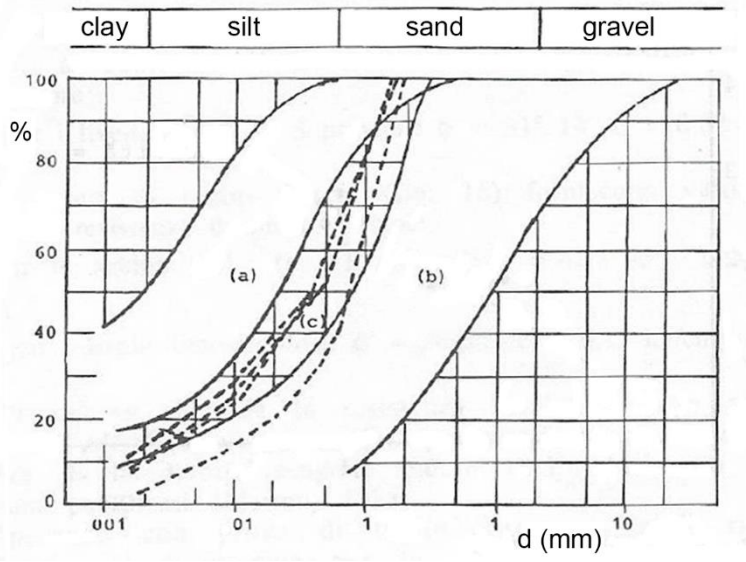

Figure 3.11 - Grain size distribution curves: a) clayey-silt levels; b) yellow sand; c) blue-grey clay (adapted from Viggiani & Di Maio (1991))

Standard penetration tests gave results taken as refusal for depths greater than a couple of meters; only data obtained within the body of landslide are smaller and much variable. Such an investigation allowed the distinction between the fractured masses of the body of landslide and the intact underlayer. In particular, the results of the standard penetration tests described by Del Prete & Hutchinson (1988) showed low values of N_{SPT} until the depth of 10.50 m, an increase of this latter value until the depth of 14 m, whereas it is taken as refusal at depths greater

than 14.30 m. Such measurements allowed the depth of the slip surfaces to be detected.

Therefore, the main slip surface is located at the depth of about 14 m below the ground surface, in the central part of the body of landslide, whereas a secondary slip surface was recognized at the depth of about 10.50 m. Such conclusions were confirmed by the results obtained from some inclinometers installed inside the boreholes, whose results are schematically reported in Figure 3.12. Both the main and the secondary slip surfaces were located in correspondence of thin clayey silt layers interbedded in the sand formation.

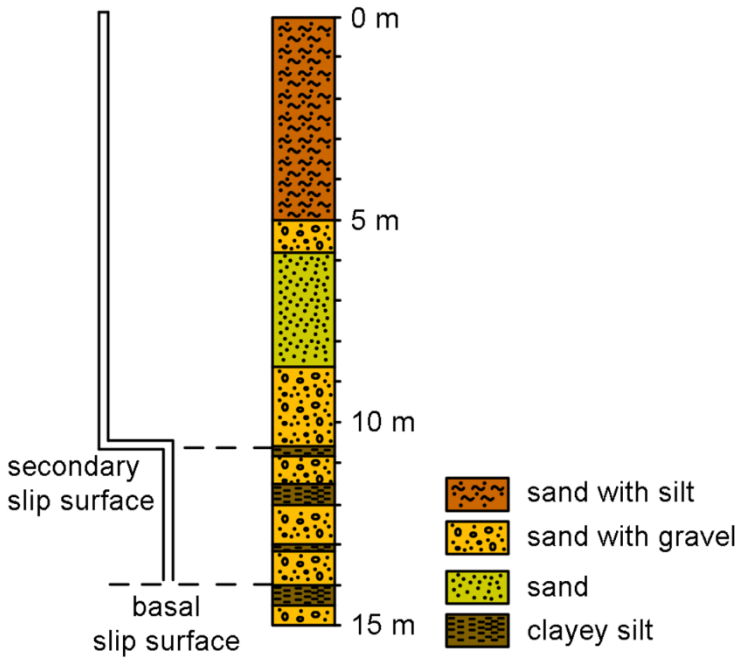

Figure 3.12 – Soil profile and deformation of the inclinometer (adapted from Del Prete & Hutchinson (1988))

The shear strength of the involved soils was investigated by carrying out some triaxial tests and direct shear tests. As shown

in Figure 3.13, one peculiar aspect of these soils is their mechanical instability, pointed out by a pronounced strain-softening behavior after the peak is reached.

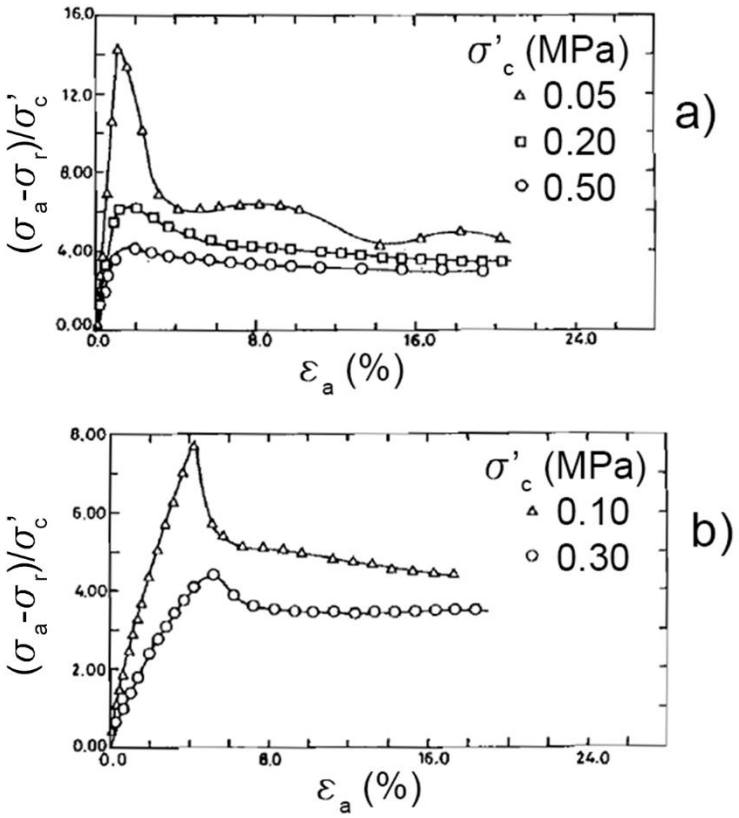

Figure 3.13 – Results of triaxial tests: a) sand; b) clayey silt (adapted from Del Prete & Hutchinson (1988))

The shear strength envelopes are synthesized in Figure 3.14, Figure 3.15 and Figure 3.16. From the triaxial tests conducted on 16 samples of yellow sand, a peak angle of shearing resistance, φ'_p, of about 36° and a peak cohesion, c'_p, ranging from 0 to 137 kPa were obtained (Figure 3.14). The high values of c'_p were attributed by Del Prete & Hutchinson (1988) and Viggiani & Di Maio (1991) to the significant degree of cementation presented by this soil. The triaxial tests carried out on three samples of clayey

silt provided peak values for φ'_p and c'_p of about 31° and 82 kPa respectively.

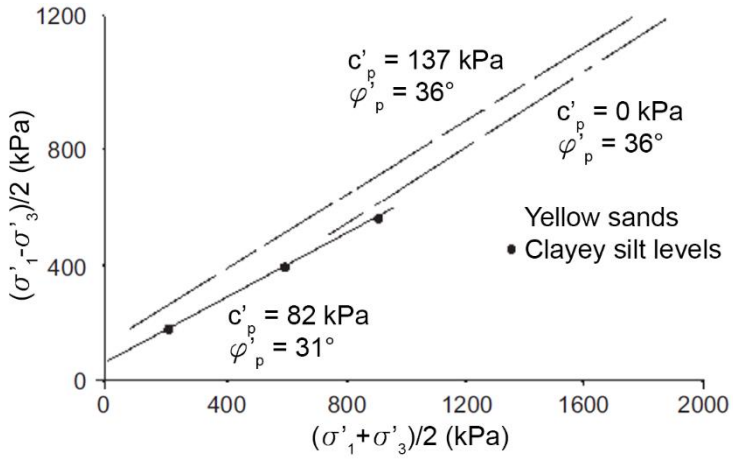

Figure 3.14 – Peak strength envelope from triaxial tests (adapted from Viggiani & Di Maio (1991))

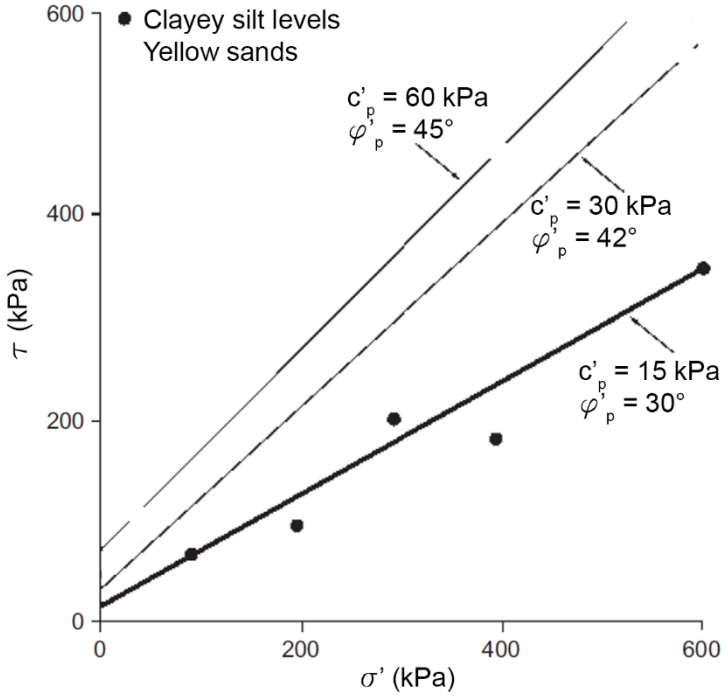

Figure 3.15 – Peak strength envelope from direct shear tests (adapted from Viggiani & Di Maio (1991))

The peak strength parameters deduced from the direct shear tests were: $\varphi'_p = 42 - 45°$ and $c'_p = 30 - 60\ kPa$ for the yellow sand, and $\varphi'_p \cong 30°$ and $c'_p = 15\ kPa$ for the clayey silt (Figure 3.15).

The values of the residual angle of shear resistance of the yellow sand ranged from 34° to 37°, and it was about 12° for the clayey silt (Figure 3.16); the residual cohesion was nil for both these soils. Furthermore, the laboratory tests showed that both the sand and silt are characterized by a pronounced strain-softening behavior (Figure 3.13).

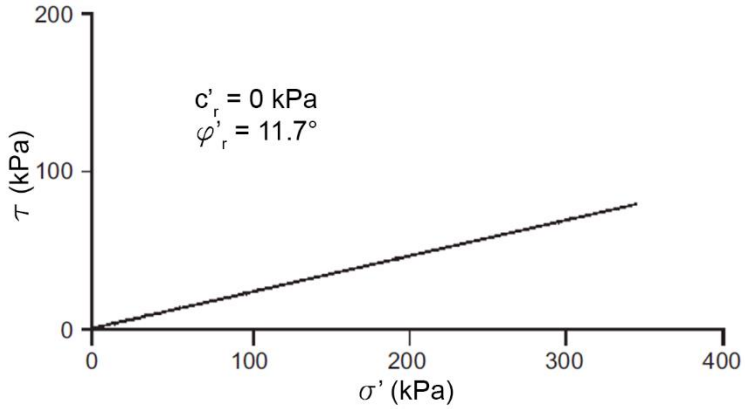

Figure 3.16 – Residual strength envelope from direct shear tests (adapted from Viggiani & Di Maio (1991))

3.5 – Interpretation of the landslide

Based on stability analyses carried out by means of limit equilibrium methods, different interpretations of the landslide were proposed in the previously mentioned studies. Del Prete & Hutchinson (1988) asserted that the landslide was predominantly a first-time sliding, with the soil resistance mobilized along the slip surface close to the residual strength of the clayey silt layer. These authors attributed this finding (unexpected for this type of landslide) to ancient morpho-tectonic conditions. Guerricchio &

Melidoro (1988) came to a similar conclusion. In disagreement with such opinions, Viggiani & Di Maio (1991) pointed out the absence of any trace of ancient movements, and interpreted the landslide in terms of progressive failure, using the simplified model proposed by Christian & Whitman (1969). Nevertheless, all these authors agree on the fact that the event was triggered, or at least influenced, by the deep excavations performed at the toe of the slope in order to allow the construction of some new buildings (Figure 3.3). The cuts were essentially vertical and sustained by reinforced concrete retaining walls. The heights of excavation estimated by Del Prete & Hutchinson (1988) are plotted in Figure 3.17, against the date of the construction permission for each building.

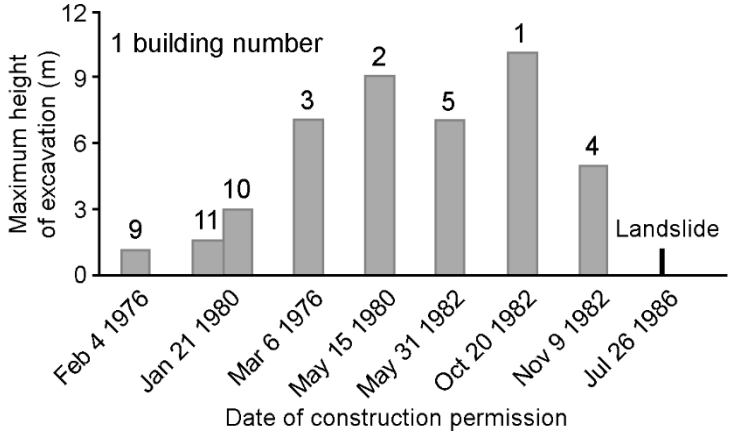

Figure 3.17 – Details of heights of excavation performed in order to allow the construction of the new buildings (adapted from Del Prete & Hutchinson (1988))

By comparing this graph and the plan reported in Figure 3.3, it is apparent that the excavations progressed from the south-west edge of the landslide body to the shaded area indicated in Figure

3.18, with an increasing height up to maximum values of 9-10 m, which were reached behind buildings 1 and 2. Therefore, it can be inferred that the landslide was delayed with respect to the excavations, and the movement occurred approximately along the A-A direction of Figure 3.8.

3.6 – Geotechnical model of the slope

All the analyses described in this chapter are referred to the cross section of trace A-A shown in the plan of the interested area (Figure 3.18). Based on the investigations described in the previous sections, Troncone et al. (2014) obtained the geotechnical model reported in Figure 3.19. The two main formations are the yellow sand and the blue-grey clay. Besides, a thin layer of clayey silt (with an inclination of about 18° with respect to the horizontal direction and a thickness of 30 centimeters) is located at an average depth of about 14 meters from the ground surface, in the same position where Del Prete & Hutchinson (1988) found the main sliding surface, thanks to the installation of inclinometers. As previously described, Del Prete & Hutchinson (1988) found a secondary sliding surface, located at an average depth of 10.5 m from the ground surface, which developed in another thin layer of clayey silt as well. Therefore, Troncone et al. (2014) proposed a further version of the

geotechnical model, accounting for also this second thin layer of clayey silt, which is shown in Figure 3.20.

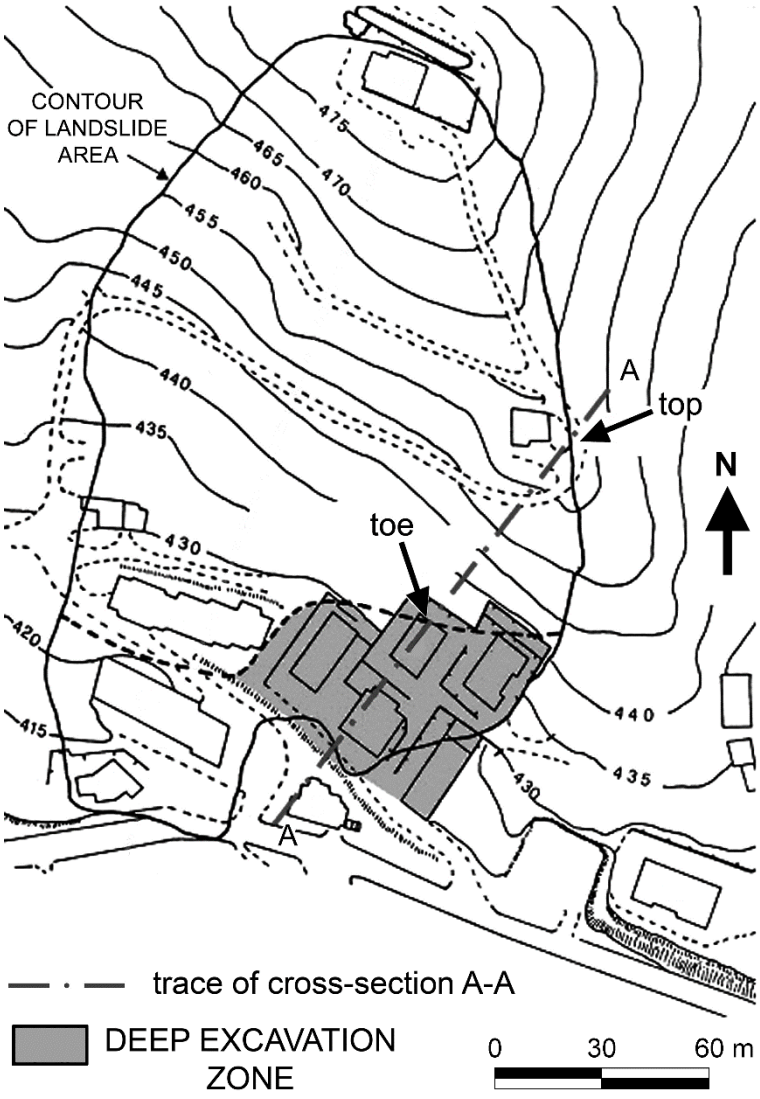

Figure 3.18 – Plan of the landslide with an indication of the area interested by the excavations and the trace of the cross section A-A (adapted from Del Prete & Hutchinson (1988))

The values of soils parameters, deduced on the basis of the investigation previously described, are reported in Table 3.I, where γ is the unit weight, E' is Young's modulus, ν' is Poisson's ratio, c'_p and φ'_p are the peak effective strength parameters (cohesion and angle of shearing resistance, respectively), c'_r and

φ'_r are the residual effective strength parameters, ψ is the angle of dilation, whereas k^p_{shear} and k^r_{shear} are the thresholds values of the deviatoric plastic strain defined by Equation (2.160) and discussed in Section 2.8.5.

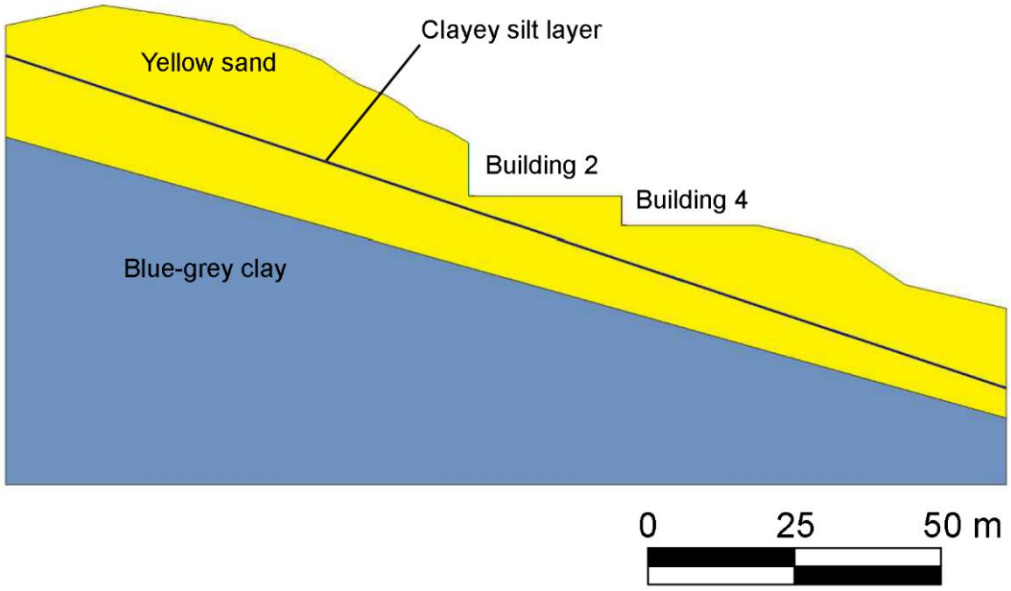

Figure 3.19 – Slope geometry and subsoil conditions used in the analyses carried out by Troncone et al. (2014), accounting for one layer of clayey silt

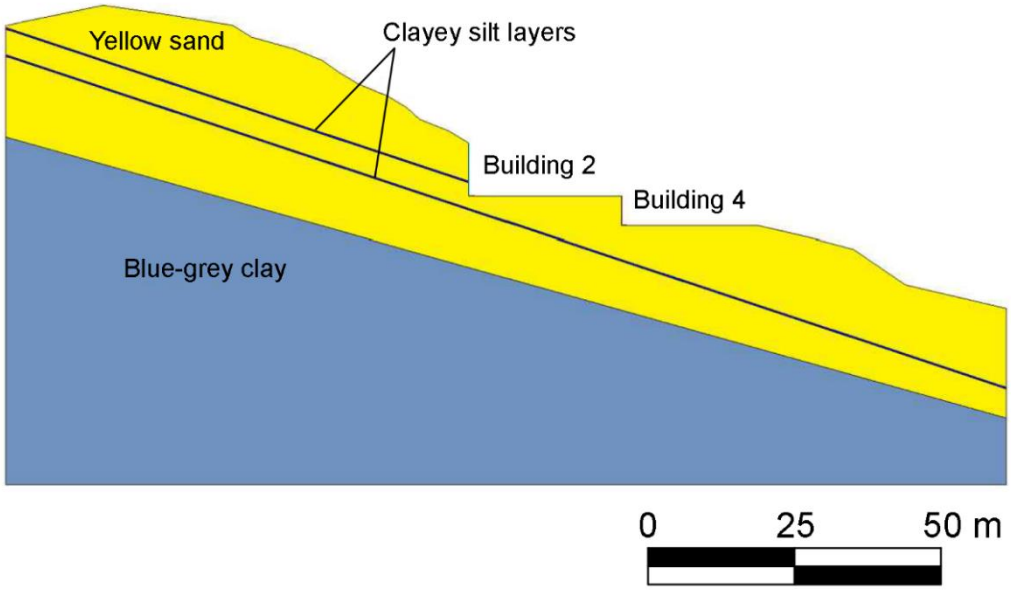

Figure 3.20 – Slope geometry and subsoil conditions used in the analyses carried out by Troncone et al. (2014), accounting for two layers of clayey silt

Since no groundwater level was detected during the investigation campaign, all soils are assumed dry in all the analyses described in the following sections.

Table 3.I – Soils parameters used in the analyses. Adapted from Troncone et al. (2014)

	γ $\left(\frac{kN}{m^3}\right)$	E' (MPa)	ν' $(-)$	c'_p (kPa)	φ'_p (°)	c'_r (kPa)	φ'_r (°)	ψ (°)	k^p_{shear} (%)	k^r_{shear} (%)
Yellow sand	20	70	0.25	37	43	0	34-35	0	0	4
Clayey silt	20	25	0.25	15	30	0	10.5-14	0	0	4
Blue-grey clay	20	70	0.25	150	31	-	-	0	-	-

3.7 – Slope stability analysis

Firstly, a traditional slope stability analysis is carried out by calculating the safety factor of the slope affected by the landslide. With this aim, two different approaches are used, i.e. the limit equilibrium method (LEM) and the finite element method (FEM). In both cases, the safety factor is assessed with referring to the model reported in Figure 3.19, i.e. accounting for only the layer of clayey silt where the main sliding surface developed (at an average depth of about 14 m from the ground surface). Since the involved soils are both characterized by a pronounced strain-softening behavior (Figure 3.13) and in order to give a first interpretation of the phenomenon, the safety factor is assessed with referring to both the peak and residual conditions. Obviously, the safety factor

is calculated with referring to the geometry corresponding to the post-excavation condition.

Regarding the use of the limit equilibrium method, the safety factor is evaluated within this research by using the method proposed by Morgenstern & Price (1965), with referring to a non-circular slip surface characterized by a shape and position as much as possible close to that observed in field. Moreover, since the landslide involved only the formation of sand and the interbedded layers of clayey silt, whereas the blue-grey clay was not involved, this latter formation is excluded from the model, for the sake of simplicity.

Therefore, the consequent model used for the computation of the safety factor, which derived from the model reported in Figure 3.19, with a representation of the sliding surface and the division of the unstable soil mass in different slices, in reported in Figure 3.21.

The safety factor obtained by using the peak strength parameters is SF = 1.97, whereas SF = 0.63 is obtained when the residual strength parameters are used. Particularly, since a range of values rather than a unique value for the angle of shearing resistance was found for both soils at residual condition, the safety factor was calculated using the values suggested by Troncone et al. (2014), i.e. φ_r' = 35° for the sand and φ_r' = 12° for the clayey silt. The other required parameters are those reported in Table 3.I.

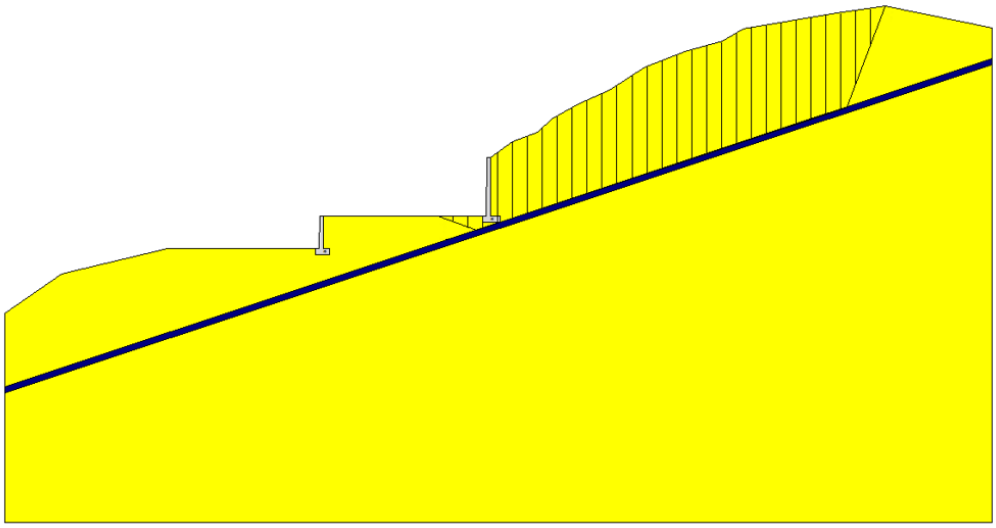

Figure 3.21 – Geometrical model used for the computation of the safety factor, with the indication of the sliding surface and the division of the unstable soil mass in different slices

Regarding the use of the finite element method, the safety factor is calculated by progressively reducing the shear strength parameters until the collapse of the slope is reached (Brinkgreve & Bakker (1991)). The calculation is performed by means of the software PLAXIS 2D (www.plaxis.com). In this approach, also known as *safety approach* or *phi-c reduction*, the shear strength parameters $\tan\varphi'$ and c' of the soil are successively reduced until failure of the system occurs.

The angle of dilation ψ is, in principle, not affected by the phi-c reduction procedure. Therefore, the safety factor calculated by the finite element method is defined according to Equation (3.1).

$$SF = \frac{\tan\varphi'_{input}}{\tan\varphi'_{reduced}} = \frac{c'_{input}}{c'_{reduced}} \qquad (3.1)$$

In Equation (3.1), the strength parameters with the subscript 'input' refer to the initial properties of the material whereas the

parameters with the subscript 'reduced' refer to the reduced values at the time of failure.

Within this context, the soil behavior is described with an elastic-perfectly plastic Mohr-Coulomb model with a non-associated flow rule and, as for the limit equilibrium method analyses, the calculations are carried out considering first the peak strength parameters and then those corresponding to the residual condition. Also in this case, the factor of safety is calculated with referring to a slip surface characterized with a shape and position as much as possible close to that actually observed. The correspondent volume of unstable soil mass and the mesh used in the analyses are reported in Figure 3.22.

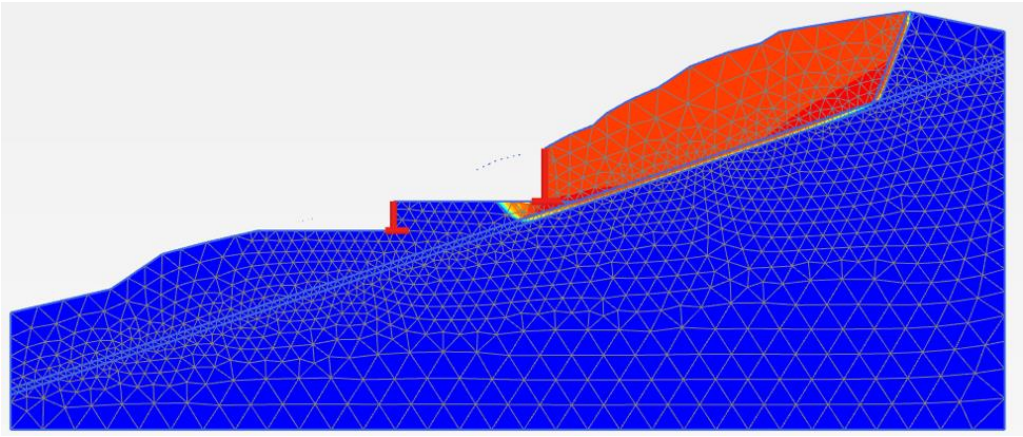

Figure 3.22 – Mesh used to calculate the safety factor with the indication of the unstable soil mass

The safety factor obtained by using the peak strength parameters is SF = 1.96, whereas SF = 0.72 is obtained when the residual strength parameters are used. Similar values were obtained from Troncone et al. (2014). It is worth noticing that the values of the

safety factor obtained using the finite element method are consistent with those previously obtained with the limit equilibrium method. In both cases, the safety factor is quite higher than unit when the peak strength parameters are used, whereas the slope is unstable when the residual strength parameters are considered. This means that, when the slope reached the failure ($SF = 1$), the operative values of the shear strength parameters were neither the ones corresponding to the peak nor the ones corresponding to the residual condition. Rather, the operative values were intermediate between the two situations. Based on these results and according to Bjerrum (1967), it can be asserted that a progressive failure occurred in the Senise slope.

The analyses above-discussed are suitable to assert that a phenomenon of progressive failure occurred, but nothing can be said about deformation mechanisms that occurred within the slope before and after failure. More advanced analyses were performed by Troncone (2005) and Troncone et al. (2014), who analyzed the pre-failure deformation mechanisms of such a landslide in both bi-dimensional and tri-dimensional conditions. The bi-dimensional analyses, performed by the afore-mentioned authors, will be summed up in this section, since their results represent the starting point for the analysis of the post-failure stage of this landslide, which is one of the goal of this dissertation. Instead, the tri-dimensional analysis performed by Troncone et al.

(2014) will not be mentioned, since it falls outside of the aims of this research.

Since a phenomenon of progressive failure occurred, the process can be successfully analyzed only using an approach that properly accounts for the brittle behavior of the involved soils, and which can reliably simulate the formation and development of the shear zones in the slope owing to the excavation. With this purpose, the abovementioned authors used an approach based on an elasto-viscoplastic constitutive model in conjunction with a Mohr-Coulomb model with strain-softening. The characteristics of this approach are described in Section 2.8. Particularly, regarding the strain-softening model, the used one is that proposed by Potts et al. (1990) (see Figure 2.14). The values of the parameters required to use the model are those reported in Table 3.I, including the threshold values k^p_{shear} and k^r_{shear}. The angle of dilation is assumed nil, i.e. a non-associated flow rule is employed. Shear strength parameters are those obtained from the laboratory tests previously described, whereas the elastic modulus *E'* and the threshold values of k_{shear} are deduced by Troncone (2005). Particularly, the values of the elastic modulus *E'* are deduced from the results of the available triaxial tests, considering the confining stresses that correspond approximately to those acting on average in the slope, whereas the values of k^p_{shear} and k^r_{shear} are established by matching the stress-strain

curves from the laboratory tests with those obtained numerically simulating these curves using the abovementioned approach. Besides, owing to the lack of specific experimental values, the Poisson's ratio is reasonably assumed 0.25. Finally, since the model is viscoplastic, other two constitutive parameters are required, as described in Section 2.8.6. These latter are $\bar{\gamma}$ and α. In order to simulate a rapid response of the slope to the excavation and consequently to reduce the time of analysis, typical values of $\bar{\gamma}$ and α for sand are assumed for both sand and clayey silt. Specifically, Troncone (2005) assumed $\bar{\gamma} = 10^{-6} s^{-1}$ and $\alpha = 61$. These values are similar to those deduced by di Prisco & Imposimato (1996) from some creep tests conducted on sand. It is worth noticing that, if different values of these parameters are used, the response of the slope to the excavation is only delayed or anticipated with time.

All the analyses cited in this section are performed using the finite element code Tochnog (www.tochnogprofessional.nl).

The analyses are initially performed with referring to the model accounting for only one layer of clayey silt (Figure 3.19). The mesh adopted is shown in Figure 3.23 and consists of triangular elements with three nodes and one Gauss point. The thickness of the thin clayey silt layer is assumed equal to 30 cm. Other simulations performed assuming a different thickness for this layer (50 and 100 cm) gave similar results. The initial stress state

of the slope (i.e. before the excavation) is simulated by using the well-known gravity loading procedure, under the assumption that the soil behaves as an elastic-perfectly plastic material with Mohr-Coulomb criterion, i.e. the strain-softening behavior is not accounted for in this stage of the calculation. At the end of the gravity loading, the associated displacements and strains are reset to zero. Then, the retaining walls are inserted in the subsoil with no change in the stress state of the slope, before carrying out the associated excavation. The main function of these structures is to support the vertical walls generated by the excavations, and consequently to prevent the occurrence of local failure in the slope. Indeed, the presence of retaining walls did not influence the slope response, considering that the slip surface developed below them and emerged just behind buildings 1 and 2, as observed by Del Prete and Hutchinson (1988). The retaining walls are modeled by using truss-beam elements with linear elastic behavior. The Young's modulus of these structures, E_c, is assumed equal to 28500 MPa, whereas their thickness is assumed equal to 80 cm. Besides, the height of each wall is equal to the depth of the respective excavation to be supported (Figure 3.17). Excavations are simulated by a progressive removal of the soil elements in front of the retaining walls. In order to account for the strain-softening behavior of both the yellow sand and the clayey silt, the elasto-viscoplastic constitutive model in conjunction with a Mohr-

Coulomb model with strain-softening described in Section 2.8 is adopted.

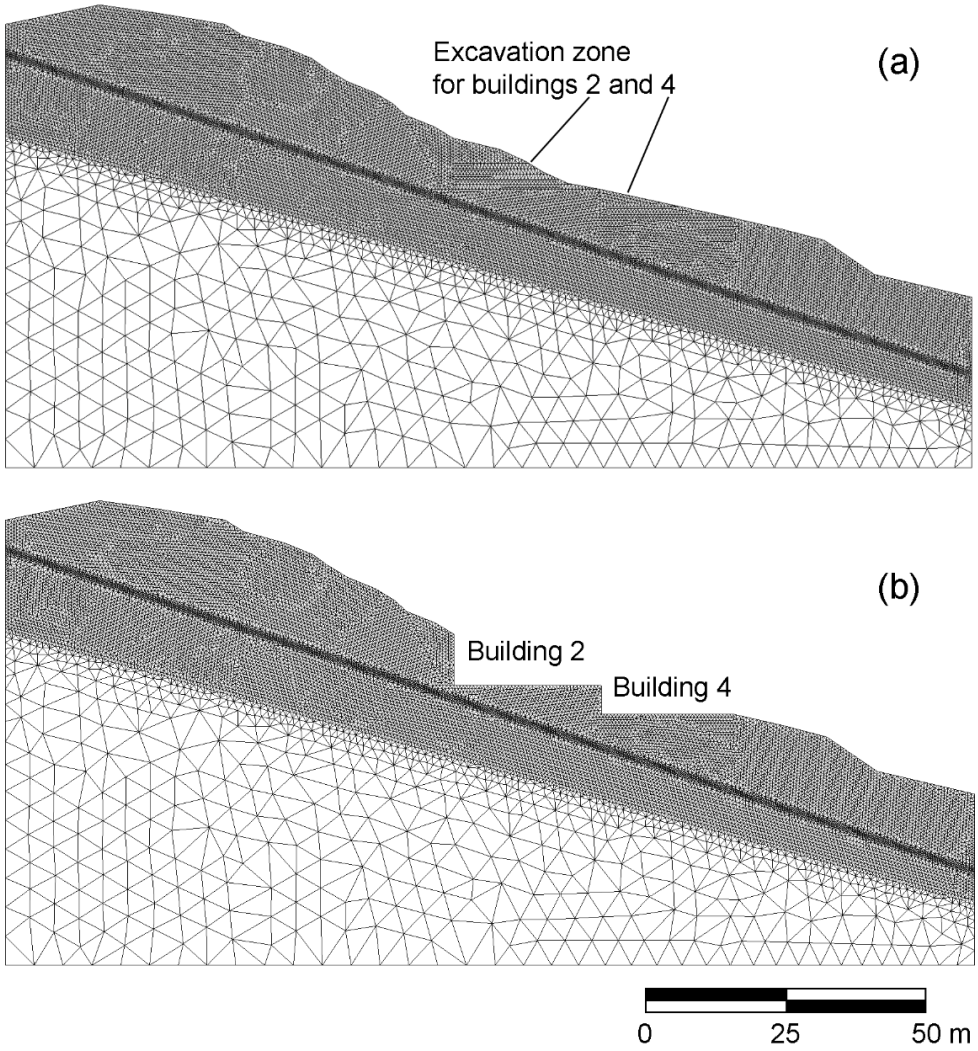

Figure 3.23 – Mesh adopted in the analyses: (a) before the excavation; (b) after the excavation

Since the landslide involved only the Aliano formation (Del Prete & Hutchinson (1988); Guerricchio & Melidoro (1988); Viggiani & Di Maio (1991)) and since specific data concerning the underlying blue-grey clay formation are not available, the behavior of this latter geological formation is assumed as elastic-perfectly plastic with the Mohr-Coulomb failure criterion, for the sake of simplicity.

After simulating the excavation by removing the respective elements, the induced displacements increase in magnitude and propagate upwards starting from the area surrounding the retaining wall behind building 2. At the final time of analysis (i.e. when the analysis stops due to the great distortions owing to the great displacements calculated) a large portion of the slope behind the retaining wall is affected by large displacements. Principal results are reported in Figure 3.24 and Figure 3.25.

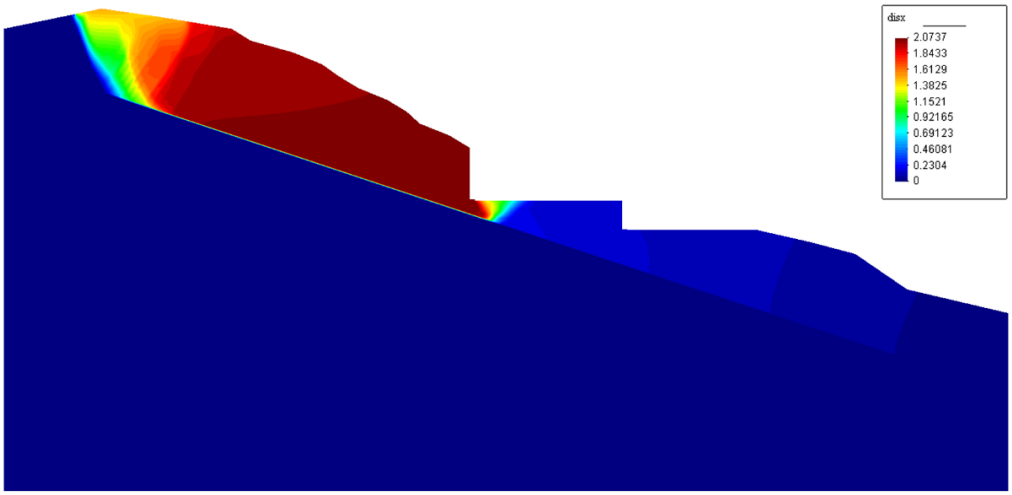

Figure 3.24 – Horizontal displacements calculated at the final step of the simulation carried out by Troncone et al. (2014)

Particularly, Figure 3.24 shows the horizontal displacements obtained at the end of the simulation, pointing out that a mechanism of general failure of the slope occurred. Additionally, Figure 3.25 shows the accumulated deviatoric plastic strains expressed by the parameter k_{shear} (Eq. (2.160)), highlighting that a shear zone characterized with high values of this latter parameters developed mainly in the clayey silt layer and partially

in the overlaying sand as well. The results reported in Figure 3.24 and Figure 3.25, which represent respectively the unstable soil mass and the slip surface, are satisfactorily in good agreement with the observations actually made in field. Indeed, the slip surface that actually developed into the slope is characterized by a shape and position close enough to that predicted by the numerical simulation.

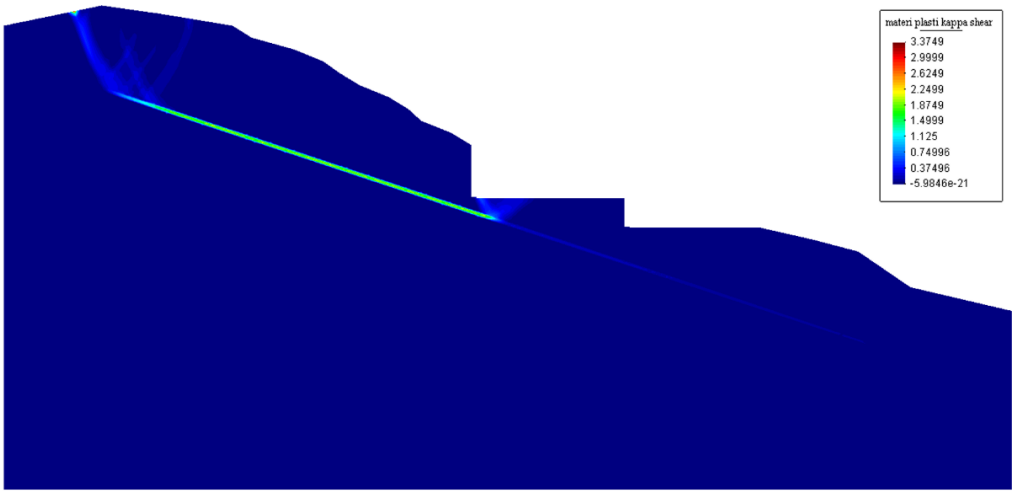

Figure 3.25 – Accumulated deviatoric plastic strain calculated at the final step of the simulation carried out by Troncone et al. (2014)

Further analyses are described by Troncone et al. (2014) in view of the interbedded nature of the Aliano formation. Particularly, such analyses are carried out considering the presence of two additional silt layers, located respectively above and below the unique silt layer considered in the simulation previously described. These two additional layers have the same characteristics of the other one concerning the thickness and the inclination. Regarding the position, the upper one is located at an average depth of 10.5 m from the ground surface, whereas the

lowest one is located at a depth of about 18 m. The obtained results show that the lowest silt layer is practically unaffected by deformations, therefore, for the sake of simplicity, this layer can be disregarded as shown in Figure 3.20. Results show that the soil mass involved in the landslide is essentially controlled by the silt layer located at an average depth of 14 m from the ground surface, where the main slip surface was observed in field. Further, a secondary slip surface develops in the upper silt layer. However, the unstable soil mass involved in the landslide remains unchanged. These results are consistent with the field observations documented by Del Prete and Hutchinson (1988). Besides, these results demonstrate that the presence of more additional layers of silt does not significantly affect the response of the slope to the excavations performed to allow the construction of the new buildings, since only the layer located at 14 m from the ground surface plays a key role in the pre-failure stage of this landslide.

Summarizing, the results obtained from the bi-dimensional analyses carried out by Troncone et al. (2014), accordingly to those performed by Troncone (2005), show that a progressive failure, related to the brittle behavior of the involved soils, occurred in the slope due to the deep excavations performed. Specifically, the failure started at the toe of the slope and

propagated upwards developing essentially in a thin layer of clayey silt, resulting in the collapse of the slope.

3.8 – Post-failure analysis of the landslide using MPM

The FEM analyses performed by Troncone (2005) and Troncone et al. (2014) gave a satisfactory interpretation of the pre-failure and failure stages of the Senise landslide, since the obtained results are pretty close to what actually observed during the field investigation. Indeed, the slip surface obtained from the numerical simulations is characterized by a shape and a position that are in good agreement with those actually observed and, consequently, the predicted volume of unstable soil mass represents well the volume of soil actually involved in the landslide. However, due to the excessive mesh distortion and the consequent loss of accuracy of the calculation, the calculated soil displacements after the development of the slip surface are considerably smaller than those actually detected after the landslide. Indeed, as can be seen from Figure 3.24, the maximum value of the predicted soil displacement is about 2 m, whereas the actual soil mass underwent an average displacement of about 30 m. This result points out the unsuitability of the finite element method for analyzing the deformation mechanisms that occur after the failure phase of a landslide. In order to overcome this drawback, the post-failure stage of the Senise landslide is

analyzed separately in this dissertation by the author using the Material Point Method. The analysis carried out can be meant as an extension of those performed by Troncone (2005) and Troncone et al. (2014). Consequently, the initial conditions of the MPM simulation correspond to the final conditions of the FEM simulation. This means that, in the initial condition of the MPM simulation, excavations have already been performed, slip surfaces have already developed, the unstable soil mass is already defined and structures (i.e. buildings and retaining walls) have already been built up. Therefore, the operative values of the shear strength parameters assumed in the analyses for the soil belonging to the slip surfaces and the unstable soil mass are those corresponding to the residual condition. This hypothesis is supported by the high values of accumulated plastic strains calculated by Troncone (2005) and Troncone et al. (2014). Furthermore, according to the field observations carried out by Del Prete & Hutchinson (1988) and Viggiani & Di Maio (1991), a tension crack was used to account for the graben observed by the above-mentioned authors. The tension crack was modeled with an elastic perfectly plastic material in conjunction with the Mohr-Coulomb failure criterion described in Section 2.8.4, and assuming a nil value for the angle of shearing resistance, the cohesion and the angle of dilation. In order to properly simulate the kinematics of the landslide and to catch in a sufficiently

precise way the final profile, several typologies of analysis are carried out:

- including only of the slip surface located at the depth of 14 m and disregarding the presence of structures;
- including both slip surfaces and disregarding the presence of structures;
- including both slip surfaces and accounting for the presence of structures.

Besides, since there are some uncertainties about the values of the residual friction angle for both sand and clayey silt (see Table 3.I), a parametric study is carried out as well, assuming different values for this latter parameter, chosen from the range obtained experimentally.

All analyses are carried out using the software Anura3D, developed by the Anura3D MPM Research Community (www.anura3d.com), with referring to the cross-section of trace A-A and indicated in Figure 3.18. The computational mesh is made up of tetrahedral elements with an average size of 1 m. Since MPM suffers from mesh dependency, this value of mesh size is selected based on a preliminary mesh sensitivity analysis. Particularly, the solution tends to converge when meshes with finer elements are used. Therefore, the element size chosen in this dissertation corresponds to maximum one showing consistent results, allowing also the computational effort to be reduced. The analyses

are performed under the hypothesis of plane-strain conditions, which are simulated by means of boundary conditions restricting out-of-plane deformations with referring to a thin slice of one element thickness. The thickness is equal to the size of one element in order to guarantee the regularity of the mesh as much as possible and, therefore, an optimal mesh discretization. Initially, four material points are distributed within each element. Since Anura3D uses an explicit-dynamic formulation to solve the calculation scheme (see Chapter 2), the critical time-step criterion defined by Equation (2.109) must be satisfied. Particularly, according to this expression, a value of the critical time-step $\Delta t_{crit} = 0.17\ s$ is obtained. Therefore, each analysis is carried out using a time-step $\Delta t = 0.10\ s$. Although in the analyses carried out by Troncone (2005) and Troncone et al. (2014) the layers of clayey silt were simulated with a thickness of 30 cm, a thickness of 1 m is used in this study, in order to reduce the computational costs. The initial stress state is simulated by using the well-known procedure of gravity loading (see Section 2.6.2), under the assumption that all materials behave elastically. The main reason of this choice is to avoid local instabilities in correspondence of the vertical cuts (especially when retaining walls are not accounted for) during the generation of the initial stress state. Since the gravity loading is a quasi-static problem, to accelerate the convergence to the quasi-static equilibrium and to avoid

unrealistic oscillations, a coefficient of local damping $\alpha = 0.75$ is used. This value is reduced to $\alpha = 0.05$ during the simulation of the post-failure stage, according to the indication provided in Section 2.6.3. After the initial stress state being generated, the analysis of the post-failure stage of the landslide is started by switching the materials behavior from elastic to elastic-perfectly-plastic in conjunction with the Mohr-Coulomb failure criterion described in Section 2.8.4 and a non-associated flow rule. Particularly, as already previously said, the residual shear strength parameters are assigned to all materials belonging to the slip surface and the unstable soil mass, whereas the peak strength parameters are assigned to the materials not involved in the landslide. Under these conditions, in the first calculation step after the gravity loading, the material points belonging to the unstable soil mass are not in equilibrium anymore, only due to the effect of gravity. Therefore, such material points start moving until a new condition of equilibrium is reached. Every analysis stops when there are no material points moving anymore, i.e. after each material point reaching its final position of equilibrium. The final configuration of material points defines the numerical post-failure profile that needs to be compared to that actually detected in field. Indeed, such analysis is encouraged by the availability of accurate information regarding the geometry before and after the collapse. A comparison between the geometry detected before and

after the collapse with referring to the cross-section of trace A-A (Figure 3.18) is shown in Figure 3.26.

Besides, a further analysis is performed by accounting for the strain-softening behavior of the yellow sand formation. The reason why this analysis is performed is that, as already said, in the analyses of the pre-failure and failure phases performed by Troncone (2005) and Troncone et al. (2014), extremely high values of the accumulated deviatoric plastic strain are obtained.

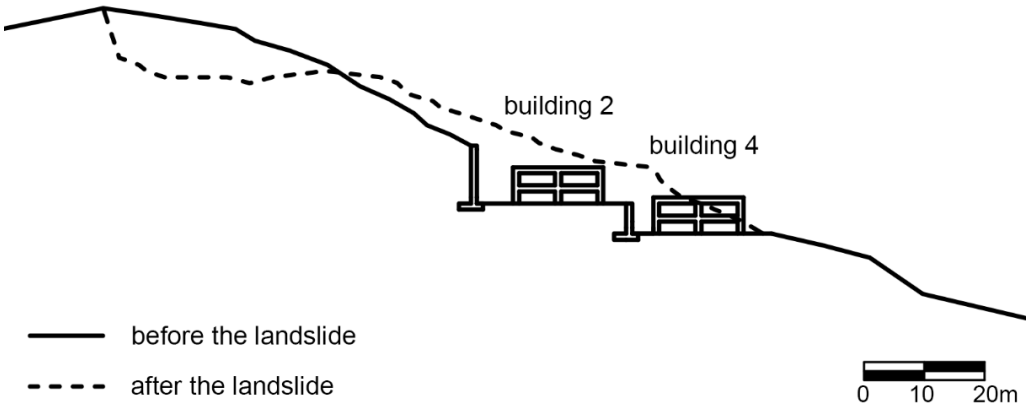

Figure 3.26 – Topographic profile of section A-A before and after the landslide (the trace of section A-A is indicated in Figure 3.18)

However, these values refer only to the slip surface, which develops within the clayey silt layer and only partially in the yellow sand, whereas almost the whole landslide body displaced like a rigid body, i.e. without undergoing any deformation, in the simulation performed by Troncone et al. (2014). Therefore, at the beginning of the post-failure stage, this soil should be at the peak condition and only during the deformation process the shear strength should decrease until the residual condition is reached. This transitory condition is neglected in all the other analyses,

because it should not significantly affect the final results as well as for saving up computational time. However, for the sake of completeness, the strain-softening behavior of the formation involved in the landslide body is accounted for in this last analysis, in order to proof that the same results can be obtained by assigning the residual strength parameters directly from the beginning of the post-failure stage, allowing a decisively faster simulation to be performed.

3.8.1 – Analysis with one slip surface without existing structures

The first typology of analysis carried out in this research, whose input geometry is reported in Figure 3.27, is the extension of the analysis performed by Troncone (2005) and of the first analysis performed by Troncone et al. (2014).

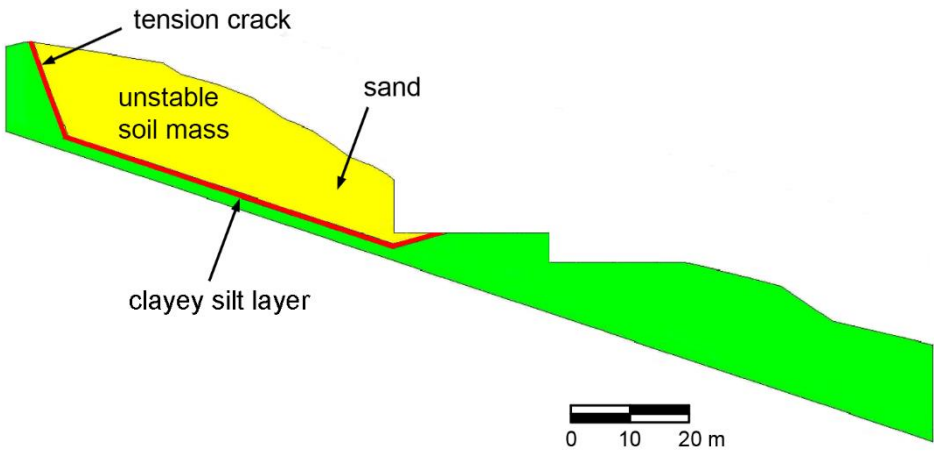

Figure 3.27 – Input geometry for the analysis performed accounting for only the main slip surface

Therefore, the unstable soil mass (already existing) is defined by a unique block made up of yellow sand, which is separated from the stable soil by the slip surface (already developed) that was found in correspondence of a layer of clayey silt at an average depth of 14 m from the ground surface (Figure 3.27). The computational mesh used in the analyses is reported in Figure 3.28. A first analysis is performed using the shear strength parameters assumed by Troncone (2005) and Troncone et al. (2014). Particularly, the assumed values of the residual angle of shearing resistance are $\varphi_r' = 35°$ for the sand and $\varphi_r' = 12°$ for the clayey silt. The other parameters are reported in Table 3.I.

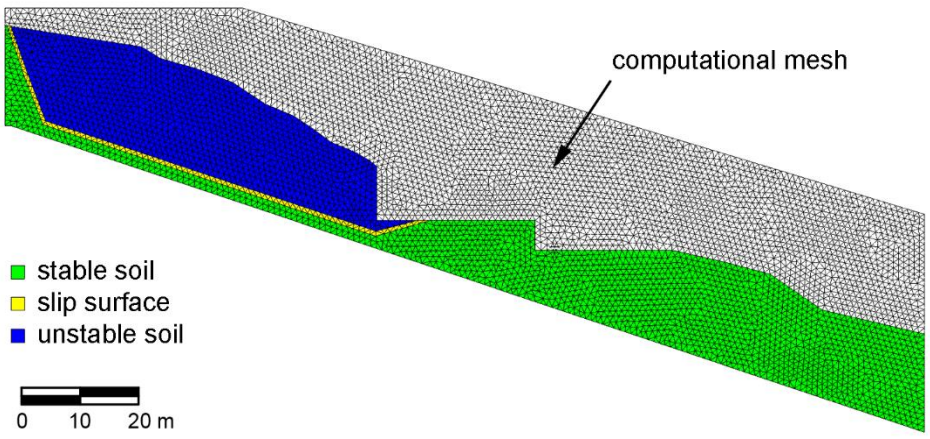

Figure 3.28 – Computational mesh used in the analysis performed accounting for only the presence of the main slip surface

A comparison between the post-failure profile detected after the event and the final configuration of material points after reaching a new condition of equilibrium (i.e. when the velocity of each material point is nil) is reported in Figure 3.29.

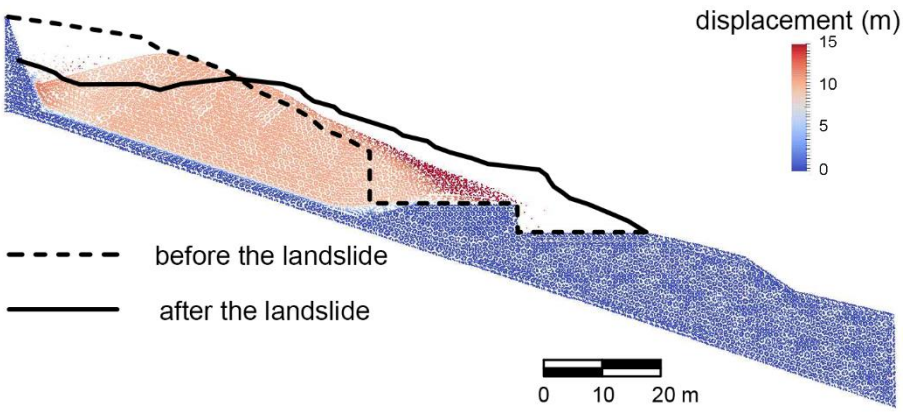

Figure 3.29 – Comparison between the post-failure profile detected after the event and the final configuration of material points, accounting for only the main slip surface and assuming the following values for the residual angle of shearing resistance: $\varphi_r' = 35°$ for the sand and $\varphi_r' = 12°$ for the clayey silt

As can be seen, there is no agreement at all between the measured and calculated post-failure profiles. Besides, the calculated displacement in the body of landslide is on the order of about 13 m against a measured value of about 30 m.

Therefore, it can be asserted that although such a geotechnical model is suitable for satisfactorily predicting the trigger phase of the Senise landslide, it fails when the post-failure phase is analyzed.

However, since lower values of the residual angle of shearing resistance were obtained from laboratory tests (Del Prete& Hutchinson (1988); Viggiani & Di Maio (1991); Table 3.I), another simulation is carried out as well, using these latter values of the shear strength parameters.

Particularly, the values of the residual angle of shearing resistance are $\varphi_r' = 34°$ for the sand and $\varphi_r' = 10.5°$ for the clayey silt. A comparison between the post-failure profile detected after

the event and the final configuration of material points at the end of this latter simulation is reported in Figure 3.30.

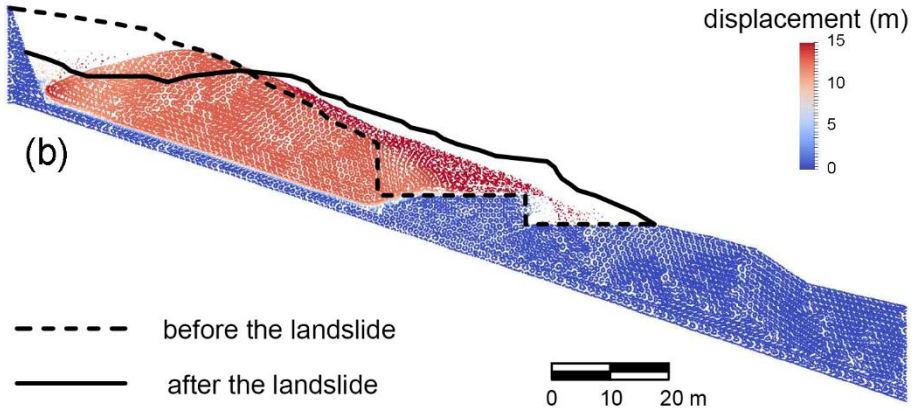

Figure 3.30 - Comparison between the post-failure profile detected after the event and the final configuration of material points, accounting for only the main slip surface and assuming the following values for the residual angle of shearing resistance: $\varphi_r' = 34°$ for the sand and $\varphi_r' = 10.5°$ for the clayey silt

Although displacements of material points are greater than those calculated in the previous analysis (15 m on average), there still is an unacceptable disagreement between the measured and calculated post-failure profiles.

Consequently, it can be asserted that even though the lowest values of the shear strength parameters obtained experimentally are used, the model accounting for only the main slip surface is not suitable for satisfactorily simulating the kinematics of the Senise landslide after the collapse.

3.8.2 – Analysis with two slip surfaces without existing structures

Based on the two analyses described in the previous section, it can definitely be asserted that the secondary sliding surface, found by Del Prete & Hutchinson (1988) at an average depth of 10.5 m from the ground surface, must be accounted for as well in the analysis in order to properly simulate the post-failure stage of the Senise landslide. Therefore, with this purpose, the unstable soil mass, already existing and made up of yellow sand, is split up into two different blocks, which are separated from one another by the secondary slip surface at the average depth of 10.5 m from the ground surface.

Besides, the whole unstable soil mass is separated from the stable soil by the main slip surface at the average depth of 14 m from the ground surface. As previously said, both slip surfaces are located in correspondence of thin layers of clayey silt and are already developed when the initial stage of the analysis is started. The geometry described is shown in Figure 3.31, whereas the computational mesh is reported in Figure 3.32. In the first analysis performed, the upper limits of the residual angle of shearing resistance reported in Table 3.I are assumed.

In particular, the value $\varphi_r' = 35°$ for the sand is the one considered in the analysis carried out by Troncone (2005) and Troncone et al. (2014), whereas the value $\varphi_r' = 14°$ for the clayey silt is the greater

value of the residual angle of shearing resistance found experimentally (Viggiani & Di Maio (1991)).

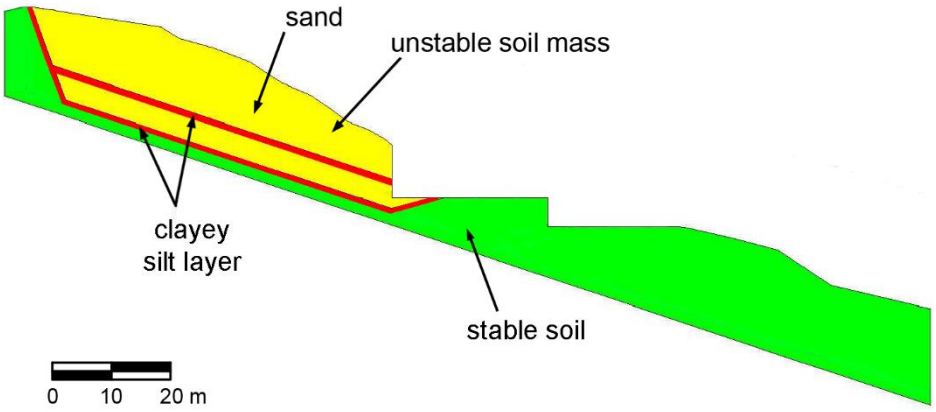

Figure 3.31 - Input geometry for the analysis performed accounting for both slip surfaces

A comparison between the post-failure profile detected after the event and the final configuration of material points at the end of this simulation is reported in Figure 3.33.

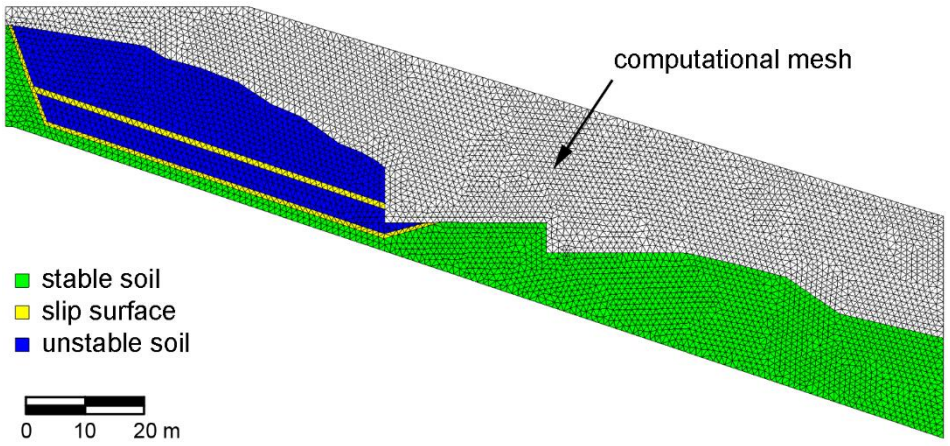

Figure 3.32 – Computational mesh used in the analysis performed accounting for both slip surfaces

By comparing the results reported in Figure 3.33 with those reported in Figure 3.29 and Figure 3.30, it is possible to observe that the agreement between prediction and observation is better when the secondary slip surface is accounted for as well. In this

case, indeed, due to the presence of this further sliding surface, the body of landslide is subdivided into two parts that undergo relative displacements from one another.

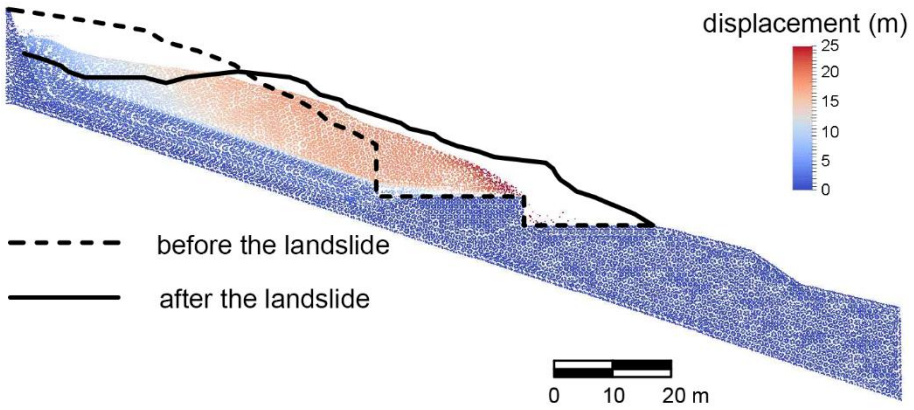

Figure 3.33 – Comparison between the post-failure profile detected after the event and the final configuration of material points, accounting for both slip surfaces and assuming the following values for the residual angle of shearing resistance: $\varphi_r' = 35°$ for the sand and $\varphi_r' = 14°$ for the clayey silt

Therefore, the calculated displacements of the upper part of the landslide body are higher than the previous cases. Particularly, the average value of the calculated displacement is higher than 20 m. However, although the results presented in Figure 3.33 are better than those obtained in Section 3.8.1, there still is a relevant difference with the displacements actually detected in field (which are on the order of about 30 m). Furthermore, the calculated post-failure profile is more similar to the measured one if compared to those obtained accounting for only the main slip surface, but there still are some discrepancies with the detected one, which can be attributed to the upper limit of the residual strength parameters assumed in this analysis. In particular, the value of the residual angle of shearing resistance of the clayey silt (φ_r' =

14°) tends to restrain the displacements of material points, which cannot reach the excavation on the right side of the model, which was actually totally buried. Therefore, a second analysis is performed. Particularly, the residual angle of shearing resistance is kept unchanged for the sand (i.e. $\varphi_r' = 35°$), whereas the value $\varphi_r' = 12°$ is assumed for the clayey silt (instead of $\varphi_r' = 14°$). It is worth noticing that this set of shear strength parameters is the same of that used by Troncone (2005) and Troncone et al. (2014). A comparison between the post-failure profile detected after the event and the final configuration of material points at the end of this latter simulation is reported in Figure 3.34.

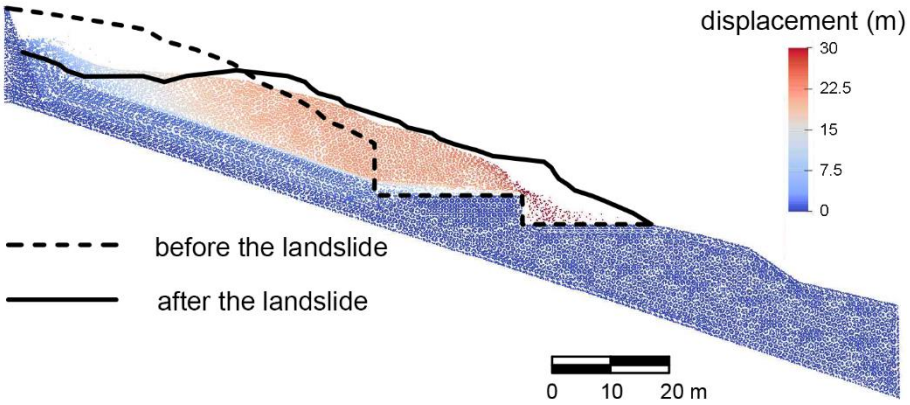

Figure 3.34 – Comparison between the post-failure profile detected after the event and the final configuration of material points, accounting for both slip surfaces and assuming the following values for the residual angle of shearing resistance: $\varphi_r' = 35°$ for the sand and $\varphi_r' = 12°$ for the clayey silt

As expected, material points undergo greater displacements than those of the simulation whose results are reported in Figure 3.33. Indeed, the maximum value of the calculated displacement for some material points is about 30 m. However, this value is limited only to a small portion of the body of landslide, whereas almost

the whole upper part of the landslide body is subjected to an average displacement of about 23 m, against 30 m actually detected in field.

Furthermore, the agreement between the measured and calculated post-failure profiles begins now to be satisfactory. Indeed, some material points reach also the excavation on the right side of the model. However, some discrepancies still keep on persisting between the measured and calculated post-failure profiles in this part of the model. Therefore, in an attempt to improve the analysis, a last simulation is performed by assuming the lowest values of the residual angle of shearing resistance obtained experimentally for both soils, i.e. $\varphi_r' = 34°$ for the sand and $\varphi_r' = 10.5°$ for the clayey silt. A comparison between the post-failure profile detected after the event and the final configuration of material points at the end of this latter simulation is reported in Figure 3.35.

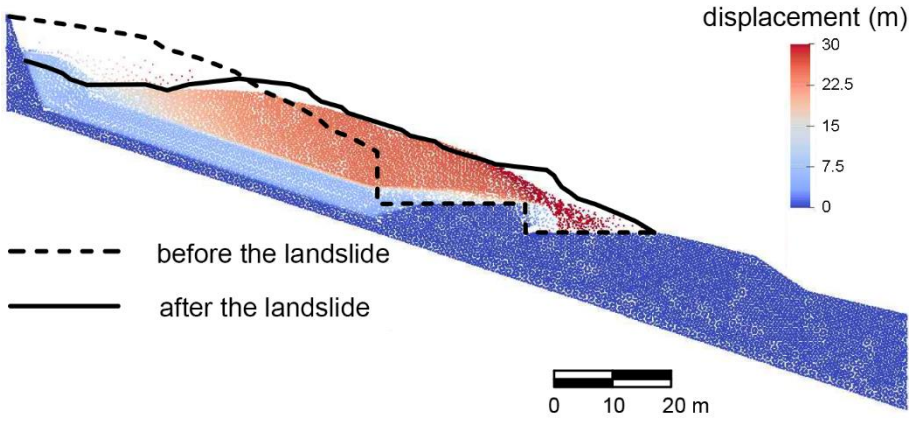

Figure 3.35 – Comparison between the post-failure profile detected after the event and the final configuration of material points, accounting for both slip surfaces and assuming the following values for the residual angle of shearing resistance: $\varphi_r' = 34°$ for the sand and $\varphi_r' = 10.5°$ for the clayey silt

As can be seen from such a figure, this latter simulation allows reasonably good results to be obtained. Indeed, the average displacement of material points in the part of the landslide body above the secondary slip surface is comparable to that detected in field (about 30 m). Moreover, the calculated post-failure profile reasonably matches the measured one. The maximum difference between the predicted and detected profiles is just on the order of few meters. This happens also because, due to the low values of the residual strength parameters, material points are able to reach the area of the excavation on the right side of the model, burying the excavation plane, according to what actually observed. Summarizing, the results of the analyses described in this section point out that the slip surface located in the upper clayey silt layer, which was not recognized important in the previous studies concerning the trigger phase of this landslide (Troncone (2005); Troncone et al. (2014)), played instead a paramount role in the post-failure stage of the Senise landslide.

3.8.3 – Analysis with two slip surfaces and existing structures

Although the analysis whose results are reported in Figure 3.35 can be considered a satisfactory simulation of the post-failure stage of the Senise landslide, it is considered worthwhile enhancing the analyses discussed in the previous sections in order to reduce the existing discrepancies between numerical

results and field measurements as well as to reduce the gap between the numerical model the and the real problem. With this aim, the model discussed in Section 3.8.2 is improved by accounting for the presence of structures as well. Particularly, the buildings indicated with the numbers 2 and 4 in Figure 3.3 as well as the retaining walls built up behind such structures are taken into account. Each building is represented in an approximate manner by a 15 m-wide and 6 m-high reinforced concrete frame. According to the hypothesis of plane-strain conditions, all structures are continuous in the direction normal to the considered cross-section. The retaining walls are characterized by a thickness of 1 m, whereas the height is 9 m for the upper wall and 5 m for the lower one, according to the analysis performed by Troncone et al. (2014). All structures are modeled by means of linear elastic elements during the generation of the initial stress state, analogously to the other materials. Afterwards, during the simulation of the post-failure stage, the behavior of structures is switched from linear elastic to elastic-perfectly plastic in conjunction with the Mohr-Coulomb failure criterion, with a non-associated plastic flow rule. The parameters used in the analyses are obtained by considering opportune Mohr's circles and assuming that buildings and retaining walls are made up of masonry and reinforced concrete, respectively (Table 3.II). The material properties indicated in Table 3.II are the unit weight γ,

Young's modulus E, Poisson's ratio υ, the tensile strength σ_t and the strength parameters c and φ. Since the constitutive model is the Mohr-Coulomb one, the dilation angle ψ is required as well, but it is obviously assumed nil for structural materials.

Table 3.II –Parameters of structural elements used in the analyses

	γ $\left(\frac{kN}{m^3}\right)$	E (MPa)	ν $(-)$	c (kPa)	φ (°)	σ_t (kPa)	ψ (°)
Retaining walls	24	70	0.20	4400	55	2800	0
Buildings	8	70	0.20	440	55	280	0

It is worth noticing that the numerical value of Young's modulus is considerably smaller than the real value of both concrete and masonry. It actually is the same stiffness of the yellow sand formation. The main reason of this choice is that a strong difference of stiffness between the materials involved in the model leads to a much more expensive simulation in terms of computational costs. Besides, the aim of this research is not to study the structural behavior of buildings and retaining walls, rather to analyze their influence on the kinematics of the body of landslide after the collapse. In other words, the aim of such structures in the analyses is simply to simulate an obstacle which the unstable soil mass found on its path during the post-failure stage of the landslide. As pointed out by Del Prete & Hutchinson (1988) and Viggiani & Di Maio (1991), such structures were tore

down and partially buried by the displaced soil mass during the post-failure stage of the landslide. The failure of these structures is simulated by reducing the parameters c, φ and σ_t from their initial values (Table 3.II) to an artificial final value. For the sake of simplicity, the final value of the cohesion, c, and tensile strength, σ_t, are assumed to be zero, whereas the final value of the friction angle is assumed to be the same of the residual angle of shearing resistance of the sand. The reduction of such parameters is imposed in the simulation after reaching a threshold deformation value in the structural elements. Particularly, this threshold value is assumed to be reached when the difference of displacement between the top and the bottom of each structure is equal to about 80 cm for retaining walls and about 20 cm for buildings.

However, other attempt simulations proved that any reasonable choice of these thresholds (as well as the structural parameters) does not affect the results presented in the following. The geometrical model used in the analyses is the same of that shown in Figure 3.31, with the addition of structures (Figure 3.36). The associated computational mesh is shown in Figure 3.37. Analogously to the analyses described in Section 3.8.2, a parametric study is carried out by assuming different values of the residual angle of shearing resistance for the soils included in the landslide body. In the first analysis, a residual angle of

shearing resistance φ_r' = 35° is assumed for the sand whereas the value φ_r' = 14° is assumed for the clayey silt.

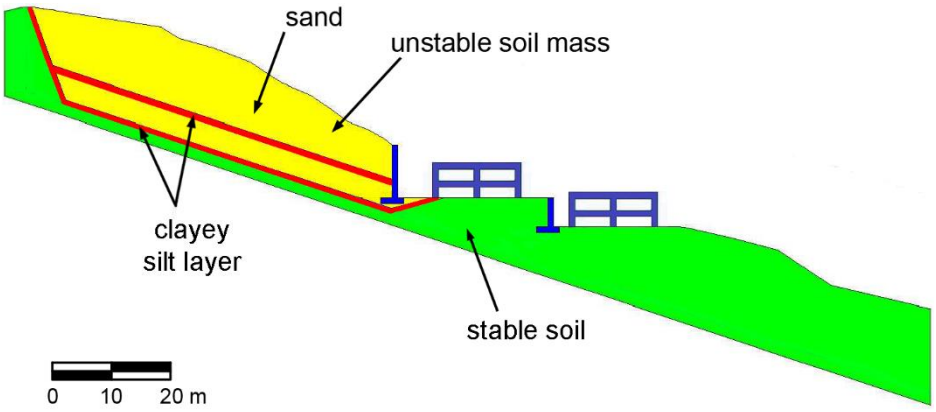

Figure 3.36 – Input geometry for the analysis performed accounting for both slip surfaces as well as structures

The comparison between the post-failure profile detected after the event and the final configuration of material points at the end of the simulation is reported in Figure 3.38.

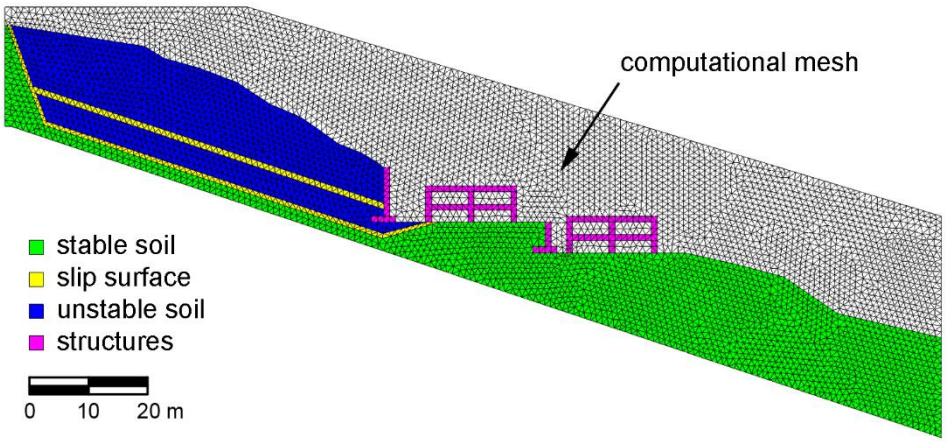

Figure 3.37 – Computational mesh used in the analysis performed accounting for both slip surfaces as well as structures

As can be seen, since structures represent an obstacle for the body of landslide, the average displacement calculated in this

latter analysis is reduced respect to the same case without accounting for the presence of structures (Figure 3.33).

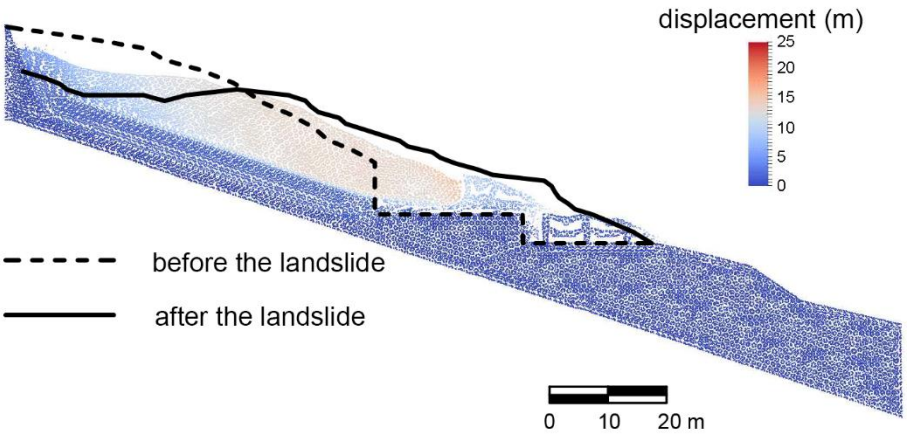

Figure 3.38 – Comparison between the post-failure profile detected after the event and the final configuration of material points, accounting for both slip surfaces and structures, and assuming the following values for the residual angle of shearing resistance: $\varphi_r' = 35°$ for the sand and $\varphi_r' = 14°$ for the clayey silt

Indeed, the calculated average displacement is less than 20 m and, consequently, the discrepancies between the calculated and measured post-failure profiles are more remarkable than the case without structures, especially upstream. Instead, the agreement between calculated and measured profiles is now better downstream, owing to the presence of the debris resulting from the destroyed buildings.

In the second analysis, the residual angle of shearing resistance is kept $\varphi_r' = 35°$ for the sand, whereas the value $\varphi_r' = 12°$ is assumed for the clayey silt (instead of $\varphi_r' = 14°$). It is worth noticing that these are the parameters used by Troncone (2005) and Troncone et al. (2014). The comparison between the post-failure profile detected after the event and the final configuration

of material points at the end of this latter simulation is reported in Figure 3.39.

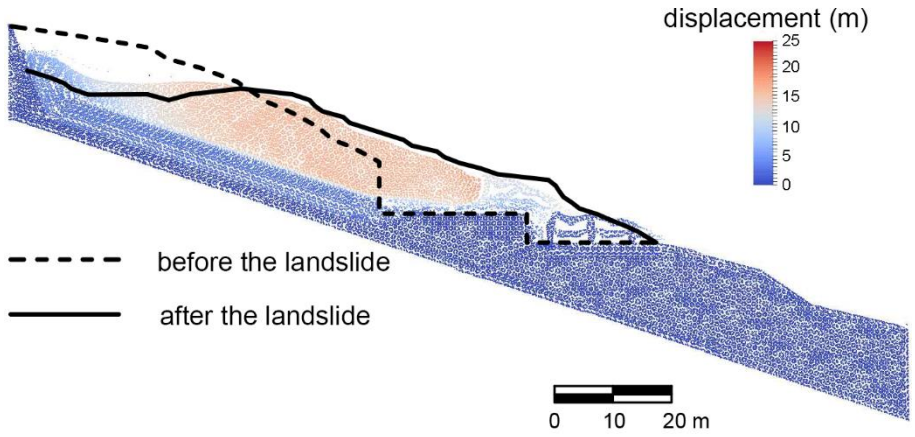

Figure 3.39 – Comparison between the post-failure profile detected after the event and the final configuration of material points, accounting for both slip surfaces and structures, and assuming the following values for the residual angle of shearing resistance: $\varphi_r' = 35°$ for the sand and $\varphi_r' = 12°$ for the clayey silt

Contrary to the previous case, the obtained results represent a good interpretation of the phenomenon. Indeed, the average calculated displacement is on the same order of that reported in Figure 3.34; besides the agreement between numerical and measured post-failure profiles can be considered satisfying. Finally, analogously to the case without accounting for the presence of structures, a last simulation is performed by assuming the lowest values of the residual angle of shearing resistance obtained experimentally, i.e. $\varphi_r' = 34°$ for the sand and $\varphi_r' = 10.5°$ for the clayey silt. A comparison between the post-failure profile detected after the event and the final configuration of material points at the end of this latter simulation is reported in Figure 3.40.

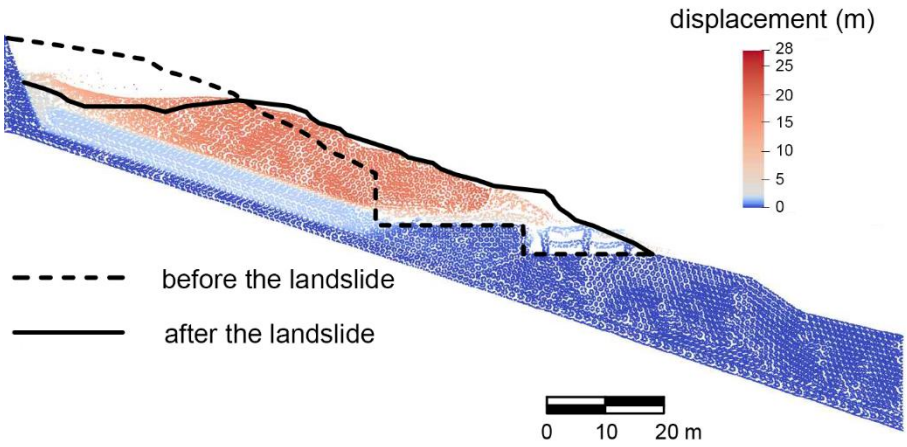

Figure 3.40 – Comparison between the post-failure profile detected after the event and the final configuration of material points, accounting for both slip surfaces and structures, and assuming the following values for the residual angle of shearing resistance: $\varphi_r' = 34°$ for the sand and $\varphi_r' = 10.5°$ for the clayey silt

Among all the analyses performed, this latter is the one which provides the best results, both in terms of average displacement and agreement between measured and calculated post-failure profiles. Indeed, the upper part of the body of landslide undergoes an average displacement on the order of about 28 m, which is pretty close to the value of 30 m measured by Del Prete & Hutchinson (1988) and Viggiani & Di Maio (1991). Further, the calculated post-failure profile matches satisfactorily the measured one, even better than the same analysis without accounting for the presence of structures (Figure 3.35).

These results confirm that the operative values of the residual shear strength parameters of both sand and clayey silt are the lowest limit obtained experimentally. Furthermore, they highlight the influence that structures had on the kinematics of the Senise landslide.

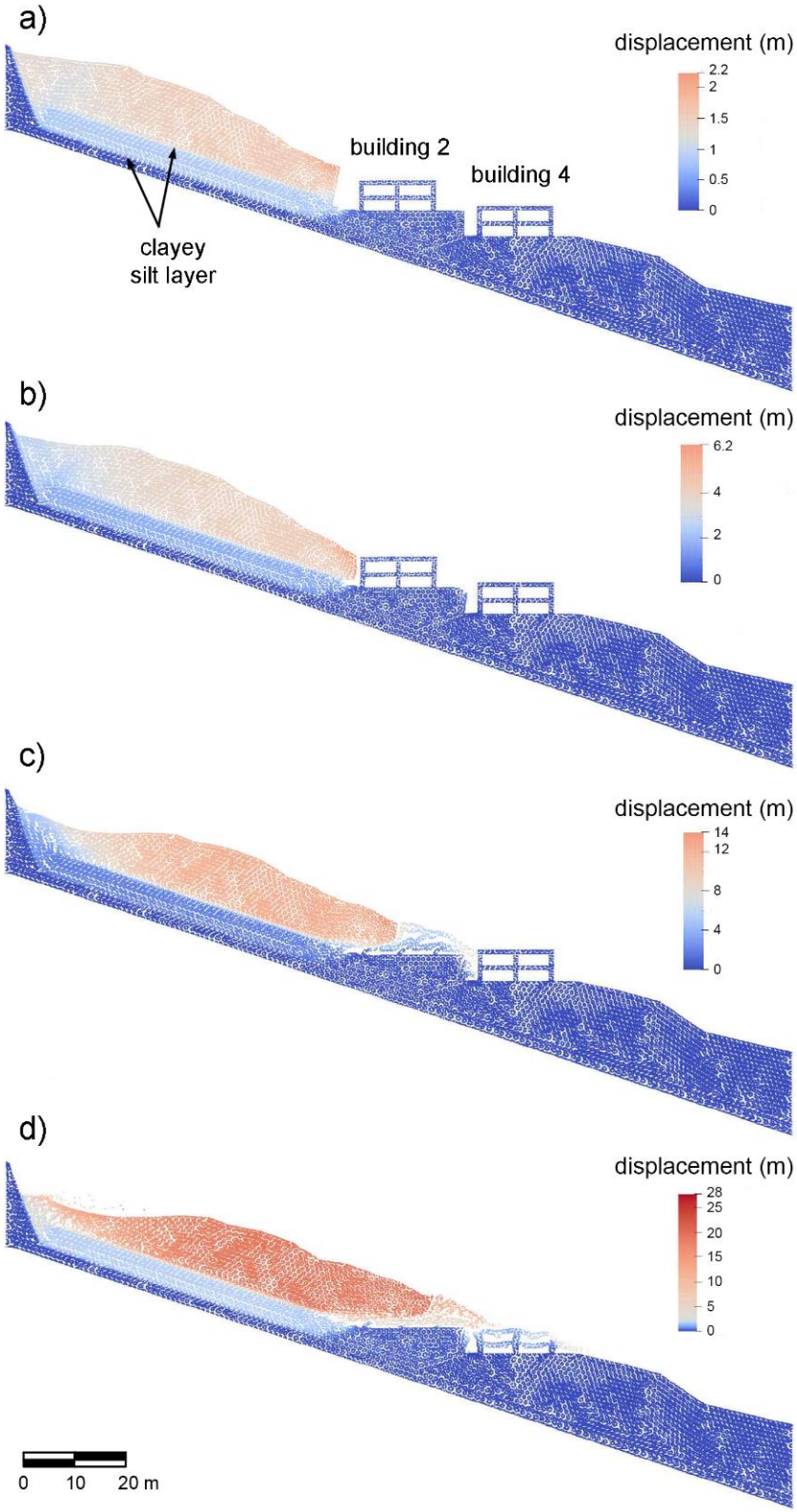

Figure 3.41 – Evolution of displacements of material points for different time steps of the simulation (assuming φ_r' = 34° for the sand and φ_r' = 10.5° for the clayey silt): a) t = 1.5 s; b) t = 2.5 s; c) t = 5 s; d) t = 12 s (final configuration)

For the sake of completeness, Figure 3.41 reports the landslide kinematics. In particular, this figure shows the evolution of the Senise landslide at different times, from a configuration immediately after failure (Figure 3.41a) to the final one (Figure 3.41d). Moreover, it is worth noticing that the analysis is able to simulate the translational typology of the landslide as well. Indeed, in the post-failure stage, after the deformation mechanisms occurred during the pre-failure one, the unstable soil mass moved like a rigid body above the slip surfaces, which the sliding occurred above. This observation is supported by the results reported in Figure 3.42 and Figure 3.43. Particularly, Figure 3.42 shows the evolution of both displacement and velocity for two different points arbitrarily chosen on the ground surface. The maximum velocity is on the order of 3–4 m/s and the time elapsed from start to stop of the motion is approximately 9s, which is consistent with the short time in which the landslide occurred (8 people died owing to the sudden collapse of their houses). The translational character of the landslide is pointed out by the fact that the curves related to both points A and B are practically superimposable, both for displacement and velocity. Besides, as shown in Figure 3.43, the calculated horizontal displacement profile is practically constant with the depth, except in correspondence of the secondary slip surface (that in correspondence of the vertical that this profile refers to is at a

depth of about 11 m from the ground surface) where a jump is observed. This means that the body of landslide is subdivided into two blocks, which slid like rigid bodies but whose displacements are characterized by different intensities. All these results are consistent with the results of the field investigation carried out by Del Prete & Hutchinson (1988) and Viggiani & Di Maio (1991).

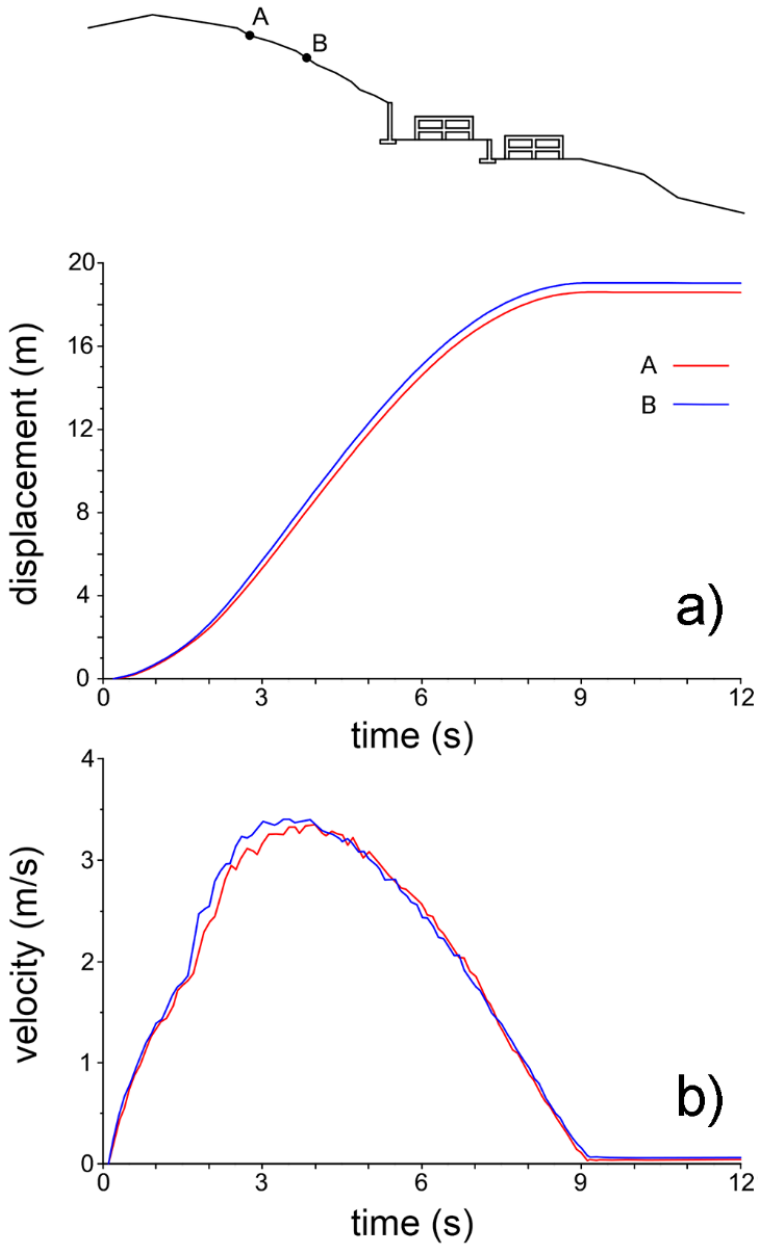

Figure 3.42 – Evolution of a) displacement and b) velocity of two point located on the ground surface of the slope

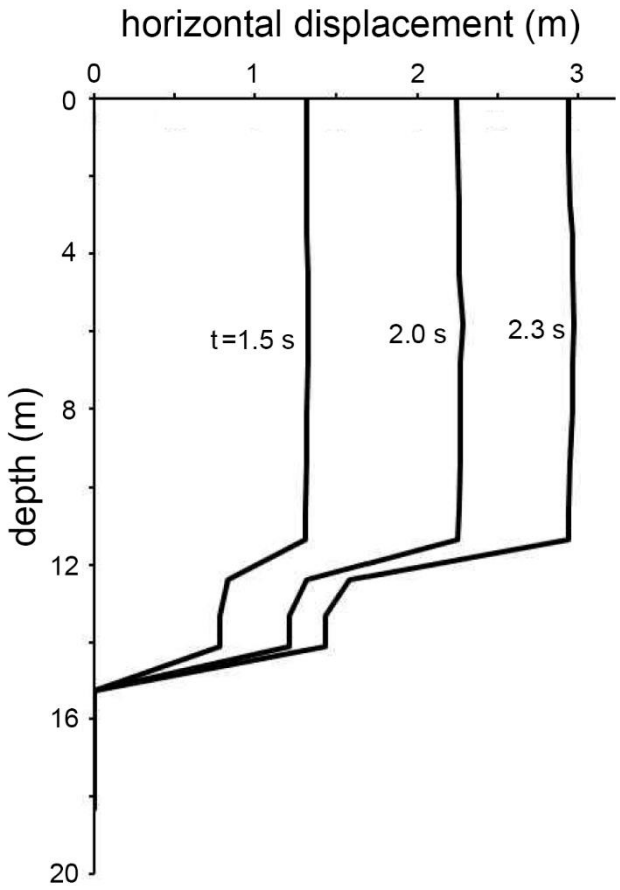

Figure 3.43 – Calculated horizontal displacement of material with depth for different time steps of the simulation, with referring to the vertical line passing for the point A shown in Figure 3.42

3.8.4 – Strain-softening analysis

As already pointed out, the simulation of the post-failure stage of the Senise landslide presented in this research is meant as the extension of the analysis of the pre-failure and failure phases previously carried out by Troncone (2005) and Troncone et al. (2014). Therefore, the initial condition of the analysis of the post-failure stage should be the same of the final condition of the above-mentioned analyses (see Section 3.8). The soil belonging to the slip surface is undoubtedly at residual, due to the extremely

high values of accumulated deviatoric plastic strain, as proved by Troncone (2005) and Troncone et al. (2014) (see Section 3.7). On the other hand, the soil above the slip surface, i.e. the one belonging to the landslide body, is characterized by a nil value of the accumulated deviatoric plastic strain at the time of failure (Troncone (2005); Troncone et al. (2014)), therefore, it actually is at the peak condition at the beginning of the post-failure stage. However, according to the previous studies concerning the Senise landslide (Del Prete & Hutchinson (1988); Guerricchio & Melidoro (1988); Viggiani & Di Maio (1991)), the landslide body was undergone an average displacement of about 30 m. In this condition, the soil belonging to the landslide body must have undoubtedly been at residual, analogously to the soil belonging to the slip surface. This means that a transitional phase occurred, in which the shear strength parameters of the soil belonging to the landslide body were undergone a deterioration process from the peak to the residual condition. However, all the analyses presented in the previous sub-sections are performed by assigning the residual strength parameters at the soil belonging to the landslide body from the beginning of the simulation of the post-failure stage. This assumption corresponds to the implicit hypothesis that the transition from peak to residual occurred in a short time period, which can be neglected. Since the results obtained under this assumption are in good agreement with field

observations (Figure 3.35 and Figure 3.40), this hypothesis can be considered satisfied. However, for the sake of completeness and to proof the truthfulness of the above-discussed hypothesis, a further simulation is carried out accounting for the strain-softening behavior of the soil belonging to the body of landslide as well. Particularly, the analysis is performed accounting for the presence of both slip surfaces, whereas structures are not taken into account. Therefore, this analysis can be seen as an extension of those presented in Section 3.8.2.

The input geometry is analogous to that shown in Figure 3.31, then both slip surfaces, located respectively at an average depth of 14 m and 10.5 m from the ground surface, are considered so that the unstable soil mass is split up into two different blocks. The only difference with respect to the problem shown in Figure 3.31 is represented by the behavior of the involved materials. Particularly, as shown in Figure 3.44, the clayey silt layers (red in Figure 3.44) and the stable soil (green in Figure 3.44) behave according to an elastic perfectly plastic law in conjunction with the Mohr-Coulomb failure criterion and a non-associated flow rule (Section 2.8.4). Specifically, the residual strength parameters are assigned to the clayey silt layers, whereas the ones corresponding to the peak are assigned to the stable soil (Table 3.I). On the contrary, the yellow sand formation, which represents the unstable soil mass, is assumed to be an elastic perfectly plastic

material with strain-softening (see Section 2.8.5) in conjunction with the Mohr-Coulomb failure criterion and a non-associated flow rule (Equations (2.161) and (2.162)).

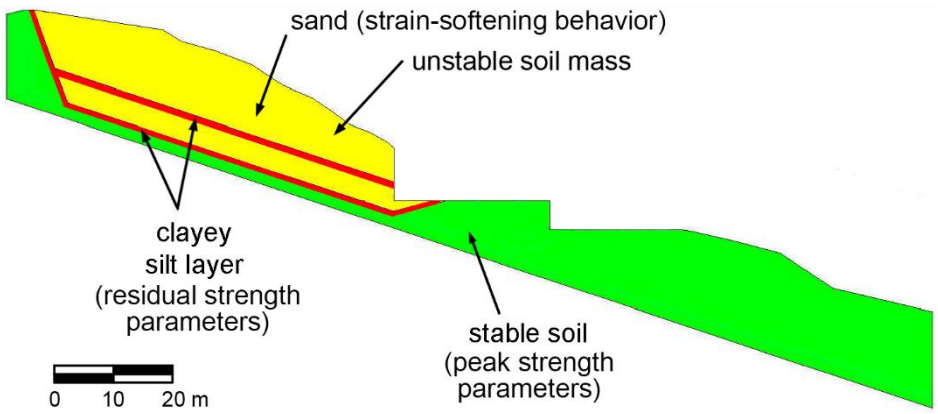

Figure 3.44 – Input geometry for the analysis performed accounting for both slip surfaces and the strain-softening behavior of the yellow sand formation

The values of the shear strength parameter are those reported in Table 3.I. Besides, an additional parameter, η, is required to use Equations (2.161) and (2.162). Such a parameter is calibrated in this study so that the curves of deterioration of the shear strength parameters corresponding to Equations (2.161) and (2.162) are as much similar as possible to those used by Troncone (2005) and Troncone et al. (2014) (Figure 2.14). The most reasonable agreement between the two methods is found in correspondence of the value η = 50, which is therefore used to carry out the analysis described in this section. However, it is well known in the literature (Brinkgreve (1994); Galavi & Schweiger (2010); Rezania et al. (2012); Schadlich (2012)) that the solution is affected by a severe mesh-dependency when constitutive models with strain softening are used. This problem can be partially overcome by

means of regularization techniques, such as a non-local approach (whose development and applications are described by the above-mentioned authors). However, this is an aspect that falls outside the purposes of this dissertation. Therefore, no regularization techniques are used in this context. Anyway, based on the judgement of the author of this dissertation, the influence that the strain softening behavior has on the results should not significantly affect the conclusions of the present study. The computational mesh used to perform the simulation (which is analogous to the mesh reported in Figure 3.32) is shown in Figure 3.45, with the indication of the type of behavior assumed for each involved soil. In the previous sections, it was already pointed out that some uncertainties exist about the exact values of the residual shear strength parameters for both sand and clayey silt.

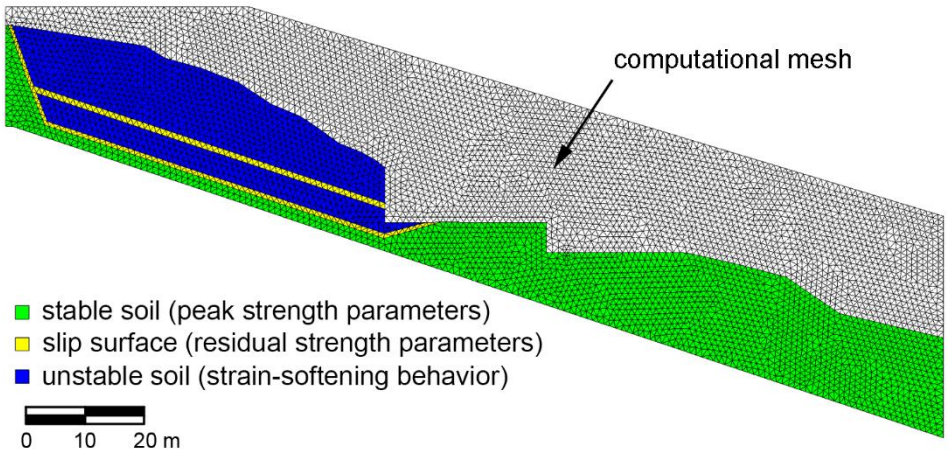

Figure 3.45 – Computational mesh used in the analysis performed accounting for both slip surfaces and the strain-softening behavior of the yellow sand formation

The analysis described in this section is carried out by using the lowest limits obtained experimentally (Table 3.I). The comparison

between the post-failure profile detected after the event and the final configuration of material points at the end of the simulation is reported in Figure 3.46. It can be easily observed that such results are substantially the same of those obtained for the analogous case performed without accounting for the strain softening behavior (see Figure 3.35). Indeed, analogously to this case, the average displacement of material points in the part of the landslide body above the secondary slip surface is on the same order of that detected in field (i.e. about 30 m). Besides, there is a pretty good agreement between the predicted and measured profiles.

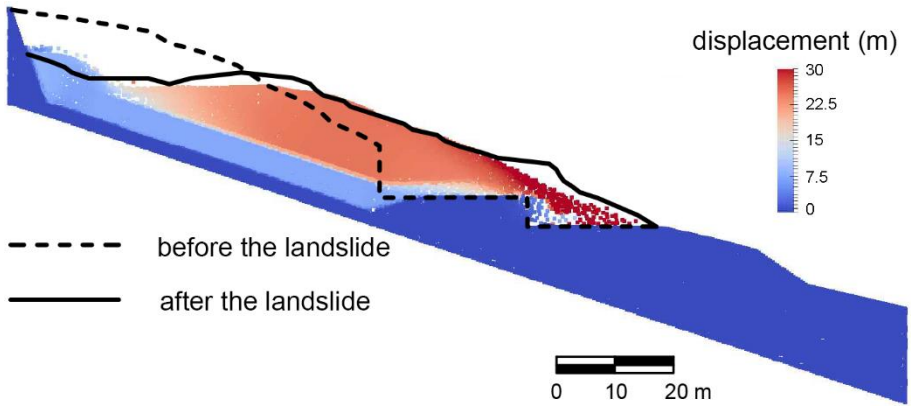

Figure 3.46 – Comparison between the post-failure profile detected after the event and the final configuration of material points, accounting for the presence of both slip surfaces and the strain-softening behavior of the yellow sand formation

Therefore, based on these results and considering that the time required to complete this simulation is extremely longer than that required to complete the simulations presented in the previous sub-sections, it can definitely be asserted that, contrary to the analysis of the pre-failure and failure phases (in which it plays an

essential role), the strain softening behavior of the soils involved in the landslide body can be disregarded in the study of the kinematics of landslides after failure when the post-failure stage is analyzed separately from the trigger phase.

3.9 – Discussion

In this chapter the analysis of the deformation mechanisms of the Senise landslide is presented. Particularly, after the description of the state of the art about this landslide, the analyses of the pre-failure, failure and post-failure stages are described. Since the pre-failure and failure stages were already analyzed in other studies (Troncone (2005) and Troncone et al. (2014)), the available knowledge of these two stages is simply mentioned in this context, whereas attention is mainly focused on the analysis of the kinematics of the landslide after failure (i.e. the post-failure stage), which represents one of the goals of this research. All analyses are performed using the material point method, in order to overcome the shortcomings that characterize other numerical techniques, such as the finite element method, when dealing with problems involving large deformations and large displacements.

After carrying out all the analyses described in the previous sections, some considerations can be made, which are discussed in the following. Referring to the Senise landslide, which is well-documented in the literature, the obtained results are in good

agreement with field measurements, in terms of both magnitude of soil displacements and morphology of the slope at the end of the landslide. However, this study points out that the analysis of the post-failure stage of a landslide is the most complex one and, consequently, requires a more accurate geotechnical model than that required to analyze the pre-failure and failure phases. Indeed, some information could sometimes be negligible for analyzing the trigger phase, whereas the same information could have a paramount importance in order to satisfactorily analyze the kinematics of the landslide after the failure. This is what arises from the analyses presented in this chapter. Indeed, the obtained results show that, contrary to the FEM analysis of the trigger phase, it is indispensable to account for the layer of clayey silt placed at about 10.5 m from the ground surface (where a secondary slip surface developed), which actually played an essential role in the post-failure stage of such a landslide. Indeed, the numerical results obtained taking into account this layer represent a valid interpretation of the phenomenon actually occurred. On the contrary, in the previous studies concerning the Senise landslide, the presence of this latter layer of clayey silt was not recognized important to account for the slope failure.

Besides, the present study accounts for also the effects that the structures existing at the time of failure have on the post-failure stage of this landslide. Although not crucial to reproduce the run-

out process of the landslide, the presence of these structures contributes to improve the agreement between prediction and observation, minimizing the discrepancies existing between the numerical and observed post-failure profiles.

Moreover, to obtain the best results, a parametric study is carried out to characterize the more appropriate values of the geotechnical parameters among those experimentally obtained. As a result, it is necessary to employ some little changes to the parameters used in the analyses of the pre-failure and failure stages, in order to ensure the best agreement between numerical results and field measurements. The best agreement between prediction and observation is achieved using the minimum values of the soil strength parameters found experimentally.

All these results indicate that an analysis focused only on the failure stage (as usually happens) could lead to a partial understanding of the complex mechanical mechanisms of landslides. An approach capable to capture the post-failure and deposition stages should be used to overcome this limitation and make the study more comprehensive.

Furthermore, the strain-softening behavior, which plays an essential role in the pre-failure and failure stages, can be disregarded in the study of the post-failure stage, since it has been proved that it has a negligible influence on the kinematics of landslides when the post-failure stage is analyzed separately from

the other phases that the deformation and failure mechanisms of slopes is classified into.

Results from numerical simulations also show that the landslide is a translational slide with kinematical features similar to those of a sliding block. On the basis of the calculated velocity and time elapsed from start to stop of the motion, this slide can be defined very rapid. All these results are consistent with what really occurred.

Chapter 4 - The Maierato landslide

4.1 – Introduction

On 15 February 2010, a landslide of great dimensions occurred at Maierato, a little village located about 8 km away from Vibo Valentia, Southern Italy (Figure 4.1), after a long rainy period, in a site with elevation ranging from 200 to 320 m a.s.l.. On 20 February 2010, an additional failure occurred, causing the retreat of the main crown of the landslide (Figure 4.2).

Figure 4.1 – Location of Maierato in Italy

This landslide can be classified as a roto-translational slide that evolved into a rapid flow after the activation phase (Leroueil (2001), Hungr et al. (2014)). Several authors studied the Maierato

landslide, providing a detailed description of the geological, geomorphological and tectonic setting where the landslide occurred (Guerricchio et al. (2010); Doglioni et al. (2011); Gattinoni et al. (2012); Gattinoni & Scesi (2013); Borrelli et al. (2014); Conte et al. (2016)). In the present study, the numerical analyses performed to simulate the pre-failure and failure stages of this landslide, using a traditional finite element approach, is described. However, these analyses are not able to simulate the kinematics of the landslide after the collapse, because of the unsuitability of the finite element method for dealing with problems involving large deformations, as already pointed out in Chapter 2. Therefore, the main aim of this chapter is to go beyond and analyze the post-failure stage of this landslide using the material point method. Analogously to the previous chapter, the description of the analyses will follow an initial description of the main characteristics of the landslide.

4.2 – Landslide description and kinematics

Figure 4.2 shows an aerial view of the landslide taken the day after the event, and it clearly points out the mechanism occurred and the dimensions of the involved area. The dimension of the landslide body are over 1000 m in length and about 500 m in width. The maximum height of the main scarp is approximately 50 m and the estimated volume of the displaced soil mass is about

10^7 m^3. The event was preceded by a long rainy period that involved the two preceding years (2008 and 2009) and almost all days from the beginning of 2010 to the date of the landslide.

Figure 4.2 – Aerial view of the Maierato landslide

Fortunately, the landslide did not cause any fatalities because the site was not urbanized. However, the landslide caused the collapse of a bypass road located on the left flank of the landslide body, the destruction of the main road SP55 in the lower part of the slope and the loss of many hectares of farmland. Besides, the landslide moved a building for a distance of over 100 m and caused the formation of a small lake on the right flank of the body of landslide (Borrelli et al. (2014)). Although the zone was affected by continuous movements before the landslide, especially during the wet seasons, no monitoring system was installed before the occurrence of the landslide. Nevertheless, the area had been

under observation for some days due to the occurrence of large deformations along the SP55 road. Therefore, many photos and videos were taken during the failure process of the slope. These photos and videos were used by Conte et al. (2016), (2018) to reconstruct the kinematics of the landslide. Figure 4.3 shows some scarps existing before the 15 February 2010 landslide, which were recognized as possible crowns of pre-existing landslide bodies (Gattinoni et al. (2012); Borrelli et al. (2014)), and which will be useful to refer to in the following description of the landslide.

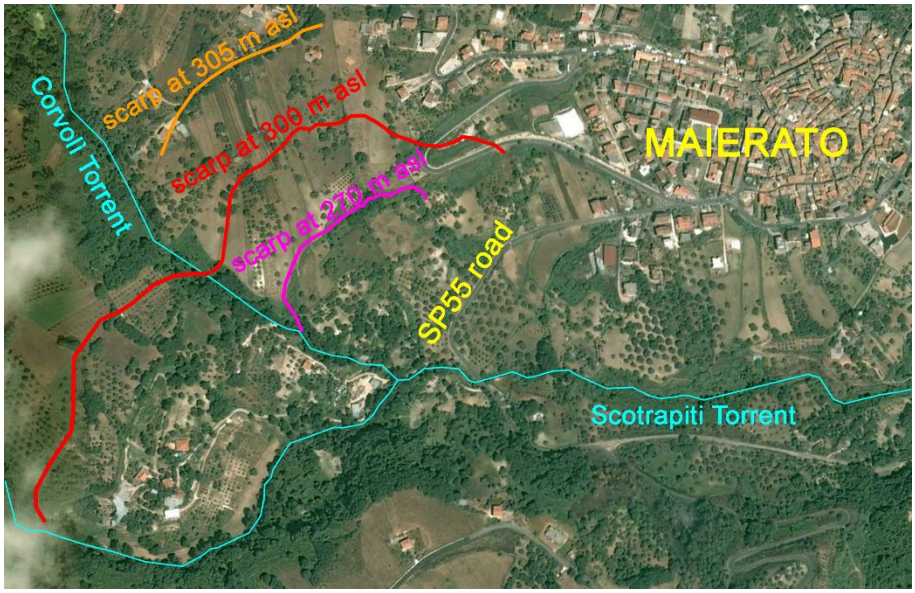

Figure 4.3 – View of the Maierato territory with an indication of some scarps (at 270, 300 and 305 m of elevation) existing before the 15 February 2010 landslide

The failure process started on 15 February 2010, in the morning, with the occurrence of large deformations that affected the SP55 road and the portion of the slope from this road to the scarp at

270 m of elevation (Figure 4.4), whose height further increased with respect to the height previously estimated.

Figure 4.4 – Increase in the height of the scarp at 270 m a.s.l.

With the progression of time, the slope movements caused the formation of large cracks and bulges on the ground surface and along the SP55 road. At 4:55 pm, a deep trench formed at the elevation of 300 m a.s.l., just in correspondence of a pre-existing scarp (Figure 4.5). After some minutes, another transversal fracture occurred at the elevation of 285 m a.s.l. (Figure 4.6). While the height of the scarps at 285 and 300 m a.s.l. was progressively increasing, a soil mass consisting mainly of evaporitic limestone broke away from the scarp at 270 m a.s.l. causing the complete collapse of the hairpin road that had been

damaged during a previous event in 2009. On the contrary, the pre-existing scarp at 305 m a.s.l. (Figure 4.3) was not involved in the deformation process (Figure 4.7).

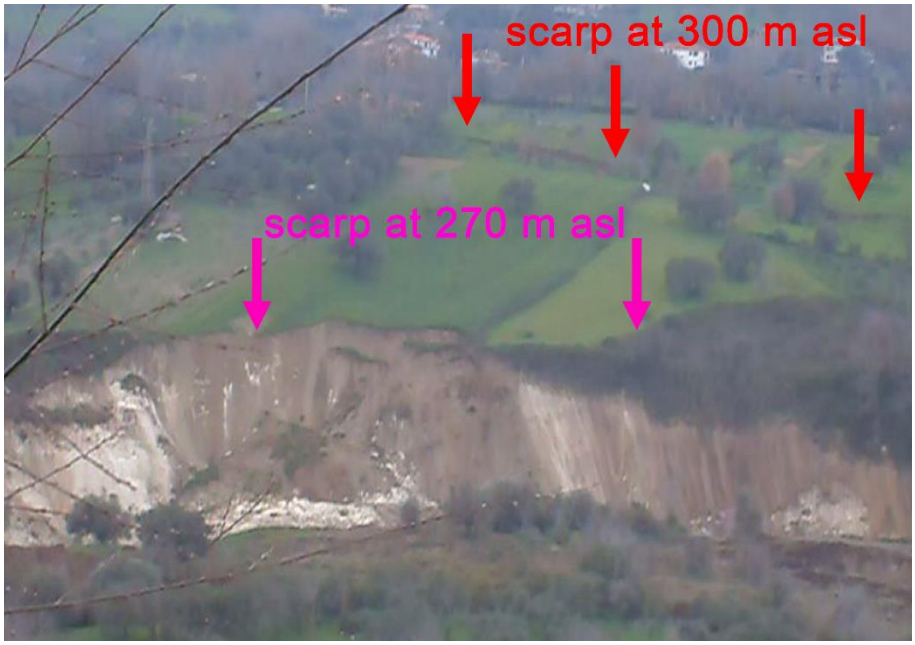

Figure 4.5 – The slip surface emerging at the elevation of 300 m a.s.l. (indicated by the red arrows)

The displaced soil moving quickly downstream covered a portion of the SP55 road that was already highly deformed due to the soil movements occurring along a slip surface located below the roadbed. At 5:10 pm, the crown of the landslide body was completely developed. Immediately afterwards, most of the displaced material rapidly evolved into a flow. Additionally, some small lakes formed inside the landslide body and along its contour. On 20 February 2010, and additional soil volume of about $5x10^5$ m^3 collapsed causing a retreat of about 80 m of the landslide body (Figure 4.2).

Figure 4.6 – The slip surface emerging at the elevation of 285 m a.s.l. (indicated by the blue arrows)

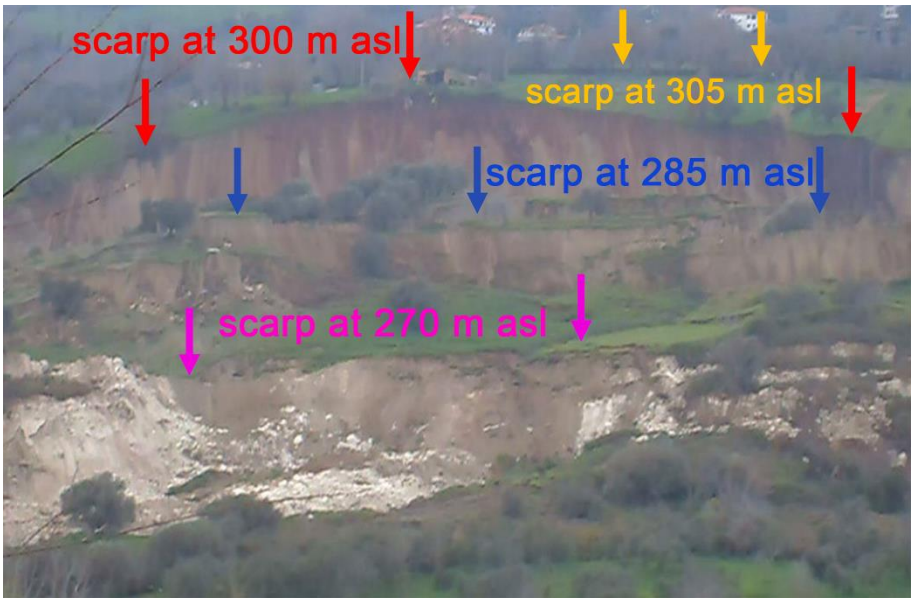

Figure 4.7 – Failure surfaces of the 15 February 2010 landslide. The pre-existing scarp at 305 m a.s.l. (indicated by the yellow arrows) was not involved in the failure process

4.3 – Geological and geomorphological setting

The area interested by the landslide was carefully investigated from the geological and geomorphological point of view by Gattinoni et al. (2012) and Borrelli et al. (2014). Some of the main features will be presented in this section. Figure 4.8 shows the area surveyed in detail.

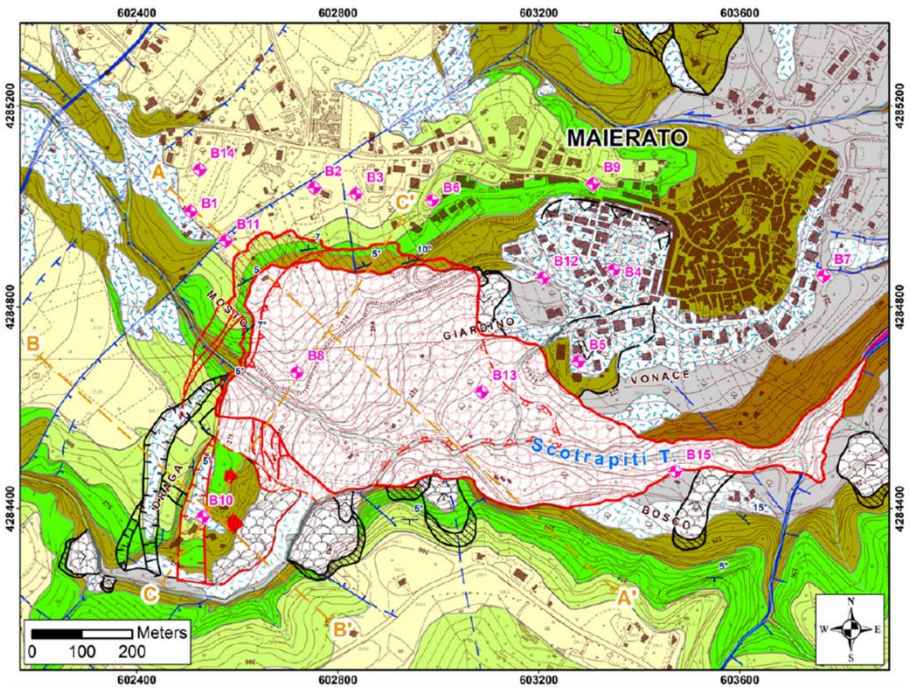

Figure 4.8 – Geostructural and landslides map carried out after the event (from Borrelli et al. (2014))

According to the abovementioned authors, the main outcropping geological formations from the top to the bottom are:

- Pleistocene eluvio-colluvial deposits of variable thickness (0-10 m) with a predominance of conglomerates in a silt-sandy matrix;
- Middle Pliocene deposits of alternating clayey sands with macrofossils and clay layers having thicknesses of 5-25 m;

- Highly porous Upper Miocene evaporitic limestone with clayey and marl-clayey layers, with thicknesses ranging from 25 to 45 m;
- Late Miocene clays that are well consolidated with thin sand-silty layers with a thickness of 10-20 m;
- Middle to Late Miocene alternating sandstone and sandy clays, poorly cemented, with thicknesses ranging from 10 to 40 m;
- Middle to Late Miocene conglomerates with rounded clasts and blocks of bedrock within a gravel-sand matrix, with a thickness ranging from 0 to 5 m and with a limited lateral continuity;
- Paleozoic crystalline metamorphic bedrock, highly fractured and weathered.

The sedimentary succession is characterized by bedding dips in the range from 0° to 15° dipping towards the east-south-east. The stratigraphic succession reduces in thickness toward west.

According to Borrelli et al. (2014), the Maierato landslide can be subdivided into three sectors: upper, intermediate and lower (Figure 4.9).

Figure 4.10, Figure 4.11, Figure 4.12 and Figure 4.13 show some pictures taken by Borrelli et al. (2014) during their investigation, which highlight the main characteristics of the three sectors that the landslide was subdivided into.

Figure 4.9 – Partition of the Maierato landslide (from Borrelli et al. (2014))

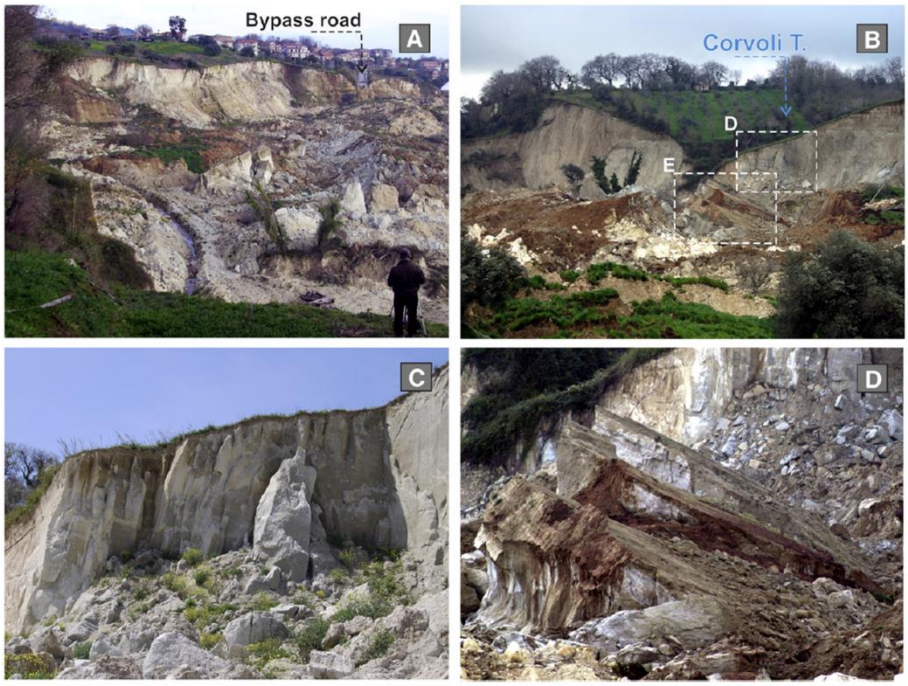

Figure 4.10 – Photos taken in the upper sector of the landslide: (A) main scarp (about 600 m) that extends from NE to SW, making a gentle curve; (B) valley of the Corvoli Torrent that split the main scarp into two parts; (C) bands of parallel joints (about 15 m wide), NE-SW trending, related to the decompression that occurred during the landslide movement along the main scarp; (D) large rock blocks rotated backwards. (From Borrelli et al (2014))

In the upper sector of the landslide, the main scarp (which is characterized by a length of about 600 m and which develops itself from NE to SW) makes a gentle curve (Figure 4.10A); it is split into

two parts by the valley of the Corvolì Torrent (Figure 4.10B). A 15 m wide band of parallel joints, NE-SW trending, is present on a section of the main scarp parallel to the mass movement direction and located to the NE of the Corvolì Torrent (Figure 4.10C).

Figure 4.11 – Photos taken in the intermediate sector of the landslide: (E) large rock blocks of evaporitic limestone, little deformed, translated downstream; (F) laminated marl strata, interbedded inside the evaporitic limestone, stretched and deformed asymmetrically; (G) secondary sliding surfaces exposed on the remnant marl strata; (H) toe of the failure surface of the Maierato landslide daylighting (for about 20 m) in the terminal part of the intermediate sector. (From Borrelli et al. (2014))

Joints are subvertical, with an average spacing of about 1 m. Immediately downstream from the main scarp, in the whole upper portion of the landslide body, large blocks are rotated backwards up to 40° where the original stratigraphy is considerably preserved (Figure 4.10D).

In the intermediate sector of the landslide, some highly large rock blocks are present. Such blocks, whose base is made up of

evaporitic limestone, are slightly deformed (Figure 4.11E), and were displaced over a distance of up to 400 m.

Tongues of destructured evaporitic limestone and completely reworked hemipelagic marls were observed through the large blocks and along the flanks of the landslide (Borrelli et al. (2014)). The trenches dug to drain the landslide body showed brownish-red and green strata of laminated marls interbedded inside the blocks of evaporitic limestone. Such marls are stretched and deformed with asymmetrical centimeter-size folds verging toward the direction of the landslide movement.

These layers are locally doubled and wedged into the cracks of the rafted blocks (Figure 4.11F). Where the top of the laminated marl strata is exposed to daylight, slightly striated sliding surfaces were locally observed (Figure 4.11G). In the terminal part of the intermediate sector, the excavations performed to facilitate water drainage after the mobilization exposed the toe of the failure surface of the Maierato landslide. The sliding surface is clearly exposed for about 20 m inside the hemipelagic marls (Figure 4.11H). In the lower sector of the landslide, there is a chaotic mixture made up of yellowish-white limestone fragments, ranging in size from sand to small blocks, and reworked blue marls (Figure 4.12I); it is the flow tongue overlapping the in situ Tortonian sandstones (Figure 4.12J).

Figure 4.12 – Photos taken in the lower sector of the landslide: (I) chaotic mixture of yellowish-white limestone, ranging in size from sand to small blocks, and reworked blue marls of the flow tongue filling the valley bottom of the Scotrapiti Torrent; (J) particular of the flow tongue overlapping the in situ Tortonian sandstones. (From Borrelli et al. (2014))

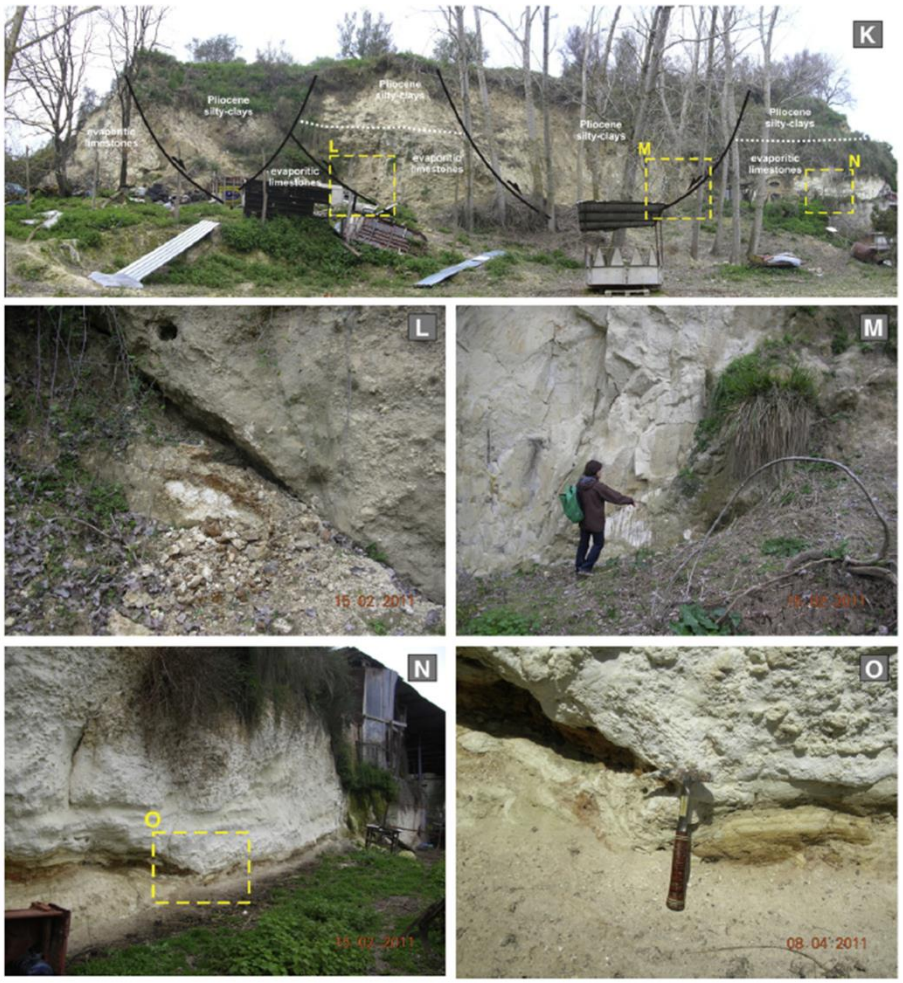

Figure 4.13 – Photos taken along a steep cliff along the left side of the Scotrapiti Torrent: (K) panoramic view of the Trenches, typical of a translational sliding, that caused the spreading of the limestone bank and the sinking of the overlying Pliocene deposits (K)-(M); (N) decametric brownish-red and green laminated marl layer, interbedded within the evaporitic limestone, and showing evidence of ductile deformation (O) with a folding that could have been caused by a translational movement of the overlying limestone bank. (From Borrelli et al. (2014))

In an ancient landslide, named Draga landslide (Figure 4.8), the upper trench develops as a prolongation of the Maierato main scarp, probably as a consequence of the structural control exerted by joints and/or minor faults. Such a trench is dormant and extends down to the thalweg of the Scotrapiti Torrent, whose left side slope forms a steep cliff (Figure 4.13K). Such a trench clearly shows NNE-SSW trending shear surfaces of gravitative origin. These structures, bifurcated in the south end (Figure 4.13K), form a single graben-like trench to the north, which caused the spreading of the limestone bank and the sinking of the overlying Pliocene deposits (Figure 4.13K-M). Furthermore, immediately SE of the trench, a decametric brownish-red and green laminate marl layer, interbedded with the evaporitic limestone (Figure 4.13N), shows evidence of ductile deformations (Figure 4.13O) that could have been caused by a translational movement of the overlying limestone bank.

4.4 - Geotechnical characterization

4.4.1 – Site investigation

A site investigation consisting of boreholes and field tests was carried out after the landslide, whose location is reported in Figure 4.14. Particularly, the borehole $S_{UNICAL,1}$ is located close to the landslide crown and extended 80 m in depth, the borehole $S_{UNICAL,2}$ is located on the left side of the landslide and extended

for a depth of 60 m, whereas the borehole SUNICAL,3 is located at the middle of the landslide body near the Maierato-Filogaso road and extended 32 m in depth. Additionally, the boreholes indicated with V1 and V2 are located close to SUNICAL,1 and SUNICAL,2 respectively.

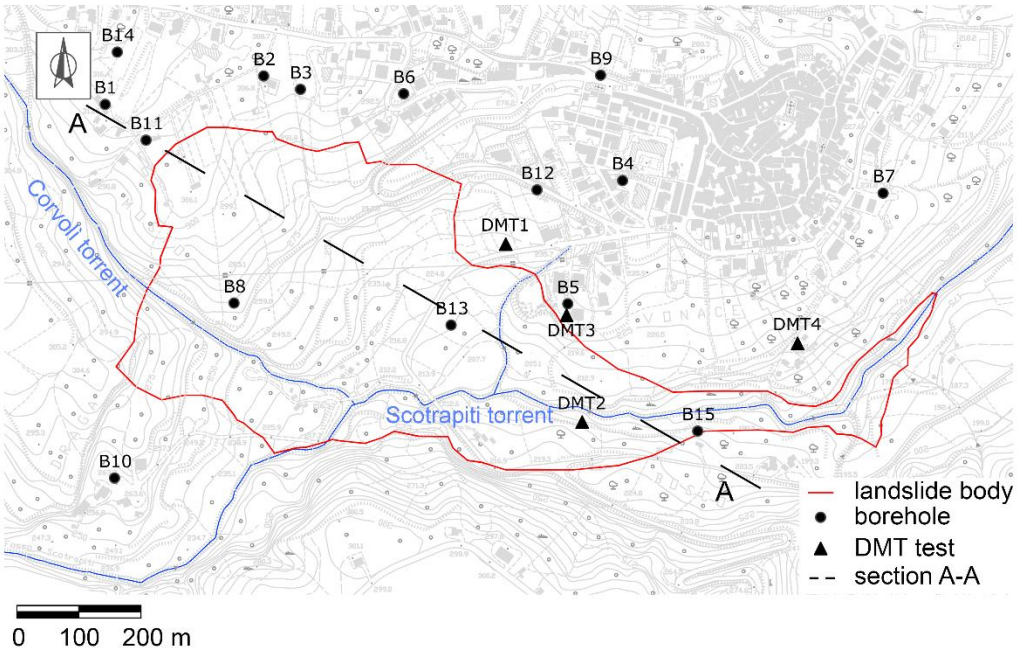

Figure 4.14 – Position of the boreholes

Other boreholes were performed by Borrelli et al. (2014), whose position is shown in Figure 4.14 as well. The boreholes SUNICAL,1 and SUNICAL,2 were instrumented with inclinometers, whereas open pipe piezometers were installed along the boreholes SUNICAL,3, V1 and V2. During the drilling phase, standard penetration tests (SPT) and Mènard pressumeter tests (PMT) were performed. Additionally, some undisturbed specimens were taken to carry out laboratory tests. A description of the stratigraphic profiles concerning the boreholes SUNICAL is provided in the following.

Figure 4.15 shows the stratigraphic profile in correspondence of the borehole $S_{UNICAL,1}$. It consists of a 25 m thick Pliocene silty sand layer overlying an evaporitic limestone formation which extends up to the depth of 50 m.

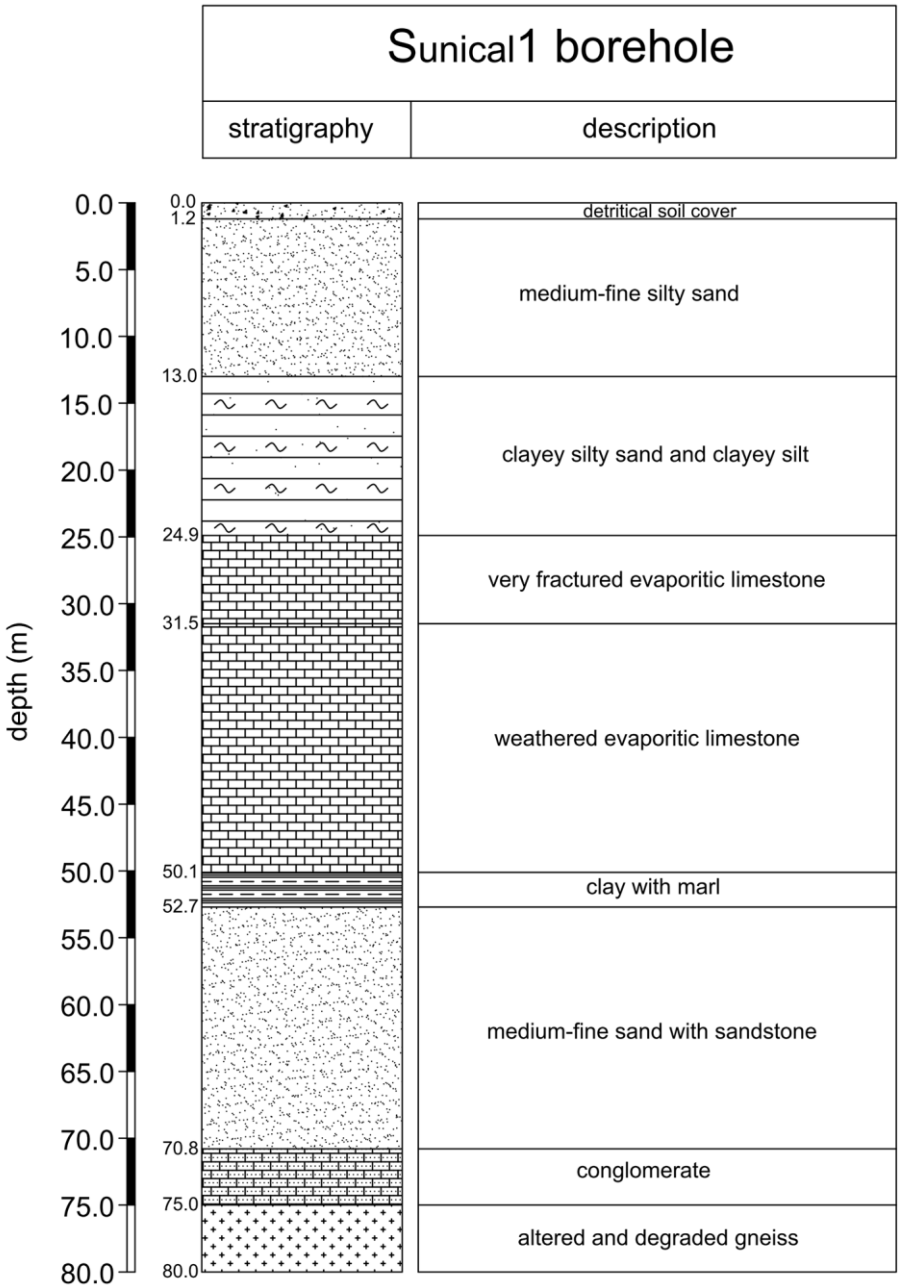

Figure 4.15 – Borehole $S_{UNICAL,1}$ stratigraphic description

Afterwards, a 3 m thick Miocene clay layer was found above a formation of Miocene sand with sandstone, which in turn overlies a conglomeratic 4 m thick, and in succession a gneiss-schists formation.

The stratigraphic profile in correspondence of the borehole SUNICAL,2 is shown in Figure 4.16.

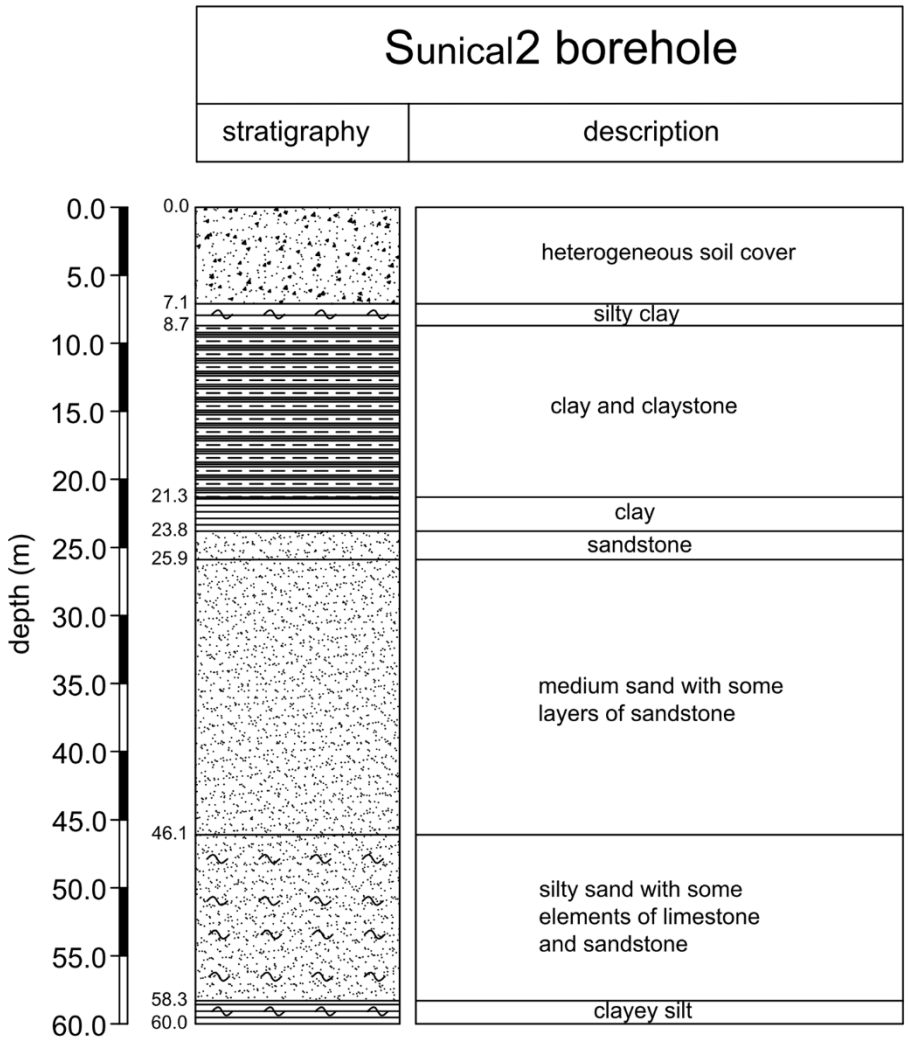

Figure 4.16 – Borehole SUNICAL,2 stratigraphic description

A 16 m thick Miocene clay layer was found at the depth of 7 m from the top of the borehole. Such a layer is interbedded between a cover soil and a sequence of Miocene sand layers and sandstone.

It is worth noticing that the evaporitic limestone formation was not found in such a borehole, probably due to the occurrence of antecedent shallow landslides.

Finally, the stratigraphic profile in correspondence of the borehole SUNICAL,3 is shown in Figure 4.17.

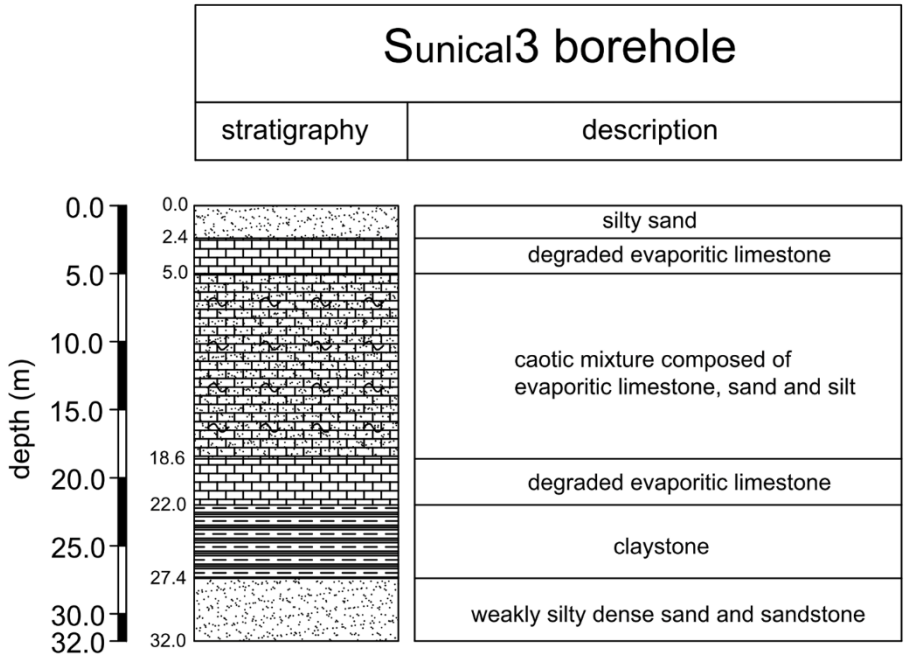

Figure 4.17 – Borehole SUNICAL,3 stratigraphic description

This borehole is characterized by a chaotic mixture made up of sand, silt and weathered evaporitic limestone. It extends up to a depth of 18.6 m and represents the material involved in the landslide body. Beneath this soil, a 3.5 m thick layer of limestone and a 5.4 m thick Miocene clay layer were found. From the depth of 27.4 m, dense sand and sandstone were found. For the sake of completeness, the stratigraphic profiles provided by Borrelli et al. (2014) are reported in Figure 4.18, including some photos of the

samples taken during the drilling. Drilling depth varies from about 20 m (borehole B15) to about 100 m (borehole B8).

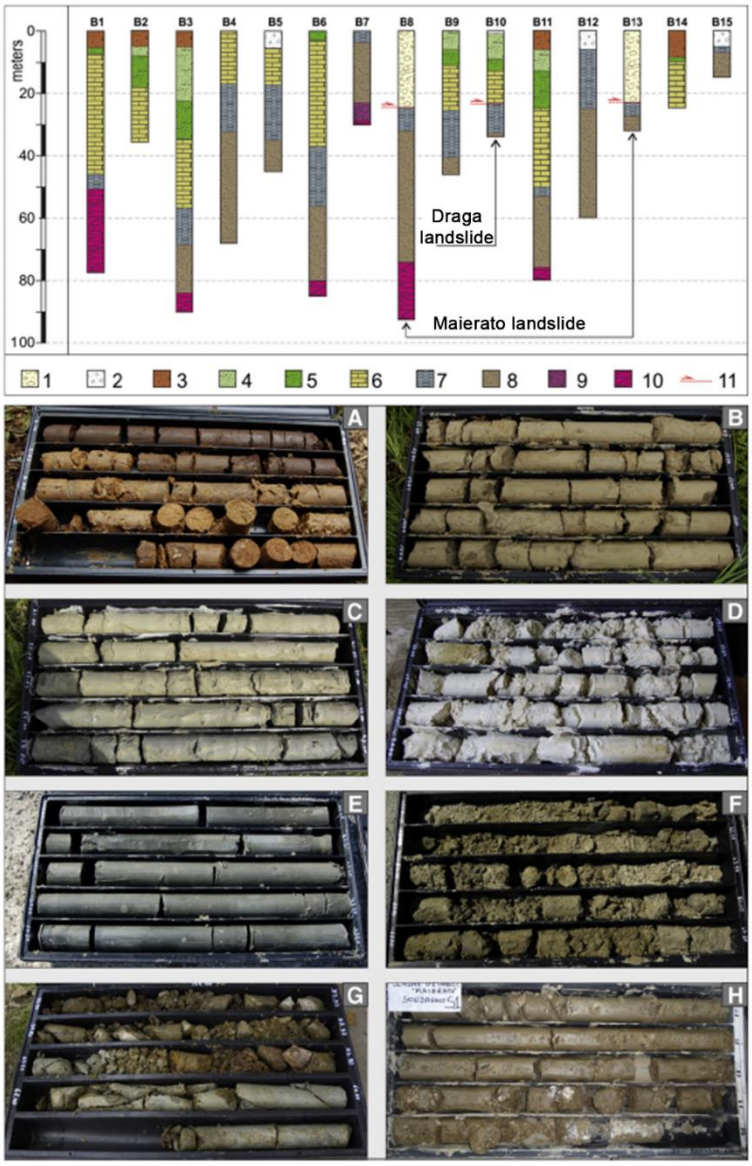

Figure 4.18 – Stratigraphy from the geotechnical boreholes carried out inside the landslide body and in the surrounding areas along with photos of the principal rock types detected. Legend: 1) Maierato landslide debris; 2) anthropic cover; 3) Pleistocene gravel and sand (photo A); 4) Pliocene sand (photo B); 5) Pliocene silty clays (photo C); 6) Messinian evaporitic limestone (photo D); 7) upper Tortonian/early Messinian hemipelagic marls (photo E); 8) Tortonian sandstone (photo F); 9) Tortonian conglomerates; 10) Palaeozoic gneissic basement, moderately (photo G) and completely (photo H) weathered; 11) sliding surfaces. (From Borrelli et al. (2014))

4.4.2 – Standard penetration tests

The standard penetration tests were carried out in the sandy layers, i.e. in the Pliocene cover soil and in the Miocene sandstone. All the obtained results are reported in Figure 4.19, Figure 4.20 and Figure 4.21. Values of N_{SPT} ranging from 20 to 40 blows/30 cm were found in the Pliocene sand. On the contrary, the tests in the deeper Miocene sandstone provided rejection after few centimeters of penetration owing to the high mechanical properties of the soil.

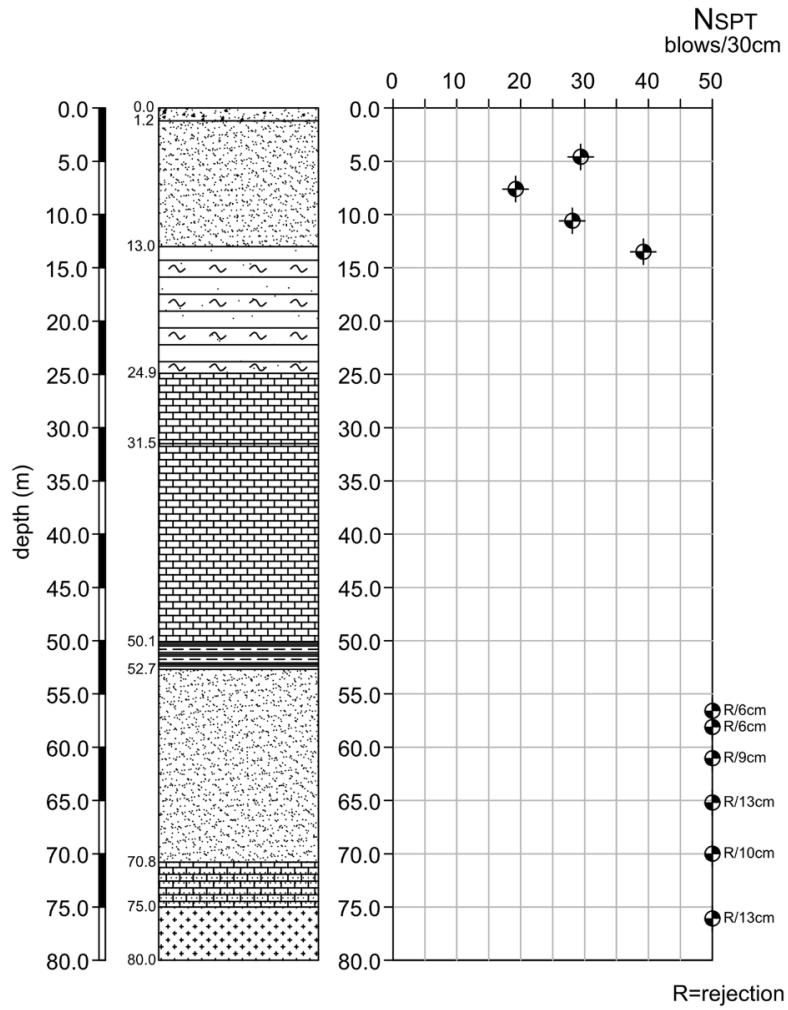

Figure 4.19 – Standard penetration test results for the borehole $S_{UNICAL,1}$

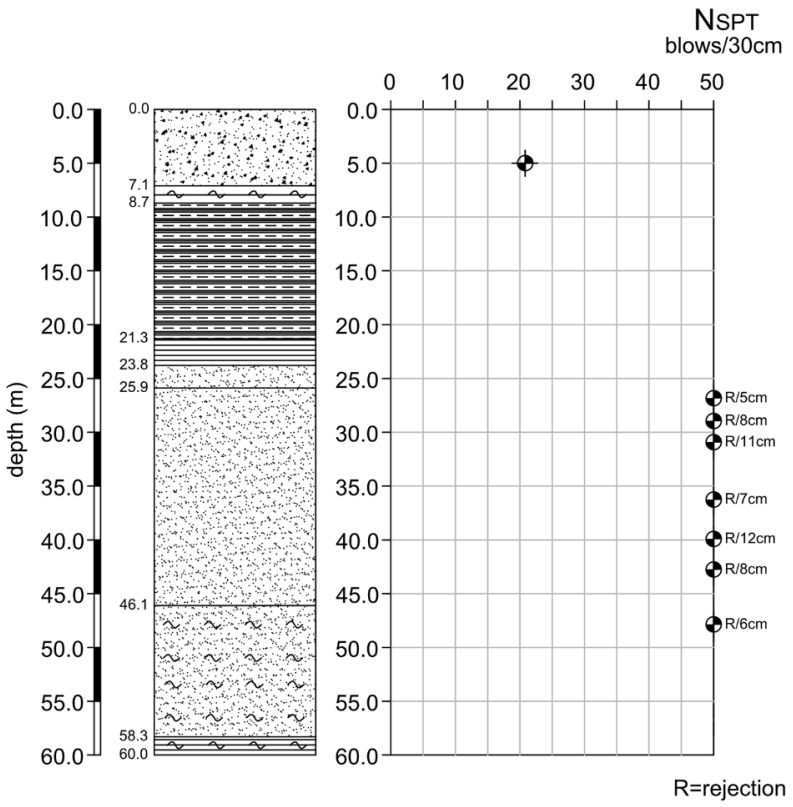

Figure 4.20 – Standard penetration test results for the borehole $S_{UNICAL,2}$

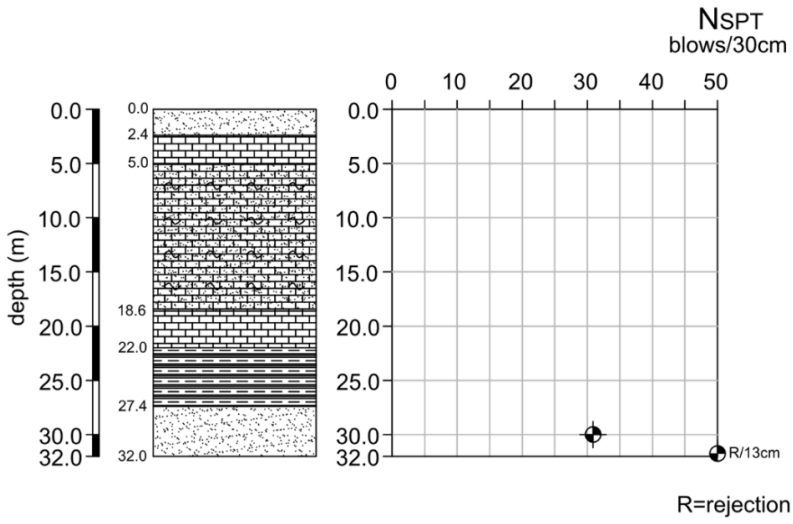

Figure 4.21 – Standard penetration test results for the borehole $S_{UNICAL,3}$

4.4.3 – Mènard pressumeter tests

Mènard pressumeter tests were performed in the evaporitic limestone and in the Miocene sandstone formation. From these tests, the pressiometric modulus, E_M, and the limit pressure, p_{LIM}, were obtained.

The pressiometric modulus, E_M, is calculated using Equation (4.1) and refers to the 'pseudo-elastic' part of the pressure-volume curve.

$$E_M = 2.66 V_m \frac{\Delta p}{\Delta V} \tag{4.1}$$

In Equation (4.1), ΔV is the volume change of the pressiometric cell owing to the applied pressure change, Δp, whereas V_m is the average volume of the cell associated to ΔV. Instead, the limit pressure, p_{LIM}, is calculated from the 'high-strains' part of the pressure-volume curve and using the 'inverse of volumes' method. The obtained results are reported in Figure 4.22 and Figure 4.23. Specifically, E_M varies from 10.2 to 27.8 MPa and p_{LIM} varies from 1.4 to 3.7 MPa for the evaporitic limestone, whereas E_M varies from 25 to 47 MPa and p_{LIM} varies from 3 to 4.5 MPa for the Miocene sand.

Besides, the obtained values increase with depth for the evaporitic limestone, whereas for the Miocene sand the lowest values of E_M and p_{LIM} are obtained at depths greater than 45 m, in correspondence of the vertical $S_{UNICAL,2}$, where the soil is characterized by a high fine percentage.

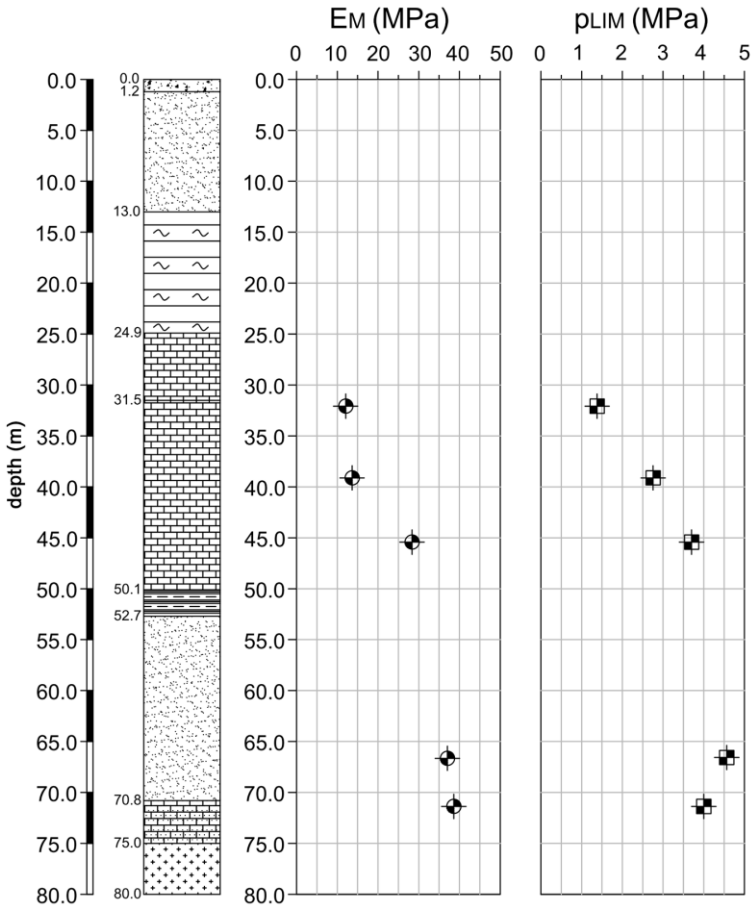

Figure 4.22 – Mènard pressumeter test results for the borehole SUNICAL,1

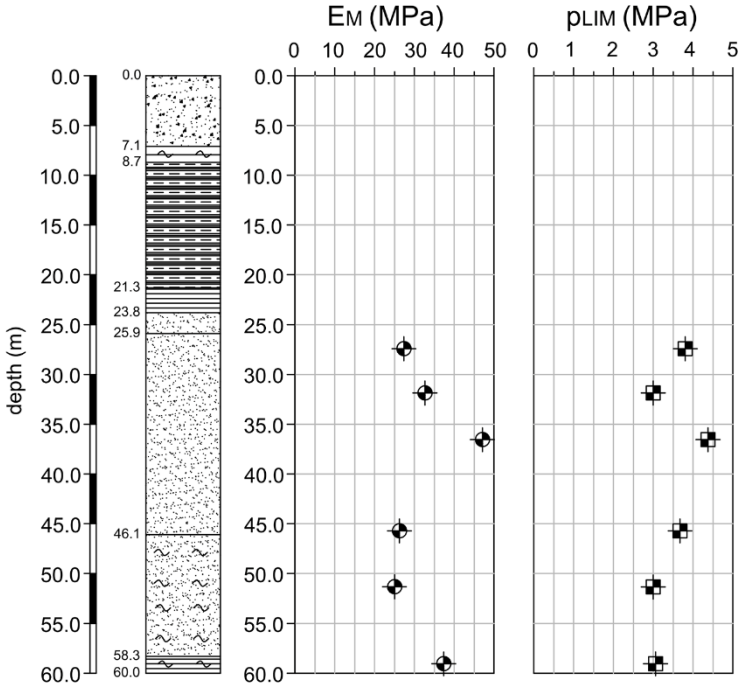

Figure 4.23 – Mènard pressumeter test results for the borehole SUNICAL,2

4.4.4 – Marchetti dilatometer tests

Four Marchetti dilatometer tests were performed in the locations indicated in Figure 4.14. The maximum depth reached for each test is reported in Table 4.I. These location were chosen in order to detect the main formation involved in the landslide. Particularly, DMT1 mainly concerned the clay formation, DMT2 and DMT3 the evaporitic limestone whereas DMT4 the Miocene sandstone. The parameters obtained from these tests are the soil index, I_d, the horizontal pressure index, K_d, and the dilatometric modulus, E_D. The soil index accounts for the soil nature, the horizontal pressure index provides information about the loading history, whereas the dilatometric modulus is related to the deformability of soil.

Table 4.I – Maximum depth reached by DMT tests

test	max depth (m)
DMT1	10
DMT2	19
DMT3	19.4
DMT4	4.6

Several geotechnical parameters, such as the undrained cohesion, c_u, and the overconsolidation ratio, *OCR*, for the cohesive soils, as well as the angle of shearing resistance for cohesionless soils, φ', can be evaluated by using some empirical relationships (Marchetti (1980)). Additionally, the oedometric modulus, *M*, can be

assessed. DMT1 was located at the side of the Filogaso-Maierato road. As shown in Figure 4.24, K_d is about 15 for the silty clay. This soil is characterized by values of the oedometric modulus, M, of the order of 100 MPa, with c_u that ranges from 200 to 400 kPa.

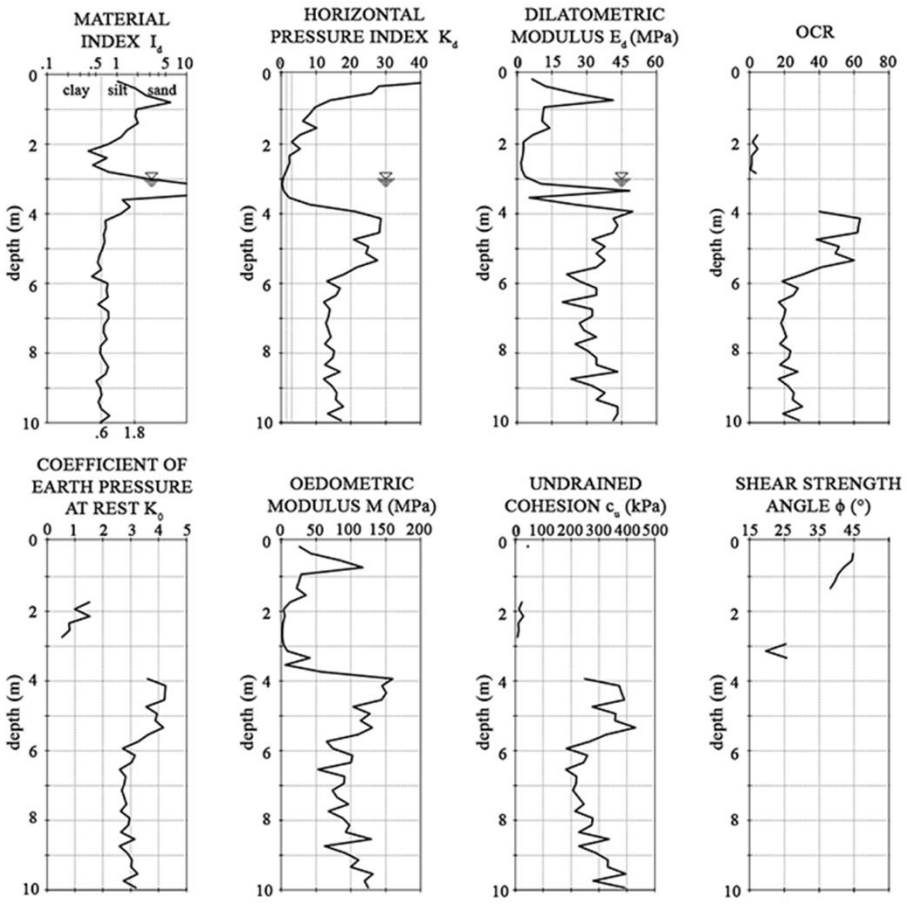

Figure 4.24 – DMT1 test results

DTM2 was located close to the toe of the landslide. Results are shown in Figure 4.25, which point out that the probe passed through a weak silty-clayey layer with M ranging from 2 to 6 MPa and c_u ranging from 10 to 20 kPa, which constitutes the landslide material. Below the depth of 16 m, the soil can be classified as

silty sand with better mechanical properties than the upper layers (*M* ranges from 100 to 200 MPa).

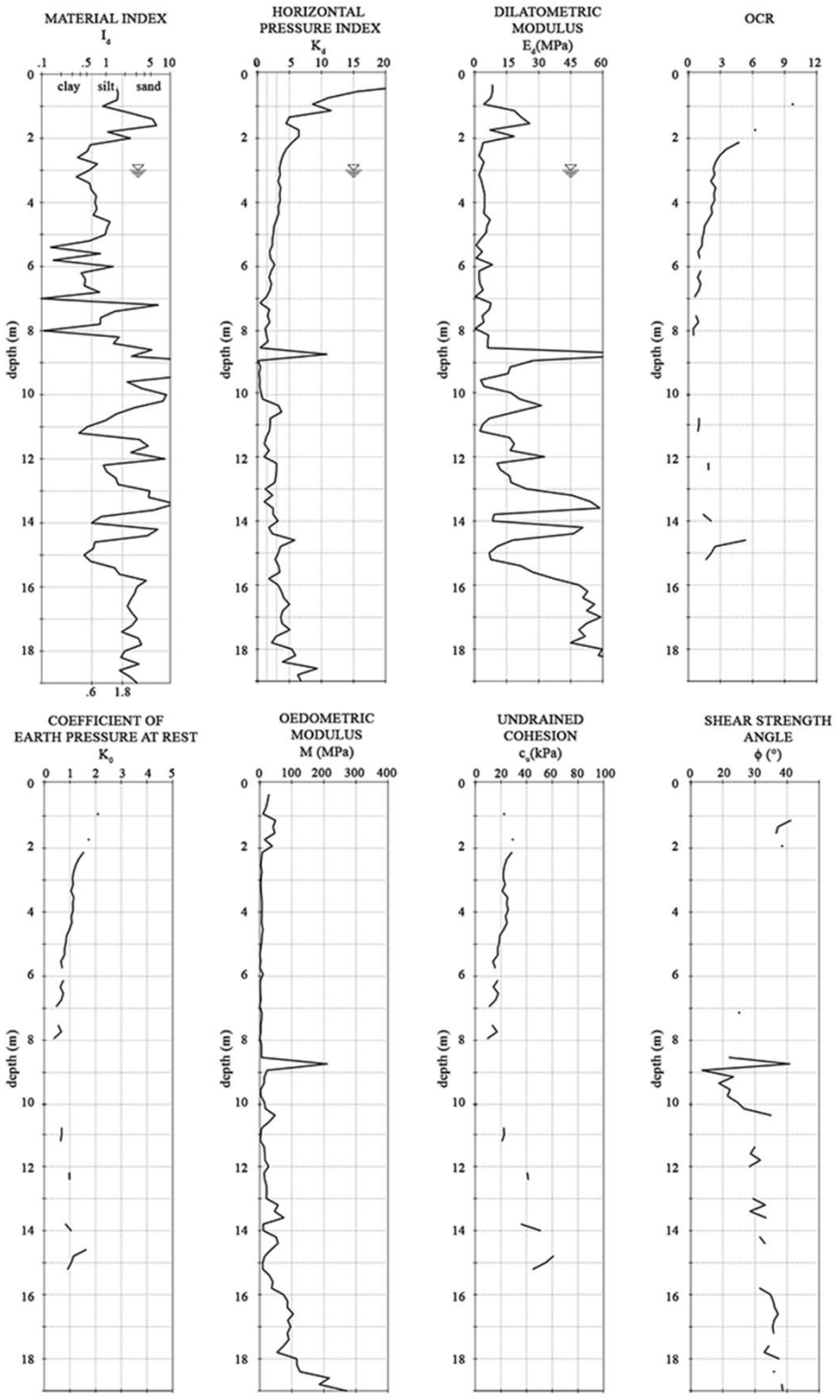

Figure 4.25 – DMT2 test results

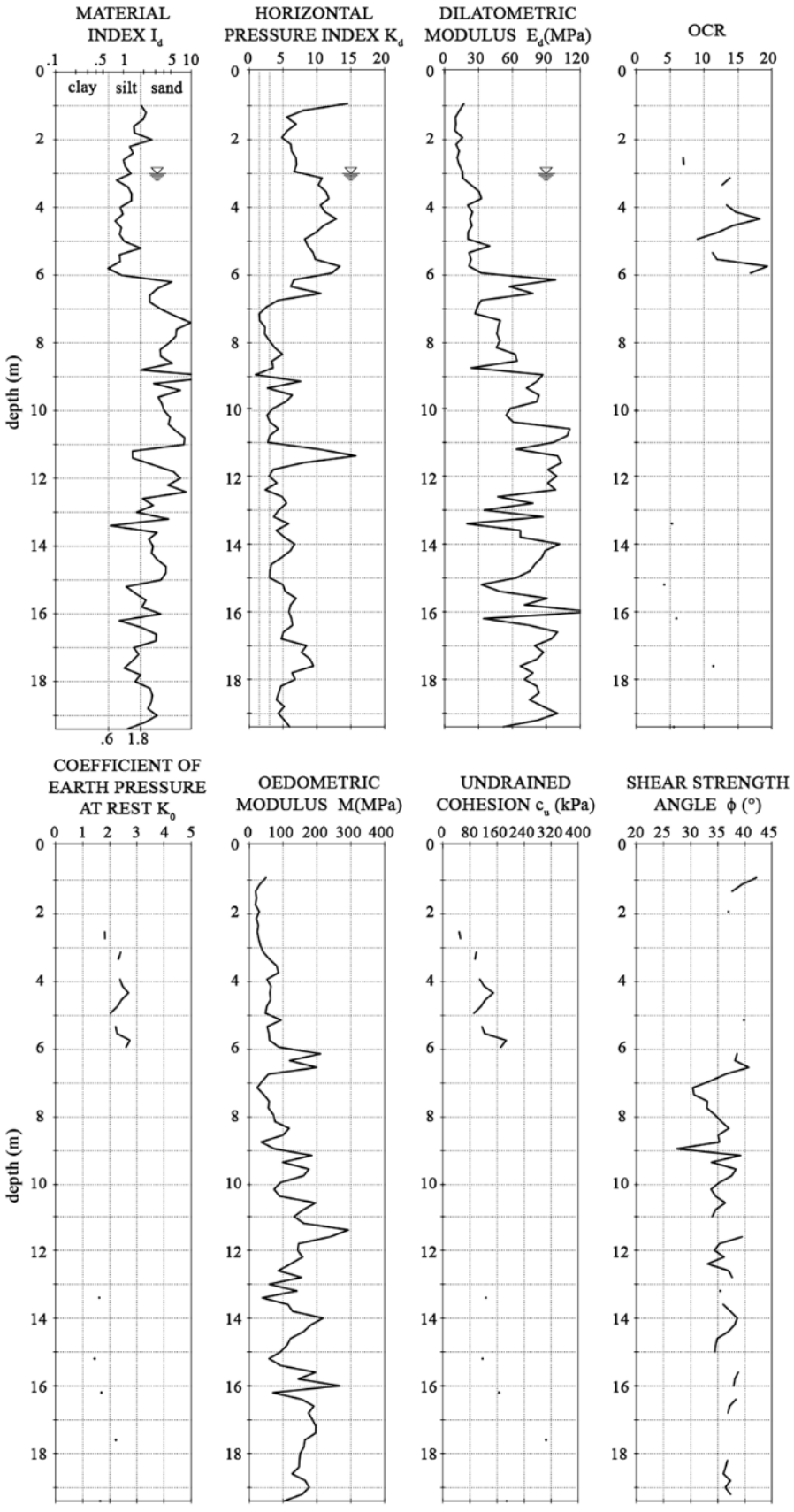

Figure 4.26 – DMT3 test results

Figure 4.26 reports the results concerning the DMT3, whose profile shows the presence of a silty layer with a thickness of 6 m overlying the evaporitic limestone formation that extends up to the depth of 17 m. At the bottom of the profile, a clay layer is found. The values of I_d, are similar to those of DMT2 for the evaporitic limestone although in the former test the mechanical properties of the soils are higher than those of DMT2. For instance, the oedometric modulus, M, exceeds 100 MPa.

Lastly, as shown in Figure 4.27, DMT4 concerned only the Miocene sand up to a depth of 4.6 m, because the probe could not penetrate at greater depths due to the high resistance of this formation. According to the SPT and MPT results, this soil is characterized by good mechanical properties (for instance M is of the order of 500 MPa).

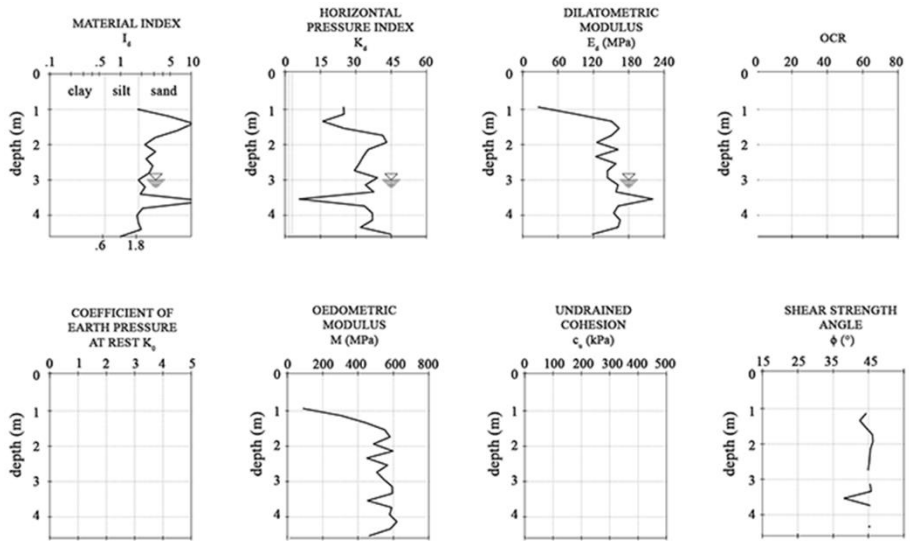

Figure 4.27 – DMT4 test results

4.4.5 – Piezometric measurements

As previously said, open pipe piezometers were installed inside the boreholes V1 and V2. Particularly, the first one is provided with three different uptakes at 18, 48 and 65 m of depth, whereas the second one is equipped with two uptakes respectively at 35 and 55 m of depth. As an example, the measurements carried out on 27 April 2012 are reported in Table 4.II.

Moreover, an electric transducer inside the borehole V2 was installed at 18 m of depth (in correspondence of the Miocene clay layer), but the concerning measurements are not available. Besides, other piezometers of Casagrande type were installed inside the CNR boreholes (Figure 4.14).

Two of these latter, i.e. S1 (located in the upper part of the slope) and S5 (located in the lower part, on the left side of the body of landslide) are useful to define the position of the groundwater table before the landslide.

Table 4.II – Measurements recorded on 27 April 2012 in the piezometers installed in the boreholes V1 and V2

borehole	piezometer depth (m)	measurement from the ground level (m)
V1	18	--
	48	44.20
	65	63.40
V2	35	33.90
	55	33.90

The piezometer S1 is made up of three Casagrande probes (a, b, c) installed at different depths. The available measurement are reported in Table 4.III and shown in Figure 4.28.

Table 4.III – Depth of groundwater level (m) in the piezometer S1

Date	Pipe a (7.7 m)	Pipe c (26 m)	Pipe b (67 m)
Oct 16 2010	--	--	44.95
Nov 02 2010	--	--	44.40
Nov 19 2010	--	--	44.24
Dec 07 2010	--	--	43.73
Dec 21 2010	--	--	43.70
Jan 21 2011	--	--	42.55
Jan 31 2011	--	--	42.40
Mar 27 2012	--	--	43.60
Apr 04 2012	--	--	43.50

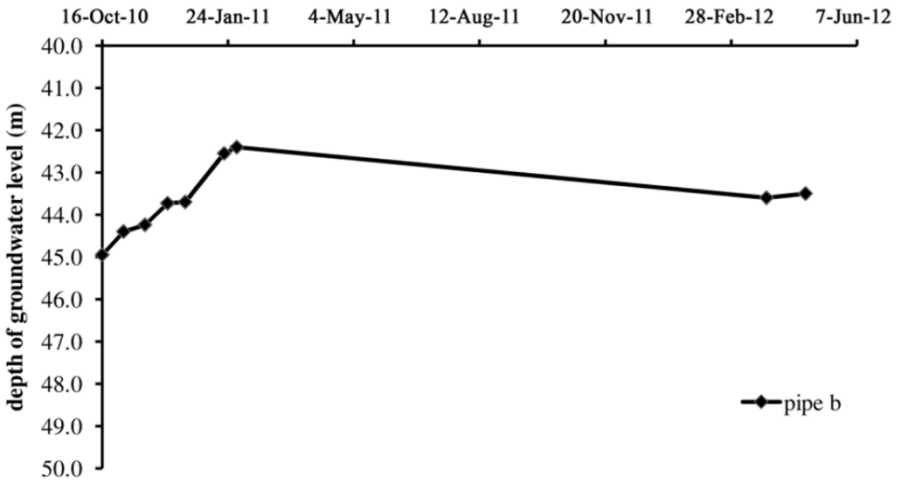

Figure 4.28 – Piezometric readings at piezometer S1

The piezometer S5 is made up of three Casagrande probes as well. The available measurements are reported in Table 4.IV and shown in Figure 4.29.

Table 4.IV – Depth of groundwater level (m) in the piezometer S5

Date	Pipe a (4.8 m)	Pipe c (18.20 m)	Pipe b (41.40 m)
Oct 16 2010	--	6.65	28.80
Nov 02 2010	4.55	5.85	--
Nov 19 2010	--	5.65	29.65
Dec 12 2010	--	5.15	29.55
Dec 21 2010	4.70	5.50	29.42
Jan 21 2011	4.75	4.90	29.40
Jan 31 2011	4.18	4.62	29.25
Mar 27 2012	--	5.55	28.97
Apr 04 2012	--	5.70	28.84

These data suggest that two different aquifers are present in the subsoil, with the groundwater tables located respectively at the depths of about 5 m and 29 m. Finally, it has to be highlighted that the piezometer installed inside the borehole SUNICAL,3 and located in the body of landslide, indicated the presence of a groundwater level at the depth of 20.2 m from the ground surface.

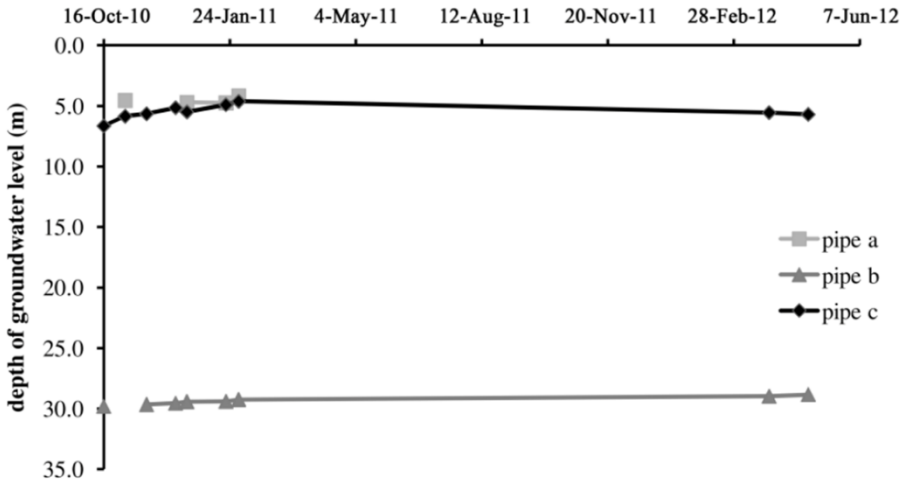

Figure 4.29 – Piezometric readings at piezometer S5

4.4.6 – Laboratory tests

Undisturbed specimens and cores extracted during the drilling were undergone laboratory tests. The available results are reported in the following for each considered soil, from the shallowest one (Pliocene sand) to the deepest one (Miocene sand).

Pliocene sand

This material can be classified as silty sand from the grain size point of view. Based on the Atterberg limits, it is an inorganic clay with medium plasticity.

Evaporitic limestone

Evaporitic limestone is the most heterogeneous lithotype, due to different degrees of weathering that affect this material. According to Figure 4.30, the grain size distribution of this material varies from silty sand to sandy clayey silt.

Furthermore, the material can be substantially classified as an inorganic clay with low-medium plasticity (Figure 4.31). The activity index is always less than 0.75. Therefore the material can be defined as inactive.

The average values of porosity, n, and unit weight, γ, are respectively 0.38 and 19.5 kN/m^3.

Furthermore, the direct shear tests carried out on undisturbed specimens provide a linear failure envelope (Figure 4.32). The

peak strength parameters are c_p' = 15 kPa and φ_p' = 36°, whereas the residual strength parameters are c_r' = 0 kPa and φ_r' = 28°.

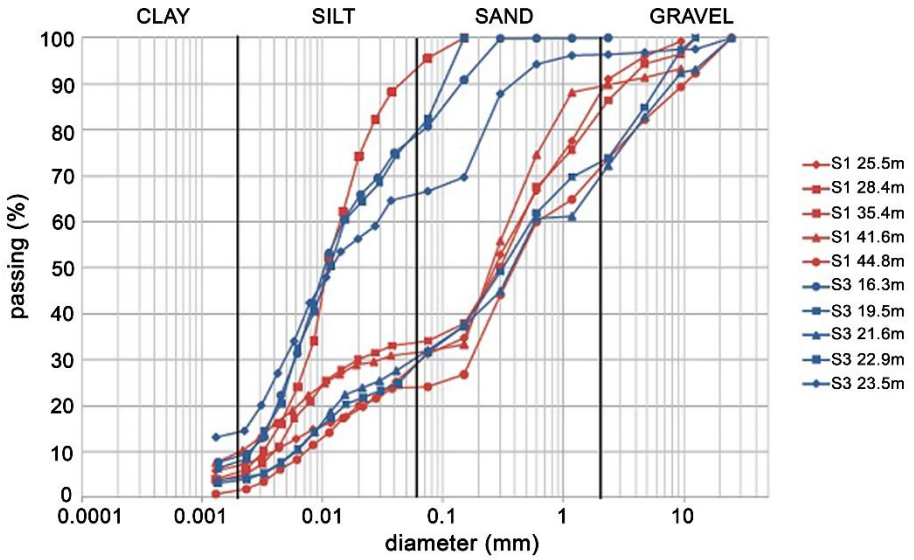

Figure 4.30 – Available grain size distribution for evaporitic limestone

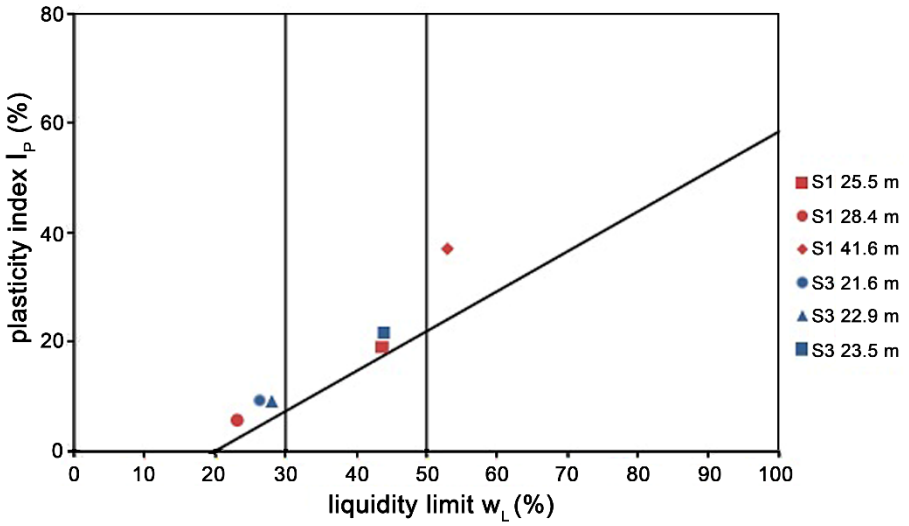

Figure 4.31 – Casagrande plasticity chart for the evaporitic limestone

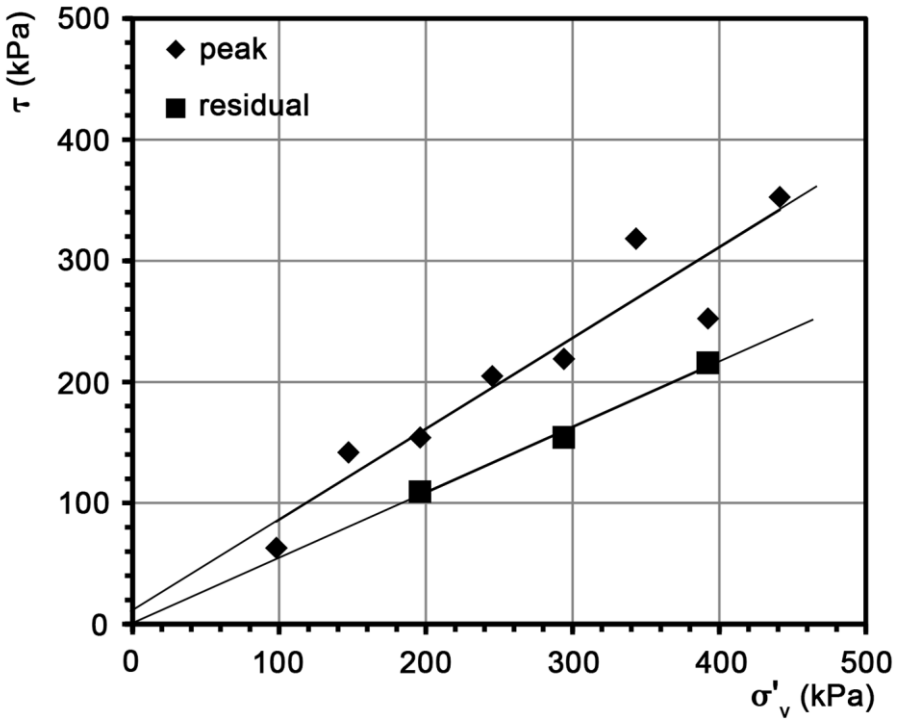

Figure 4.32 – Direct shear tests results for the evaporitic limestone

Miocene clay

The results of the laboratory tests carried out on the samples of Miocene clay show that this soil can be classified as a clay with silt (Figure 4.33), and as an inorganic clay with high plasticity (Figure 4.34).

The activity index ranges between 0.75 and 1.25, therefore the material can be classified as normally active. The average values of porosity, n, and unit weight, γ, are respectively 0.56 and 18.2 kN/m^3.

The average values of the compression ratio, *RR*, and the swelling ratio, *SR*, obtained from the oedometric test (Figure 4.35) are respectively 0.22 and 0.036.

The direct shear tests carried out on undisturbed specimens provided the following peak strength parameters c_p' = 57 kPa and φ_p' = 25°, whereas the values obtained at residual are c_r' = 0 kPa and φ_r' = 13° (Figure 4.36).

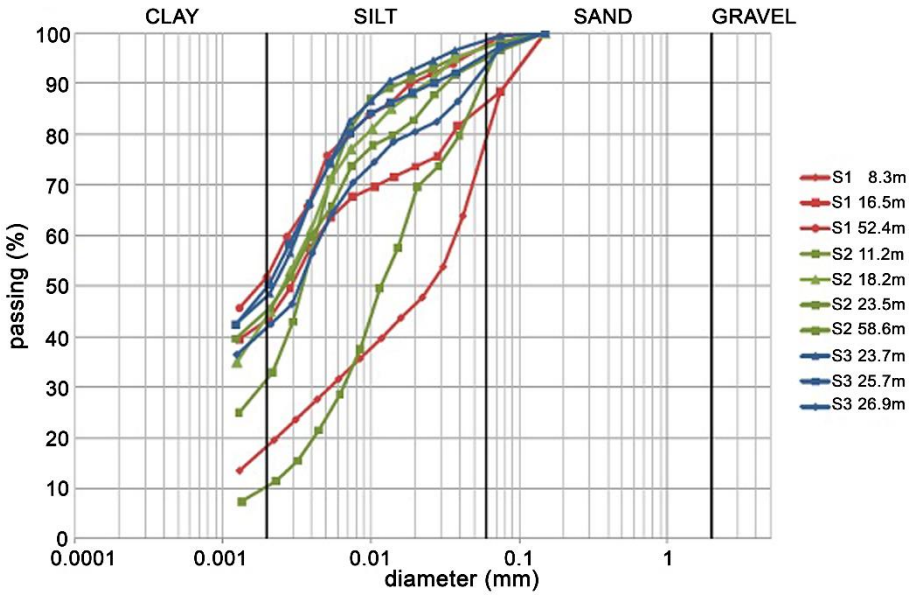

Figure 4.33 – Available grain size distribution for Miocene clay

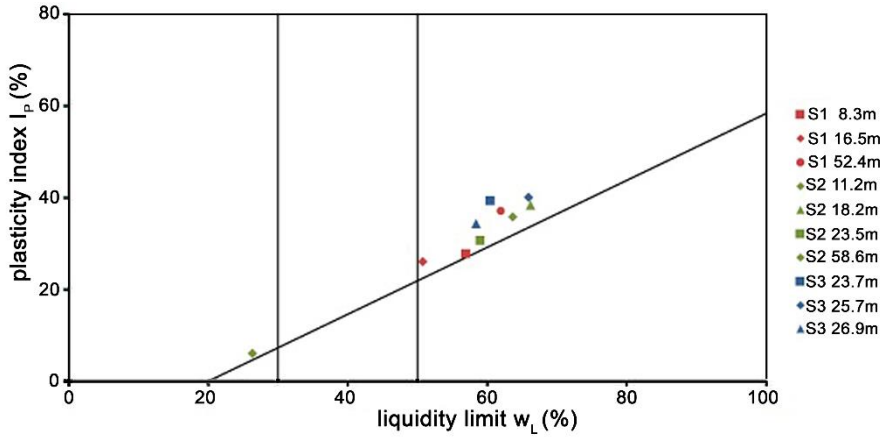

Figure 4.34 – Casagrande plasticity chart for Miocene clay

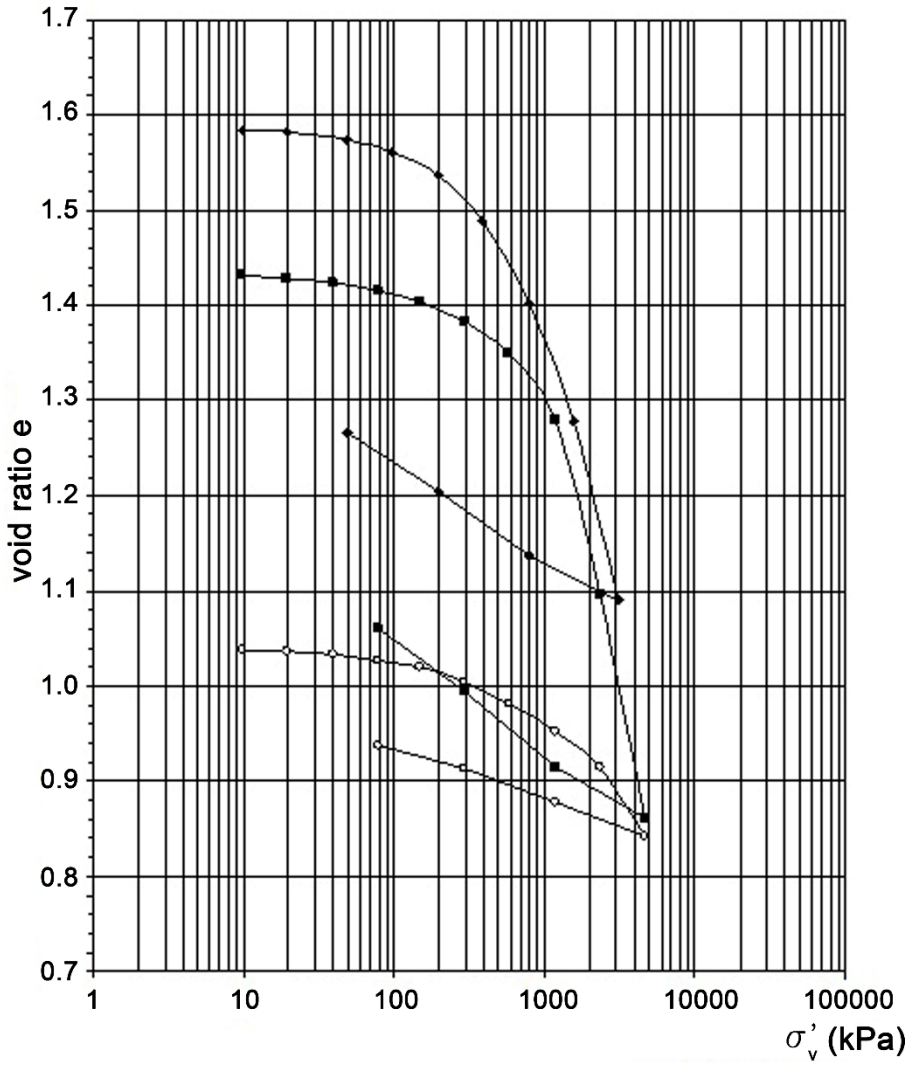

Figure 4.35 – Available results obtained for the oedometric tests carried out on the Miocene clay

Miocene sand

Based on the grain size distribution shown in Figure 4.37, this formation is quite homogeneous and can be classified as gravelly sand with silt. The Atterberg limits, obtained from the samples with higher fine percentage, define this soil as an inorganic clay with medium-low plasticity (Figure 4.38).

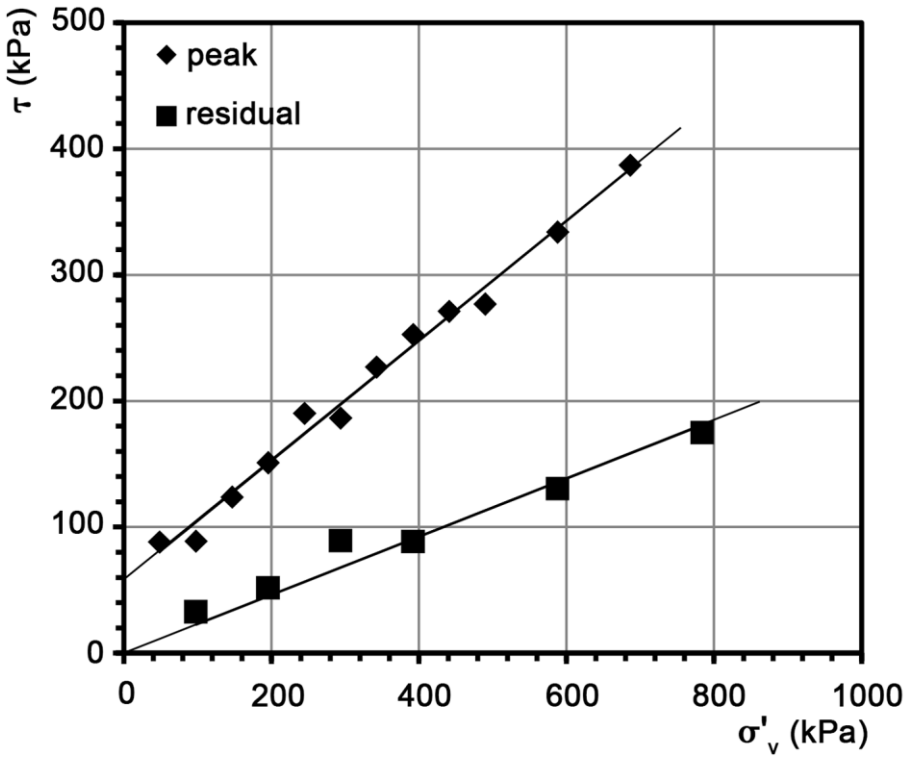

Figure 4.36 – Direct shear tests results for Miocene clay

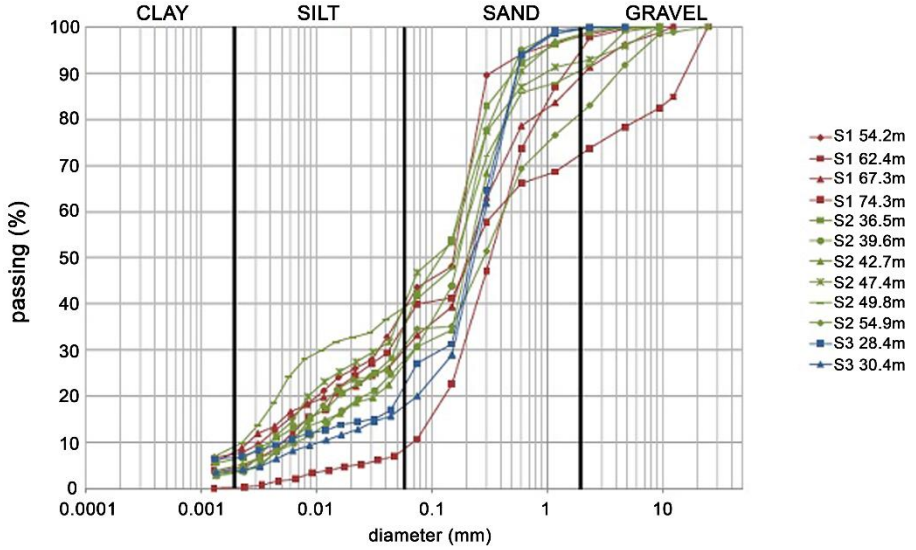

Figure 4.37 – Available grain size distribution for Miocene sand

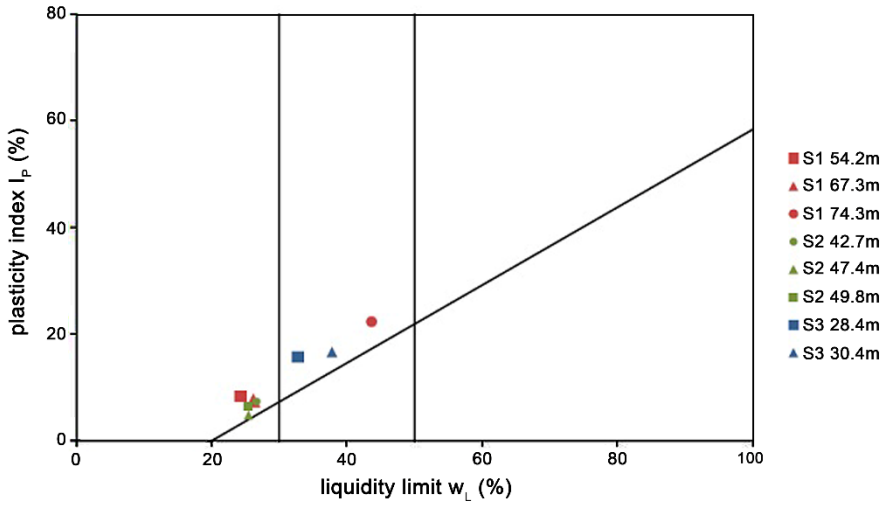

Figure 4.38 – Casagrande plasticity chart for Miocene sand

4.5 – Rainfall preceding the landslide

The landslide that occurred at Maierato on 15 February 2010 was preceded by a long rainy period which involved the years 2008 and 2009 as well as almost all the days of 2010 before the landslide. It is worth noticing that a great number of landslides occurred in the region of Calabria during this period. From 1 September 2009 to 15 February 2010 (for overall 168 days), a cumulative rain of about 900 mm was recorded at the rain gauge station of Vibo Valentia (about 8 km away from Maierato), where the daily recordings are available since 1919. Figure 4.39 shows in blue the cumulative rain in 168 consecutive days of the wettest hydrogeological years, from 1919 to the date of the landslide. Conte et al. (2018) defined a hydrological year the time period from 1 September of a year to 31 August of the following year. As can be seen from Figure 4.39, a cumulative rain of 900 mm was

exceeded only three times in the analyzed period, i.e. in 1920-1921, 1923-1924 and 1938-1939. It is worth noticing that the cumulative rain of 2008-2009 ranks ninth in the time series. Daily rainfall recorded at Vibo Valentia station from 1 September 2009 to 15 February 2010 is shown in Figure 4.40. Although the rain depths are not significantly high (the maximum value is 35.6 mm), precipitation is well distributed over the time period considered.

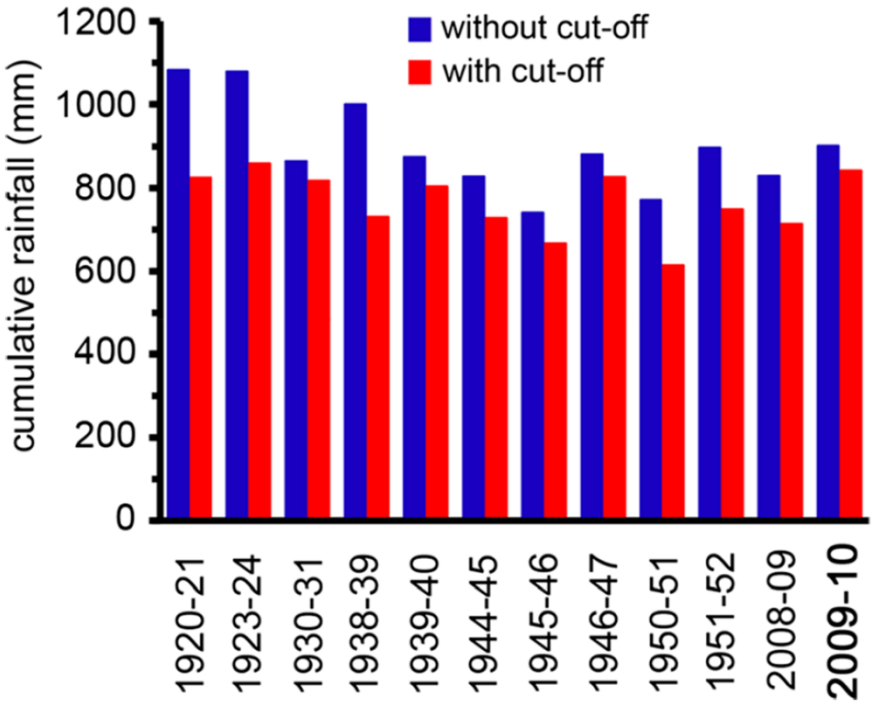

Figure 4.39 – Cumulative rain in 168 consecutive days of the wettest hydrological years from 1919 to the date of the landslide (in blue) and filtered cumulative rain in 168 consecutive days of the same years (in red)

Theoretically, this characteristic should facilitate infiltration (rather than the surface flow) and, consequently, it should provide a significant supply of groundwater. For this reason, Doglioni et al. (2013) proposed to filter the daily rain recordings using a cut-off threshold of 25 mm to approximately account for the effect of

runoff on infiltration. In other words, they assumed that rainfall exceeding that threshold did not contribute to infiltration but only to surface flow. The threshold value was established by Doglioni et al. (2013) accounting for the hydraulic properties of the outcropping soils. Based on this approximate assumption, they showed that the cumulative rain of the 20 days preceding the 15 February 2010 landslide has a return period of 105 years, and the first two months of 2010 are the wettest months of the last 20 years. Based on what just said, Conte et al. (2018) used the threshold established by Doglioni et al. (2013) to filter the daily rainfall recorded at Vibo Valentia station from 1 September 2009 to 15 February 2010. The respective cumulative rain is presented in red in Figure 4.39 along with the filtered cumulative rain in 168 consecutive days of the wettest hydrological years of the time series. As can be seen the cumulative rain of the 168 days preceding the landslide (841 mm) ranks second in the time series, being exceeded only by the cumulative rainfall of the hydrological year 1923-1924 (858 mm). Besides, Figure 4.39 shows that, except in the period 2008-2009, the last hydrological year with a significant value of the filtered cumulative rain dates back to the years 1951 and 1952 (i.e. about 60 years before the occurrence of the 2010 landslide), when the territory of Maierato was different. Indeed, a large area surrounding the landslide site has been almost completely urbanized in the last decades.

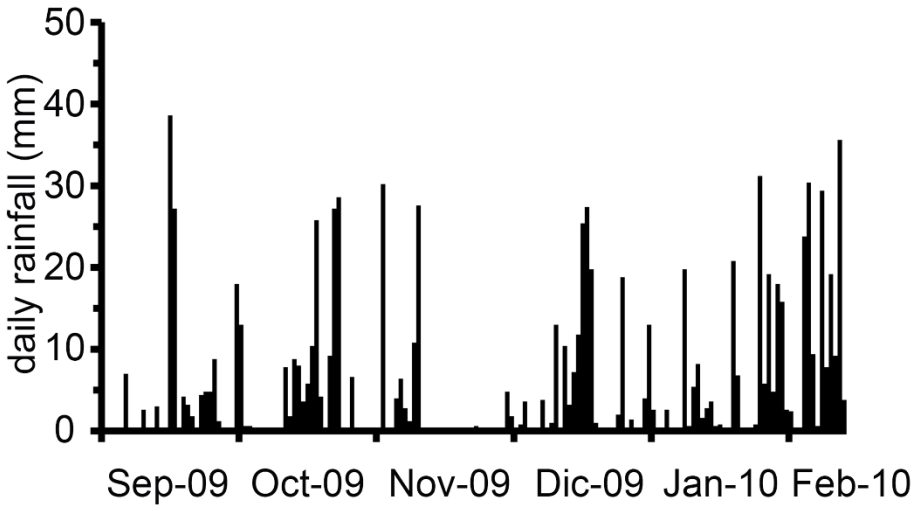

Figure 4.40 – Daily rainfall recorded at Vibo Valentia station from 1 September 2009 to 15 February 2010

Therefore, it is reasonable to suppose that this urbanization and the associated works, as well as the abandonment of some wells and springs previously employed for the water supply of Maierato, could have contributed to increase the groundwater supply in the long rainy period preceding the 2010 landslide.

4.6 – Interpretation of the landslide

Different interpretations of the Maierato landslide were provided by the different authors who studied it (Guerricchio et al. (2010); Gattinoni et al. (2012); Doglioni et al. (2013); Gattinoni & Scesi (2013); Borrelli et al. (2014); Conte et al. (2018)). Particularly, Guerricchio et al. (2010) and Doglioni et al. (2013) asserted that the landslide was a first-time slide although its activation was influenced by an ancient DSGSV. A similar opinion was given by Gattinoni et al. (2012) and Gattinoni and Scesi (2013), who

presented the results of a slope stability analysis carried out using the peak strength parameters for the involved soils. Additionally, these authors sustained that the slip surface developed almost completely in the Miocene sandstone and, only in the final part, it involved the evaporitic limestone formation. In disagreement with these authors, based on field surveys and examination of aerial photos, Borrelli et al. (2014) interpreted the 2010 landslide as the reactivation of a pre-existing landslide with the slip surface prevalently located in the Miocene marly clay overlying the sandstone formation. This hypothesis is confirmed during the work carried out for this dissertation by means of a FEM back-analysis, which is also documented in Conte et al. (2018). However, all these studies agree on the fact that a role of paramount importance for triggering the failure process was played by a significant increase in pore water pressure due to the abundant rainfall of the months preceding the event.

4.7 – Geotechnical model of the slope

Based on the results obtained from the investigations described in Section 4.4, a subsoil model was reconstructed and it is shown in Figure 4.41. This model was obtained with referring to the cross section of trace A-A (Figure 4.14). The mechanical properties assigned to each soil layer are specified in Table 4.V. These parameters were obtained from the results of the laboratory tests

previously described or by using reliable empirical relationships between these parameters and the data of the available field tests (Totani et al. (1999); Lancellotta (2009)).

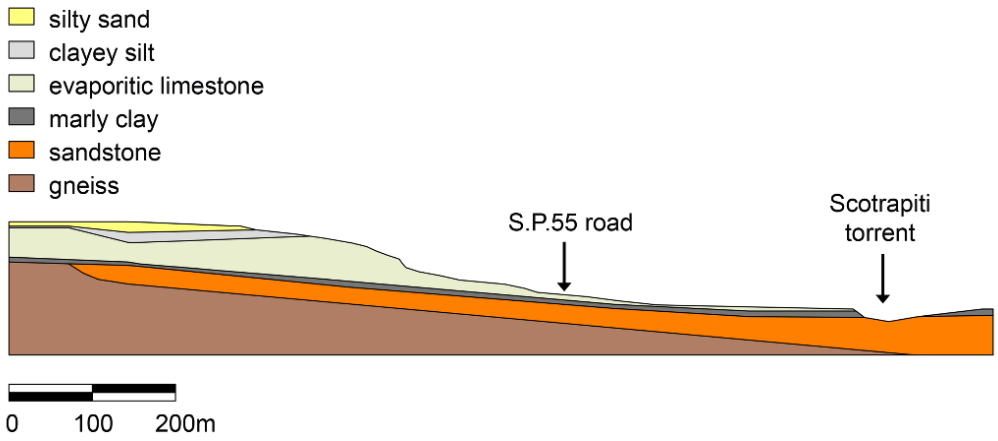

Figure 4.41 – Subsoil model of the slope before the 2010 landslide

Table 4.V – Soil parameters used in the analyses

	γ $\left(\frac{kN}{m^3}\right)$	E' (MPa)	ν' $(-)$	c'_p (kPa)	φ'_p (°)	c'_r (kPa)	φ'_r (°)	k $\left(\frac{m}{s}\right)$
Silty sand	19	80	0.30	0	37	0	31	1×10^{-6}
Clayey silt	19	20	0.30	15	26	0	15	2×10^{-9}
Evaporitic limestone	19	50	0.30	15	36	0	28	1×10^{-7}
Marly clay	18	12	0.40	57	25	0	13	1×10^{-9}
Sandstone	20	200	0.30	0	45	--	--	5×10^{-8}
Gneiss	21	400	0.30	--	--	--	--	1×10^{-8}

4.8 – Slope stability analysis

As already said in Section 4.6, one of the different interpretations of the Maierato landslide is presented in this study, by performing

an analysis of the trigger stage, described in this section, which will be extended in the following one in order to study the kinematics of the landslide during the post-failure stage. The same analysis is also presented by Conte et al. (2018). Considering the lack of field measurements before and during the failure process, a finite element analysis is performed in order to define, along with the available photos and videos taken during the event, the main factors of triggering and to interpret the failure mechanism of the slope. Particularly, the evolution of the deformation process occurring in the slope due to an increase of groundwater level is characterized by the development of zones where plastic strains are localized (shear zones). Such shear zones, propagating within the slope, lead to the development of a sliding surface. For this reason, the plastic strain invariant, k_{shear}, defined by Equation (2.160) is employed. Additionally, the safety factor of the slope is calculated as well, based on an approach similar to that followed in Section 3.7. Slope failure is attained by progressively raising the groundwater levels, starting from the levels measured after the landslide (Figure 4.42). The critical condition of groundwater regime is established in correspondence of a value of the safety factor equal to one and when the associated failure mechanism is similar to the one documented by the available images. The analysis refers to the time period from 1 September 2009 to 15 February 2010 (for overall 168 days) and

accounts for the effect of soil-water coupling. All analyses are carried out using the finite element code Tochnog (www.tochnogprofessional.nl).

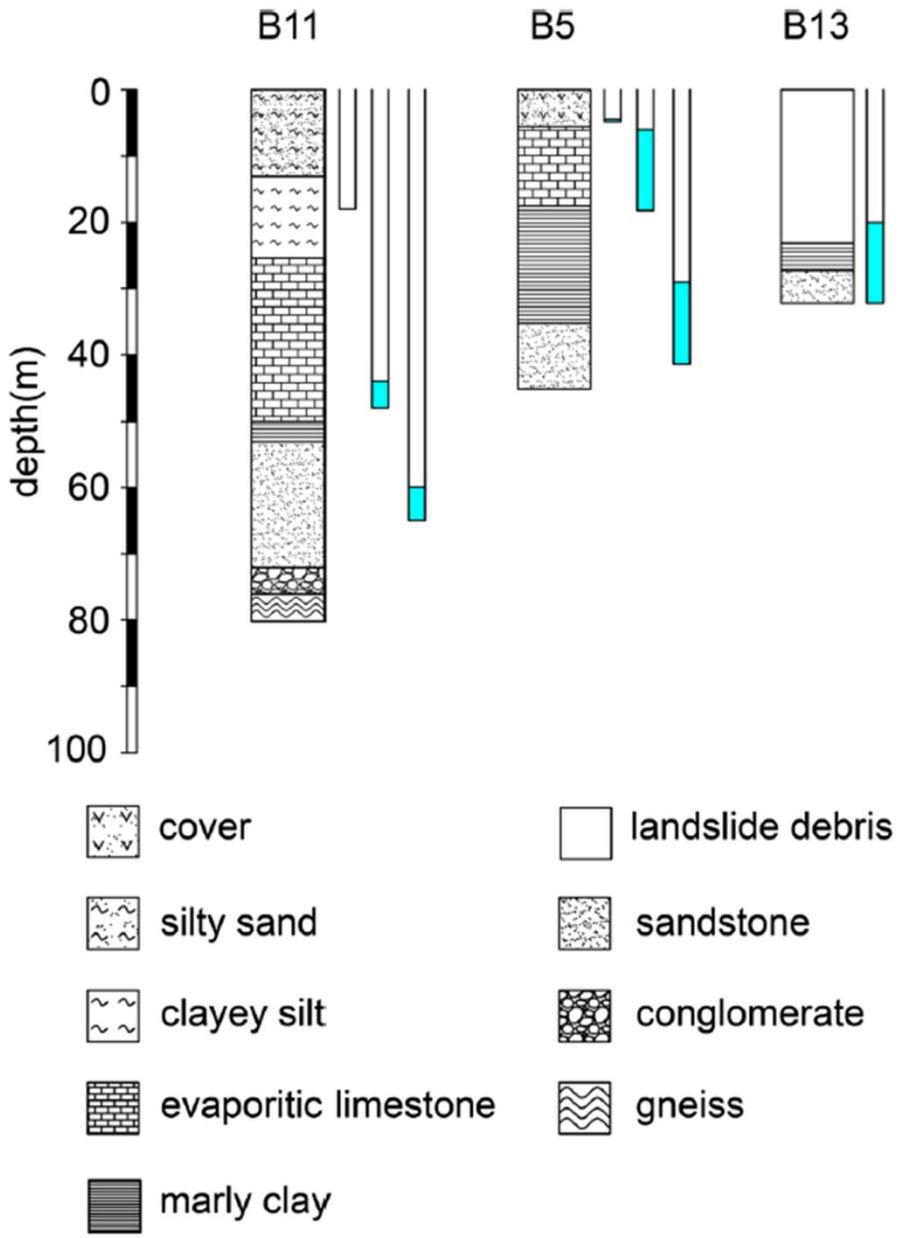

Figure 4.42 – Soil profile of some boreholes with the indication of the piezometric levels measured after the 2010 landslide (names of boreholes refer to Figure 4.8)

The mesh adopted in the calculation is shown in Figure 4.43. It refers to the same cross-section of the subsoil model shown in Figure 4.41, where the two pre-existing scarps at the elevations of

300 and 305 m a.s.l. are added. These pre-existing scarps are simulated by means of a 1 m thick layer characterized by the residual strength parameters of the concerning soil.

Figure 4.43 – Finite element mesh adopted in the analyses of the pre-failure phase of the Maierato landslide

The mesh shown in Figure 4.43 is made up of triangular elements with three nodes and one Gauss point (CTS elements). The base is impervious and fixed, whereas the vertical sides are constrained by rollers to prevent horizontal displacements. Two hydraulic heads are imposed at the upstream boundary to account for the presence of a different groundwater level in the evaporitic limestone and in the underlying soils. Such heads are initially established on the basis of the available measurements at the piezometers installed in the borehole B11 (Figure 4.42). Instead, due to the presence of the Scotrapiti torrent, a water table is set at the ground surface where the topographic section intercepts the torrent on the downstream side.

Since the landslide occurred after a long rainy period that likely saturated the soil up to a significant depth, it is assumed that the

effect of suction on soil properties is negligible. A linear elastic perfectly plastic Mohr-Coulomb model with angle of dilation equal to zero (confirmed from laboratory tests) is used to model the behavior of all soils with the exception of the gneiss and the marly clay. Particularly, a linear elastic behavior is assumed for the gneiss since this geological formation was not involved in the landslide. Additionally, to account for the strain-softening behavior of the marly clay (Figure 4.44), a Mohr-Coulomb plastic law is adopted and the strain-softening behavior of the soil is simulated by reducing the shear strength parameters with the accumulated deviatoric plastic strain k_{shear}, as explained in Section 2.8.5.

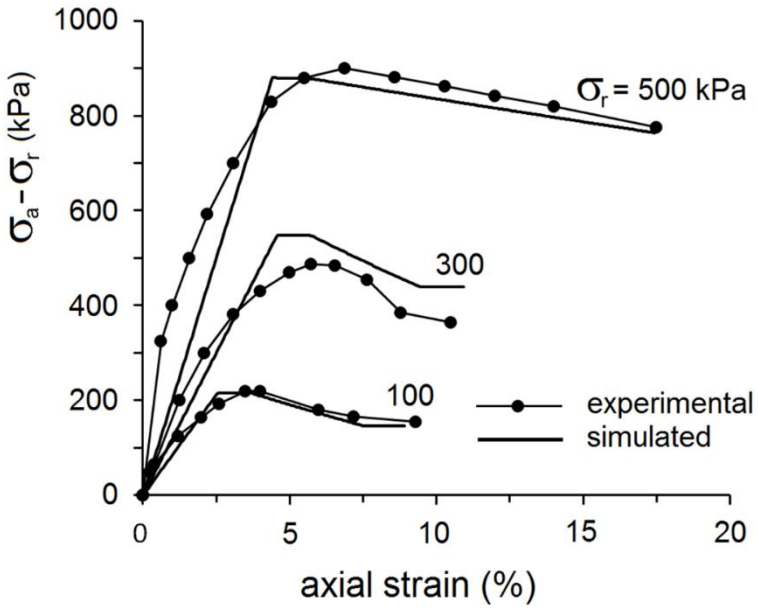

Figure 4.44 – Experimental and simulated results of some consolidated-drained triaxial tests performed on samples of marly clay

The threshold values of the deviatoric plastic strain k^{p}_{shear} and k^{r}_{shear} are required. Particularly, the first one represents the

maximum strain corresponding to the peak behavior of the soil, whereas the second one denotes the strain level beyond which the soil strength parameters assume their residual values. These two threshold values as well as the elastic modulus E are assessed by matching the experimental results obtained from the triaxial tests and reported in Figure 4.44 with those obtained simulating numerically the same tests within the framework of a trial and error procedure. The shear strength parameters used to perform this simulation are those obtained from the same tests and reported in Table 4.V. A comparison between the experimental stress-strain curves and those predicted using the above-described constitutive model in conjunction with the calibrated parameters is reported in Figure 4.44. As can be seen, the results of the numerical simulation agree reasonably well with those obtained from the laboratory tests. For the stress-strain curve with a confining pressure of 300 kPa, which corresponds approximately to the stress level acting on average in the clay layer, the calibrated values of k_{shear}^{p} and k_{shear}^{r} are respectively 0.01 and 0.05. Additionally, the value of E that provides the best agreement between experimental and theoretical results is 12 MPa in conjunction with a value of the Poisson's ratio equal to 0.4. As shown by Nova et al. (2003), the occurrence of plastic volumetric strains may also contribute to a mechanical degradation of the limestone. Additionally, this material may

experience significant deformations when it is undergone a saturation process (Ciantia et al. (2015)). However, these effects are disregarded in the present study. The initial stress state of the slope is reproduced using the well-known procedure of gravity loading. Afterwards, the associated displacements are reset to zero. For the sake of completeness, an alternative procedure is also used to generate the initial stress state within the slope. Particularly, a soil deposit with initially horizontal ground surface is first considered. Afterwards, a volume of soil is progressively removed until the pre-failure configuration of the slope is obtained. The results obtained in this latter case are the same of those obtained starting with the gravity loading procedure. By considering four possible scenarios, different analyses are performed assuming that the marly clay behaves as a strain-softening material simulated as previously described. An overview of the four scenarios accounted for is reported in Table 4.VI. They are carefully explained in the following sub-sections.

Table 4.VI – General overview of the FEM analysis carried out

Analysis A	Analysis B	Analysis C	Analysis D
Peak strength parameters for all materials.	Residual strength parameters for a shear zone at the base of the evaporitic limestone formation and for two additional shear zones (in the same soil) emerging on the ground surface at 300 and 305 m a.s.l.. Peak strength parameters for the other materials.	Residual strength parameters for a shear zone located in the marly clay. Peak strength parameter for the other materials.	As Analysis C, with two additional shear zones, located in the evaporitic limestone formation, emerging on the ground surface at 300 and 305 m a.s.l. characterized by residual strength parameters.

4.8.1 - Analysis A

The first analysis is performed under the hypothesis that all the soils involved in the landslide are characterized by the peak strength parameters, in order to check out if the 15 February 2010 Maierato landslide was a first-time failure. Results in terms of accumulated deviatoric plastic strain, k_{shear}, are shown in Figure 4.45. Such results are obtained under the assumption that the groundwater level raised up to the ground surface. As can be seen, the deviatoric plastic strains generated in the slope due to the raising of the groundwater level are quite small everywhere (k_{shear} < 0.003). Particularly, in the marly clay layer $k_{shear} \ll k^{p}_{shear}$, i.e. the shear strength parameters are those corresponding to the peak condition although a strain-softening behavior is assumed for this formation.

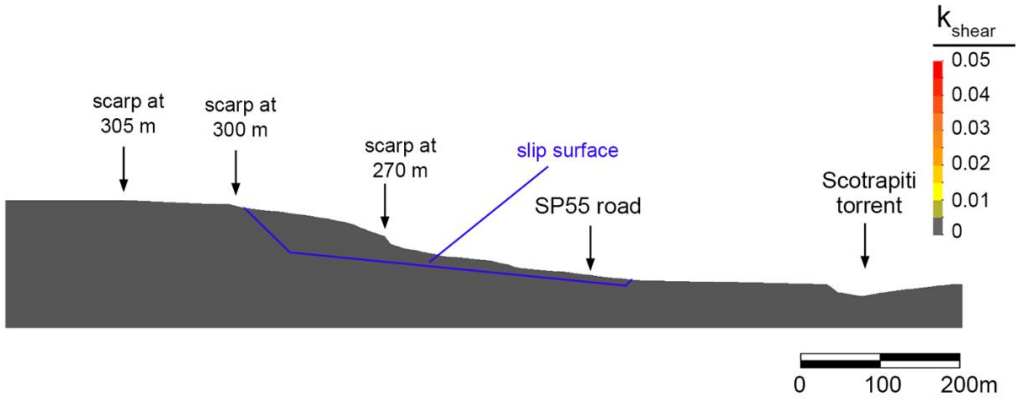

Figure 4.45 – Accumulated deviatoric plastic strain, k_{shear}, calculated in the Analysis A, with the indication of the failure surface considered for the assessment of the safety factor of the slope

Similar results are obtained under the conservative assumption that the evaporitic limestone behaves as a strain-softening

material as well, assuming the same values of the marly clay for the threshold deviatoric plastic strains. These results point out that no progressive failure occurred in the slope even if the groundwater level is raised up to the ground surface. Besides, referring to the slip surface shown in Figure 4.45, a value of SF = 1.73 is obtained. A practically identical result (SF = 1.74) is obtained using the limit equilibrium method. Based on these results, it could be concluded that the 15 February 2010 Maierato landslide was not a first-time failure.

4.8.2 – Analysis B

The second analysis is carried out by assigning the residual strength parameters of the evaporitic limestone to a shear zone located at the base of this geological formation and to two additional shear zones (located in the same formation) connecting the former shear zone with the ground surface at 300 and 305 m a.s.l. (Figure 4.43). The location of these shear zones is established accounting for the observations on the landslide body. Peak shear strength parameters are assumed for the other materials. This scenario corresponds to the assumption that a reactivation of a pre-existing landslide occurred with the sliding surface completely developed in the evaporitic limestone formation. The most critical situation is obtained by raising the groundwater table of about 44 m respect the initial level measured

in the borehole B11 (Figure 4.42), i.e. with the final position of the groundwater level quite close to the ground surface. In this condition, significant plastic shear strains occurred only in the shear zone that intercepts the ground surface at the elevation of 300 m a.s.l. (Figure 4.46).

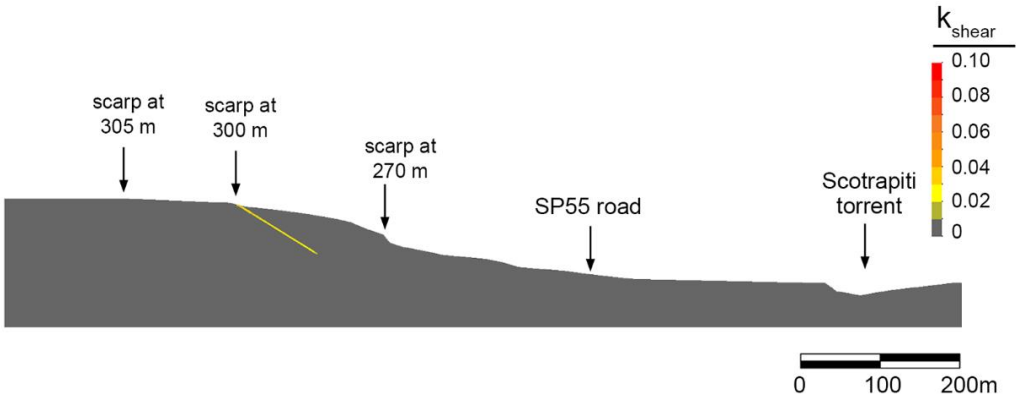

Figure 4.46 – Accumulated deviatoric plastic strain, k_{shear}, calculated in the Analysis B

However, the complete formation of a failure surface does not occur. The value of the safety factor obtained with referring to the same slip surface shown in Figure 4.45, is *SF* = 1.16. Analogously to Analysis A, the safety factor obtained with the limit equilibrium methods is practically the same (*SF* = 1.17). Therefore, these results exclude the possibility that the failure process occurred along a pre-existing failure surface localized exclusively in the evaporitic limestone formation.

4.8.3 – Analysis C

The third analysis is performed by assigning the residual shear strength parameters only to a shear zone located in the marly clay

layer, whereas the peak strength parameters are assumed for all the other materials. This scenario corresponds to the assumption that the marly clay was affected in the past by significant shear strains that reduced the strength of this soil to the residual condition. By increasing the piezometric levels, plastic strains develop in this shear zone involving the overlying soils as well (Figure 4.47). Consequently, a slip surface develops in the slope with a safety factor which equals one when the groundwater level is undergone a raising of about 8 m with respect to the condition initially assumed (Figure 4.42). This slip surface is consistent with what observed in the lower portion of the slope, where a slip surface of new formation developed at the elevation of 285 m a.s.l. (Figure 4.6).

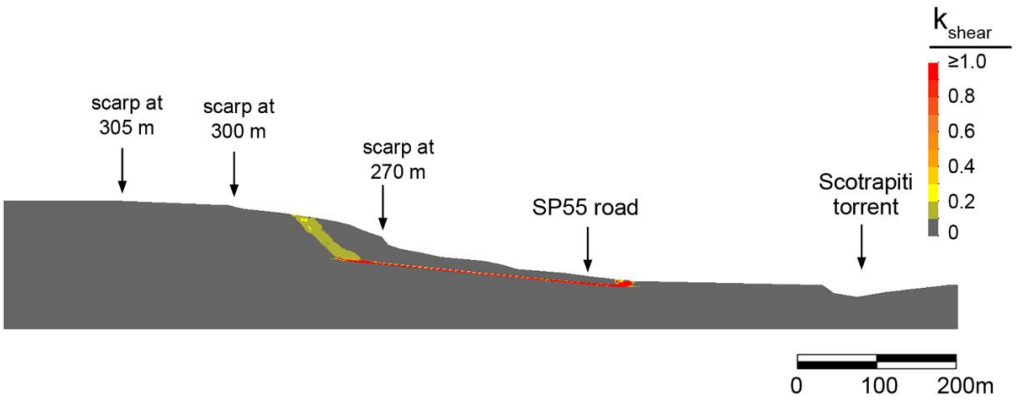

Figure 4.47 – Accumulated deviatoric plastic strain, k_{shear}, calculated in the Analysis C

However, the pre-existing slip surface that reaches the ground surface at the elevation of 300 m a.s.l. is not involved. Therefore, although the assumption that the marly clay was affected in the past by important shear strains is reasonable, the obtained

results do not completely account for properly the observed failure mechanism. This results are confirmed by a simple calculation carried out by means of the limit equilibrium method. Indeed the safety factor calculated on the slip surface indicated in Figure 4.45 is *SF* = 1.04, which means that the soil mass above this slip surface is stable although with a low level of safety, whereas the safety factor calculated on the slip surface defined by the shear zone defined by the accumulated plastic strain (Figure 4.47) is *SF* = 0.92.

4.8.4 – Analysis D

In the last analysis carried out, two shear zones are added in the upper portion of the slope in the model considered in Analysis C. These shear zones develop in the evaporitic limestone and connect the underlying shear zone in the marly clay layer with the pre-existing scarps at the elevation of 300 m and 305 m a.s.l. (Figure 4.43). In Analysis D, the residual strength parameters are assumed for the soils in these shear zones, whereas the peak strength parameters are assigned to the other soils. In other words, it is assumed that the slope failure occurred along a pre-existing slip surface defined by the above-specified shear zones. Figure 4.48 shows the evolution of accumulated deviatoric plastic strain induced by the progressive raising of the piezometric levels

detected in the evaporitic limestone and in the sandstone after the landslide (Figure 4.42).

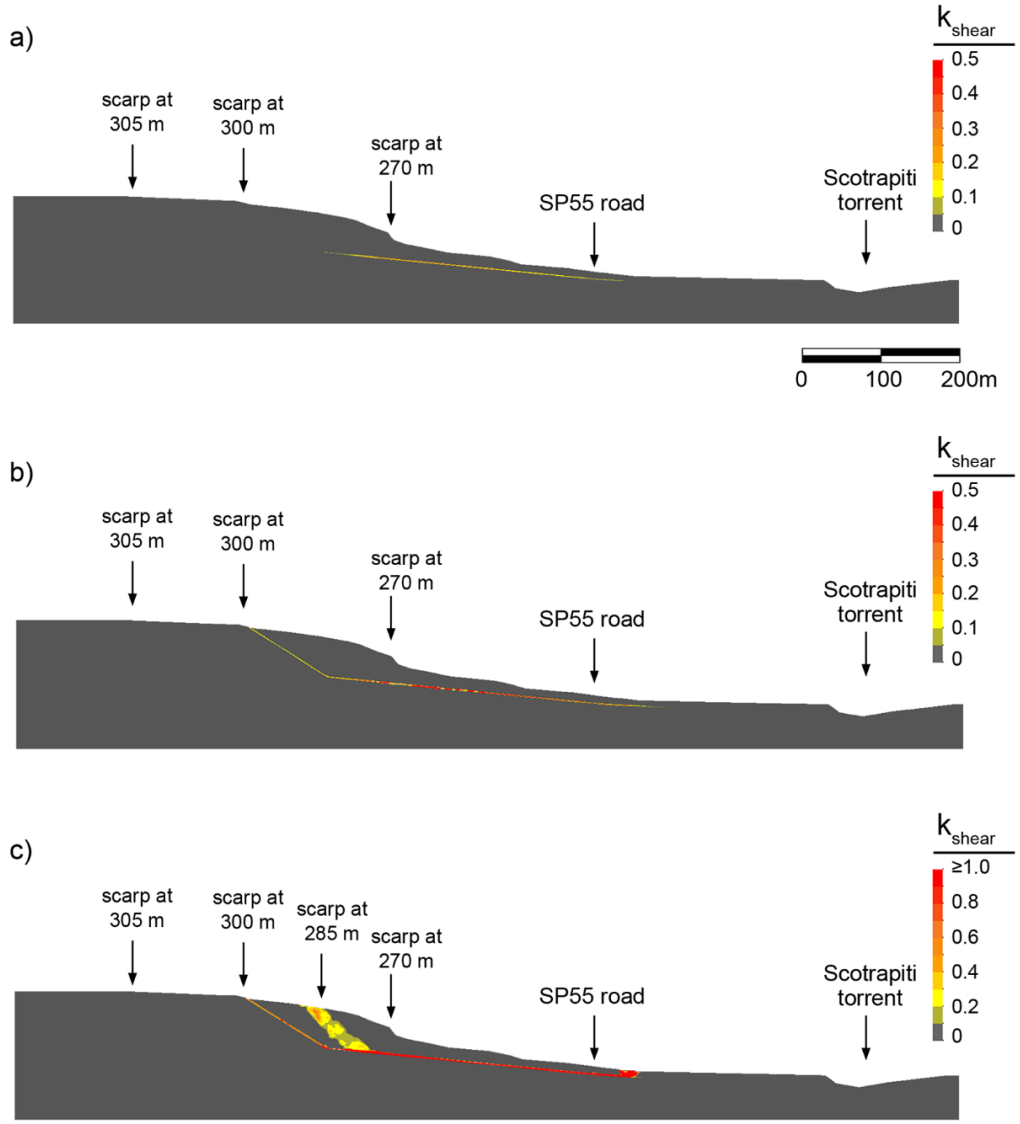

Figure 4.48 – Accumulated deviatoric plastic strain, k_{shear}, calculated in the Analysis D. a) deformation process affecting the shear zone in the marly clay layer; b) formation of the slip surface emerging at the elevation of 300 m a.s.l.; c) formation of the second slip surface emerging at the elevation of 285 m a.s.l.

As can be seen, the deformation process initially affects the lower portion of the slope, developing within the shear zone in the marly clay (Figure 4.48a). By furtherly increasing the groundwater level, plastic strains involve also the shear zone (in the evaporitic

limestone) that intersects the pre-existing scarp at the elevation of 300 m a.s.l. (Figure 4.48b). Consequently, a slip surface developed in the marly clay and in the limestone, whose location is consistent with that indicated by the red arrows in Figure 4.5. Afterwards, a second failure surface emerged at the elevation of 285 m a.s.l. (Figure 4.48c), consistently with the position of the slip surface indicated by blue arrows in Figure 4.6. The upstream part of this failure surface developed in the evaporitic limestone where the parameter assigned are the peak ones.

Therefore, this analysis shows that the first slip surface is a pre-existing slip surface, whereas the second slip surface is in part a first-time failure surface. Besides, these results clarify the different interpretations of the 15 February 2010 Maierato landslide provided by other authors (Guerricchio et al. (2010); Doglioni et al. (2013); Gattinoni et al. (2012); Gattinoni & Scesi (2013); Borrelli et al. (2014)).

It is worth noticing that the shear zone connecting the marly clay layer to the scarp at the elevation of 305 m a.s.l. is not affected by significant strains (Figure 4.48c) although the residual strength parameters are assigned to the soil of this zone (evaporitic limestone).

Besides, this result is consistent with what really observed (as shown by the orange arrows in Figure 4.7). A unit value of the safety factor is obtained when the groundwater level is raised for

about 8 m in the upper portion of the slope, with respect to the piezometric level measured in the borehole B11 after the landslide (Figure 4.42). Similar results are obtained using the limit equilibrium methods. Indeed, a value of the safety factor $SF = 0.92$ is obtained with referring to both the slip surfaces obtained from the FEM simulation.

This result is consistent with what found by Gattinoni & Scesi (2013), who numerically simulated the change of groundwater regime occurred in the subsoil of Maierato owing to the rainfall preceding the landslide. Particularly, they found that this rainfall was potentially able to raise the hydraulic heads of at least 10 – 15 m higher than those observed during the investigation field carried out after the landslide. In the lower portion of the slope, the critical position of groundwater level is close to the ground surface.

Lastly, as reported in Figure 4.49 (in an exaggerated scale), the evolution of the calculated soil displacements is also provided. As can be seen, the portion of the slope extending from the SP55 road to the scarp at the elevation of 270 m a.s.l. is the first zone to move, accordingly to what really observed (Figure 4.4). With the progressive raising of the groundwater level, the soil volume affected by movement extended upstream causing a consequent increase of the height of the scarps at 270, 285 and 300 m a.s.l..

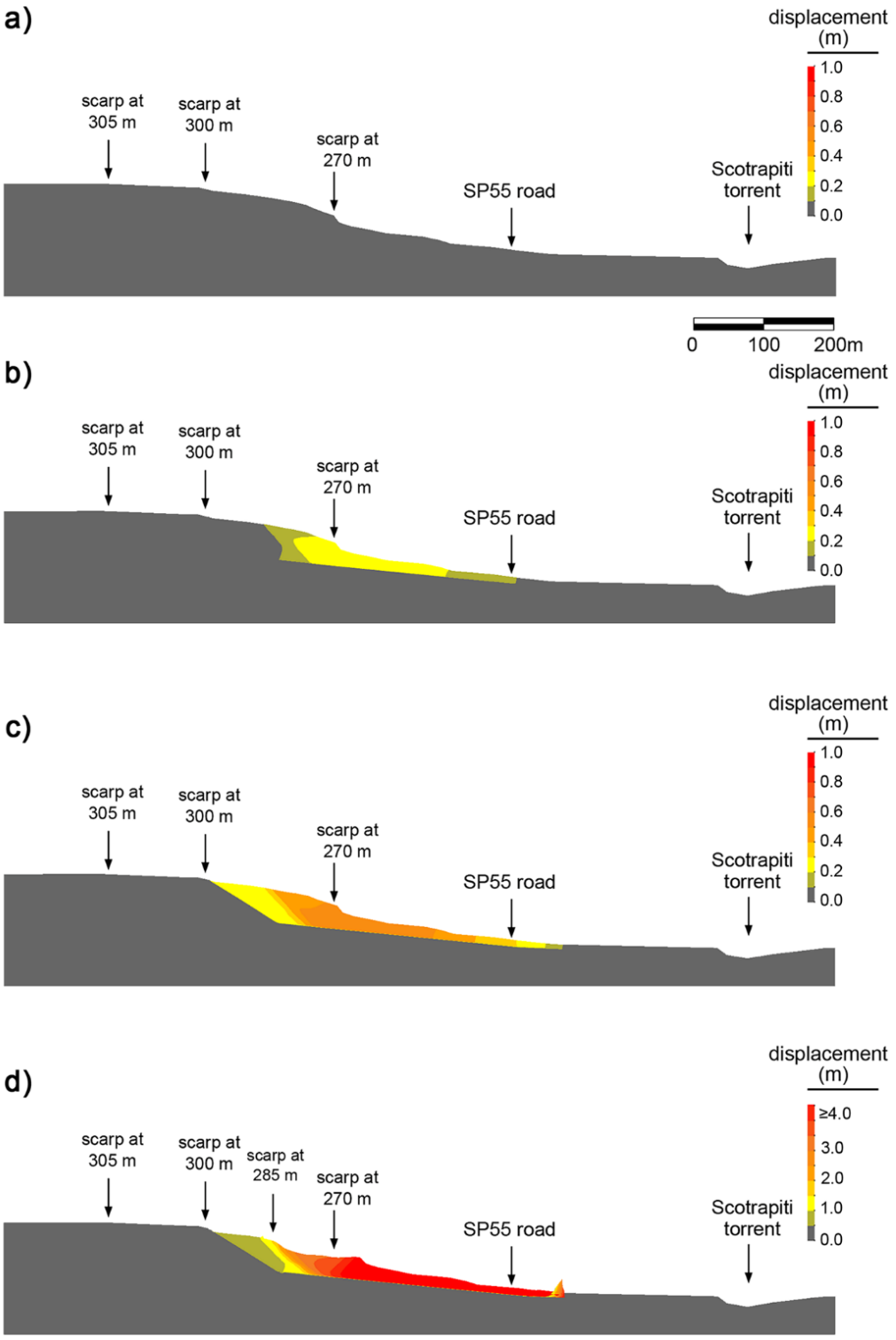

Figure 4.49 – Snapshots of the total displacement field (in an exaggerated scale) caused by a progressive increase in the groundwater level, Δh, measured from the piezometric level in the borehole B11 (Figure 4.42). a) Δh = 0 m; b) Δh = 6 m; c) Δh = 7 m; d) Δh = 8 m.

4.9 – Post-failure analysis of the landslide using MPM

The finite element analysis of the trigger phase of the 15 February 2010 Maierato landslide carried out in the present study (described in Section 4.8) allows a reasonable interpretation of the event to be given, since the failure mechanism obtained from the simulation is in pretty good agreement with what actually observed in field and documented by the photos and videos taken during the event. Indeed, shape and position of the slip surfaces as well as the progressive development of soil displacements for the different portions of the landslide body are consistent with those actually observed. On the other hand, the simulation is not suitable to simulate the post-failure stage owing to the severe mesh distortion and consequent loss of accuracy of the calculation. Indeed, the soil displacements predicted by the FEM simulation, which are reported with an exaggerated scale in Figure 4.49, are characterized by a maximum value of about 4 m, whereas the soil displacements that really occurred were so high that the landslide body could reach and bury the Scotrapiti torrent. Analogously to the Senise landslide, these results highlight the unsuitability of the finite element method for analyzing problems involving extremely large displacements and deformations. To overcome such a limitation, the post-failure stage of the Maierato landslide is analyzed separately in the present study using the material point method. Similarly to the

Senise landslide, the analysis of the post-failure stage of the Maierato landslide can be seen as an extension of the analysis of the pre-failure and failure stages described in Section 4.8. Consequently, the initial condition of the MPM simulation corresponds to the final condition of the FEM analysis. Therefore, in the initial condition of the MPM analysis the groundwater table has already undergone the raising from the initial position to the critical one that led the slope to failure in the finite element analysis (i.e. 8 m above the initial condition of the FEM analysis), slip surfaces have already developed and the unstable soil mass is completely defined.

All analyses are performed by means of the software Anura3D, developed by the Anura3D MPM Research Community (www.anura3d.com), with referring to the cross-section A-A indicated in Figure 4.14. The hypothesis of plane-strain condition is assumed by means of a computational mesh made up of triangular elements, whose average size is about 5 m, with the exception of the elements belonging to the shear band, which are characterized by an average size of 1 m. This mesh size is selected based on a preliminary mesh sensitivity analysis (see Chapter 3). The strain smoothing procedure described in Section 2.6.4 is used. The soils below the groundwater table are modelled as saturated materials, whereas the ones above the groundwater table are modelled as dry. The effect of suction on soil properties

is considered negligible. In both cases the single-point formulation is used. Initially, three material points are distributed within each element. The initial stress state is reproduced by using the well-known procedure of gravity loading (see Section 2.6.2), i.e. by multiplying the gravity acceleration (9.81 m/s^2) for a multiplier which is gradually increased from 0 to 1, under the hypothesis that all materials behave elastically. Since the gravity loading is a quasi-static problem, a coefficient of local damping $\alpha = 0.75$ is used in this stage of the simulation, according to Section 2.6.3. The next stage of the analysis consists in the simulation of the post-failure stage of the landslide, which is triggered by switching the behavior of all the involved materials from elastic to elastic perfectly plastic in conjunction with the Mohr-Coulomb failure criterion described in Section 2.8.4. Indeed, under this hypothesis, the material points belonging to the unstable soil mass are no longer in equilibrium and, therefore, they start moving until a new condition of equilibrium is reached. Every analysis is stopped when there are no material points moving anymore, i.e. after each material point reaching its final position of equilibrium. No damping is used during this stage.

The configuration of material points at the end of the simulation defines the final numerical profile of the landslide that has to be compared to the one detected in field. Indeed, analogously to the Senise landslide, also the analysis of the post-failure stage of the

Maierato landslide is encouraged by the availability of accurate information regarding the geometry of the slope before and after the event. A comparison between the slope profiles detected before and after the landslide with referring to the cross-section of trace A-A (Figure 4.14) is reported in Figure 4.50.

The analyses carried out to simulate the post-failure stage of the 15 February 2010 Maierato landslide are reported in the following subsections. Particularly, three possible scenarios are accounted for, in order to identify the one that better resembles what really happened.

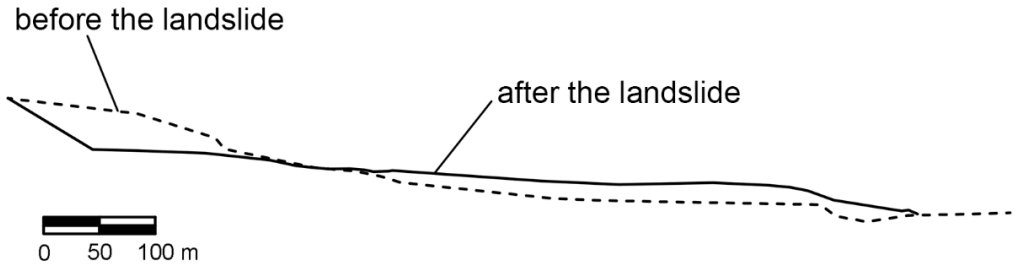

Figure 4.50 – Topographic profile of section A-A before and after the landslide (the trace of section A-A is indicated in Figure 4.14)

4.9.1 – Analysis I

The first analysis corresponds to the exact extension of the analysis of the pre-failure stage described in Section 4.8.4. Then, the aim of this analysis is to simulate the deformation mechanisms which could not be simulated in the analysis described in Section 4.8.4 due to the lack of convergence of the finite element method after the development of the slip surface.

Therefore, the unstable soil mass is already existing and it is separated from the stable soil mass by the slip surface, which is already and completely developed. The one-phase single-point formulation is used to model the behavior the soil above the groundwater level, whereas the two-phase single-point formulation is used to model the soil below it. In order to reduce the computational cost of the analysis as well as to obtain a reasonable value for the critical time step (Equation (2.111)), a high value of permeability is used ($k = 10^{-2}\ m/s$) for all the soils involved in the landslide. Therefore, the analysis is performed in drained conditions. However, according to Yerro (2015), a different value of permeability should not affect the final result in terms of soil displacement and final profile. Due to the high values of the accumulated deviatoric plastic strains calculated in the analysis of the pre-failure stage, the assumed values of the operative shear strength parameters of the soils involved in the landslide are those corresponding to the residual condition. Based on the results discussed in Section 3.8.4, this assumption concerns all the materials involved in both the slip surfaces and the body of landslide. On the contrary, the peak strength parameters are assumed for the materials not involved in the landslide. The values of the geotechnical parameters reported in Table 4.V are used. Besides, the groundwater level is located in the position corresponding to the final step of the Analysis D described in

Section 4.8.4, i.e. 8 m above the initial position deduced on the basis of the borehole B11 (Figure 4.42). The geometrical model corresponding to this situation is shown in Figure 4.51.

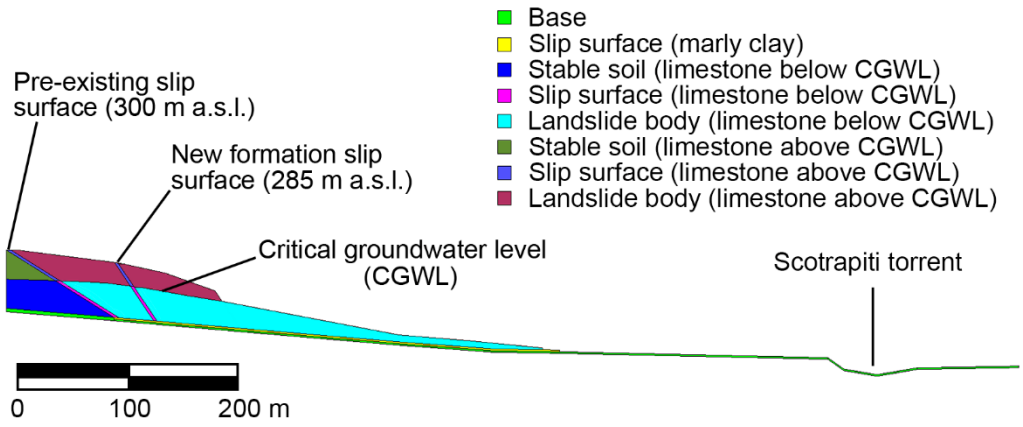

Figure 4.51 – Scheme showing the geometry of the unstable soil mass for Analysis I

It is worth noticing that the model reported in this figure is limited only to the portions of the slope required to simulate the post-failure stage of the landslide, i.e. other additional information included in the model reported in Figure 4.41 to perform the analysis of the pre-failure stage are discarded. Particularly, since the pre-existing slip surface emerging at the elevation of 305 m a.s.l was not reactivated in the landslide (as also confirmed by the FEM analysis of the trigger phase), this latter is excluded from the model along with the whole geometry behind the pre-existing slip surface emerging at the elevation of 300 m a.s.l.. Besides, the soil beneath the part of slip surface that developed in the marly clay as well as the portion of slope which the landslide body moved above are synthetized as a thin layer of elastic material, indicated as 'Base' in Figure 4.51. This choice allows a great number of

useless material points to be avoided from the calculation, resulting in a much faster simulation, without affecting the final results. The slip surface of new formation that emerged at the elevation of 285 m a.s.l., which is part of the result of the analysis of the trigger phase, is already existing at the beginning of the simulation of the post-failure stage and is therefore accounted for in the analysis as well. Residual strength parameters are assigned to the materials indicated as “slip surface” and “landslide body” in Figure 4.51, whereas peak strength parameters are assigned to the materials indicated as “stable”, which are those not involved in the landslide. The computational mesh used to perform the simulation is reported in Figure 4.52.

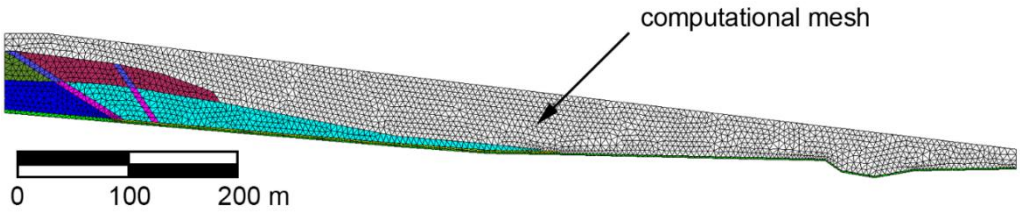

Figure 4.52 – Computational mesh used for Analysis I (material legend is that reported in Figure 4.51)

The FEM analysis of the trigger stage stopped when the groundwater level was raised of 8 m above the initial level, with no possibility to simulate what happened after failure. This limitation is overtaken in the present study with the use of the material point method. Therefore, after the gravity loading procedure, the second stage of the calculation consists in the analysis of the post-failure stage of the landslide, which is

simulated by switching the behavior of the involved materials from elastic to elastic perfectly plastic. The comparison between detected and calculated post-failure profiles is reported in Figure 4.53.

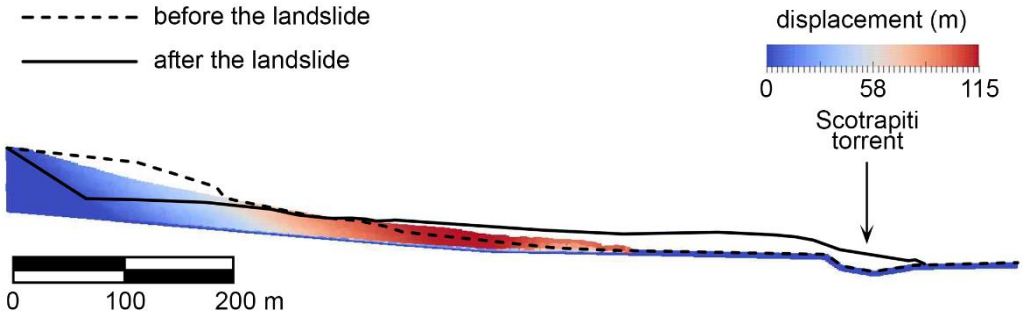

Figure 4.53 – Comparison between predicted and observed post-failure profiles of the landslide for Analysis I

Although no benchmark was available to measure the average displacement of a reference point on the landslide body, it is clear that the calculated maximum displacement, which is about 115 m, is not enough to catch the detected post-failure profile.

Indeed, the soil involved in the landslide was actually undergone so high displacements that it could reach, cover and bury the riverbed of the Scotrapiti torrent, whereas the calculated run-out distance (which is on the order of 65 m) is not enough to cover this length.

Therefore, the post-failure profile obtained from the numerical simulation is completely different from the detected one.

Consequently, it can be asserted that this analysis does not account for what really occurred.

4.9.2 – Analysis II

In an attempt to improve the simulation described in Section 4.9.1, a second analysis is carried out by considering a higher groundwater level. Indeed, Gattinoni & Scesi (2013) asserted that the Maierato landslide could have been triggered due to a raising of the groundwater level ranging between 10 m and 15 m (against the value of 8 m adopted in the previous section). Therefore, the analysis presented in this section is performed assuming the groundwater table in a position raised of 15 m with respect to the initial position defined in Section 4.8 on the basis of the piezometric measurements concerning the borehole B11 (Figure 4.42). All the other characteristics of the analysis are kept unchanged. The obtained results in terms of comparison between post-failure profile obtained from the numerical simulation and post-failure profile detected in field are reported in Figure 4.54.

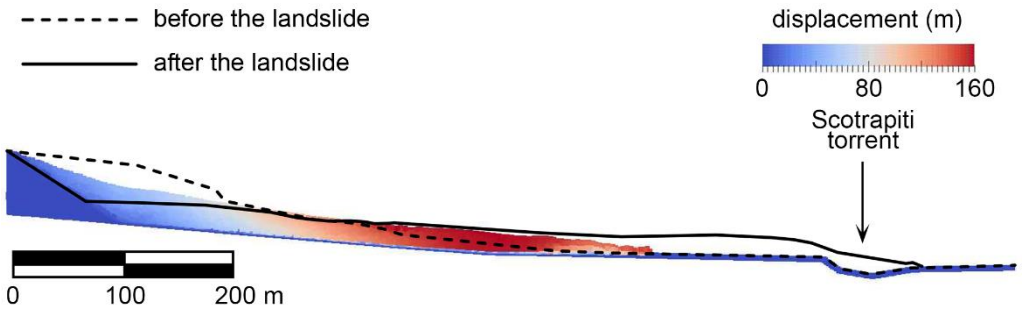

Figure 4.54 – Comparison between predicted and observed post-failure profiles of the landslide for Analysis II

As can be observed, due to the higher values of pore water pressure, a maximum displacement of the landslide body of about 160 m is obtained, which is greater than that calculated in the

previous section. However, although also the run-out distance is greater (on the order of 85 m), it is still not enough to reach the Scotrapiti torrent. Therefore, analogously to the previous case, this analysis is not representative of the post-failure stage of the Maierato landslide.

4.9.3 – Analysis III

A possible explanation to the discrepancies between the results obtained in Sections 4.9.1 and 4.9.2 with the observed phenomenon could be because these analyses are not capable to account for the change of mechanical behavior underwent by the body of landslide. Indeed, as documented by Borrelli et al. (2014) and by the videos filmed during the event, the evaporitic limestone formation was subjected to a change of its mechanical characteristics, assuming consequently a behavior similar to that of a viscous fluid. Hungr et al. (2014) stated about this landslide: "*The high velocity and flow-like character of the landslide suggests that increase of pore-pressure took place, so that the climax of the movement seen on the video could also be termed a flowslide*". According to the same authors, indeed, saturated granular soils (as those involved in this landslide) can fully or partially liquefy during or after failure and create extremely rapid flowslides. In addition, also Gattinoni & Scesi (2013) considered the possibility that a phenomenon of static liquefaction occurred.

These statements are also confirmed by Figure 4.55, which shows that the envelope of the different grain size distribution curves obtained from the available samples of evaporitic limestone coming from the borehole $S_{UNICAL,3}$ (Figure 4.30) is totally included in the range of the grain size distribution of liquefiable soils.

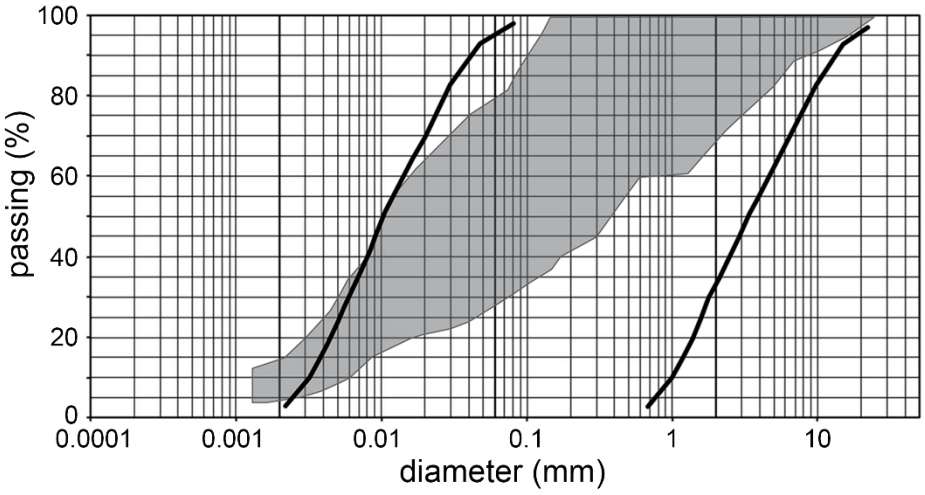

Figure 4.55 – Comparison between the grain size distribution of the evaporitic limestone (grey shaded area) with that of the liquefiable soils (black curves)

Therefore, with the purpose of improving the simulation, a further analysis is performed by accounting for the crucial role that the evaporitic limestone formation played in the post-failure stage of this landslide. To this aim, the analysis is carried out by assuming an undrained behavior for this latter soil (which the whole body of landslide is mainly made up of), using the Tresca model to capture the rapid response of the soil materials to loading and deformation, following Yerro et al. (2018). Indeed, a change in undrained shear strength associated with excess pore water generation should have occurred. Therefore, a strain-softening analysis capable to account for the degradation in undrained

resistance, down to its residual value, with increasing pore-water pressure would be appropriate. However, due to the complexity of the problem as well as the lack of experimental data concerning this latter aspect, it is considered worthwhile to use a representative value of strength, capable to properly account for the real phenomenon. Then, a back-analysis is performed in order to find an operative value of the liquefied strength which provides the best agreement between prediction and observation. The geometrical model considered to perform this analysis is analogous to that reported in Figure 4.51. The undrained behavior is considered for the portion of evaporitic limestone below the groundwater level. Among all the analyses carried out, the best results are obtained when an operative value of the liquefied strength $c_u = 35\ kPa$ is used. The comparison between the post-failure profile obtained from the numerical simulation and the one detected in field is reported in Figure 4.56.

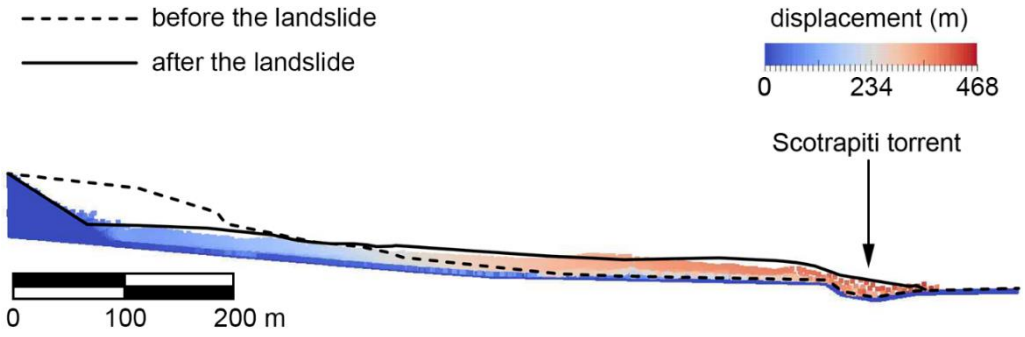

Figure 4.56 – Comparison between predicted and observed post-failure profiles of the landslide for Analysis III

The results of this latter simulation are characterized by a post-failure profile that matches the detected one sufficiently well,

providing a calculated run-out distance comparable to the detected one. Indeed, as really happened, the unstable soil mass is able to travel a distance of over 450 m so that it can cover and bury the riverbed of the Scotrapiti torrent.

Furthermore, to analyze the landslide kinematics, the results of Figure 4.57 are presented. This figure shows the evolution of the Maierato landslide at different times.

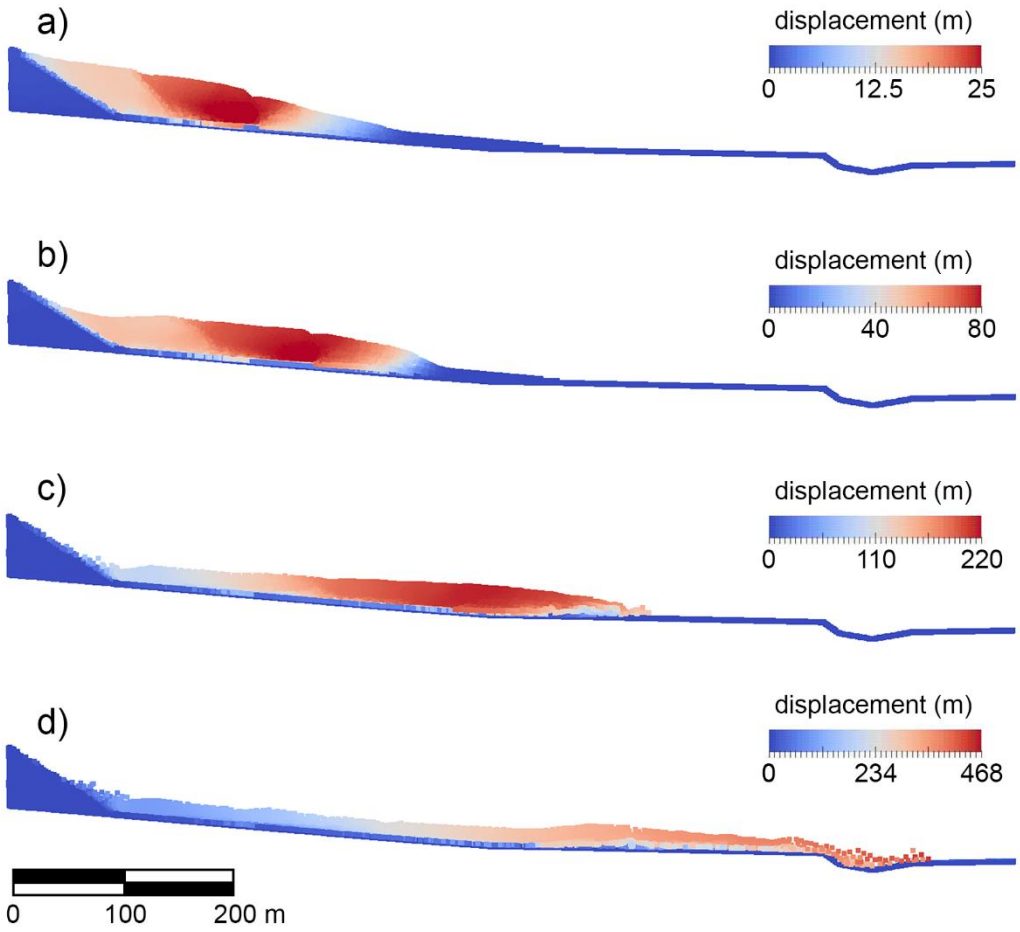

Figure 4.57 – Evolution of the landslide with time during the post-failure stage: a) 5 seconds; b) 10 seconds; c) 20 seconds; d) 60 seconds (final configuration)

As can be seen, the landslide is characterized in this latter analysis by a kinematics which well resembles the documented one. The motion initially involves only the portion of the unstable

soil mass upstream, while the lower portion of the slope is not interested by the movement yet. Indeed, as can be observed, the motion starts from the upper portion of the slope and propagates downstream as a wave. In this way, the tip of the body of landslide is involved in the movement only in a subsequent time of the post-failure stage.

The results of this simulation are consistent with what really occurred, which is also confirmed by the videos filmed during the event. For the sake of completeness, some screenshots taken from these videos and corresponding to the different situations plotted in Figure 4.57 are shown in the following.

Figure 4.58 refers to the initial instants of the post-failure stage of the landslide.

Figure 4.58 – Screenshot taken from a video filmed during the post-failure stage of the landslide, corresponding to the output plotted in Figure 4.57a (black arrows indicate the scarp at 300 m a.s.l., whereas red arrows indicate the scarp at 270 m a.s.l.)

At this time, only the portion of the body of landslide included between the scarps at 300 m a.s.l. and 270 m a.s.l. (indicated

respectively by black and red arrows in Figure 4.58) is involved in the motion, whereas the soil downstream is not interested by the movement yet. This picture corresponds to the output plotted in Figure 4.57a.

The motion proceeds with the increment of the soil displacement of the portion of soil mass currently involved in the movement, with the consequent increase of the height of the scarp at 300 m a.s.l.. Figure 4.59 shows a screenshot taken from the video filmed during the post-failure stage of the landslide, corresponding to the situation just described, in which it is possible to observe the greater height of the scarp at 300 m a.s.l. (indicated with black arrows) as well as the development of the portion of landslide body involved in the movement. This picture corresponds to the output plotted in Figure 4.57b.

Figure 4.59 – Screenshot taken from a video filmed during the post-failure stage of the landslide, corresponding to the output plotted in Figure 4.57b (black arrows indicate the scarp at 300 m a.s.l.)

Figure 4.57c shows that the unstable soil mass is at this time totally involved in the post-failure stage of the landslide, highlighting the huge increment of the height of the scarp at 300 m a.s.l., which has substantially reached its final height.

Figure 4.60 – Screenshot taken from a video filmed during the post-failure stage of the landslide, corresponding to the output plotted in Figure 4.57c

This condition is confirmed by the screenshot reported in Figure 4.60, which points out the height of the scarp at 300 m a.s.l. (indicated with black arrows) as well as the involvement of the portion of the unstable soil mass located downstream (indicated with blue arrows).

Figure 4.61 reports a screenshot referring to the final configuration of the unstable soil mass at the end of the post-failure stage of the landslide. This condition corresponds to the output plotted in Figure 4.57d.

Figure 4.61 – Screenshot taken from a video filmed during the post-failure stage of the landslide, corresponding to the output plotted in Figure 4.57d

The final configuration of material points (Figure 4.57d) is reached in a timeframe of almost one minute, whereas the time actually elapsed between the screenshots reported in Figure 4.58 and Figure 4.61 is about two minutes. Considering the complexity of this phenomenon, the duration of the landslide obtained from the numerical simulation can be considered comparable to that recorded by the available videos.

Finally, some considerations are required about the value of liquefied strength that provides the best agreement between prediction and observation, i.e. $c_u = 35\,kPa$. It is important to specify that this result is understood as a value of *residual strength* (following Seed et al. (1988)), which refers to the liquefied material and accounts for the change of mechanical behavior that affected the soils involved in the landslide body, which behaved

as a viscous fluid. This value of c_u is consistent with experimental data published in the literature, as documented later.

First of all, similar values are obtained from the Marchetti dilatometer tests described in Section 4.4.4. In particular, it is necessary to refer to the test indicated as DMT2, which is located in the landslide body (Figure 4.14) and which interested therefore the unstable soil mass after it travelled all the run-out distance.

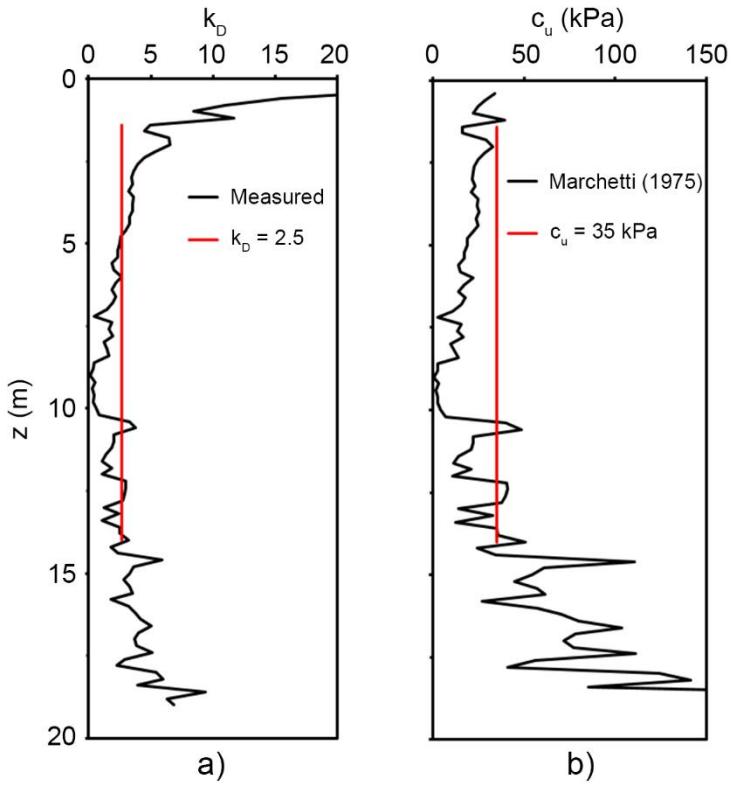

Figure 4.62 – a) Measured and average values of the lateral stress index, k_D; b) Estimated values of the undrained strength in function of the lateral stress index, k_D

The values of undrained strength obtained as a function of the lateral stress index, k_D, using the relationship proposed by Marchetti (1975) are reported in Figure 4.62. As can be seen from this latter figure, the Marchetti dilatometer test performed in the landslide body provides values of the undrained strength whose

average within the depth of interest (which is about 14 m in correspondence of the test DMT2) is consistent with the liquefied strength obtained from the MPM simulation (i.e. 35 kPa), indicated with a red line in Figure 4.62b.

Besides, Figure 4.63 shows a relationship proposed by Seed et al. (1988) between the residual strength of a liquefied sand and the corrected value of the SPT resistance, $(N_1)_{60}$, defined according to Seed et al. (1985).

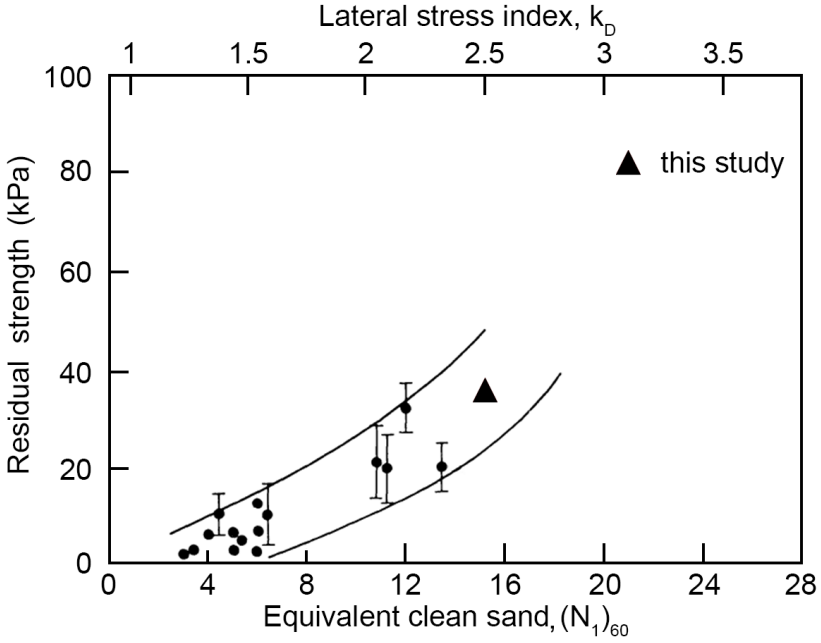

Figure 4.63 – Relationship between residual strength, corrected SPT resistance for sand and lateral stress index (modified after Seed et al. (1988))

Although some standard penetration tests were performed after the event (as documented in Section 4.4.2), there are no available results of SPT resistance within the evaporitic limestone involved in the landslide body. However, many correlations are available in the literature relating the Marchetti lateral stress index, k_D, to the standard penetration test results. Particularly, the correlation

proposed by Robertson & Campanella (1986), which is shown in Figure 4.64, is used to estimate the relative density, D_r, of the liquefied material.

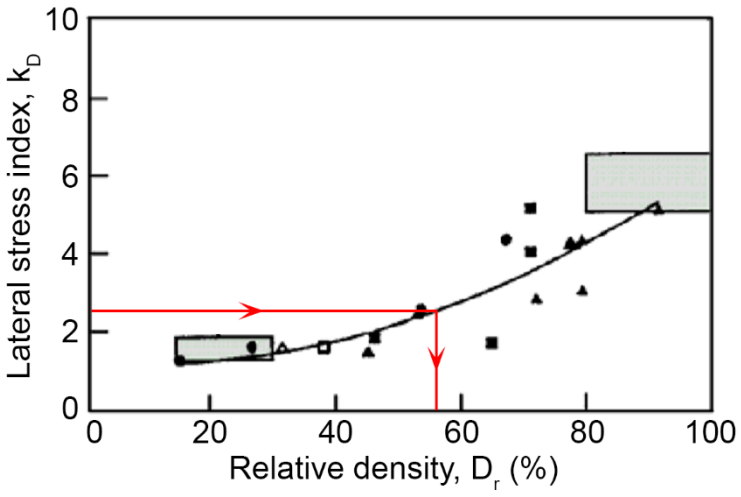

Figure 4.64 – Correlation k_D-D_R for uncemented sands originally proposed by Robertson & Campanella (1986) and including data from Reyna & Chameau (1991) and Tanaka & Tanaka (1998) (modified from Monaco & Marchetti (2007))

After D_r being estimated, some available relationships are used to calculate the value of $(N_1)_{60}$. Specifically, the relationships that this study refers to are those proposed by Gibbs & Holtz (1957), Meyerof (1957) and Skempton (1986). For the case under examination, the average value of the lateral stress index is k_D = 2.5 in the depth of interest (Figure 4.62a), which corresponds to a value of relative density D_r = 56% (Figure 4.64). The average value of $(N_1)_{60}$ calculated using the relationships proposed by the authors afore-mentioned is $(N_1)_{60} = 15.2$. Using the same procedure, the graph proposed by Seed et al. (1988) is updated in this study (Figure 4.63) with the indication of the values of the lateral stress index, k_D, corresponding to the values of $(N_1)_{60}$

originally indicated on the x-axis. For the case under examination, a point representative of the Maierato landslide can be found in the graph proposed by Seed et al. (1988), whose coordinates are defined by $(N_1)_{60} = 15.2$ (which corresponds to the measured average value $k_D = 2.5$) on the x-axis and by the value of the residual strength assessed in this study from the numerical simulation that is 35 kPa on the y-axis. As can be seen from Figure 4.63, this point falls inside the area that defines the liquefiable soils.

From what just said, it emerges that the value of 35 kPa calibrated from the analysis presented in this section is a representative value of the residual strength for the soils involved in the Maierato landslide to properly account for their change of mechanical behavior.

4.10 – Discussion

In this chapter the analysis of the deformation mechanisms of the Maierato landslide is presented. In particular, the analyses of the pre-failure, failure and post-failure stages are reported after a detailed description of the landslide. Indeed, the attention is mainly focused on the analysis of the kinematics of the landslide after failure (i.e. the post-failure stage), which is one of the goal of this dissertation. However, the analyses of the pre-failure and failure stages are also reported for the sake of completeness as

well as to help the understanding of the analysis shown afterwards. The analysis is performed using the material point method (MPM), in order to overcome the drawbacks that emerged during the FEM simulation of the trigger phase after the development of the slip surface, as usual when large displacements are involved in pure Lagrangian calculations. The analysis is performed using the *single-point* formulation. A back-analysis is carried out accounting for different possible scenarios, in order to identify the one that reproduce better the final geometry of the displaced material observed after the event as well as the observed kinematics. Particularly, two different types of analysis are performed.

The first type of analysis can be seen as the natural extension of the FEM analysis of the triggering of the landslide. Therefore, it allows the simulation of the soil displacements that could not be simulated in the FEM analysis due the lack of convergence of this latter method when dealing with large deformations. However, the results obtained in this case are not consistent with what really observed and, consequently, this type of analysis is not representative of the phenomenon that really occurred.

The second type of analysis accounts for the change of mechanical behavior that interested the soil involved in the landslide body after failure, i.e. the evaporitic limestone. In order to take into account the fast nature of the landslide and to implicitly simulate

the excess pore water pressure that could have developed in the interested formation, this analysis is performed in undrained conditions using the liquefied strength of the material, which is calibrated by means of a back-analysis. Numerical results are in good agreement with field observations in terms of both post-failure profile and run-out distance. Besides, also the kinematics obtained from the numerical simulation resembles the real one, which is well documented by some photos and videos taken during the event.

Therefore, it can be finally asserted that the analysis of the post-failure stage of the Maierato landslide carried out accounting for the change of mechanical behavior is satisfactorily representative of the phenomenon really occurred.

Conclusion and final remarks

This dissertation deals with the modeling of problems involving large deformations in geotechnical engineering field. Particularly, the attention is given to the post-failure stage of landslides, whose analysis is currently neglected in engineering practice due to the lack of adequate tools capable for dealing with this kind of problem. Indeed, deformation and failure mechanisms of slopes, which are generally classified in pre-failure, failure, post-failure and reactivation stages, are commonly analyzed by means of simplified methods or traditional numerical techniques. Among simplified methods, the most common ones are the limit equilibrium methods, which do not account for any deformation preceding or following the collapse, and which are therefore suitable for analyzing only the failure and reactivation stages, focusing the attention only on the computation of the safety factor. Instead, traditional numerical techniques, such as the finite element method or the finite difference method, are suitable for adequately simulating the pre-failure stage as well as those of failure and reactivation. On the other hand, these techniques manifest some shortcomings and drawbacks when the calculated deformations and displacements begin to assume high values, as usually happens in the post-failure stage of many landslides. However, an adequate analysis of this latter stage and a reliable prediction of the landslide kinematics after failure could be

particularly useful for minimizing the risk of catastrophic damages. Therefore, the availability of more advanced numerical techniques is required. Different numerical techniques alternative to the traditional ones have been developed in the last years. Among them, the material point method (MPM) is employed to pursue the goals of this dissertation.

In particular, the material point method is used to analyze the post-failure stage of the Senise landslide (26 July 1986) and the Maierato landslide (15 February 2010), which are both well documented in the literature. In both cases, the post-failure profiles obtained from the numerical simulations as well as the calculated run-out distances match satisfactorily well the ones observed in field. Furthermore, there is a good agreement also between the kinematics obtained from the numerical simulations and those really observed.

Some general conclusions, regarding both the method and the analyzed cases, coming from the work carried out in the context of this research, are discussed in the following.

Firstly, the analyses presented in this dissertation demonstrate the suitability and capability of the material point method for dealing with problems involving large deformations and large displacements, avoiding the typical shortcomings of other numerical techniques that are currently more common in engineering practice, such as the finite element method. Indeed,

contrary to this latter method, which suffers a sever mesh distortion after the development of the slip surface with the consequence of lack of accuracy of the solution and underestimation of soil displacements, the material point method does not lose its accuracy independently on the entity of the displacements of material points.

Besides, this work proves the capability of the material point method for analyzing problems involving large deformations and large displacements not only for ideal cases study, but for real landslides as well, which are characterized by the typical difficulties of geotechnical engineering. This finding represents a good perspective from a practical and engineering point of view, since it proves that the material point method can be used for analyzing real problems, helping to establish and design adequate stabilization measures and to prevent or reduce the risk of catastrophic damages.

Regarding the Senise landslide, the back-analysis carried out shows that also the shallower slip surface (i.e. that at 10.5 m from the ground surface) has to be accounted for in the analysis in order to satisfactorily predict the post-failure profile and the run-out distance. Therefore, it can be asserted that this slip surface, which was not recognized important to explain the triggering of this landslide, assumes instead a crucial role during the post-failure stage. Moreover, the analysis performed accounting for

also the presence of the existing structures provides the best agreement between prediction and observation. It is important to point out that their presence is not crucial, but contributes to improve the agreement between the numerical post-failure profile and that detected in field. Finally, in order to obtain the best agreement between prediction and observation, it is necessary to employ the minimum values of the angle of shearing resistance among those belonging to the range found experimentally.

Concerning the Maierato landslide, which has received the attention of researchers from all over the world and which was considerable due to its dimension, run-out distance and catastrophic failure, the analysis presented in this study allows to gain results that would be inconceivable to obtain using traditional numerical techniques. Indeed, despite the complexity of this landslide, the MPM analysis provides a satisfactory agreement between prediction and observation, in terms of run-out distance, post-failure profile and landslide kinematic.

Finally, it can be asserted that a suitable analysis of the post-failure stage can lead to a better understanding of the complex mechanical mechanisms that characterize some landslides, and thereby help in establishing the most effective stabilization measures.

References

Abbo, A., & Sloan, S. (1995). A smooth hyperbolic approximation to the Mohr-Coulomb yield-criterion. *Computers & Structures, 54(3)*, 427-441.

Alonso, E., Yerro, A., & Pinyol, N. (2015). Recent developments of the material point method for the simulation of landslide. *IOP Conf. Ser. 26, 012003 (Int. Symp. Geohazards Geomech, Warwick (UK)).* Warwick (UK).

Alvarado, M. (2018). *Landslide motion assessment including thermal interaction. An MPM approach.* Barcelona: PhD thesis. Universitat politècnica de catalunya.

Anderson, S., & Riemer, M. (1995). Collapse of saturated soil due to reduction in confinement. *J. Geotech. Engng Div., ASCE 121, No. 2*, 216-220.

Anderson, S., & Sitar, N. (1995). Analysis of rainfall-induced debris flow. *J. Geotech. Engng Div., ASCE 121, No. 7*, 544-552.

Bandara, S. (2013). *Material point method to simulate large deformation problems in fluid-saturated granular medium.* Cambridge (UK): PhD thesis, University of Cambridge.

Bandara, S., & Soga, K. (2015). Coupling of soil deformation and pore fluid flow using material point method. *Comput. Geotech. 63(1)*, 199-214.

Bandara, S., Ferrari, A., & Laloui, L. (2016). Modelling landslides in unsaturated slopes subjected to rainfall infiltration using material point method. *International journal for numerical and analytical methods in geomechanics 40(9).*

Bathe, K. (1996). *Finite Element Procedures.* Prentice-Hall, New Jersey.

Belytschko, T., Liu, W., Moran, B., & Elkhodary, K. (2014). *Nonlinear Finite Elements for Continua and Structures, 2nd Edition.* John Wiley & Sons, Chichester.

Bertini, T., Cugusi, F., D'Elia, B., & Rossi-Doria, M. (1986). Lenti movimenti di versante nell'Abruzzo Adriatico: caratteri e criteri di stabilizzazione. *Atti del 16° Convegno Italiano di Geotecnica, Vol. 1*, (pp. 91-100). Bologna.

Bhandari, T., Hamad, F., Moormann, C., Sharma, K., & Westrich, B. (2016). Numerical modelling of seismic slope failure using MPM. *Comput. Geotech.*, 126-134.

Biot, M. (1941). General Theory of Three-Dimensional Consolidation. *Journal of Applied Physics, 12(2)*, 155.

Biot, M. (1955). Theory of Elasticity and Consolidation for a Porous Anisotropic Solid. *Journal of Applied Physics 26(2)*, 182.

Biot, M. (1972). Theory of finite deformations of porous solids. *Indiana University Mathematics Journal 21(7)*, 597-620.

Bishop, A. (1967). Progressive failure - with special reference to the mechanism causing it. *Proc. Geotech. Conf., 2*, (pp. 142-150). Oslo.

Bjerrum, L. (1967). Progressive failure in slopes in overconsolidated plastic clay and clay shales. *J. Soil Mech. Found. Div., ASCE 93, No. 5*, 3-49.

Bolognin, M., Martinelli, M., Bakker, K., & Jonkman, S. (2017). Validation of material point method for soil fluidisation analysis. *J. Hydrodyn., 29*, 431-437.

Bonet, J., & Kulasegaram, S. (2000). Correction and stabilization of smooth particle hydrodynamics methods with applications in metal forming simulations. *Int. J. Numer. Methods Engng 47, No 6*, 1189-1214.

Borrelli, L., Antronico, L., Gullà, G., & Sorriso-Valvo, G. (2014). Geology, geomorphology and dynamics of the 15 February 2010 Maierato landslide (Calabria, Italy). *Geomorphology 208*, 50-73.

Bracegirdle, A., Vaughan, P., & Hight, D. (1992). Displacement prediction using rate effects on residual shear strength. *Proc. 6th Int. Symp. Landslides 1* (pp. 343-347). Christchurch: Balkema, Rotterdam.

Brand, E. (1981). Some thougths on rain-induced slope failure. *Proc. 10th Int. Conf. Soil Mech. Found. Engng, 3*, (pp. 373-376). Stockholm.

Brinkgreve, R. (1994). *Geomaterial Models and Numerical Analysis of Softening.* Delft (NL): PhD Thesis - Technische Universiteit Delft (NL).

Brinkgreve, R., & Bakker, H. (1991). Non-linear finite element analysis of safety factors. *Proc. 7th Int. Conf. on Comp. Methods and Advances in Geomechanics*, (pp. 1117-1122). Cairns, Australia.

Bromhead, E. (1992). *The stability of slopes.* Glasgow: Blackie Academic & Professional.

Bromhead, E. (1998). Lessons from the Selborne slope stability experiment. *Proc. 2nd Simp. Int. "The Geotechnics of Hard Soils-Soft Rocks", Vol. III.* Naples.

Bui, H., Fukagawa, R., Sako, K., & Wells, J. (2011). Slope stability analysis and discontinuous slope failure simulation by elasto-plastic smoothed particle hydrodynamics (SPH) (DPmodel). *Géotechnique 61(7)*, 565-574.

Burland, J. (1990). On the compressibility and shear strength of natural clays. *Géotechnique 3*, 327-378.

Burland, J., Longworth, T., & Moore, J. (1977). A study of ground movement and progressive failure caused by a deep excavation in Oxford clay. *Géotechnique 27, No. 4*, 557-591.

Calvetti, F., di Prisco, C., & Vairaktaris, E. (2017). DEM assessment of impact forces of dry granular masses on rigid barriers. *Acta Geotech. 12*, 129-144.

Casagrande, A. (1975). Liquefaction and cyclic deformation of sands, a critical review. *Proc. 5th Panamerican Conf. Soil Mech. Found. Engng., 5*, (pp. 79-133). Buenos Aires.

Ceccato, F. (2015). *Study of large deformation geomechanical problems with the material point method.* Padova: PhD Thesis.

Ceccato, F., & Simonini, P. (2019). Numerical features used in simulations. In J. Fern, A. Rohe, K. Soga, & E. Alonso, *The material point method for geotechnical engineering: a practical guide* (pp. 101-123). CRC Press.

Ceccato, F., Beuth, L., & Simonini, P. (2016). Analysis of Piezocone Penetration under Different Drainage Conditions with the Two-Phase Material Point Method. *J. Geotech. Geoenvironmental Eng.*

Ceccato, F., Beuth, L., Vermeer, P., & Simonini, P. (2016). Two-phase material point method applied to the study of cone penetration. *Computers and Geotechnics 80*, 440-452.

Ceccato, F., Bisson, A., & Cola, S. (2017). Large displacement numerical study of 3D plate anchors. *European Journal of Environmental and Civil Engineering*.

Ceccato, F., Redaelli, I., Di Prisco, C., & Simonini, P. (2018). Impact forces of granular flows on rigid structures: Comparison between discontiuous (DEM) and continuous (MPM) numerical approaches. *Computers and Geotechnics, 103*, 201-217.

Chan, D., & Morgenstern, N. (1987). Analysis of progressive deformation of the Edmonton Convention Centre excavation. *Canadian Geotechnical Journal*, 430-440.

Chandler, R. (1984). Recent European experience of landslides in over-consolidated clays and soft rocks. *Proc. 4th Int. Symp. Landslides, 1*, (pp. 61-81). Toronto.

Christian, J., & Whitman, R. (1969). A one-dimensional model for progressive failure. *Proc. 7th Int. Conf. Soil Mech. Found. Engng. 2*, (pp. 541-545). Mexico City.

Ciantia, M., Castellanza, R., & Di Prisco, C. (2015). Experimental study on the water-induced weakening of calcarenites. *Rock Mech Rock Eng 48(2)*, 441-461.

Conte, E., Donato, A., Pugliese, L., & Troncone, A. (2016). Kinematics of the Maierato landslide (Calabria, Southern Italy). *Procedia Engineering 158*, 194-199.

Conte, E., Donato, A., Pugliese, L., & Troncone, A. (2018). Analisys of the Maierato landslide (Calabria, Southern Italy). *Landslides (15)*, 1935-1950.

Conte, E., Pugliese, L., & Troncone, A. (2019). Post-failure stage simulation of a landslide using the material point method. *Engineering Geology 253*, 149-159.

Cooper, M., Bromhead, E., Petley, D., & Grant, D. (1998). The Selborne cutting stability experiment. *Géotechnique 48, No. 1*, 83-101.

Courant, R., Friedrichs, K., & Lewy, H. (1967). On the Partial Difference Equations of Mathematical Physics. *IBM J. Res. Dev., 11*, 215-234.

Cruden, D., & Varnes, D. (1996). Landslide types and processes. *In: Turner, A.K.; Schuster, R.L. Landslides investigation and mitigation. Transportation reaserch board, US National Reaserch Council. Special Report 247, Washington DC*, 36-75.

Dai, Z., Huang, Y., Cheng, H., & Xu, Q. (2014). 3D numerical modeling using smoothed particle hydrodynamics of flow-like landslide propagation triggered by the 2008 Wenchuan earthquake. *Engineering Geology*, 21-33.

Del Prete, M., & Hutchinson, J. (1988). La frana di Senise del 26-7-1986 nel quadro morfologico del versante meridionale della collina Timpone. *Rivista Italiana di Geotecnica, Vol. 22, No 1*, 7-34.

D'Elia, B., Picarelli, L., Leroueil, S., & Vaunat, J. (1998). Geotechnical characterization of slope movements in structurally complex clay soils and stiff jointed clay. *Italian Geotech. J. No. 32, No. 3*, 5-32.

Demers, D., Leroueil, S., & D'Astous, J. (1999). In situ testing in a landslide area at Maskinongé, Québec. *Can. Geotech. J., 36, No. 6*, 1001-1014.

Detournay, C., & Dzik, E. (2006). Nodal Mixed Discretization for tetrahedral elements. *4th International FLAC Symp. Numer. Model. GeoMechanics.* Madrid: Itasca Consulting Group, Inc.

di Prisco, C., & Imposimato, S. (1996). Time dependent mechanical behaviour of loose sands. *Mechanics of cohesive-frictional materials, Vol. 1*, 45-73.

Di Prisco, C., & Imposimato, S. (2002). Static liquefaction of a saturated loose sand stratum. *Int. J. Solids Struct., 39*, 3523-3541.

Doglioni, A., Galeandro, A., Guerricchio, A., Fortunato, G., Guglielmo, E., Ponte, M., & Simeone, V. (2011). Analysis of the rainfall preceding the activation of the large Maierato landslide in 2010. *Proceedings of the 2nd World Landslide Forum.* Rome.

Doglioni, A., Galeandro, A., Guerricchio, A., Fortunato, G., Guglielmo, E., Ponte, M., & Simeone, V. (2013). Analysis of the rainfall preceding the activation of the large Maierato landslide in 2010. *Landslide Sci Practice: Global Environ Change 4*, 107-114.

Eckersley, D. (1990). Instrumented laboratory flowslides. *Géotechnique 40, No. 3*, 489-502.

Eden, W. (1977). Evidence of creep in steep natural slopes in Champlain sea clays. *Can. Geotech. J., 14 No. 4*, 620-627.

Eigenbrod, K., Graham, J., & Burak, J. (1992). Influence of cycling porewater pressures and principal stress ratios on drained deformations in clay. *Canadian Geotechnical Journal*, 326-333.

Esu, F. (1986). La scelta del tipo e delle modalità di intervento nei pendii. *Atti del 16° Convegno Italiano di Geotecnica, vol III*, (pp. 257-272). Bologna.

Fern, E., de Lange, D., Zwanenburg, C., Teunissen, J., Rohe, A., & Soga, K. (2017). Experimental and numerical investigations of dyke failures involving soft materials. *Engineering Geology*, 130-139.

Fern, J., Rohe, A., Soga, K., & Alonso, E. (2019). *The Material Point Method for Geotechnical Engineering. A Practical Guide. 1st Edn.* CRC Press.

Flanagan, D., & Belytschko, T. (1981). Simultaneous relaxation in structural dynamics. *Journal of the Engineering Mechanics Division 107*, 1039-1055.

Fleming, R., Ellen, S., & Algus, M. (1989). Transformation of dilative and contractive landslide debris into debris flows - An example from Marin County, California. *Engng Geol 27*, 201-223.

Fredlund, D. (2000). The 1999 R.M. Hardy Lecture: The implementation of unsaturated soil machanics into geotechnical engineering. *Can Geotech Journal 37, No. 5*, 963-986.

Fredlund, D., Xing, A., Fredlund, M., & Barbour, S. (1996). The relationship of the unsaturated soil shear strength to the soil-water charateristic curve. *Can Geotech Journal 33, No. 3*, 440-448.

Galavi, V., & Schweiger, H. (2010). Nonlocal Multilaminate Model for Strain Softening Analysis. *International Journal of Geomechanics. ASCE*, 30-44.

Gattinoni, P., & Scesi, L. (2013). Landslide hydrogeological susceptibility of Maierato (Vibo Valentia, Southern Italy). *Nat. Hazards 66*, 629-648.

Gattinoni, P., Scesi, L., Arieni, L., & Canavesi, M. (2012). The February 2010 large landslide at Maierato, Vibo Valentia, Southern Italy. *Landslides (9)*, 255-261.

Gibbs, H., & Holtz, W. (1957). Research on determining the density of sands by spoon penetration testing,. *Proc. IV ICSMFE.* London.

Guerricchio, A., & Melidoro, G. (1988). Urbanizzazione e franosità delle formazioni sabbiose plio-pleistoceniche in Basilicata: il caso di Senise. *Mem. Soc. Geol. Ital. 37*, 745-774.

Guerricchio, A., Fortunato, G., Guglielmo, E., Ponte, M., & Simeone, V. (2010). Condizionamenti idrologici da DGPV nell'attivazione della grande frana di Maierato (VV) del 2010. *XXXI Corso di aggiornamento in tecniche per la difesa dall'inquinamento, EdiBios*, (pp. 661-706).

Guerriero, G. (1995). *Modellazione sperimentale del comportamento meccanico di terreni in colata.* PhD Thesis, Iniversità degli studi di Napoli Federico II.

Hallquist, J. (2006). *ANSYS/LS-DYNA Theoretical Manual.* Livermore Software Technology Corporation.

Harlow, F. (1964). The particle-in-cell computing method for fluid dynamics. *Methods in computational physics, Vol. 3, No. 3*, 319-343.

Harp, E., Weels, W. I., & Sarmiento, J. (1990). Pore pressure response during failure in soils. *Geol. Soc. Am. Bull. 102, No. 4*, 428-438.

Hungr, O. (1981). *Dynamics of rock avalanches and other types of slope movements.* PhD Thesis, University of Alberta, Edmonton.

Hungr, O., Leroueil, S., & Picarelli, L. (2014). The Varnes classification of landslide type, an update. *Landslides (11)*, 167-194.

Hungr, O., Morgan, G., & Kellerhals, R. (1984). Quantitative analysis of debris torrent hazards for design of remedial measures. *Canadian Geot. J.*, 663-677.

Hutchinson, J. (1987). Mechanisms producting large displacements in landslides on pre-existing shears. *Mem. Geol. Soc. of China, 9*, 175-200.

Irons, B. (1970). *Applications of a theorem of eigenvalues to finite element problems (cr/132/70).* Tech. Rep. University of Wales, Department of Civil Engineering, Swansea.

Kularathna, S., & Soga, K. (2017). Projection Method in Material Point Method for Modeling Incompressible Materials. *Procedia Engineering, 175*, 57-64.

Lancellotta, R. (2009). *Geotechnical engineering, II edition.* London: Taylor & Francis.

Lancellotta, R. (2011). *Progettazione geotecnica secondo l'Eurocodice 7 (UNI EN 1997) e le Norme Tecniche per le Costruzioni (NTC 2008).* Hoepli.

Lee, H., Ellen, S., & Kayen, R. (1988). Predicting transformation of shallow landslides into high-speed debris flows. *Proc. 5th Int. Symp. Landslides, Lausanne 1*, (pp. 713-718). Balkema, Rotterdam.

Leroueil, S. (2001). Natural slopes and cuts: movements and failure mechanism. *39th Rankine Lecture. Géotechnique, 51, 3*, 197-243.

Leroueil, S., & Marques, M. (1996). State of the art on the importance of strain rate and temperature effects in geotechnical engineering. *Proc. ASCE Conv.* (pp. 1-60). Washington: Geotechnical Special Pubblication No. 61.

Leroueil, S., & Vaughan, P. (1990). The general and congruent effects of structure in natural soils and weak rocks. *Géotechnique 40, No. 3*, 467-488.

Leroueil, S., Vaunat, J., Picarelli, L., Locat, J., Lee, H., & Faure, R. (1996). Geotechnical characterization of slope movements. *Proc. 7th Int. Symp. on Landslides, Vol. 1*, (pp. 53-74). Trondheim.

Li, X., Wu, Y., He, S., & Su, L. (2016). Application of the material point method to simulate the post-failure runout processes of the Wangjiayan landslide. *Engineering Geology*, 1-9.

Maljaars, J., Labeur, R., Moller, M., & Uijttewaal, W. (2017). A Numerical Wave Tank Using a Hybrid Particle-mesh Approach. *Procedia Engineering, 175*, 21-28.

Marchetti, S. (1975). A new in situ test for the measurement of horizontal soil deformability. *Proceedings of the Conference on In Situ Measurement of Soil Properties, ASCE*, (pp. 255-259). Raleigh, NC, USA.

Marchetti, S. (1980). In situ tests by flat dilatometer. *Journal of the Geotech. Engin. Division, ASCE 106*, 299-321.

Martinelli, M., & Rohe, A. (2015). Modelling fluidization and sedimentation using material point method. *Proceedings of the 1st Pan-American Congress on Computational Mechanics, 27-29 April 2015*, (pp. 1-12). Buenos Aires (Argentina).

Martinelli, M., Luger, D., Talmon, A., & Galavi, V. (2019). *Unstable behaviour of a sand cap placed over a weak sensitive clay deposit.* Delft (The Netherlands): Deltares.

Martinelli, M., Rohe, A., & Soga, K. (2017). Modeling dike failure using the Material Point Method. *Procedia Engineering 175(2016)*, 341-348.

Meyerhof, G. (1957). The Ultimate Bearing Capacity of Foundations on Slopes. *Proc. 4th ICSMFE*, (pp. 384-386). London.

Mieremet, M. (2015). *Numerical stability for velocity-based 2-phase formulation for geotechnical dynamic analysis.* Delft (The Netherlands): Report 15-03, ISSN 1389-6520, Reports of the Delft Institute of Applied Mathematics, Delft University of Technology.

Moller, B., Rankka, K., Sallfors, G., & Ahnberg, H. (1989). Horizontal stresses amd deformations in slopes - Case histories. *Commission on Slope Stability Report* (pp. 2-89). Linkoping, Sweden: Royal Swedish Academy of Engineering Sciences.

Monaco, P., & Marchetti, S. (2007). Evaluating liquefaction potential by seismic dilatometer (SDMT) accounting for aging/stress history. *4th International Conference on Earthquake Geotechnical Engineering.*

Morgenstern, N. (1977). Slopes and excavations in heavily overconsolidated clays. *Proc. 9th Int. Conf. Soil Mechanics and Foundation Engineering, Vol. II*, (pp. 567-581). Tokyo.

Morgenstern, N., & Price, V. (1965). The analysis of the stability of general slip surfaces. *Gèotechnique, vol. 15, n. 1*, 79-93.

Morgenstern, N., & Tchalencko, J. (1967). Microscopic observations on shear zones from slips in natural clays. *Proceeding of the geotechnical conference, Vol. 1*, (pp. 147-152). Oslo.

Morgenstern, N., & Tchalenko, J. (1967). Microscopic structures in kaolin subjected to direct shear. *Géotechnique 17*, 309-328.

Nemcok, A., Pasek, J., & Rybar, J. (1972). Classification of landslides and other mass movements. *Rock Mechanics*, 71-78.

Nova, R. (2002). *Fondamenti di meccanica delle terre.* Mc Graw Hill Education.

Nova, R., Castellanza, R., & Tamagnini, C. (2003). A constitutive model for bonded geomaterials subject to mechanical and/or chemical degradation. *Int J Numer Anal Methods Geomech 27(9)*, 705-732.

Ottosson, E., & Johansson, L. (1995). Behaviour of a natural slope close to failure. *Proc. 11th Eur. Conf. Soil Mech. Found. Engng, 4*, (pp. 98-100). Copenhagen.

Pastor, M., Haddad, B., Sorbino, G., Cuomo, S., & Drempetic, V. (2009). A depth-integrated, coupled SPH model for flow-like landslides and related phenomena. *Int. J. Numer. Anal. Methods Geomech. 33(2)*, 143-172.

Perzyna, P. (1963). The constitutive equations for rate sensitive plastic materials. *Q. Appl. Math., 20*, 321-332.

Picarelli, L. (1993). Structure and properties of clay shales involved in earthflows. *Proc. Int. Symp. "The Geotechnical Engineering of Hard Soils-Soft Rocks", Vol. III*, (pp. 2009-2019). Athens.

Picarelli, L. (1999). Alcune considerazioni sui meccanismi di innesco e di propagazione delle colate in terreni sciolti e detritici. *Convegno su Previsione e Prevenzione di Movimenti Franosi Rapidi*, (pp. 163-179). Trento.

Picarelli, L. (2000). *Meccanismi di deformazione e rottura dei pendii.* Napoli: Hevelius edizioni.

Pinyol, N., Alvarado, M., Alonso, E., & Zabala, F. (2018). Thermal effects in landslide mobility. *Géotechnique 68, 6*, 528-545.

Pirulli, M. (2005). *Numerical modelling of landslide runout.* Ph.D. Thesis, Politecnico di Torino.

Pirulli, M., & Pastor, M. (2012). Numerical study on the entrainment of bed material into rapid landslides. *Géotechnique 62(11)*, 959-972.

Popescu, M. (1993). General co-report, Session 4: Slope stability and protection. *Proc. Int. Symp. Geotech. Engng Hard Soils - Soft Rocks, Athens 3*, (pp. 1965-2006). Balkema, Rotterdam.

Potts, D., & Zdravkovic, L. (1999). *Finite element analysis in geotechnical engineering.* Thomas Telford.

Potts, D., Dounias, G., & Vaughan, P. (1990). Finite element analysis of progressive failure of Carsington embankment. *Géotechnique 40, No. 1*, 79-101.

Potts, D., Kovacevic, N., & Vaughan, P. (1997). Delayed collapse of cut slopes in stiff clay. *Géotechnique 47, No. 5*, 953-982.

Redaelli, I., Ceccato, F., di Prisco, C., & Simonini, P. (2017). Solid-fluid Transition in Granular Flows: MPM Simulations with a New Constitutive Approach. *Procedia Engineering, 175*, 80-85.

Reik, G., & Hesselmann, F. (1977). A study of kinematics and dynamics aspects of rock slides. *ISMES, No. 9*, 97-122.

Remmerswaal, G., Bolognin, M., Vardon, P., Hicks, M., & Rohe, A. (2019). Implementation of non-trivial boundary conditions in MPM for geotechnical applications. *Conference: MPM 2019 - 2nd International Conference on the Material Point Method for Modelling Soil-Water-Structure Interaction.* Cambridge, UK.

Reyna, F., & Chameau, J. (1991). Dilatometer Baased Liquefaction Potential of Sites in the Imperial Valley. *Second International Conference on Recent Advances in Geotechnical Earthquake Engineering and Soil Dynamics*, (pp. 385-392). St. Louis, Missouri.

Rezania, M., Bonnier, P., Brinkgreve, R., & Karstunen, M. (2012). Non-local regularization of Drucker-Prager softening model. *Proceedings of the 20th UK Conference of the Association for Computational Mechanics in Engineering*, (pp. 275-278). Manchester.

Riedel, W. (1929). Zur mechanik geologischer brucherscheinungen. Ein Beitrag zum Problem der `Fiederspalten'. *Centralblatt fur Mineralogie, Geologie, und Paleontologie, Part B*, 354-368.

Robertson, P., & Campanella, R. (1986). Estimating liquefaction potential of sands using the flat dilatometer. *Geotech. Testing J. Vol. 9, No. 1*, 38-40.

Rohe, A., & Liang, D. (2017). Modelling large deformation and soil-water-structure interaction with the material point method: Briefing on MPM2017. *Journal of Hydrodynamics, Ser. B, 29(31)*, 393-396.

Rohe, A., & Martinelli, M. (2017). Material point method and applications in geotechnical engineering. *Conference Proc. of the Workshop on Numerical Methods in Geotechnics*, (pp. 57-72). Hamburg, Germany.

Russo, C. (1997). *Caratteri evolutivi dei movimenti traslativi e loro interpretazione meccanica attraverso l'analisi numerica.* Tesi di Dottorato, Università di Napoli Federico II.

Santos, O., Lacerda, W., & Ehrlich, M. (1996). Discussion of 'Collapse of saturated soil due to reduction in confinement' by Anderson & Riemer (1995). *J. Geotech. Engng. Div., ASCE 122, No. 6*, 505-506.

Scaringi, G., Fan, X., Xu, Q., Liu, C., Ouyang, C., Domènech, G., . . . Dai, L. (2018). Some considerations on the use of numerical methods to

simulate past landslides and possible new failures: the case of the recent Xinmo landslide (Sichuan, China). *Landslides*.

Schadlich, B. (2012). *A Multilaminate Constitutive Model for Stiff Soils.* Graz: PhD Dissertation. Institute for Soil Mechanics and Foundation Engineering. Graz University of Technology, Austria.

Seed, H., Seed, R., Harder, L., & Jong, H. (1988). *Re-evaluation of the lower San Fernando dam. Report 2: Examination of the post-earthquake slide of February 9, 1971.*

Seed, H., Tokimatsu, K., & Chung, R. (1985). Influence of SPT procedures in soil liquefaction resistance evaluations. *Journal of Geotechnical Engineering, ASCE, Vol. 111, No. 12*, 1425-1445.

Skempton, A. (1964). 4th Rankine Lecture: Long term stability of clay slopes. *Géotechnique 14, No. 2*, 77-101.

Skempton, A. (1967). Some observations on tectonic shear zone. *Proc. 2nd Int. Conf. Rock Mechanics, 1*, (pp. 329-335). Belgrade.

Skempton, A. (1970). First-time slides in overconsolidated clays. *Géotechnique*, 320-324.

Skempton, A. (1985). Residual strength of clays in landslides, folded strata and the laboratory. *Géotechnique 35, No. 1*, 3-18.

Skempton, A. (1986). Standard penetration test procedures and the effects in sands of overburden pressure, relative density, particle size, aging and overconsolidation. *Géotechnique, 36, 3*, 425-447.

Skempton, A., & Hutchinson, J. (1969). Stability of natural slopes and embankment foundation. *State of the Art report, 7th ICSMFE*, (pp. 291-340). Mexico City.

Skempton, A., & Petley, D. (1967). The strength along structural discontinuities of stiff clay. *Proceedings of the geotechnical conference, Vol. 2*, (pp. 29-46). Oslo.

Soga, K., Alonso, E., Yerro, A., Kumar, K., & Bandara, S. (2016). Trends in large-deformation analysis of landslide mass movements with particular emphasis on the material point method. *Géotechnique 66 (3)*, 248-273.

Solowsky, W., & Sloan, S. (2015). Evaluation of material point method for use in geotechnics. *Int. J. Numer. Anal. Methods Geomech. 39(7)*, 685-701.

Sulsky, Chen, & Schreyer. (1994). A particle method for hystory-depend materials. *Comput Methods Appl Mech Eng 118*, 179-196.

Sulsky, Zhou, & Schreyer. (1995). Application of a particle-in-cell method to solid mechanics. *Computer Physics Communications*, 236-252.

Tanaka, H., & Tanaka, M. (1998). Characterization of sandy soils using CPT and DMT. *Soils and foundations, Vol. 38, No. 3*, 55-65.

Tang, H., Liu, X., Hu, X., & Griffiths, D. (2015). Evaluation of landslides mechanisms characterized by high-speed mass ejection and long-run-out based on events following the Wenchuan earthquake. *Engineering Geology, 194*, 12-24.

Tavenas, F. (1984). Landslides in Canadian sensitive clays: a state-of-the-art. *Proc. 4th Int. Symp. Landslides, 1*, (pp. 141-153). Toronto.

Terzaghi, K. (1950). Mechanism of landslides. *In: Application of geology to engineering practice (Berkley volume) (ed. S. Paige)* (pp. 83-123). New York: Geological Society of America.

Terzaghi, K., & Peck, R. (1948). *Soil mechanics in engineering practice.* New York: John Wiley.

Totani, G., Marchetti, S., Monaco, P., & Calabrese, M. (1999). Impiego della prova dilatometrica (DMT) nella progettazione geotecnica. *Proceedings of the 20th Convegno Nazionale di Geotecnica*, (pp. 301-308). Parma, Italy.

Tran, Q., & Solowski, W. (2019). Generalized Interpolation Material Point Method modelling of large deformation problems including strain-rate effects - Application to penetration and progressive failure problems. *Computers and Geotechnics*, 249-265.

Troncone, A. (2005). Numerical analysis of a landslide in soils with strain-softening behaviour. *Géotechnique 55, No 8*, 585-596.

Troncone, A., Conte, E., & Donato, A. (2014). Two and three-dimensional numerical analysis of the progressive failure that occured in an excavation-induced landslide. *Engineering Geology 183*, 265-275.

Troncone, A., Conte, E., & Pugliese, L. (2019). Analysis of the Slope Response to an Increase in Pore Water Pressure Using the Material Point Method. *Water, 11, 1446*.

Urciuoli, G. (1990). *Contributo alla caratterizzazione geotecnica delle frane dell'Appennino.* Università di Napoli Federico II: Istituto di Tecnica delle Fondazioni e Costruzioni in Terra.

Varnes, D. (1978). Slope movement types and processes. *In: Schurster, R.L.; Krizek, R.J. Landslides, analysis and control, special report 176: Transportation reaserch board, National Academy of Sciences, Whashington DC*, 11-33.

Vaughan, P., & Hamza, M. (1977). Clay embankments and foundations: Monitoring stability by measuring deformations. Specialy Session 8: Deformation of earth-rockfill dams. *Proc. 9th Int. Conf. Soil. Mech. Found. Engng*, (pp. 37-48). Tokyo.

Vaunat, J., Leroueil, S., & Faure, R. (1994). Slope movements: a geotechnical perspective. *Proc. 7th Cong. Int. Assoc. Engng Geol.*, (pp. 1637-1646). Lisbon.

Viggiani, C., & Di Maio C. (1991). Resistenza a taglio mobilitata nella frana di Senise. *Gruppo nazionale di coordinamento per gli studi di ingegneria geotecnica del C.N.R., Convegno sul tema: Deformazioni in prossimità della rottura e resistenza dei terreni naturali e delle rocce, Vol. 1*, (pp. 133-158). Ravello (SA).

Viggiani, C., & Di Maio, C. (1991). Resistenza a taglio mobilitata nella frana di Senise. In C. Gruppo Nazionale di Coordinamento per gli Studi di Ingegneria Geotecnica, *Convegno sul tema: Deformazioni in prossimità della rottura e resistenza dei terreni naturali e delle rocce 1* (pp. 133-158). Ravello, Italy: C.N.R., Rome.

Vulliet, L. (1986). *Modélisation des pentes naturelles en mouvement.* Ecole Polytechnique Fédérale de Lausanne, Switzerland: Thesis No. 635.

Wang, B., Hicks, M., & Vardon, J. (2016). Slope failure analysis using the random material point method. *Géotechnique Letters 6*, 1-6.

Wilcox, R., Harding, T., & Seely, D. (1973). Basic wrench tectonics. *Am. Assoc. Petroleum Geol. Bull. 57*, 74-96.

Wobbes, E., Moller, M., Galavi, V., & Vuik, C. (2018). Conservative Taylor least squares reconstruction with application to material point methods. *Internationa Journal for Numerical Methods in Engineering / Volume 117, Issue 3*.

Yerro, A. (2015). *MPM modeling of landslides in brittle and unsaturated soils.* Barcelona: PhD Thesis.

Yerro, A., Alonso, E., & Pinyol, N. (2015). The material point method for unsuturated soils. *Géotechnique (65)*, 201-217.

Yerro, A., Alonso, E., & Pinyol, N. (2016). Run-out of landslides in brittle soils. *Gomputers and Geotechnics 80*, 427-439.

Yerro, A., Soga, K., & Bray, J. (2018). Runout evaluation of Oso landslide with the material point method. *Can. Geotech. J.*

Zabala, F., & Alonso, E. (2011). Progressive failure of Aznalcòllar dam using the material point method. *Géotechnique 61(9)*, 795-808.

Zhang, Chen, & Liu. (2017). *The Material Point Method - A continuum-based particle method for extreme loading cases.* Elsevier.

Zhang, X., Krabbenhoft, K., Sheng, D., & Li, W. (2015). Numerical simulation of a flow-like landslide using the particle finite element method. *Comput. Mech. 55(1)*, 167-177.

Zienkiewicz, O. (1982). Basic formulation of static and dynamic behaviour of soil and other porous media. In *Numerical methods in geomechanics* (pp. 39-55). Springer.

Zienkiewicz, O., & Cormeau, I. (1974). Viscoplasticity, plasticiy and creep in elastic solids: a unified numerical solution approach. *Int. J. Numer. Methods Eng., 8*, 821-845.

Zienkiewicz, O., & Shiomi, T. (1984). Dynamic behaviour of saturated porous media; the generalized Biot formulation and its numerical solution. *International Journal for Numerical and Analytical Methods in Geomechanics 8*, 71-93.

Zienkiewicz, O., Chan, A., Pastor, M., Schrefler, B., & Shiomi, T. (1999). *Computational geomechanics.* Wiley Chichester.

Zienkiewicz, O., Chan, H., Pator, M., Paul, D., & Shiomi, T. (1990). Static and Dynamic Behaviour of Soils: A Rational Approach to Quantitative Solutions. I. Fully Saturated Problems. *Proceedings of the Royal Society A: Mathematical, Physical and Engineering Sciences 429 (1877)*, (pp. 285-309).

Zienkiewicz, O., Chang, C., & Bettess, P. (1980). Drained, undrained, consolidating and dynamic behaviour assumptions in soils. *Géotechnique 30(4)*, 385-395.